Lawrence Berkeley National Laboratory
Lawrence Berkeley National Laboratory

Title
The IceCube Collaboration:contributions to the 30 th International Cosmic Ray Conference (ICRC 2007),

Permalink
https://escholarship.org/uc/item/1nr13682

Authors
Ackermann, M.
IceCube Collaboration

Publication Date
2008-11-26

Peer reviewed

The IceCube Collaboration: contributions to the 30 th International Cosmic Ray Conference (ICRC 2007),

The IceCube Collaboration

arXiv:0711.0353v1 [astro-ph] 2 Nov 2007

The IceCube Collaboration:

contributions to the
30 th International Cosmic Ray Conference (ICRC 2007),
Merida, Yucatan Mexico,
August 2007

Abstract

This paper bundles 40 contributions by the IceCube collaboration that were submitted to the 30th International Cosmic Ray Conference ICRC 2007. The articles cover studies on cosmic rays and atmospheric neutrinos, searches for non-localized, extraterrestrial ν_e, ν_μ and ν_τ signals, scans for steady and intermittent neutrino point sources, searches for dark matter candidates, magnetic monopoles and other exotic particles, improvements in analysis techniques, as well as future detector extensions.

The IceCube observatory will be finalized in 2011 to form a cubic-kilometer ice-Cherenkov detector at the location of the geographic South Pole. At the present state of construction, IceCube consists of 52 paired IceTop surface tanks and 22 IceCube strings with a total of 1426 Digital Optical Modules deployed at depths up to 2350 m. The observatory also integrates the 19 string AMANDA subdetector, that was completed in 2000 and extends IceCube's reach to lower energies. Before the deployment of IceTop, cosmic air showers were registered with the 30 station SPASE-2 surface array.

IceCube's low noise Digital Optical Modules are very reliable, show a uniform response and record waveforms of arriving photons that are resolvable with nanosecond precision over a large dynamic range. Data acquisition, reconstruction and simulation software are running in production mode and the analyses, profiting from the improved data quality and increased overall sensitivity, are well under way.

The IceCube Collaboration

M. Ackermann[34], J. Adams[11], J. Ahrens[22], K. Andeen[21], J. Auffenberg[33], X. Bai[24], B. Baret[9], S. W. Barwick[16], R. Bay[5], K. Beattie[7], T. Becka[22], J. K. Becker[13], K.-H. Becker[33], M. Beimforde[6], P. Berghaus[8], D. Berley[12], E. Bernardini[34], D. Bertrand[8], D. Z. Besson[18], E. Blaufuss[12], D. J. Boersma[21], C. Bohm[28], J. Bolmont[34], S. Böser[34], O. Botner[31], A. Bouchta[31], J. Braun[21], T. Burgess[28], T. Castermans[23], D. Chirkin[7], B. Christy[12], J. Clem[24], D. F. Cowen[30, 29], M. V. D'Agostino[5], A. Davour[31], C. T. Day[7], C. De Clercq[9], L. Demirörs[24], F. Descamps[14], P. Desiati[21], G. de Vries-Uiterweerd[32], T. DeYoung[30], J. C. Diaz-Velez[21], J. Dreyer[13], J. P. Dumm[21], M. R. Duvoort[32], W. R. Edwards[7], R. Ehrlich[12], J. Eisch[21], R. W. Ellsworth[12], P. A. Evenson[24], O. Fadiran[3], A. R. Fazely[4], K. Filimonov[5], C. Finley[21], M. M. Foerster[30], B. D. Fox[30], A. Franckowiak[33], R. Franke[34], T. K. Gaisser[24], J. Gallagher[20], R. Ganugapati[21], H. Geenen[33], L. Gerhardt[16], A. Goldschmidt[7], J. A. Goodman[12], R. Gozzini[22], T. Griesel[22], A. Groß[15], S. Grullon[21], R. M. Gunasingha[4], M. Gurtner[33], C. Ha[30], A. Hallgren[31], F. Halzen[21], K. Han[11], K. Hanson[21], D. Hardtke[5], R. Hardtke[27], Y. Hasegawa[10], T. Hauschildt[24], J. Heise[32], K. Helbing[33], M. Hellwig[22], P. Herquet[23], G. C. Hill[21], J. Hodges[21], K. D. Hoffman[12], B. Hommez[14], K. Hoshina[21], D. Hubert[9], B. Hughey[21], J.-P. Hülß[1], P. O. Hulth[28], K. Hultqvist[28], S. Hundertmark[28], M. Inaba[10], A. Ishihara[10], J. Jacobsen[21], G. S. Japaridze[3], H. Johansson[28], J. M. Joseph[7], K.-H. Kampert[33], A. Kappes[21, a], T. Karg[33], A. Karle[21], H. Kawai[10], J. L. Kelley[21], J. Kiryluk[7], F. Kislat[6], N. Kitamura[21], S. R. Klein[7], S. Klepser[34], G. Kohnen[23], H. Kolanoski[6], M. Kowalski[6], L. Köpke[22], T. Kowarik[22], M. Krasberg[21], K. Kuehn[16], T. Kuwabara[24], M. Labare[8], K. Laihem[1], H. Landsman[21], R. Lauer[34], H. Leich[34], D. Leier[13], I. Liubarsky[19], J. Lundberg[31], J. Lünemann[13], J. Madsen[27], R. Maruyama[21], K. Mase[10], H. S. Matis[7], T. McCauley[7], C. P. McParland[7], K. Meagher[12], A. Meli[13], T. Messarius[13], P. Mészáros[30, 29], H. Miyamoto[10], T. Montaruli[21, b], A. Morey[5], R. Morse[21], S. M. Movit[29], K. Münich[13], R. Nahnhauer[34], J. W. Nam[16], P. Nießen[24], D. R. Nygren[7], A. Olivas[12], M. Ono[10], S. Patton[7], C. Peña-Garay[26], C. Pérez de los Heros[31], A. Piegsa[22], D. Pieloth[34], A. C. Pohl[31, c], R. Porrata[5], J. Pretz[12], P. B. Price[5], G. T. Przybylski[7], K. Rawlins[2], S. Razzaque[30, 29], P. Redl[12], E. Resconi[15], W. Rhode[13], M. Ribordy[17], A. Rizzo[9], S. Robbins[33], W. J. Robbins[30], P. Roth[12], F. Rothmaier[22], C. Rott[30], C. Roucelle[7], D. Rutledge[30], D. Ryckbosch[14], H.-G. Sander[22], S. Sarkar[25], K. Satalecka[34], S. Schlenstedt[34], T. Schmidt[12], D. Schneider[21], D. Seckel[24], B. Semburg[33], S. H. Seo[30], Y. Sestayo[15], S. Seunarine[11], A. Silvestri[16], A. J. Smith[12], C. Song[21], G. M. Spiczak[27], C. Spiering[34], M. Stamatikos[21, d], T. Stanev[24], T. Stezelberger[7], R. G. Stokstad[7], M. C. Stoufer[7], S. Stoyanov[24], E. A. Strahler[21], T. Straszheim[12], K.-H. Sulanke[34], G. W. Sullivan[12], T. J. Sumner[19], Q. Swillens[8], I. Taboada[5], O. Tarasova[34], A. Tepe[33], L. Thollander[28], S. Tilav[24], M. Tluczykont[34], P. A. Toale[30], D. Tosi[34], D. Turčan[12], N. van Eijndhoven[32], J. Vandenbroucke[5], A. Van Overloop[14], V. Viscomi[30], C. Vogt[1], B. Voigt[34], W. Wagner[30], C. Walck[28], H. Waldmann[34], T. Waldenmaier[24], M. Walter[34], Y.-R. Wang[21], C. Wendt[21], C. H. Wiebusch[1], C. Wiedemann[28], G. Wikström[28], D. R. Williams[30], R. Wischnewski[34], H. Wissing[1], K. Woschnagg[5], X. W. Xu[4], G. Yodh[16], S. Yoshida[10], J. D. Zornoza[21, e]

[1] III Physikalisches Institut, RWTH Aachen University, D-52056 Aachen, Germany
[2] Dept. of Physics and Astronomy, University of Alaska Anchorage, 3211 Providence Dr., Anchorage, AK 99508, USA
[3] CTSPS, Clark-Atlanta University, Atlanta, GA 30314, USA
[4] Dept. of Physics, Southern University, Baton Rouge, LA 70813, USA
[5] Dept. of Physics, University of California, Berkeley, CA 94720, USA
[6] Institut für Physik, Humboldt-Universität zu Berlin, D-12489 Berlin, Germany
[7] Lawrence Berkeley National Laboratory, Berkeley, CA 94720, USA
[8] Université Libre de Bruxelles, Science Faculty CP230, B-1050 Brussels, Belgium
[9] Vrije Universiteit Brussel, Dienst ELEM, B-1050 Brussels, Belgium
[10] Dept. of Physics, Chiba University, Chiba 263-8522 Japan
[11] Dept. of Physics and Astronomy, University of Canterbury, Private Bag 4800, Christchurch, New Zealand

[12] Dept. of Physics, University of Maryland, College Park, MD 20742, USA

[13] Dept. of Physics, Universität Dortmund, D-44221 Dortmund, Germany

[14] Dept. of Subatomic and Radiation Physics, University of Gent, B-9000 Gent, Belgium

[15] Max-Planck-Institut für Kernphysik, D-69177 Heidelberg, Germany

[16] Dept. of Physics and Astronomy, University of California, Irvine, CA 92697, USA

[17] Laboratory for High Energy Physics, École Polytechnique Fédérale, CH-1015 Lausanne, Switzerland

[18] Dept. of Physics and Astronomy, University of Kansas, Lawrence, KS 66045, USA

[19] Blackett Laboratory, Imperial College, London SW7 2BW, UK

[20] Dept. of Astronomy, University of Wisconsin, Madison, WI 53706, USA

[21] Dept. of Physics, University of Wisconsin, Madison, WI 53706, USA

[22] Institute of Physics, University of Mainz, Staudinger Weg 7, D-55099 Mainz, Germany

[23] University of Mons-Hainaut, 7000 Mons, Belgium

[24] Bartol Research Institute and Dept. of Physics and Astronomy, University of Delaware, Newark, DE 19716, USA

[25] Dept. of Physics, University of Oxford, 1 Keble Road, Oxford OX1 3NP, UK

[26] Institute for Advanced Study, Princeton, NJ 08540, USA

[27] Dept. of Physics, University of Wisconsin, River Falls, WI 54022, USA

[28] Dept. of Physics, Stockholm University, SE-10691 Stockholm, Sweden

[29] Dept. of Astronomy and Astrophysics, Pennsylvania State University, University Park, PA 16802, USA

[30] Dept. of Physics, Pennsylvania State University, University Park, PA 16802, USA

[31] Division of High Energy Physics, Uppsala University, S-75121 Uppsala, Sweden

[32] Dept. of Physics and Astronomy, Utrecht University/SRON, NL-3584 CC Utrecht, The Netherlands

[33] Dept. of Physics, University of Wuppertal, D-42119 Wuppertal, Germany

[34] DESY, D-15735 Zeuthen, Germany

[a] on leave of absence from Universität Erlangen-Nürnberg, Physikalisches Institut, D-91058, Erlangen, Germany

[b] on leave of absence from Università di Bari, Dipartimento di Fisica, I-70126, Bari, Italy

[c] affiliated with School of Pure and Applied Natural Sciences, Kalmar University, S-39182 Kalmar, Sweden

[d] NASA Goddard Space Flight Center, Greenbelt, MD 20771, USA

[e] affiliated with IFIC (CSIC-Universitat de València), A. C. 22085, 46071 Valencia, Spain

Acknowledgments

Table of Contents

19. G.C. Hill for the IceCube Collaboration, *Likelihood deconvolution of diffuse prompt and extra-terrestrial neutrino fluxes in the AMANDA-II detector*, pages 79-82.

20. O. Tarasova, M. Kowalski and M. Walter, *Search for neutrino-induced cascades with AMANDA data taken in 2000-2004*, pages 83-86.

21. A. Ishihara for the IceCube Collaboration, *EHE neutrino search with the IceCube 9 string array*, pages 87-90.

22. J. Bolmont, B. Voigt and R. Nahnhauer for the IceCube Collaboration, *Very high energy electromagnetic cascades in the LPM regime with IceCube*, pages 91-94.

23. J. Kiryluk, M.V. D'Agostino, S.R. Klein, C. Song, and D.R. Williams for the IceCube Collaboration, *IceCube performance with artificial light sources: the road to cascade analyses*, pages 95-98.

24. J. Braun, A. Karle and T. Montaruli for the IceCube Collaboration, *Neutrino point source search strategies for AMANDA-II and results from 2005*, pages 99-102.

25. R. Franke, R. Lauer, M. Ackermann, and E. Bernardini for the IceCube Collaboration, *Point source analysis for cosmic neutrinos beyond PeV energies with AMANDA and IceCube*, pages 103-106.

26. C. Finley, J. Dumm and T. Montaruli for the IceCube Collaboration, *Nine-string IceCube point source analysis*, pages 107-110.

27. J.P. Hülss and C. Wiebusch for the IceCube Collaboration, *Search for signatures of extra-terrestrial neutrinos with a multipole analysis of the AMANDA-II sky-map*, pages 111-114.

28. K. Satalecka, E. Bernardini, M. Ackermann, and M. Tluczykont for the IceCube Collaboration, *Cluster Search for neutrino flares from pre-defined directions*, pages 115-118.

29. R. Porrata for the IceCube Collaboration, *All-sky search for transient sources of neutrinos using give years of AMANDA-II data*, pages 119-122.

30. M. Ackermann, E. Bernardini, N. Gallante, F. Goebel, M. Hayashida, K. Satalecka, M. Tluczykont and R.M. Wagner for the IceCube and MAGIC Collaboration, *Neutrino triggered Target of Opportunity (NToO) test run with AMANDA-II and MAGIC*, pages 123-126.

31. A. Kappes, M. Kowalski, E. Strahler, and I. Tabaoda for the IceCube Collaboration, *Detecting GRBs with IceCube and optical follow-up observations*, pages 127-130.

32. D. Hubert and A. Davour for the IceCube Collaboration, *Search for neutralino dark matter with the AMANDA neutrino telescope*, pages 131-134.

33. G. Wikström for the IceCube Collaboration, *Prospects of dark matter detection in IceCube*, pages 135-138.

34. H. Wissing for the IceCube Collaboration, *Search for relativistic magnetic monopoles with the AMANDA-II detector*, pages 139-142.

35. A. Pohl and D. Hardtke for the IceCube Collaboration, *Subrelativistic Particle Searches with the AMANDA-II detector*, pages 143-146.

36. B. Christy, A. Olivas and D. Hardtke for the IceCube Collaboration, *Exotic particles searches with IceCube*, pages 147-150.

37. D. Chirkin for the IceCube Collaboration, *Effect of the improved data acquisition system of IceCube on its neutrino-detection capabilities*, pages 151-154.

38. J. Lundberg for the IceCube Collaboration, *Improved Cherenkov light propagation methods for the IceCube neutrino telescope*, pages 155-158.

39. S. Grullon, D.J. Boersma, G. Hill, K. Hoshina, and K. Mase for the IceCube Collaboration, *Reconstruction of high energy muon events in IceCube using waveforms*, pages 159-162.

40. H. Landsman for the IceCube Collaboration, L. Ruckmann, G.S. Varner, *Radio detection of GZK neutrinos - AURA status and plans*, pages 163-166.

IceCube - construction status and performance results of the 22 string detector

ALBRECHT KARLE[1], FOR THE ICECUBE COLLABORATION[2]
[1]*University of Wisconsin-Madison*
[2]*See special section of these proceedings*
karle@icecube.wisc.edu

Abstract: The IceCube neutrino observatory is a cubic-kilometer ice-Cherenkov detector being constructed in the deep ice at the geographic South Pole. After a successful construction season ending in February 2007, IceCube consists of 22 strings and 26 IceTop stations with a total of 1424 Digital Optical Modules (DOMs) deployed at depths up to 2450m. Together with the commissioning of the central laboratory building and central DAQ electronics, this allowed IceCube to begin early operations and data analysis. The goal is to complete construction of the final configuration of 80 strings and IceTop stations in 2011. First results from the 22-string configuration and an overview of the project will be presented.

Overview

The IceCube neutrino observatory is a kilometer-scale neutrino telescope currently under construction at the South Pole. The existing AMANDA-II array, the precursor of IceCube, will be surrounded by and integrated into the IceCube array [5]. IceCube is designed to detect astrophysical neutrino fluxes at energies from a few $100\,\mathrm{GeV}$ up to the highest energies of 10^9 GeV [1], [2].

Project Year	Strings deployed	IceTop stations	# of Sensors
2004/05	1	4	76
2005/06	8	12	528
2006/07	13	10	820
2007 total	22	26	1424

The IceCube neutrino observatory at the South Pole will consist of 4800 optical sensors - digital optical modules (DOMs) - installed on 80 strings at depths of $1450\,\mathrm{m}$ to $2450\,\mathrm{m}$ in the Antarctic Ice, and 320 sensors deployed in 160 IceTop [4] detectors in pairs on the ice surface directly above the strings. Each sensor consists of a photomultiplier tube connected to a waveform-recording data acquisition circuit capable of resolving pulses with nanosecond precision and having a dynamic range of at least 250 photoelectrons per $10\,\mathrm{ns}$. Construction started at the South Pole in November 2004. A total of 1424 sensors have been installed to date
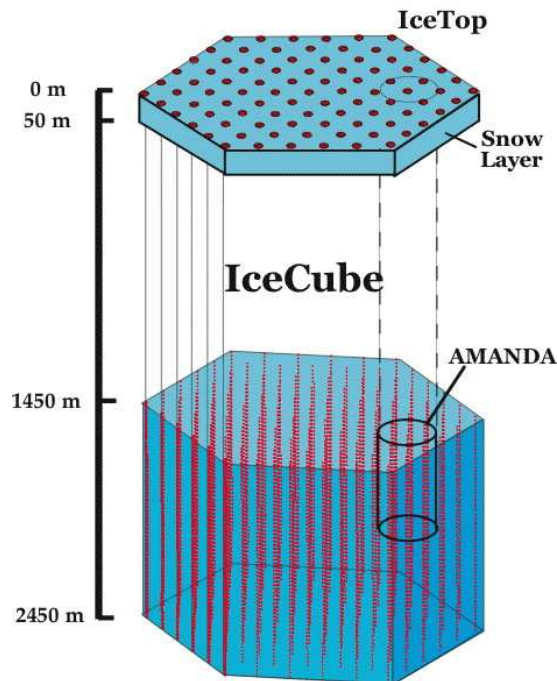
Figure 1: Schematic view of the IceCube array consisting of 80 strings with 60 sensors on each string. The surface array IceTop consists of 160 detectors, two of which are associated with each string.

7
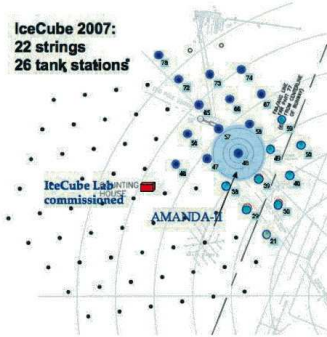
Figure 2: Schematic view of current geometry

Figure 3: Schematic view of a Digital Optical Module.
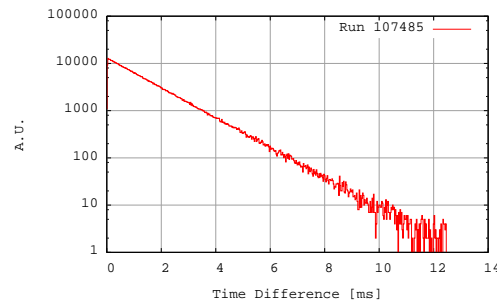
Figure 4: The time difference between subsequent events is shown for one run.

on 22 strings and in 26 IceTop surface detector stations. The table below summarizes the construction status as of February 2007.

Electrical and mechanical structure

It was a design goal to avoid single point failures in the ice, as the sensors are not accessible once the ice refreezes. High reliability and ease of maintenance were other design goals. A string consists of the following major configuration items: a cable from the counting house to the string location, a cable from the surface to 2450 m depth, and 60 optical sensors. 30 twisted-pair copper cables packaged in 15 twisted quads are used to provide power and communication to 60 sensors. To reduce the amount of cable, two sensors are operated on the same wire pair, one terminated and one unterminated. Neighboring sensors are connected to enable fast local coincidence triggering in the ice.

A schematic view of an optical sensor is shown in Fig. 3. An optical sensor consists of a 25-cm-diameter photomultiplier tube (PMT) embedded in a glass pressure vessel of 32.5-cm diameter. The HAMAMATSU R7081-02 PMT has ten dynodes, allowing operation at a gain of at least $5 \cdot 10^7$. The average gain is set to $1.0 \cdot 10^7$, providing a single photoelectron amplitude of about 5 mV. The signals are digitized by a fast analog transient waveform recorder (ATWD, 300 MSPS) and by a fADC (40 MSPS). The PMT signal is amplified by 3 different gains ($\times 0.25$, $\times 2$, $\times 16$) to extend the dynamic range of the ATWD to 16 bits. The linear dynamic range of the sensor is 400 photoelectrons

in 15 ns; the integrated dynamic range is of more than 5,000 photoelectrons in 2 μs. The digital electronics on the main board are based on a field-programmable gate array (FPGA) which contains a 32-bit CPU, 8 MB of flash storage, and 32 MB of RAM. A small communications program stored in ROM allows communication to be established with the surface computer system and new programs to be downloaded to the DOM.

The flasher board is an optical calibration device which is integrated in each DOM. The amplitude of the LED pulses can be adjusted over a wide range up to a brightness of $9 \cdot 10^{10}$ photons at a wavelength of about 405 nm.

Data acquisition and online data processing

All digitized photomultiplier pulses are to be sent to the surface. A local coincidence (LC) trigger scheme is used to apply data compression for iso-

lated hits, which are mostly noise pulses. Every string is connected to one server called a stringhub, which includes 8 custom PCI cards. They provide power, communication and time calibration to the sensors. The stringhub sorts the hits in time and buffers them until the trigger and eventbuilding process is complete. The digital architecture allows deadtime-free data acquisition (Fig. 4) with the exception of runstop and start times and maintenance times. A joint eventbuilder combines signals from the AMANDA-II array with IceCube data. The raw data rate is on the order of 100 GB/day, which are written to tapes. An online processing and filtering cluster extracts interesting phenomena, such as all upgoing muons, high-energy events, IceTop-In-ice coincidences, cascade events, events from the direction of the moon, events that are interesting for dark matter search and events in coincidence with GRB. The filtered data stream (of order 20 GB/day) is then transmitted by satellite to the Northern Hemisphere to be stored and archived in the data center. The data will then be prepared for physics data analysis by the working groups in the collaboration.

Drilling and detector installation

The strings are installed in holes which are drilled using the enhanced hot-water drill (EHWD). The drill consists of numerous pump and heating systems, hoses, a drill tower and a complex control system. It delivers a thermal power of 5 MW. The average time required for drilling a hole 60 cm in diameter to a depth of 2450 m was

∼34 hours in the most recent construction season. The subsequent installation of a string with 60 DOMs required typically 12 hours. Overall, the construction cycle time between two strings was 3 days, which allowed the installation of 2 strings per week. With some optimizations in set-up time and an improved technique for drilling through the firn layer, we expect to install up to 18 strings between December 2007 and January 2008. Based on the past season, the long-term construction schedule remains unchanged with completion expected in January 2011.

All sensors undergo a final acceptance test at their production sites before being shipped to the South Pole. They are again tested briefly on the ice prior
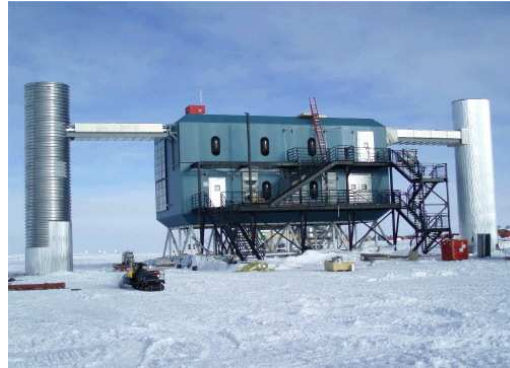
Figure 5: The IceCube Laboratory contains all surface electronics and server farms for data acquisition and online data processing.

to deployment. The installation and the subsequent freeze-in process (with temporary pressures up to more than 400 bar) places unusual demands on the string hardware. Yet, the survival rate of optical sensors is very high. For 1424 optical sensors deployed to date, only 16 (1.1%) are not usable; another 18 (1.3%) have developed minor issues, some of which are expected to be resolved. 97.6% of all sensors have been commissioned with full functionality and are in operation to date. Only two sensors failed after they were frozen in and commissioned. A total of 1000 DOMyears of integrated operation has been accumulated as of May 2007.

Operation and performance characteristics

The detector electronics and software are designed to require minimal maintenance at the remote location. For example, the time calibration system, a critical part of any neutrino telescope, is designed to be a self-calibrating, integral part of the readout system (in contrast to the AMANDA detector, which required manual calibration of all analog detector channels). The strings are calibrated as soon as they are frozen in, allowing for gradual commissioning of the instrument.

All sensors have precise quartz oscillators to provide local clocks, which are synchronized every few seconds to the central GPS clock. Using LED flashers, it was possible to verify the time reso-

lution to a precision of less than 2 ns on average. Studies with muons and flashers have shown that the timing is stable over periods of months [6]. Another important performance parameter is the dark-noise rate of the sensors. There is no known natural background of light in the deep ice other than light generated by cosmic particles. The noise rates for DOMs in the deep ice are $\approx 700\,\text{Hz}$. The rate is $\sim 320\,\text{Hz}$ with an applied dead time of $50\,\mu\text{s}$. The very low noise rates of the sensors are critical for the detection of the low energy neutrino emission associated with supernova core collapse.

-	A-II	IC9	IC22	IC80
Instr. Volume/km^3	.016	0.044	0.18	0.9
# of sensors (in ice)	677	540	1320	4800
$\mu_{Atm.}$/Hz	80	140	550	1650
Ang. res./$^\circ$ (10TeV)	2.0	2.0		0.7

Table 1: Some performance parameters for the AMANDA-II and IceCube 9-, 22- and 80-string detector configurations. Rates are given for cosmic ray muons at trigger level. The rate for the 80-string array is based on simulations [6].
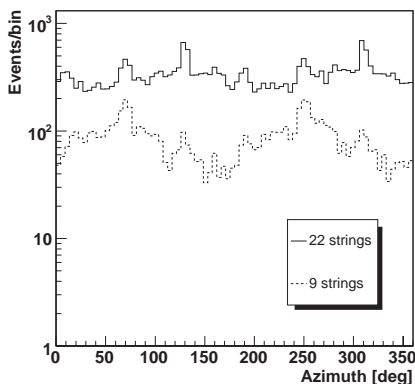
Figure 6: Azimuth distribution of atmospheric muons observed in the 9-string array in 2006 and the 22-string array in 2007.

The 9- and 22-string arrays trigger on atmospheric muons at a rate of 140Hz and 520Hz, respectively. The 22 string trigger condition requires an 8-fold coincidence within $5\,\mu\text{sec}$. Several characteristic figures of AMANDA-II, IC9, IC22 and IC80 are compared in table 2. The 22-string configuration has a significantly higher effective area and overall sensitivity. Fig. 6 shows the azimuth distribution of cosmic-ray muons for one hour of livetime of the 9- string array and the 22-string array for events with at least 20 DOMs and 3 strings hit. The azimuth distribution for IC22 is more even, and the overall rate is visibly higher as the detector is now sensitive in all directions.

First physics analyses have already been performed using data of the IceCube 9 string array[7, 8, 9]. The start of regular science operations with IC22 is scheduled for May 2007 and will continue in this configuration until March 2008.

Acknowledgments

References

[1] J. Ahrens *et al.*, Astrop. Phys. 20, 507 (2004), arXiv:astro-ph/0305196.

[2] IceCube Preliminary Design Document, Ahrens et al. (IceCube coll.) http://icecube.wisc.edu

[3] A. Achterberg et al. (IceCube Collaboration) Astropart. Phys. 26 (2006) 155

[4] T. Gaisser et al. (IceCube Coll.), these proc.

[5] A. Gross et al. (IceCube Coll.), these proc.

[6] J. Kiryluk et al. (IceCube Coll.), these proc.

[7] J. Pretz et al., (IceCube Coll.), these proc.

[8] C. Finley et al. (IceCube Coll.), these proc.

[9] K. Hoshina et al. (IceCube Coll.), these proc.

The combined AMANDA and IceCube Neutrino Telescope

A. GROSS[1], C. HA[2], C. ROTT[2], M. TLUCZYKONT[3], E. RESCONI[1], T. DEYOUNG[2], G. WIKSTRÖM[4]
FOR THE ICECUBE COLLABORATION[5]

[1] *MPI für Kernphysik, Saupfercheckweg 1, D-69117 Heidelberg, Germany*

[2] *Pennsylvania State University, Department of Physics, University Park PA 16803, USA*

[3] *DESY, Platanenallee 6, D-15738 Zeuthen, Germany*

[4] *Department of physics, Stockholm University, AlbaNova, S-10691 Stockholm, Sweden*

[5] *see special section of these proceedings*

gross@mpi-hd.mpg.de

Abstract: The IceCube Neutrino Telescope is currently under construction at the geographic South Pole and will eventually instrument a volume of one cubic kilometer by 2011. It currently consists of 22 strings with 60 Digital Optical Modules each. Additionally the AMANDA detector has been fully integrated into IceCube operation. This includes hardware synchronisation, combined triggering, common event building and a combined data analysis strategy. Monte Carlo simulations of a combined AMANDA + IceCube detector will be presented. The results of the simulations were used to implement an online filtering on data provided by the Joint Event Builder collecting data from both detectors. Data taken synchronously from both detectors serve for Monte Carlo verification. We discuss the impact of the AMANDA integration on the effective area, track reconstruction and event selection for the muon neutrino detection channel. In particular, we study fully and partially contained events at low energy. An online filter marks candidates for contained events using peripheral optical modules as a veto against atmospheric muons. The effective interaction volume for this filter is presented.

Introduction

In its 2007 configuration, IceCube consists of 22 strings in operation with 60 digital optical modules each. For details on its performance see [1]. With the deployment of 13 additional strings in the 2006/07 polar summer, the detector surrounds now its predecessor AMANDA. Since IceCube has a wide string spacing of 125 m, optimized for muon tracks above a few TeV, the integration of AMANDA with its denser array adds an important part to the low energy reach of the combined detector.

The implementation of a new DAQ system to the AMANDA detector [2] in the years 2003-2005 allowed for a reduction of the multiplicity trigger threshold. By this the energy threshold of AMANDA has been lowered below 50 GeV. Hence it is capable to complement IceCube at low energies and consequently, the AMANDA detector has been fully integrated into the IceCube detec-

tor. This includes a common run control, triggering, event building and online filtering. Every time the AMANDA detector is triggered, a readout request is sent to the IceCube detector. Since the energy threshold of AMANDA is lower, no triggering requests from IceCube to AMANDA are needed. As shown in Fig. 1, the Joint Event Builder (JEB) receives data from both detectors, merges events on a time coincidence base and provides the data to the online filtering. The online filtering selects events of interest for physics analyses and transfers the selected data to the Northern Hemisphere. With this filtering the relevant physics data can be quickly analyzed despite the constraints of limited satellite bandwidth available for data transfer from the South Pole.

Monte Carlo (MC) studies of the performance of the combined detector in muon neutrino channel are presented in this paper. The combined detector provides an improved performance at low energies: the IceCube strings directly adjacent to AMANDA
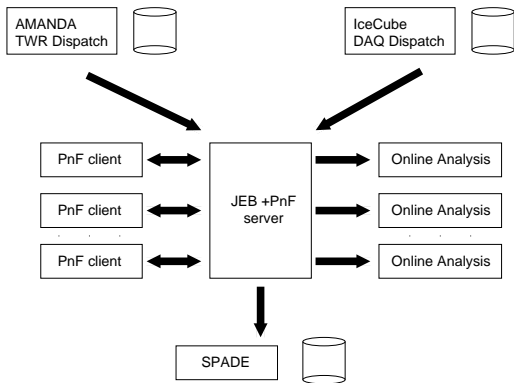
Figure 1: Data flow in the combined AMANDA and IceCube neutrino telescopes using the JEB. The processing and filtering (PnF) clients reconstruct the combined events within a few seconds of data acquisition. Online analysis is then performed before the data is transferred to the SPADE system for satellite transmission and tape archiving.

enlarge the densely instrumented region, provide a longer lever arm and thus improve the angular resolution. This reduces the background for low energy neutrinos from point-like sources compared to previous AMANDA analyses [3]. Since AMANDA is now completely embedded into the IceCube array, the identification of starting and contained tracks becomes possible using IceCube as a veto. The identification of contained events allows a better measurement of the energy. Additionally, with this technique, the rejection of down-going atmospheric muons is possible and thus, the detector is sensitive to sources in the southern sky. Furthermore, analyses for different neutrino flavors will use the combined detector as well to improve the low-energy performance.

Low energy physics with the combined detector

With its enhanced performance at low energies the combined detector will have an improved sensitivity to WIMPs (see [4]) and sources with steep energy spectra or cut-offs below 10 TeV like the Crab nebula [5]. In particular, the search for time-variable sources will profit from this enhancement

since their localization in space and time significantly reduces the number of background events. An example for such a source is LS I+61 303 emitting TeV photons periodically with a power law index of -2.6 [6]. Another region of high interest is the Galactic Center which contains a TeV gamma-ray source [7]. As it lies in the southern sky it was not accessible for AMANDA up to now. But also the analysis of atmospheric neutrinos will benefit and might even allow the detection of neutrino oscillation effects in the energy range 10 – 100 GeV and test for non-standard oscillation scenarios.

Online filtering and data analysis

Two filtering strategies make use of the combined detectors. The first strategy aims for an improved performance for up-going muon tracks, by adding a low energy online filter for combined data to the standard IceCube filter for up-going muons. Additionally, a filter using the veto strategy identifies events contained in the AMANDA array and opens a sensitivity window to the southern sky. In addition to the integration of AMANDA, the implementation of a string trigger improves the detection of vertical low energy tracks with IceCube.

The up-going muon filter

The low energy up-going muon track filter uses all hits from both detectors to reach a decision. It is complementary to an up-going muon track filter defined on IceCube hits only. The JAMS reconstruction[1] was chosen for the low energy filter. Events with a reconstructed zenith angle larger than $75°$ are selected. The combination with the IceCube only filter allows to constrain the use of this relatively slow algorithm to events with hits in the AMANDA detector not passing the IceCube filter and having less than 20 hits in IceCube. For events with more hits, the additional information from AMANDA does not result in a significantly better filtering efficiency.

The effective area for muon neutrinos of the combined detectors using the combined online filter is

---

1. JAMS is based on a cluster search in the abstract space spanned by the distance of the hit to the track and the time residual. The time residual is the difference of the measured hit time and the passing time of the Cherenkov cone for an assumed track.

shown in Fig. 2 in comparison to the IceCube only filter. Figure 3 shows the resulting expected rate of atmospheric neutrinos [8]. It is worth noting that the combined detector detects atmospheric neutrinos over four orders of magnitude in energy between 10 GeV and 100 TeV.

The neutrino signal efficiency of the combined filter is above 90% over the wide energy range from 10 GeV to 100 PeV. The rejection of the atmospheric muon background is above 95%, where less than 0.5% of all events are passing the JAMS filter on combined events. That demonstrates that the background of atmospheric muons is not significantly increased by the AMANDA integration.
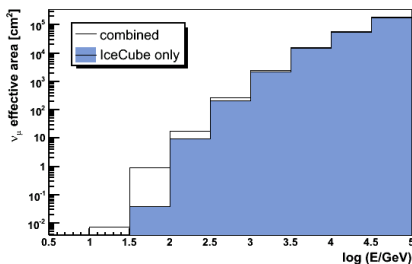
Figure 2: Effective area of the combined detectors in comparison to IceCube only at online filter level.
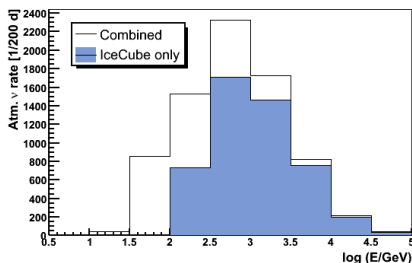
Figure 3: Atmospheric neutrino rate at online filter level for a generic run period of 200 days.

A first study of the angular resolution in the low energy regime ($E < 10$ TeV) was conducted. For this study, events triggering both detectors separately have been selected and a full likelihood reconstruction [9] has been applied. As shown in Fig. 4, a slight improvement was found.
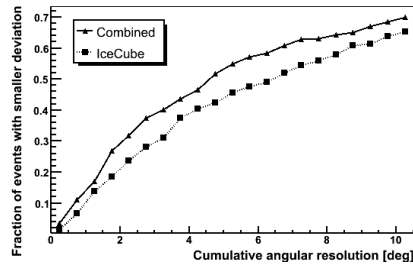
Figure 4: Cumulative distribution of the angle between simulated and reconstructed track for the combined detectors and IceCube only.

A filter for low-energy contained events

As IceCube surrounds the AMANDA detector its outer strings and top-layers can be used to veto through-going tracks and especially study low energy (100 GeV – 1 TeV) fully or partially contained tracks with 4π sensitivity. Figure 5 shows the effective volume for these events at filter level. The combined AMANDA-IceCube detector is used to reconstruct tracks and point them back to their origin. Reconstructed tracks that deposite no light in one or more peripheral strings despite of a high probability to do so assuming a through-going track, are more likely to be due to muon neutrino interactions rather than atmospheric muon background. Furthermore, the charged current interaction of the muon neutrino in the detector produces a cascade with a track attached to it. This topologically differs from a through-going muon track and can be studied in the recorded waveforms and leading edge times. A dedicated reconstruction algorithm is currently under development.

A string trigger for vertical low-energy events in IceCube

We are currently implementing a new string trigger for IceCube that requires 5 DOMs to be hit out of a sequence of 7 DOMs on a single string. The upper most part of the string isd excluded to reduce the trigger rate on down-going muons. In comparison to the standard IceCube trigger requiring 8 DOMs to be hit, for energies below 100 GeV an improvement by more than a factor of 10 is obtained. Figure 6 shows the string trigger efficiency as a function of the muon neutrino energy and zenith angle.
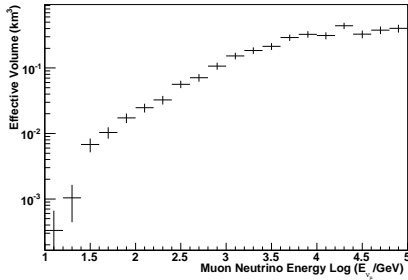
Figure 5: Effective interaction volume of the contained event filter.
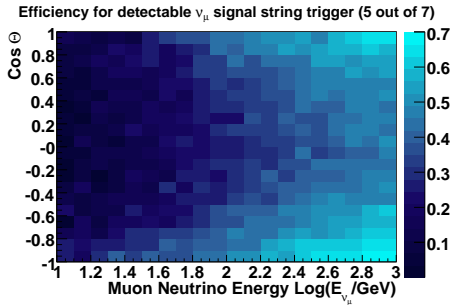
Figure 6: String trigger efficiency for muon neutrinos that produce at least one hit in the detector as a function of muon neutrino energy and zenith angle.

The good performance for vertical tracks allows to compare the fluxes of up- and down-going atmospheric neutrinos and the analysis of WIMP annihilations at the center of the Earth.

Verification of MC simulations

In order to check the viability of the MC simulation for the combined detector, we have compared the distributions of various quantities between data and simulation. The data for this comparison has been acquired in a special integrated mode test run in 2006. As an example Fig. 7 shows the comparison of the reconstructed zenith angle spectrum for data and MC. Other distributions, including that of the trigger rate and the number of hit channel were also found to be in good agreement.
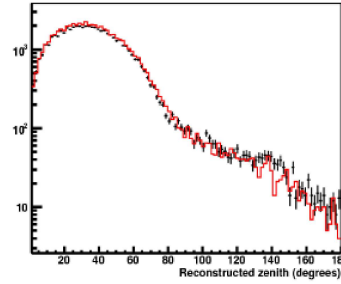
Figure 7: AMANDA-IceCube (9 strings) JAMS zenith spectrum from integrated test run 2006.

Conclusions

According to the preliminary results presented here, the combined IceCube and AMANDA detector in its current configuration provides a significantly improved performance in the low energy regime. The effective area for up-going muon neutrinos and the effective interaction volume for contained down-going events at online filter level provide improved possibilities to investigate atmospheric neutrinos as well as possible astrophysical sources emitting neutrinos with energies below 10 TeV. For the first time, the Galactic Center can be examined with a neutrino telescope on the Southern Hemisphere.

References

[1] A. Karle et al. (IceCube coll.), these proceedings (abstract 1180)

[2] W. Wagner et al. (AMANDA coll.), proceedings of the 28th ICRC 2003

[3] A. Achterberg et al. (IceCube coll.), accepted by PRD, arXiv:astro-ph/0611063

[4] G. Wikström et al. (IceCube coll.), these proceedings (abstract 0690)

[5] F.A. Aharonian et al. (HESS coll.), A&A 457, 899-915 (2006)

[6] J. Albert et al.,Science 312 (2006) 1771-1773

[7] F.A. Aharonian et al. (HESS coll.), Phys. Rev. Lett. 9, 221102 (2006)

[8] G. Barr el al., http://www-pnp.physics.ox.ac.uk/ barr/fluxfiles/

[9] J. Ahrens et al., NIM A524 (2004) 169-194

Performance of the IceTop Array

Thomas Gaisser for the IceCube Collaboration(*)

Bartol Research Institute, Department of Physics and Astronomy, University of Delaware, Newark, DE 19716, U.S.A.

gaisser@bartol.udel.edu (*)see collaboration lists at end of these Proceedings

Abstract: We present an overview of the status of IceTop, which now consists of 52 tanks at 26 stations above the 22 deep strings of IceCube. Six months of good data were taken with the previous 16 station-9 string version of IceCube during 2006.

Introduction

During 2006, IceCube ran with sixteen IceTop stations and nine IceCube strings. Ten more stations and thirteen more strings were deployed in the 2006-2007 austral summer, as shown in Fig 1. When complete, there will be 80 surface stations and a similar number of deep strings in IceCube.

The IceTop air shower array consists of pairs of tanks (A and B) separated from each other by 10 m. Each IceTop station with its pair of tanks is associated with an IceCube string. Each tank is instrumented with two standard IceCube digital optical modules (DOMs) operating at different gains to extend the dynamic range of the tank. This configuration has several advantages:

- Local coincidence between two tanks at a station is used to select potential air shower signals from the high (typically 2 kHz) event rate generated in each tank by uncorrelated photons, electrons and muons.

- Comparison of signals seen by two DOMs within a tank can be used to demonstrate that fluctuations in tank response are much smaller than intrinsic fluctuations in air showers as measured by comparing signals from the same shower in the two tanks at a station [1].

- Two identical sub-arrays (A-tanks and B-tanks) can be used to measure shower front
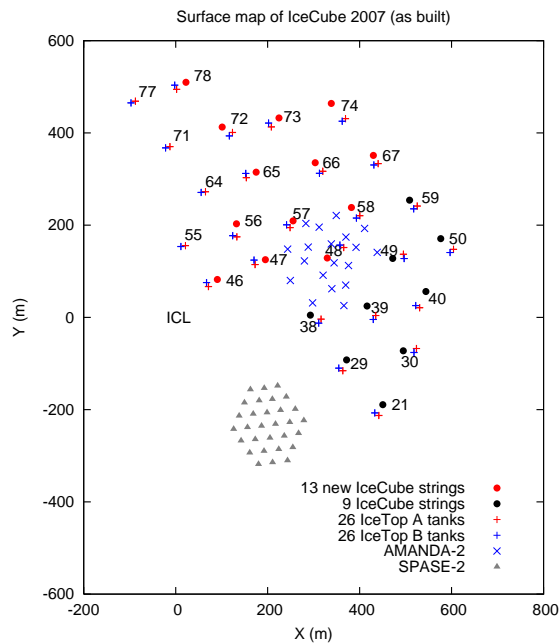
Figure 1: Surface map of IceCube/IceTop in 2007. When completed the array will be symmetric around the IceCube Laboratory (ICL).

15

curvature, lateral distribution, timing and density fluctuations, core location accuracy, angular resolution and other properties of showers.

- By selecting coincident events in which an event in deep IceCube is accompanied by exactly one hit station in the inner part of IceTop, we can identify and tag a set of events that consist almost entirely of single muons in the deep detector (as compared to the multi-muon events typical of showers big enough to trigger several stations of IceTop). Such events are useful for calibration.

- With 52 tanks we already have a total detector area of 140 m^2, which will grow to over 400 m^2 when the detector is complete. The monitoring stream includes scalar rates of IceTop DOMs that can be used to observe solar and heliospheric cosmic-ray activity.

Calibration of IceTop DOMs

IceTop DOMs are calibrated and monitored with the continuous flux of muons through the tanks [2]. Through-going muons give a broad peak in the distribution of signals from the inclusive flux of all particles that hit the tank. For a vertical muon the signal corresponds to a track length of 90 cm in ice. The peak is calibrated with a muon telescope and with simulations. Air shower signals are then expressed in terms of vertical equivalent muons (VEMs) by comparing the integrated charge of the signal to that of a vertical, through-going muon. Regular calibration runs provide monitoring information and a data base of calibration constants, which is updated weekly. The first 8 tanks deployed in December 2004 provide a 2.5 year timeline for studying stability of the response, which generally varies slowly within a range of $\pm 5\%$. In half the cases (8/16) DOMs showed a sudden decrease in response ranging from 10% in two cases to 33% in one. The shifts occurred in mid-winter of 2006, which was the first season that the tanks experienced operation at the ambient winter temperature. (In 2005 winter the freeze-control units were still in operation.)
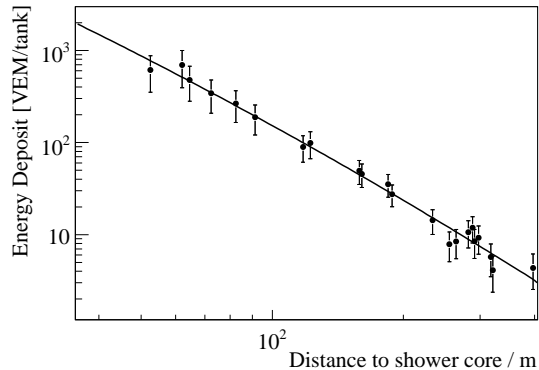
Figure 2: Signal vs distance from shower core with fitted lateral distribution for an event with an estimated energy of 100 PeV.

Air showers in IceTop

With a spacing between stations of approximately 125 m and a surface area per tank of 2.7 m^2, the effective threshold for IceTop is about 500 TeV for a trigger requirement of five or more stations, [3] somewhat higher than the nominal threshold of 300 TeV for showers near the vertical that hit four or more stations. (Here "effective threshold" is defined as the energy above which the previously measured cosmic-ray flux through a defined area-solid angle inside the array equals the observed rate of events.) Figure 2 shows an example of the lateral distribution of signals in a large shower in units of VEMs. The line is the fitted lateral distribution of energy deposition, which has a shape different from the standard NKG function. [3] The NKG function is appropriate for a scintillator array that is relatively insensitive to the photonic part of the signal ($\gamma \rightarrow e^+ + e^-$). Conversion of photons inside the tanks makes an important contribution to signals.

A convenient measure of primary cosmic-ray energy for showers observed in IceTop is the fitted signal density in VEMs at 100 m from the shower core (S_{100}). The mean energy for $S_{100} = 20$ is approximately 10 PeV for showers with zenith angle less than 30° and ~ 100 PeV for $S_{100} = 200$. A functional relation for S_{100} as a function of primary cosmic-ray energy and zenith angle for protons is given in Ref. [3], which shows a prelimi-

nary energy spectrum extending from 1 to 100 TeV based on this relation. Because of fluctuations on the steep cosmic-ray spectrum, the mean primary energy for a measured S_{100} is smaller than the energy which gives the same average S_{100}. There are also systematic differences in the relation for different primary masses (up to 25 % for Fe). The full energy spectrum analysis will require an unfolding procedure to account for fluctuations.

The same events can be reconstructed independently by the sub-array of A tanks and that of B tanks. From the comparison one can obtain an experimental measure of the accuracy of reconstruction. Such a sub-array analysis indicates that core location can be determined to an accuracy of 13 m and the reconstructed direction to about $2°$.

Primary composition from coincident events

An important physics goal is to use the downward moving events observed in coincidence by IceTop and the deep IceCube detectors to study primary composition in the knee region and above. The idea is to measure the distribution of energy deposition by muons in the deep detector as a function of primary cosmic-ray energy and hence to measure the fraction of heavy nuclei, which produce more muons. Previous studies of this type have been done by SPASE2-AMANDA-B10 [4] and by EASTOP-MACRO [5] in the knee region. Status of this analysis with 2006 IceCube data is presented in Ref. [6].

The full IceCube detector can cover the energy range from $< 10^{15}$ eV below the knee to 10^{18} eV. Showers generated by primary cosmic rays in this energy range produce multiple muons with energy sufficient to reach the depth of IceCube. For primary energy of 10^{15} eV, for example, proton-induced showers near the vertical produce on average about 10 muons with $E_\mu > 500$ GeV and iron nuclei about 20. For higher primary energies, the number of muons increases, and the multiplicity in showers generated by nuclei approaches asymptotically a factor of $A^{0.34}$ times the muon multiplicity of a proton shower, or ≈ 2.7 for $A = 56$.

As a consequence of the high altitude of IceTop, showers are observed near maximum so the detec-

tor has good energy resolution, which is important when the goal is to measure changes in composition as a function of energy. In some currently favored models [7, 8] the transition from galactic to extra-galactic cosmic rays occurs in the decade between 10^{17} and 10^{18} eV. In the model of Ref. [7] the transition would be characterized by a transition from heavy nuclei at the end of the galactic population to nearly all protons at higher energy as the extra-galactic population dominates. The details of the transition may in principle give information about the cosmology of the extragalactic cosmic ray sources if the change in composition can be measured with sufficient precision and energy resolution [9].

Calibration of IceCube with IceTop

Events reconstructed by IceTop that are also seen in the deep strings can be used in a straightforward way to calibrate event reconstruction in Ice-Cube. One can, for example, compare the directions reconstructed by IceTop with the direction of the muon core reconstructed by one of the algorithms used for muon reconstruction in the neutrino telescope. Examples of verification of timing and direction with IceTop are given in Ref. [1]. As noted above, however, showers that trigger IceTop normally produce bundles of several (at 1 PeV) or many muons in the deep detectors.

In contrast, much of the atmospheric muon background in deep IceCube consists of single muons, as does the target population of neutrino-induced muons. Figure 3 shows the response function for atmospheric muons at the top of the deep IceCube detector, 1.5 km below the surface. About 90% of downward events consist of a single muon entering the deep detector. Most of these events are from cosmic-rays with primary energy <10 TeV. The region under the lower curve shows the contribution of events with multiple muons. By selecting a sample of coincident events in which both tanks at one and only one IceTop station are hit, it is possible to discriminate against high-energy events and find a sample enriched in single muons. Coincidences involving only an interior IceTop station provide a sample in which about 75% are single muons in the deep detector. [10] The line from the hit station to
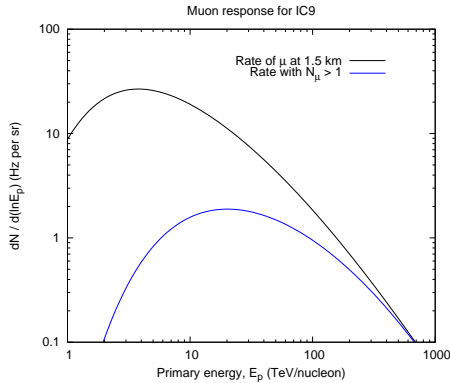
Figure 3: Distribution of primary cosmic-ray nucleons that give rise to muons near the vertical at 1.5 km in IceCube (estimated from Ref. [11]). The lower curve shows the contribution of events with more than one muon entering the deep detector.

the center of gravity of hits in the deep detector can be compared with the direction obtained from the muon reconstruction algorithm in the deep detector alone to check the reconstruction algorithm on single muon tracks. The analysis confirms that the same reconstruction algorithm used for ν_μ-induced upward muons reconstructs most events with an accuracy of better than $2°$. [10]

Heliospheric physics with IceTop

The monitoring stream of IceCube includes the scalar rates of both discriminators in each DOM. Response of IceTop DOMs to secondary cosmic rays at the surface is discussed in [12]. Signals at the rate of $\sim$2 kHz are produced by a combination of photons converting in the tanks, and electrons and muons that enter the tanks. Most of these particles come from primary cosmic rays with energies in the few GeV range. Large heliospheric events can produce sudden changes in the counting rate. Depending on the nature and orientation of the event (e.g. a coronal mass ejection associated with a large solar flare), one can detect either a decrease in the flux of galactic cosmic rays as the magnetic activity excludes the lower energy cosmic rays from the inner heliosphere or an increase due to solar energetic particles accelerated in the event.

As the setting of the discriminator is increased, the average signal rate decreases as the contribution from the lower energy cosmic-rays falls below threshold. The response of a DOM to the primary cosmic-ray spectrum can therefore be tuned significantly by changing the discriminator threshold–even within the constraint that the threshold must remain below a fraction of the VEM peak. This gives the possibility of studying heliospheric phenomena with unprecedented timing resolution and with significant energy resolution, as discussed in [13].

References

[1] A. Achterberg et al. (IceCube Collaboration) Astropart. Phys. 26 (2006) 155

[2] L. Demirörs, et al., "IceTop Tank Response to Muons", this conference.

[3] S. Klepser, et al., "Lateral Distribution of Air Shower Signals and Initial Energy Spectrum above 1 PeV", this conference.

[4] J. Ahrens et al., Astropart. Phys. 21 (2004) 565.

[5] M. Aglietta et al., Astropart. Phys. 20 (2004) 641.

[6] C. Song et al. "Cosmic Ray Composition Studies with IceTop/IceCube", this conference.

[7] R. Aloisio, V. Berezinsky, et al., Astropart. Phys. 27 (2007) 76.

[8] E.G. Berezhko & H.J. Völk, arXiv/0704.1715 [astro-ph].

[9] D. Allard, A.V. Olinto & E. Parizot, astro-ph/0703633.

[10] X. Bai, et al., "IceTop/IceCube coincidences", this conference.

[11] T. Gaisser, *Cosmic Rays and Particles Physics* (Cambridge University Press, 1990).

[12] J. Clem, P. Niessen, et al., "Response of IceTop tanks to low-energy particles", this conference.

[13] T. Kuwabara, J.W. Bieber & R. Pyle et al., "Heliospheric Physics with IceTop", this conference.

Heliospheric Physics with IceTop

T. KUWABARA[1,2], J. W. BIEBER[1], AND R. PYLE[1]

[1]*Bartol Research Institute and Department of Physics and Astronomy, University of Delaware*
[2]*For the IceCube Collaboration, described in a special section of these proceedings*
takao@bartol.udel.edu

Abstract: IceTop is an air shower array now under construction at the South Pole. It is the surface component of IceCube, an observatory primarily focused on cosmic neutrinos. When completed, IceTop will have approximately 500 square meters of collecting area in the form of 160 separate ice Cherenkov detectors. These detectors are sensitive to electrons, photons, muons and neutrons. With the high altitude and low geomagnetic cutoff at the South Pole, IceTop promises to have unprecedented statistical precision, coupled with spectral sensitivity that can be used to observe solar energetic particles and transient phenomena in the flux of galactic cosmic rays. We discuss the potential of IceCube to contribute to heliospheric physics in general, and present a preliminary analysis of a complex interplanetary disturbance that occurred in August of 2006.

Introduction

IceTop is an air shower array now under construction at the South Pole as the surface component of the IceCube neutrino telescope. When completed, IceTop will have approximately 500 square meters of ice Cherenkov collecting area arranged in an array of 80 stations on a 125 m triangular grid. Each station consists of two, two meter diameter tanks filled with ice to a depth of 90 cm. Tanks are instrumented with two Digital Optical Modules (DOM) operated at different gain settings to provide appropriate dynamic range to cover both large and small air showers. Each DOM contains a 10 inch photomultiplier and an advanced readout system capable of returning the full waveform of more complex events. For the present analysis we use two discriminator counting rates recorded in each DOM. For historical reasons, the two discriminators are termed SPE (Single Photo Electron), and MPE (Multi Photo Electron). As used in IceTop the SPE threshold corresponds typically to 10 photoelectrons, and the MPE threshold to 20 photoelectrons.

Due to the high altitude (2835m) and the nearly zero geomagnetic cutoff at the South Pole, secondary particle spectra at "ground" level retain a
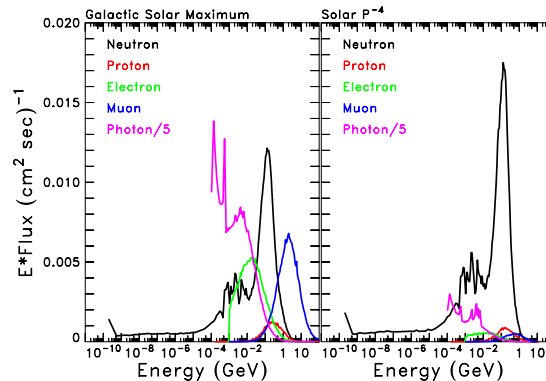
Figure 1: Calculated secondary particle spectra at the South Pole. Left: Galactic solar maximum. Right: Solar flare particle event normalized to produce a doubling of the count rate of a standard (NM64) neutron monitor.

significant amount of information on the spectra of the primary particles. This is illustrated in Figure 1, which summarizes the result of a FLUKA [4] calculation of the secondary spectra due to galactic cosmic rays at solar maximum (left panel) and a typical solar flare particle event (right panel). Of course the solar spectrum would be superimposed
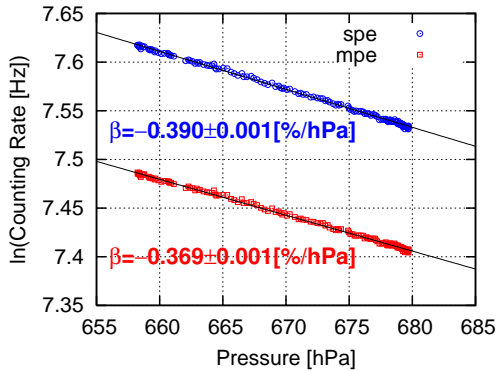
Figure 2: Correlation of scaler rate with pressure for one DOM on October 8-9, 2006.

Figure 3: Pressure correction coefficient for all DOM as a function of scaler rate.

on the galactic background. It is beyond the scope of this brief paper to show this in detail, but because the IceTop tanks are thick enough to totally absorb many of the incident particles the signal distribution in the tank contains information on the primary spectrum. More details are provided in a companion paper [2].

Barometer Correction

As with a neutron monitor, the counting rate of an IceTop detector shows a strong dependence on barometric pressure. From simulation and observation, it has been shown that barometric correction coefficients vary with the threshold energy of secondary cosmic rays [7] [3]. The energy sensitivity of IceTop detectors is nicely illustrated by the barometric coefficients we derive for them. By considering time periods in which there appears to be little variation in the primary particle intensity, it is possible to make a phenomenological estimate of the appropriate pressure correction by means of a simple correlation between detector counting rate and barometric pressure. Figure 2 shows this correlation for the two thresholds of an individual DOM. Note in particular the small but significant difference in the slope of the correlation, and hence the derived barometric correction.

In 2006 a total of 32 tanks were operational. Figure 3 shows the derived correction for each DOM (red squares for the MPE discriminators and blue circles for the SPE discriminators) plotted as a

function of the counting rate of the discriminator. At that time the tanks were all operating at the same nominal setting, but they had not been calibrated, so in fact the discriminators were triggering over a range of physical light levels. The correlation of correction with light level is nearly perfect. Those discriminators with lower counting rates, corresponding to higher light thresholds, have markedly lower barometric corrections. This is just what is expected since these signals should result preferentially from higher energy primaries. We are in the process of trying to use this information, plus simulations and calculations, to establish an energy response function for the tanks. For the remainder of this paper we rely on the approximate response functions derived from the FLUKA calculation that produced the plots shown in Figure 1.

Heliospheric Event

In Figure 4 we show several data sets characterizing a heliospheric event in August 2006. The Ice-Top measurements are shown in the second panel. We have averaged the SPE (blue) and MPE (red dashed) counting rates for all 32 DOM, after individually applying the barometric corrections described in the previous section. Ten minute averages are shown, all expressed as percent changes relative to the normalization interval on August 17 prior to the first decrease. For comparison the top panel shows the similarly treated counting rate of

Figure 4: August 17-21, 2006. From top: (1) McMurdo monitor (black) and Spaceship Earth isotropic component (green dashed). (2) IceTop SPE (blue) and MPE (red dashed) scaler rate, 32 DOM average. (3) IceTop model prediction. (4) Interplanetary magnetic field magnitude (black) and derivative (green). (5) Field direction latitude (black) and longitude (blue dots). (6) Plasma density. (7) Plasma temperature. (8) Plasma β.

the McMurdo neutron monitor. While the event is generally similar in the two detectors, the remarkably better counting statistics of IceTop stand out. In IceTop the total counting rate for the SPE channel is ∼64 kHz (2 kHz from each DOM), while the total counting rate of the 18NM64 McMurdo neutron monitor is ∼0.3 kHz [1].

From McMurdo alone, one might characterize this event as a double Forbush decrease [5]. Both decreases are associated with structures in what is evidently an interplanetary coronal mass ejection (ICME) containing at least one shock and multiple regions with different magnetic field and plasma parameters. However in IceTop the two decreases appear quite different. The second fits the conventional pattern in which the magnitude tends to scale inversely with primary rigidity [6]. Note that the decrease is consistently larger in low threshold SPE channel than high threshold MPE, and also that the higher rigidity particles tend to recover more rapidly.

In contrast, during the first decrease the higher energy channel shows a (slightly) larger deviation. There is also an intriguing feature in the IceTop data on August 18, near the time of a large change in the interplanetary magnetic field direction, that is not observed in the McMurdo neutron monitor. The *Spaceship Earth* neutron monitor network [1] measures a significant anisotropy during the event, which we can model as a dipole anisotropy with

21

a time variable magnitude and direction superimposed on a time varying isotropic cosmic ray flux. The isotropic component of our model fit is shown as the green dashed curve superimposed on the McMurdo data in Figure 4. The deviations of the McMurdo data from this line can only result from anisotropy since the Spaceship Earth stations have well matched energy response. Because IceTop has inherent spectral resolution it is possible for anisotropy to produce an apparent spectral feature. Even though the low and high rigidity channels of IceTop are derived from the same physical detector, the low and high rigidity particles will come from somewhat different asymptotic directions.

Using calculated response functions appropriate to the different discriminator levels, and asymptotic directions calculated as a function of rigidity, it is straightforward to convolute the two to make a specific prediction for IceTop. The third panel of Figure 4 gives the result of such a calculation under the simplest possible assumption, anisotropy independent of energy. We have used response functions that predict the observed counting rate corresponding to thresholds of ten photoelectrons (blue curve) and fifty photoelectrons (red dashed curve). On the scale at which the figure is reproduced it is not possible to see the small difference in the curves. Our conclusion is that the observed splitting of the red dashed and blue solid curves in the second panel results from spectral variation. We note that the overall time structure of IceTop data, and in particular the marked difference from McMurdo, is consistent with the dipole model derived from *Spaceship Earth*. The amplitude predicted for IceTop is understandably too large, particularly in the second decrease, because at these discriminator thresholds IceTop is observing at a higher average energy. Although IceTop is geographically further south than McMurdo, it is magnetically further north. Thus McMurdo looks nearly perpendicular to the ecliptic, whereas Pole has a mid latitude viewing direction.

The high statistical precision of IceTop may translate even small anisotropy into apparent spectral variation, and this must be taken into account in the analysis of interplanetary events. However there is no indication that the feature on August 18 results from such an effect. It is not clear at this time just what aspect of the complicated plasma and mag-

netic field structure at the time is responsible for the unusual spectral variation of the high energy cosmic rays. What is clear is that the high time resolution and energy resolution provided by IceTop will usher in a new era in the study of the propagation of GeV particles in the heliosphere.

Acknowledgements

References

[1] J. W. Bieber and P. Evenson. Spaceship Earth - An Optimized Network of Neutron Monitors. In *International Cosmic Ray Conference, 24th, Rome, Italy, August 28-September 8, 1995, Conference Papers. Volume 4.*, pages 1,316–1,319, 1995.

[2] J. Clem and P. Niessen. Response of Ice-Top tanks to low-energy particles. In *International Cosmic Ray Conference, 30th, Mérida, México, July 3-11, 2007, Conference Papers*, page submitted, 2007.

[3] L. Dorman. *Cosmic Rays in the Earth's Atmosphere and Underground*. Springer Verlag, 2004.

[4] A. Fassò et al. A comparison of FLUKA simulations with measurements of fluence and dose in calorimeter structures. *Nuclear Instruments and Methods in Physics Research Section A*, 332(3):459–468, 1993.

[5] S. E. Forbush. On World-Wide Changes in Cosmic-Ray Intensity. *Physical Review*, 54(12):975–988, 1938.

[6] I. Morishita et al. Long term changes of the rigidity spectrum of Forbush decrease. In *International Cosmic Ray Conference, 21st, Adelaide, Australia, January 6-19, 1989, Conference Papers. Volume 6.*, pages 217–219, 1990.

[7] M. H. Shamos and A. R. Liboff. A New Measurement of the Intensity of Cosmic-Ray Ionization at Sea Level. *Journal of Geophysical Research*, 71:4,651–4,659, 1966.

Measuring Cosmic Ray Composition at the Knee with SPASE-2 and AMANDA-II

K. G. ANDEEN[1], C. SONG[1] AND K. RAWLINS[2] FOR THE ICECUBE COLLABORATION [A].

[1]*IceCube Collaboration, University of Wisconsin-Madison, 1150 University Ave, Madison, WI*

[2] *University of Alaska Anchorage, 3211 Providence Dr, Anchorage, AK*

kandeen@icecube.wisc.edu ; [A] *See special section of these proceedings*

Abstract: Important information pertaining to the origin of high-energy cosmic rays can be gained by studying their mass composition in the region of the knee (~ 3 PeV). Thus, air showers have been observed at the South Pole using the SPASE-2 detector, which measures the electronic component at the surface, and the AMANDA-II neutrino telescope, which measures the coincident muonic component in deep ice. These two components, together with a Monte Carlo simulation and a well-understood analysis method, yield the relative cosmic ray composition in the knee region. We report on the efficacy of a new neural network technique for obtaining a composition result with the SPASE-2/AMANDA-II detectors.

Introduction

Cosmic ray composition studies can provide a greater understanding of the origin of cosmic rays, and thus lead to an increased understanding of the physical processes which accelerate these particles to Earth. At energies up to 10^{14} eV, the mass composition of cosmic rays can be measured directly; however, due to the low flux, the mass composition above 10^{14} eV must currently be gleaned from indirect measurements, involving the examination of the extensive air shower produced by the primary particle in the atmosphere. By utilizing more than one component of the air shower, such as the electronic and muonic components, an analysis technique can be developed that leads to a composition measurement.

Detectors and Reconstruction

The detectors used for this analysis the South Pole Air Shower Experiment (SPASE-2) and the Antarctic Muon And Neutrino Detector Array (AMANDA-II). The SPASE-2 detector is situated on the surface of the South Pole and is composed of 30 stations in a 30 m triangular grid. Each station contains four 0.2 m^2 scintillators. The AMANDA-II detector lies beneath the surface of the ice,

located such that the center-to-center separation between AMANDA-II and SPASE-2 is about 1730 m, with an angular offset of 12°. AMANDA-II consists of 677 optical modules (OMs) deployed on 19 detector strings at depths between 1500 and 2000 m. Each OM contains a photomultiplier tube which can detect the Cherenkov light emitted by particles–namely muon bundles–passing through the ice. Besides a composition analysis, this coincident detector configuration allows for calibration as well as measurement of the angular resolution of the AMANDA-II detector [1].

For this preliminary analysis, coincident data from the years 2003-2005 are used, with a total livetime of 369 days. For comparison with the data, Monte Carlo simulated proton and iron showers with energies between 100 TeV and 100 PeV have been produced using the MOCCA air shower generator [5] and the SIBYLL v1.7 interaction model [8]. These events are then propagated through the ice, and the detector response of AMANDA-II is simulated using AMASIM. An E^{-1} spectrum is used for generation, but for analysis the events are re-weighted to the cosmic ray energy spectrum of $E^{-2.7}$ at energies below the knee at 3 PeV, and $E^{-3.0}$ above it. Both the data and Monte Carlo are then put through the same reconstruction chain.

The first step in the reconstruction is to find the incoming direction of the air shower, as well as

the core position and shower size. The direction can be computed from the arrival times of the charged particles in the SPASE-2 scintillators, while the shower core position and shower size are acquired by fitting the lateral distribution of particle density to the Nishimura-Kamata-Greisen (NKG) function and then evaluating the fit at a fixed distance from the center of the shower (in this case 30 m) [3]. This parameter, called S30, has units of particles/m^2 and will be referred to throughout this paper as a measure of the electronic part of the air shower .

The next step in the reconstruction provides a measure of the muon component of the air shower, which is carried out using the combination of the two detectors. The core position of the shower measured at SPASE-2 is kept fixed as a vertex from which θ and ϕ are varied in the ice to obtain a good fit of the track direction in AMANDA-II. The expected lateral distribution function (LDF) of the photons from the muon bundle in AMANDA-II is then computed, fit to the OM hits, and evaluated at a perpendicular distance of 50 m from the center of the shower [7]. This parameter, called K50, has units of photoelectrons/OM and will be used throughout the rest of this paper as the measure of the muon component of the air shower.

Analysis Details

Once the reconstruction has been completed, it is important to find and eliminate poorly reconstructed events. Thus, as in the previous analysis [7], events have been discarded which:

- have cores outside either the area of SPASE-2 or the volume of AMANDA-II,

- have too low an energy to be well-reconstructed in both detectors,

- have an unphysical reconstructed attenuation length of light in the ice.

After these cuts have been made, it can be seen in Figure 1 that our two main observables, S30 and K50, form a parameter space in which primary energy and primary mass separate. This is expected, as the showers associated with the heavier primaries develop earlier in the atmosphere and
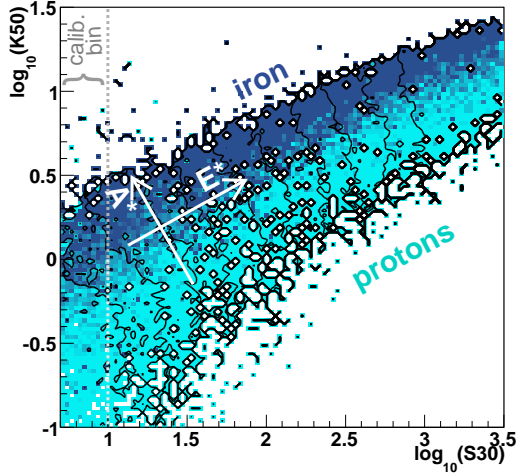
Figure 1: The two main observables, $\log_{10}$(K50) vs $\log_{10}$(S30), in the Monte Carlo simulation. The black contour lines depict gradients in energy. The axes along which mass (A*) and energy (E*) change in a roughly linear way are drawn in white, and the low-energy calibration bin is also labeled.

hence have more muons per electron by the time they reach the surface than the showers associated with lighter primaries [4]. This means that K50, which is proportional to the number of muons in the ice, will be higher for heavier primaries than for lighter primaries of the same S30, as is observed.

In the three-year data set used for this analysis, 105,216 events survive all quality cuts. It is interesting to notice that in the previous analysis, using the SPASE-2/AMANDA-B10 detector, the final number of events for one year was 5,655. Furthermore, the larger detector used here is sensitive to higher energy events. The significant increases in both statistics and sensitivity are the basis for performing a new analysis.

Calibration

To accurately measure the composition using both electron and muon information reconstructed as described above, the Monte Carlo simulations must represent the overall amplitude of light in the ice very well. However, the overall light ampli-
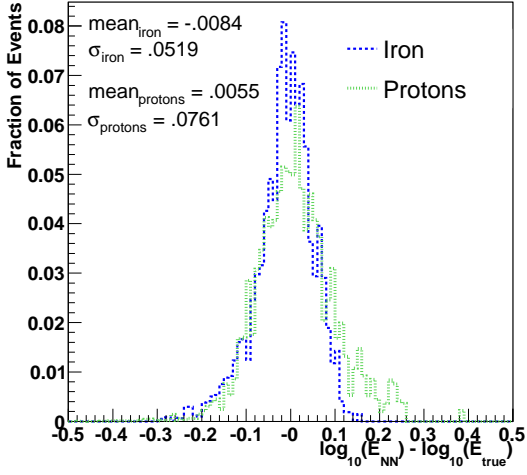
Figure 2: The energy resolution of the neural network for output energies between 1 and 10 PeV for proton and iron showers.

Figure 3: The neural network output for particle type with $\log_{10}(E_{NN}/\text{GeV})$ between 6.0 and 6.2. The three-year data set is compared to the Monte Carlo generated proton and iron showers, and a mixing ratio is found which represents the data.

tude is subject to systematic errors in the simulation. Therefore, it is important to calibrate the composition measurement at low energies where direct measurements of cosmic ray composition are available from balloon experiments. A vertical "slice" of events from Figure 1, corresponding to S30 between 5 and 10 m^{-2}, is used to perform this calibration. The K50 values of the data adjusted by an offset, chosen such that the distribution of K50 best matches a 50%-50% mixture of protons and iron [2, 7]. This mixture corresponds to $<\ln A> = 2$, which is an approximation to the value indicated by direct measurements [6].

The Neural Network

Similar past analyses [2] exploited the fact that the relationship between K50/S30 and mass/energy is approximately linear. One can then rotate to the mass/energy coordinate plane, labeled as A*/E* in Figure 1, and utilize further analysis techniques to extract the energy and mean log mass after the rotation. However, the relationship is not perfectly linear, nor should exact linearity necessarily be expected. In fact, as seen in Figure 1, the non-linear effects become more pronounced at higher ener-

gies. As the data set for this new analysis has more statistics at high energies than previous analyses, it has become important to find a technique that can resolve these events with accuracy. A neural network should be able to take these non-linear effects into account.

The neural network chosen for this analysis was the TMultiLayerPerceptron class from ROOT, which is a simple, feed-forward network, although other neural networks were also tested with similar results. The network configuration which best separates the pure proton from the pure iron scenarios and yields the best energy resolution in the Monte Carlo was a very simple 2:5:2 network, meaning there are two input variables, five hidden nodes, and two output variables. In this case, the two input variables are $\log_{10}(K50)$ and $\log_{10}(S30)$, and the two outputs are energy and particle type (0 for protons, 1 for iron). The network is trained on half of the Monte Carlo and tested on the other half (to evaluate its effectiveness) before being applied to the data. Figure 2 shows the energy resolution of the neural network for proton and iron showers. The "type" output of the neural network for one

energy bin is plotted in Figure 3. Notice that, since it was trained on pure proton and iron samples, the neural network tends to classify every event strictly as one or the other, resulting in the strong peaks in the data at 0 and 1. It is expected that the simulation of more primary nuclei would yield a more accurate result.

It is assumed that the data can be described by some mixture of proton and iron showers, and a technique is developed to find the mixing ratio in each energy bin which best fits the data. In order to find this proportion, the proton, iron, and data outputs are normalized and a minimization technique is applied. The result is one mixing ratio for each "slice" in energy; an example of this is shown by the solid black line in Figure 3 This method was verified using various mixtures of proton and iron simulations as input "data" and comparing with the non-mixed monte-carlo results. The ratio of heavy particles in each energy bin can also be expressed as the mean log mass. The difference between $<lnA>$ for the neural network technique described herein and $<lnA>$ for a rotation method similar to that used for the previous SPASE-2/AMANDA-B10 analysis is reported in Figure 4. (Note that the same data set was used for both methods.)

Discussion

It is clear from Figure 4 that the percent difference in $<lnA>$ between the two types of analysis methods is generally quite small, especially below $\log_{10}(E/GeV) = 6.8$, which is the highest energy measured in the previous analysis. Furthermore, it seems promising that the percent difference increases at higher energies where the neural network is expected to be more reliable. The systematic errors for this data sample have yet to be fully examined, and a new Monte Carlo simulation with a variety of primary nuclei–including helium, carbon and oxygen in addition to protons and iron– is currently being generated. Nevertheless, there is a clear indication that the neural network technique is a valid method for understanding SPASE-2/AMANDA-II data, and it is hoped that, together with the new simulation and new data from the IceCube/IceTop coincident detectors, this new technique will allow us to probe energies up to 10^{18} eV.
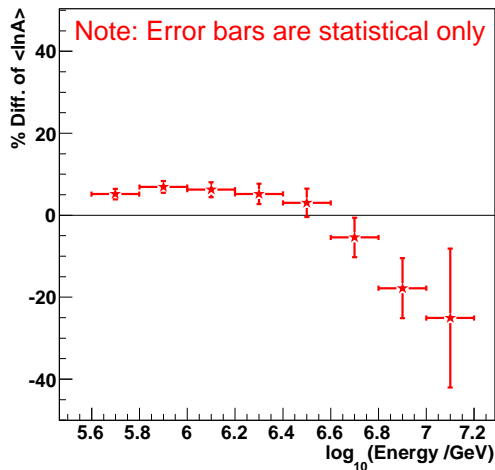
Figure 4: The percent difference in $<lnA>$ between two analysis techniques applied to the same three-years of SPASE-2/AMANDA-II data.

Acknowledgements

References

[1] J. Ahrens et al. *Nuclear Instruments and Methods*, 522:347–359, 2004.

[2] J. Ahrens et al. *Astroparticle Physics*, 21:565–581, 2004.

[3] J.E. Dickinson et al. *Nuclear Instruments and Methods*, 440:95–113, 2000.

[4] T. Gaisser. *Cosmic Rays and Particle Physics*. Cambridge University Press, 1988.

[5] A.M. Hillas. *Proceedings of the 24th International Cosmic Ray Confrence*, 1:270, 1995.

[6] J.R. Hörandel. *International Journal of Modern Physics A*, 20(29):6753–6764, 2005.

[7] K. Rawlins. PhD thesis, University of Wisconsin, Madison, 2001.

[8] R.S. Fletcher T.K. Gaisser, P. Lipari and T. Stanev. *Phys. Rev. D*, 50:5710, 1994.

Cosmic Rays in IceCube: Composition-Sensitive Observables

C. SONG[1], P. NIESSEN[2] AND K. RAWLINS[3] FOR THE ICECUBE COLLABORATION[*]

[1] *University of Wisconsin, 5th Floor Suite, 222 W. Washington Ave. Madison, WI 53717, USA*

[2] *Bartol Research Institute, University of Delaware, 104 Center Mall, Newark, DE 19716, USA*

[3] *University of Alaska, 3211 Providence Drive, Anchorage, AK 99508, USA*

[*] *See a special section of the proceedings*

csong@icecube.wisc.edu

Abstract: Cosmic ray showers that trigger the IceTop surface array generate high energy muons that are measured by the IceCube detector. The large surface and underground area of this 3-dimensional instrument at completion guarantees significant statistics for shower energies up to about 1 EeV. Since the number of muons is sensitive to the type of the primary cosmic ray nucleus, these events can be used for the measurement of cosmic ray composition. Using the data taken in the existing array, we measure the observables sensitive to the primary mass as a function of shower energy estimated by the surface array. The result is compared to simulations of the coincident events of different primary nuclei.

Introduction

Cosmic rays follow a steep power-law spectrum which spans a wide energy range up to a few 10^{20} eV. One of the interesting features in the all-particle energy spectrum is that the cosmic ray spectrum steepens around 3 PeV, which is called the 'knee'. The origin of the knee is generally understood to be due to the limiting energy attained during the acceleration process and/or leakage of charged particles from the galaxy. The mass composition of cosmic rays at the knee region provides important clues to their origin.

The IceCube Observatory located at the South Pole, a 3-dimensional instrument which consists of the IceTop surface detector and IceCube optical sensor arrays, is uniquely configured to measure cosmic ray composition. The IceTop surface array will consist of 80 pairs of frozen water tanks which measure the energy deposition at the surface, and 80 strings of 60 digital optical modules (DOMs) in ice will measure Cherenkov photons from muon bundles. The DOMs are attached to a cable every 17 m, between depths of 1,450 and 2,450 m. A pair of the IceTop tanks separated by 10 m is located above each IceCube string and a tank employs two DOMs which are identical to in-ice DOMs but with different PMT gains, which results in a wide dynamic range.

Data and simulation

IceTop/IceCube coincident data taken in 2006 were used for this analysis. In 2006, 16 pairs of IceTop tanks and 9 IceCube strings were operational. Events were recorded when the following trigger conditions were satisfied: 6 hits within 2 μs for IceTop DOMs, and 8 hits within 5 μs for in-ice DOMs. The coincident rate is about 0.2 Hz. A threshold of 300 TeV allows us to measure cosmic rays below the knee.

Air shower events were simulated with CORSIKA[1], and GHEISHA[2] and SIBYLL-2.1[3] were selected as the low and high energy hadronic interaction models, respectively. Proton and iron showers were generated over an area of 4.5 km^2 covering the IceTop array, from energies of 50 TeV to 5 PeV, using the South Pole atmospheric model[4]. The events were generated according to E^{-1} spectrum and re-weighted to the cosmic ray energy spectrum with spectral index of -2.7 below the knee at 3 PeV, and -3.0 above it.
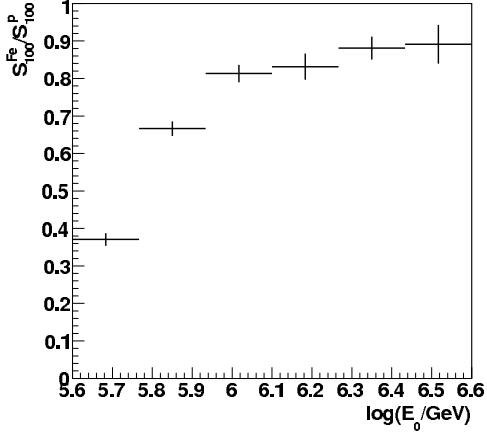
Figure 1: Ratio of S_{100}^{Fe} to S_{100}^{p} as a function of the total energy per nucleus (E_0).

Figure 2: Average charge per in-ice DOM is shown as a function of a perpendicular distance from a primary track for proton and iron showers [$0.5 < \log(S_{100}) < 1.3$].

As a first guess, the shower core is determined by calculating the center of gravity of tank positions by weighting with the square root of pulse amplitude. The shower direction is determined on the basis of shower front arrival times measured by the IceTop tanks. The energy deposition at the surface as a function of distance from the shower core is fitted to the function given by[5]:

$$f(r) = S_{100} \left(\frac{r}{100\mathrm{m}} \right)^{-\beta - \kappa \log(r/100\mathrm{m})} \qquad (1)$$

where r is a distance from shower core, κ is 0.303 for hadronic showers, and S_{100} is the signal in vertical equivalent muon (VEM) per tank at 100 m from the shower core. The parameter β is roughly correlated with shower age via $s = -0.94\beta + 3.4$. S_{100} is an energy estimator and depends on primary mass, as shown in Figure 1.

The events which passed the following quality cuts are used in this study:

- Reconstructed shower core lands 60 m inside of IceTop array.

- β in Eq. (1) is less than 6.

- Reconstructed zenith angle is less than 20°.

- The number of hit strings is greater than 1.

The number of hit strings is required to be equal to or greater than 2 since the lateral distribution fit in ice which will be described in the next session fails if a reconstructed track is vertical.

Cosmic ray composition

The IceCube detector is located deep in ice, so only muons can reach the detector, and useful information about primary cosmic rays can be inferred from muon bundles with the 3-dimensional instrument. The total number of muons in a bundle is dependent on the type of primary nucleus. Cherenkov photons from the muon bundle are detected by optical sensors in ice, and the photon intensity is measured as a function of perpendicular distance from a primary muon track and fitted by an exponential function. The primary muon track is the shower axis determined by the IceTop array. Figure 2 shows the average charge per in-ice DOM as a function of the distance from a primary track to each hit DOM in a range of S_{100} between 0.5 and 1.3 showing separation between proton and iron

28
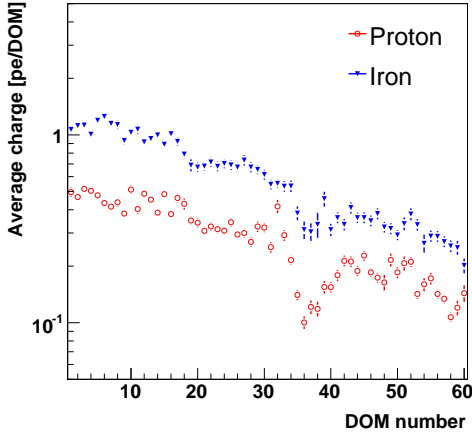
Figure 3: Average charge vs. DOM number for proton and iron showers $[0.5 < \log(S_{100}) < 1.3]$.

Figure 4: Average charge vs. DOM number for proton showers only at different distance ranges $[0.5 < \log(S_{100}) < 1.3]$.

showers. It was found, for the SPASE/AMANDA detectors, that the photon intensity at 50 m (K_{50}) is most sensitive to the mass of primary cosmic rays[6]. Ranging-out of muons and depth dependence of light scattering in the ice are taken into account in the lateral distribution fit. However, these corrections are not made in Figure 2. Once we find all observables sensitive to primary mass, we will feed them into a neural network (see [7] for detailed description) for composition analysis.

Figure 3 shows the average charge as a function of DOM number for proton and iron showers. Overall the average charge decreases with depth, featuring changes in the optical properties of ice. For instance, a thick dust layer observed by a dust logger during string deployment is seen around DOM 36. Figure 4 shows the same as Figure 3 but with three different distance ranges only for proton showers, and indicates that using the hits close to muon bundles gives measurement less dependent on ice properties. An appropriate correction for the dust layer needs to be made, or those DOMs around the dust layer can be removed in the analysis.

In addition to charge, we looked into timing information to see whether or not it is sensitive to primary mass. The size of the muon bundle depends on the type of the primary nucleus at a given en-

ergy and can affect the time residual (observed minus expected times from the primary muon track). The expected time is the travel time of a direct Cherenkov photon from the primary muon track to each hit DOM. The time residual distribution is fitted by $\exp(-\alpha t)$ from 50 to 400 ns where the tail of the distribution is straight in log scale, and the slope, α, of the distribution as a function of DOM number is shown in Figure 5. Separation between proton and iron showers is seen, and the slope varies depending on depth of DOM and rises at dusty layers.

Discussion

We investigated observables sensitive to primary mass. In addition to charge information from the DOMs in ice, the slope of the time residual distribution seems to be sensitive to the type of the primary cosmic ray, though it has dependence of optical properties of ice. However the dependence of ice properties can be reduced by making an appropriate correction for dusty layers or by excluding the DOMs in the thick dust layer around DOM 36. Moreover, DOMs close to a muon bundle appear to be best suited for such an analysis. Once
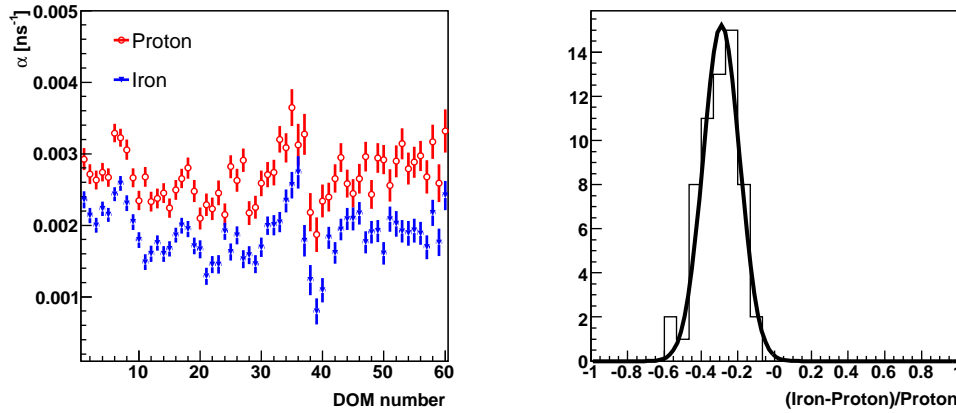
Figure 5: Slope (α) of the time residual distribution as a function of DOM number (left) and distribution of $(\alpha^{Fe} - \alpha^p)/\alpha^p$ (right) are shown.

we have all observables sensitive to primary mass, the neural network can be employed for cosmic ray composition studies.

Acknowledgments

References

[1] D. Heck, J. Knapp, J. N. Capdevielle, G. Schatz, and T. Thouw, *CORSIKA FZKA 6019*, Forschungszentrum Karlsruhe, 1998.

[2] H. Fesefeldt, *Report PITHA-85/02*, RWTH Aachen, 1985.

[3] R. S. Fletcher, T. K. Gaisser, P. Lipari, and T. Stanevi, *Phys. Rev. D*, **50** 5710, 1994.

[4] D. Chirkin, parameterization based on the MSIS-90-E model, 1997.

[5] S. Klepser, F. Kislat, H. Kolanoski, P. Niessen, and A. Van Overloop for the IceCube collaboration, *International Cosmic Ray Conference, 30th, Mérida, Mexico, July 3-11, 2007*.

[6] J. Ahrens and *et al*, *Astropart. Phys.*, **21** 565, 2004.

[7] K. Andeen, C. Song, and K. Rawlins for the IceCube collaboration, *International Cosmic Ray Conference, 30th, Mérida, Mexico, July 3-11, 2007*.

Search for TeV gamma-rays from point sources with SPASE2

KORY JAMES[1], X. BAI[1], T.K. GAISSER[1], JIM HINTON[2], PETER NIESSEN[1], TODOR STANEV[1], SERAP TILAV[1], AND ALAN WATSON[2] FOR THE SPASE2 AND ICECUBE COLLABORATIONS*

[1]*Bartol Research Institute, Department of Physics and Astronomy, University of Delaware, Newark, DE 19716, U.S.A.*
[2]*School of Physics & Astronomy, University of Leeds, LS2 9JT UK*
stanev@bartol.udel.edu, * *see special section of these proceedings*

Abstract: The South Pole Air Shower Experiment (SPASE2) began operation in 1996 and took data until it was decommissioned in December 2006. We are currently analyzing those of the 205 million reconstructed events that were taken during the last five years. In this paper we report on a search for 100 TeV gamma-rays from three specific Southern hemisphere point sources discovered by HESS. that may have gamma-ray spectra extending to energies higher than 50 TeV.

Introduction

The SPASE2 scintillator array at the Amundsen-Scott South-Pole station is at an altitude of 2835 m.a.s.l., corresponding to a year-round average atmospheric overburden of $695\,\mathrm{g cm}^{-2}$. The total area within the perimeter of the array is $16,000\,\mathrm{m}^2$ [1]. For this search we use data taken during the last five years with livetime of 171+167+204+307+322=1171 days = 3.21 years.

In this work, we focus on the following three HESS sources:
a) The shell-type supernova remnant RX J0852.0-4622 [2]. It has a spectrum observed in the energy range between 500 GeV and 15 TeV, which can be well described by a power law with a spectral index of $2.1\pm0.1_{stat}\pm0.2_{syst}$ and a differential flux at 1 TeV of $(2.1\pm0.2_{stat}\pm0.6_{syst})\times10^{-11}$ $\mathrm{cm}^{-2}\mathrm{s}^{-1}$ TeV^{-1}. The corresponding integral flux above 1 TeV was measured to be $(1.9\pm0.3_{stat}\pm0.6_{syst})\times10^{-11}$ $\mathrm{cm}^{-2}\mathrm{s}^{-1}$.
b) The Supernova Remnant MSH 15-52. Its image [3] reveals an elliptically shaped emission region around the pulsar PSR B1509-58. The overall energy spectrum from 280 GeV up to 40 TeV can be fitted by a power law with spectral index $\alpha=2.27\pm0.03_{stat}\pm0.20_{syst}$ and a differential flux at 1 TeV of $(5.7\pm0.2_{stat}\pm1.4_{syst})\times10^{-12}$ $\mathrm{TeV}^{-1}\mathrm{cm}^{-2}\mathrm{s}^{-1}$.

c) The unidentified TeV γ-ray source close to the galactic plane named HESS J1303-631 [4] is an extended source with a width of an assumed intrinsic Gaussian emission profile of $\sigma = (0.16\pm0.02)^o$. The measured energy spectrum can be described by a power-law $\mathrm{d}N/\mathrm{d}E = N_0 \cdot (E/TeV)^{-\alpha}$ with a spectral index of $\alpha=2.44\pm0.05_{stat}\pm0.2_{syst}$ and a normalization of $N_0=(4.3\pm0.3_{stat})\times10^{-12}$ $\mathrm{TeV}^{-1}\mathrm{cm}^{-2}\mathrm{s}^{-1}$.

Energy estimate

The particle density at 30 meters from the shower core, S_{30}, is used by the SPASE2 experiment to estimate the primary particle energy. Monte Carlo simulations tell us that the S_{30} for 100 TeV γ-rays is higher than for 100 TeV proton. The Monte Carlo simulates cascades as well as the response of the air shower array using Corsika with the 2.1 version of the Sibyll [6] interaction model.

Currently a Monte Carlo estimate is available for all showers with zenith angles between 20° and 50°. For example, at S_{30} of 3 m^{-2}, E_γ is about 120 TeV, while E_p is 180 TeV. We will perform more simulations to determine the energy dependence as a function of the zenith angle.

Angular resolution

The angular resolution of an air shower array is much worse that that of an air Cherenkov telescope. We have estimated the SPASE2 angular resolution in two different ways - using the experimental data with sub-array comparison and with Mote Carlo calculations.

In the sub-array approach the SPASE2 array is divided into two parts. For each one the shower angle is estimated separately. The space angle between the two sub-arrays is used to study the angular resolution.

Monte Carlo events after the standard shower reconstruction were also used to determine the angular resolution. The results from both methods fully agree with each other at higher energy. At threshold the sub-array approach suffers from statistical fluctuations because there are not enough detectors that respond to the showers.

Fig. 1 shows the integral distribution of the square of the space angle difference between the true direction of the simulated shower and the reconstructed direction Ψ^2 for γ-ray showers with $S_{30} > 3$ m^{-2}. The Ψ^2 value that contains 68% of all events is $(2.1^o)^2$. For showers of $S_{30} < 3$ m^{-2} this number is $(3.3^o)^2$. Proton showers in both energy ranges show slightly worse angular resolution.
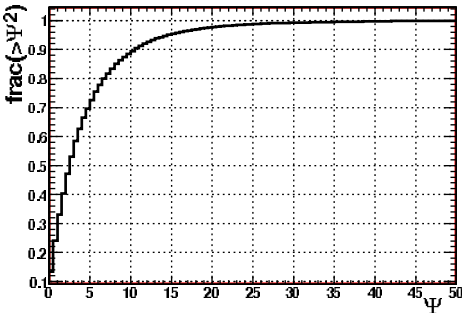
Figure 1: Integral distribution of the Ψ^2 values (in square degrees) derived from simulation of γ-induced showers.

Systematic errors

There are several possible sources of systematic errors in the data set. One is that at the beginning of 2002 the electronics of the shower ray was updated with a consequent increase of its threshold. For this reason we will first use the five years data taken after 2001.

A second source is that the response of SPASE2 has 2% variation with azimuth. Since the array typically has a lower duty cycle in the antarctic summer this could lead to a background that is not completely uniform in right ascension.

The background

We studied the possible anisotropies by looking at the scrambled RA distribution in different declination bins. Initially our data set was *blinded*. Scrambling was performed by shifting the real RA by a random amount. Figure 2 shows the rms value over the Gaussian expectation in Gaussian standard deviations σ for zenith angles from 20° to 50°. In this case the average number of entries per bin is 1.37 million and the standard deviation of Fig. 2 is 1.17×10^3 showers. Out of 60 bins 38 bins show deviation by less than 1σ and 3 bins have devia-
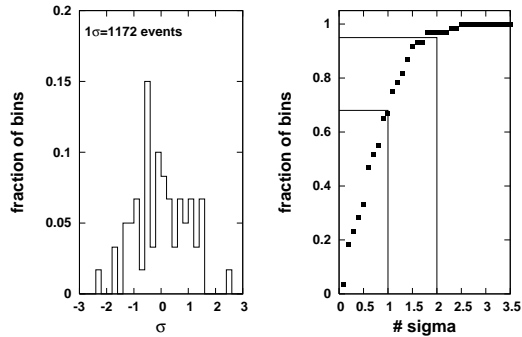
Figure 2: Left-hand panel: Distribution of the deviation from the average for 60 6° RA bins. Right-hand panel: Integral distribution in number of σ.

tions of more than 2σ which fully agrees with a Gaussian distribution.

We also looked at these distributions for smaller zenith angle bins similar to those that we will use in the source search. Fig. 3 shows the scrambled

RA distribution in $6^o \times 6^o$ bins for the zenith angle band of 41° to 47°, which almost coincides with one of the sources. The results are very similar to those for the wider zenith angle band.
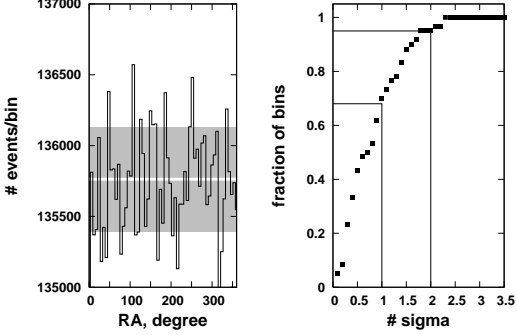
Figure 3: Left-hand panel: Number of events per bin in the declination band 41°- 47°. The average is shown with a white line and the shaded area represents $\pm 1\sigma$. Right-hand panel: Integral distribution in number of σ for the declination band.

Angular bins

The angular bins recommended for source search with air shower arrays [7] correspond to an elliptical region with axes equal to $1.59\sigma_0$ where σ_0 is the angular resolution of the detector. We decided to use equal solid angle which means that the major axis of the ellipses are bigger at low zenith angles. We will search separately for showers with S_{30} higher and lower than 3 m^{-2}. The angular resolution for S_{30} >3 m^{-2} is 2.1^o and is about 3.3^o for lower energy showers. The search ellipses would be correspondingly wider for lower energy showers. The search ellipses for the three sources and the two S_{30} values are plotted in relative RA units in Fig. 4. Since the angular area of these bins (and correspondingly the number of background events in them) is higher than those used in the previous section the expected detection probability is slightly different.

Signal expectations

Because of its flat energy spectrum the source RX J0852.0-4622 offers the highest chance for detec-
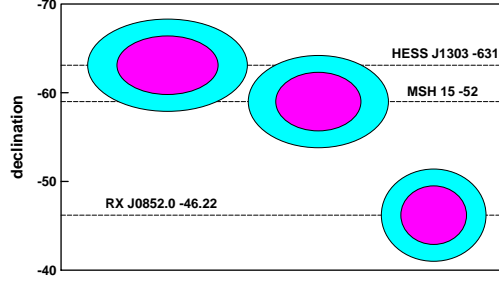
Figure 4: Relative sizes of the search ellipses for the three sources and the two S_{30} values - light shading is for S_{30} <3 and the dark shading is for S_{30} >3.

tion if its spectrum does not cut off. It is, however, at the highest zenith angle of the 3 sources studied. We will first look at the 2005 data set. Assuming conservatively the area of SPASE2 to be 10^8 cm^2 and livetime in 2005 of $2.65.10^7$ s, we expect to have 321 (149) events above E_γ^{thr} 100 (200) TeV. At zenith angle of 43.8^o this would roughly correspond to S_{30} values of 1 and 3 m^{-2}. There may be some contribution from lower energy gamma ray showers but the array efficiency below 100 TeV is less than one and we need further Monte Carlo studies to estimate it.

The backgrounds estimated from the two search ellipses for RX J0852.0-46.22 (excluding the source bins) are respectively 38656 (13739) per bin for S_{30} <3 (S_{30} >3). The background for the lower energy showers is higher because of the much steeper cosmic ray spectrum compared to the γ=1.1 for the source. The expected number of gamma showers thus corresponds to 0.88σ for S_{30} <3 and 1.27σ for S_{30} >3. SPASE2 is not, by far, the best detector for γ-ray astronomy, but the chance of detection is reasonable for a flat source spectrum and no cut off.

The other two γ-ray sources are less intense and can produce not more than several tens of events even if their spectra do not cut off. For this reason we will present only the results for RX J0852.0-46.22.

Results from the 2005 search

Figure 5 shows the observed number of showers from the direction of RX J0852.0-46.22 in the 2005 data set (which we unblinded first) for the two S_{30} values. Note that the bins do not cover the whole 24 hours of RA in the zenith angle band because of the requirement for equal space angle bins. The missing phase space is always less than one bin width. Both searches give negative results. In the
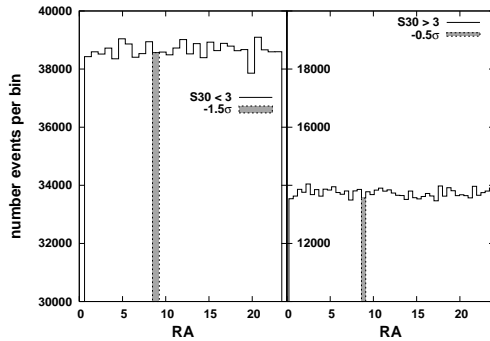
Figure 5: Observed number of showers from the position of the source RX J0852.0-4622 for the two energy bins.

$S_{30} < 3$ sample we see -1.5σ from the average expected background. In the higher energy range the lack of events is smaller (-0.5σ).

Conclusion

The search for 100 TeV γ-ray signal from RX J0852.0-46.22 in the SPASE2 data set for 2005 gave negative results - we did not observe any showers above the expected cosmic ray background. However, based on the preliminary simulation used here to relate S_{30} to primary energy, we find a limit based on one year data that is nearly inconsistent with the continuation of the spectrum of RX J0852.0-46.22 to 100 TeV without a steepening of its spectrum. We therefore plan to pursue this analysis and to search separately in all five years data and then combine the results, possibly using a more sensitive unbinned search. We will use a detailed simulation of γ-ray and cosmic ray showers appropriate for the declination of

this source which corresponds to a zenith angle of 43.8^o.

References

[1] J.E. Dickinson et al. The SPASE Collaboration Nuclear Instruments & Methods A 440:95 (2000)

[2] F. Aharonian, et al. HESS Collaboration, A&A 437, L7-L10 (2005)

[3] F. Aharonian, et al. HESS Collaboration, A&A 435, L17-L20 (2005)

[4] F. Aharonian, et al. HESS Collaboration, A&A 439, 1013-1021 (2005)

[5] D. Heck et al., Report FZKA-6019, Forschungszentrum Karlsruhe

[6] R.S. Fletcher et al., Phys. Rev. D50, 5710 (1994); R. Engel et al., in Proc. 26th Cosmic Ray Conference, Salt Lake City, **1**, 415 (1999)

[7] D.E. Nagle, T.K. Gaisser & R.J. Protheroe, Ann.Rev.Nucl.Part.Sci. 38, 609-657 (1988)

Study of High p_T Muons in Air Showers with IceCube

SPENCER R. KLEIN[1] AND DMITRY CHIRKIN[1] FOR THE ICECUBE COLLABORATION[2]
[1]*Lawrence Berkeley National Laboratory, CA, 94720 USA*
[2] *see the special section of these proceedings*

srklein@lbl.gov

Abstract: With it's 1 km^2 area, IceCube and the associated IceTop surface detector array are large enough to study high p_T muon production in air showers. The muon p_T will be determined from the muon energy and it's distance from the core. A few thousand high p_T muons are expected to be observable each year in the full array. The flux of high p_T muons may be computed using perturbative QCD calculations; the cross-section is sensitive to the composition of the incident particles.

Introduction

The number of muons produced in cosmic-ray air showers is sensitive to the nuclear composition of the incident particles. Previous studies of the cosmic-ray composition have used relatively low ($\approx$ 1 GeV) or high ($\approx$ 1 TeV) energy muons. These studies relied on muon counting. Relating the muon count to the composition requires a model for the hadronic interactions; most of the muons come from π/K decay; the bulk of the mesons are produced at low transverse momentum (p_T) with respect to the direction of the incident particle. The production of these low p_T particles cannot be described in perturbative QCD (pQCD), so phenomenological models must be used.

In contrast, the production of particles with $p_T > \sim$ 2 GeV/c is calculable in pQCD. We label these tracks high p_T particles, and consider their production in cosmic-ray air showers. High p_T muons come from the decay of charm and bottom quarks, and from π/K produced in jets. Both of these processes can be described by pQCD, allowing for calculations of the energy and p_T spectra for different incident nuclei. The predictions depend sensitively on the composition of the incident nuclei - neglecting shadowing, a nucleus with energy E and atomic number A has the same parton distribution as A nucleons, each with energy E/A. Nuclei with $A = 1$ and $A = 10$ have very different parton energy spectra.

High p_T muons in Air Showers

Previous studies of high-energy muons associated with air showers have involved relatively small detectors. AMANDA has measured muon bundles near the shower core, but did not study the muon lateral distribution [1]. MACRO measured the muon decoherence function for separations up to 65 m [2]. The most likely pair separation was 4m; only 1% of the pairs have a separation greater than 20 m. MACRO simulated air showers and studied the pair separation as a function of the p_T of the mesons that produced the muons. The MACRO analysis established a clear linear relationship between muon separation and p_T; the mean p_T rose roughly linearly with separation, from 400 MeV/c at zero separation up to 1.2 GeV/c at 50 meter separation.

IceCube will observe both high-energy muons and the associated surface air showers that accompany them. For muons with energy E_μ above 1 TeV, the muon energy is proportional to the specific energy loss (dE/dx) that is measured by the deep detectors; the muon energy resolution is about 30% in $\log_{10}(E_\mu)$ [3, 4].

The muon energy and distance from the shower core can be used to find the p_T of a muon [6]:

$$d = \frac{h p_T}{E_\mu}. \tag{2}$$

Here, h is the height of the primary cosmic-ray interaction in the atmosphere. h follows an exponential distribution and depends somewhat on the cosmic-ray composition. A full analysis would include these effects. Here, we take $h = 30$ km.

Secondary interactions (of particles produced by the first interaction) are expected be only a small contribution to the high-energy flux, contributing at most 15% of the muons [7]. For muons far from the core, multiple scattering is expected to be a small contribution d.

Here, we consider showers where the core is inside the 1 km^2 area of IceTop, and muons following the core trajectory are inside the IceCube physical volume. This corresponds to about 0.3 km^2 sr total acceptance.

IceCube will detect air showers above an energy threshold of about 300 TeV; for vertical showers, the minimum muon energy is about 500 GeV. The rate for triggered IceTop-InIce coincidences for the 9-string IceCube array is about 0.2 Hz [8], or about 6 million events/year. The full 80-strings + stations should produce a rate more than an order of magnitude higher.

For vertical showers with energies above 1 PeV, the core location is found with a resolution of about 13 meters, and the shower direction is measured to about 2 degrees [9]. This allows the core position to be extrapolated to 1500 m in depth with an accuracy of about 55 meters, corresponding to a p_T uncertainty of 1.6 GeV/c for a 1 TeV muon.

Most of these air showers are accompanied by a muon bundle. A high p_T analysis will select events with a muon (or bundle) near the core, and another muon at a large distance from it. The near-core muon(s) can be used to refine the core position, avoiding the extrapolation error. The muon positions at a given depth can be determined within a 10-20 meters, allowing for better p_T resolution. Figure 1 shows an example of an IceCube 22-string event that contains an air shower that struck Ice-Top stations, plus muon bundle. Although the bulk of the bundle follows the shower direction, as projected from IceTop, there is a well-separated light

run 107866 event 2586581
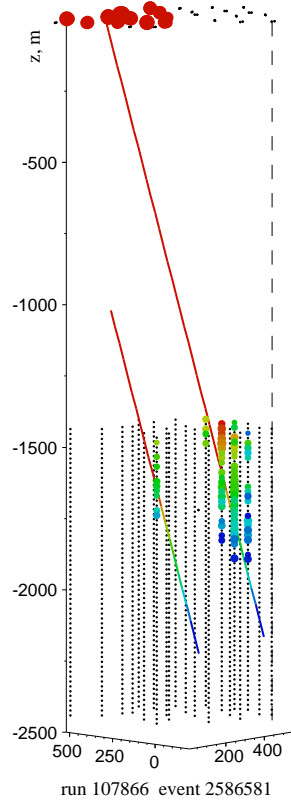
Figure 1: An IceTop air shower accompanied by a muon bundle including an apparent well-separated track. The air shower hits 11 surface stations (top of diagram). A total of 96 IceCube DOMs are hit; 84 DOMs on four strings near the extrapolated air shower direction, plus 12 DOMs on another string, about 400 m from the projection.

source, consistent with a high p_T muon, about 400 meters from the bulk of the muon bundle. This secondary track hits 12 DOMs on a single string.

For this analysis, the key performance issue is two-track resolution. This remains to be determined. However, the 125 m string spacing and the comparable (depth-dependent) light absorption length set the scale for two-track resolution. Two muons 100 meters apart in IceCube will largely deposit light in different strings; for a DOM near one muon, the first light from the farther muon will arrive about 500 nsec after the first light from the nearby muon. If the second muon (or muon bundle) is bright enough to illuminate a DOM 100 meters away,

36

this late light will be temporally separate from that from the nearby muon. A minimum ionizing muon is not bright enough to be visible 100 meters away, but muon bundles may be. Here, we estimate that IceCube can reconstruct muon pairs that are separated by 100 meters; smaller separations may be possible with optimized tracking.

For a muon with energy of 1 TeV, 100 meters separation corresponds to a p_T of 3 GeV/c. For a fixed separation, the minimum p_T rises linearly with muon energy, reaching $p_T > 150$ GeV/c for a 50 TeV muon. The highest energy muons are likely to come from high energy showers; the additional light will improve position reconstruction, and may allow for reconstruction at smaller separation distances. Still, there are unlikely to be useful events at higher energy/p_T.

Rates

High p_T muons come from two sources: prompt muons from charm/bottom decays, and non-prompt muons from decays of high p_T pions and kaons. The charm rates have been discussed previously [6, 5], about 600,000 muons per year with energy above 1 TeV are expected in the 0.3 km^2 acceptance. Only 1-2% of these muons will have $p_T > 3$ GeV/c. Still, this is a useful signal.

Bottom quark production in air showers has received much less attention. Although $b\bar{b}$ production in air showers is only about 3% of $c\bar{c}$ [10], the higher quark mass changes the kinematics, increasing the importance of $b\bar{b}$ production at high p_T. At LHC energies, about 10% of the muons from $b\bar{b}$ should satisfy the $p_T > 3$ GeV/c cut, and, at high enough p_T, they should be the dominant prompt contribution [11].

Although they are far more numerous than prompt muons, non-prompt muons have a much softer p_T spectrum. Non-prompt production may be estimated by using the measured p_T spectrum from π produced in high-energy collisions. The PHENIX collaboration has parameterized their π^0 spectrum at mid-rapidity with a power law: $dN/dp_T \approx 1/(1 + p_T/p_0)^n$, where $p_0 = 1.219$ GeV/c, and $n = 9.99$ [12]; about 1 in 200,000 π^0 has $p_T > 3$ GeV/c. This data is at mid-rapidity, while most muons seen in air showers come from far forward

production. LHC will provide good data on forward particle production at the relevant energies. Here, we neglect this difference and ignore the minor differences between π^0 and $\pi^\pm \rightarrow \mu^\pm$ and $K^\pm \rightarrow \mu^\pm$ spectra. With the acceptance discussed above, IceCube expects to see more than 100 million muons/year associated with air showers, including at least 500 of them with $p_T > 3$ GeV/c.

Overall, based on the standard cosmic-ray models, we expect $\approx 1,000 - 3,000$ muons with $p_T > 3$ GeV/c year.

Muon spectral analysis & Composition Analysis

The 'cocktail' of charm, bottom and non-prompt muons is not so different from that studied at RHIC [13][14]; the prompt fraction is also not too different. There, the muon p_T spectrum is fitted to a mixture of prompt and non-prompt sources. In air showers, the accelerator beam is unknown; it constitutes the initial object of study.

The rate of high p_T muons is sensitive to the cosmic-ray composition. High p_T particles are produced in parton-parton collisions, and, as Fig. 2 shows, the parton densities of a 10^{17} eV proton and of a 10^{17} eV $A = 10$ nucleus are quite different. In contrast to the usual presentation, these are normalized to the parton energies, although the per-nucleon energies are different for the two cases. The nuclear distribution cuts off at an energy of $10^{17}/A$ eV, limiting the maximum parton-parton center of mass energy, and thereby constraining the possible muon kinematics. Because of this, the yield of high-energy, high p_T particles is much higher for protons than for heavier nuclei.

Most of the muons seen by IceCube are produced in the forward region, where a high$-x$ parton from the incident nucleus interacts with a low$-x$ parton from a nitrogen or oxygen atom in the atmosphere. The maximum muon energy is the incident parton energy $E_p = x_p E_c$ where x_p is the parton energy fraction and E_c is the cosmic-ray energy.

In the far-forward limit, the incident parton energy $x_{inc} = E_p/E_{incident} \approx E_\mu/E_{shower}$. So, these muons are quite dependent on the high$-x$ partons that are sensitive to nuclear composition.
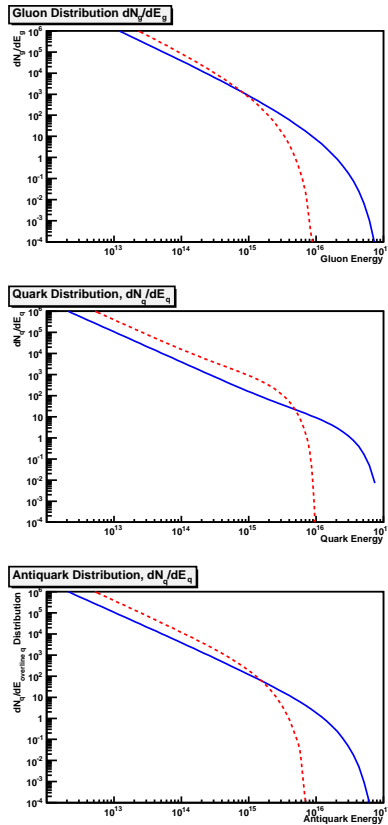
Figure 2: Quark (top), gluon (middle) and antiquark (bottom) densities (dN_{parton}/dE_{parton}) for a proton (solid line) and an $A = 10$ nucleus (dashed lines). The curves are based on the MRST99 parton distributions [15] evaluated at $Q^2 = 1000$ GeV^2. Nuclear shadowing is neglected.

Conclusions

IceCube is the first detector large enough to study high p_T muon production in cosmic-ray air showers. A 100 meter minimum muon-shower core separation would allow the study of muons with $p_T > 3$ GeV/c; a few thousand of these muons are expected each year.

By measuring the energy and core separation of muons associated with air showers, the muon p_T can be inferred. The cross-sections for high-p_T muon production can be related to perturbative QCD calculations of cosmic-ray interactions. The rate of high p_T muon production is very sensitive to the cosmic-ray composition; pQCD based composition measurements offer an alternative to existing cosmic-ray composition studies.

References

[1] J. Ahrens *et al.*, Astropart. Phys. **21**, 565 (2004).

[2] M. Ambrosio *et al.* Phys. Rev. **D60**, 032001 (1999); M. Aglietta *et al.*, Astropart. Phys. **20**, 641 (2004).

[3] J. Zornoza and D. Chirkin, these proceedings.

[4] D. Chirkin and W. Rhode, hep-ph/0407075.

[5] M. Thunman, P. Gondolo and G. Ingelman, Astropart. Phys. **5**, 309 (1996).

[6] S. Klein, astro-ph/0612051.

[7] L. Pasquali, M. H. Reno and I. Sarcevic, Phys. Rev. **D59**, 034020 (1999).

[8] X. Bai (for the IceCube Collaboration, J. Phys.: Conf. Ser. **60**, 327 (2007).

[9] T. Gaisser for the IceCube Collaboration, these proceedings.

[10] A. D. Martin, M. G. Ryskin and A. M. Stasto, Acta Phys. Polon. **B34**, 3273 (2003).

[11] G. Martinez, hep-ex/0505021.

[12] S. S. Adler *et al.*, Phys. Rev. Lett. **91**, 241803 (2003).

[13] A. Adare *et al.*, hep-ex/0609010; J. Adams *et al.*, Phys. Rev. Lett. 94, 062301 (2005).

[14] S. S. Adler *et al.*, hep-ex/0609032; A. Adare *et al.*, hep-ex/0609010.

[15] A. D. Martin *et al.*, Eur. Phys. J. **C14**, 133 (2000).

[16] A. Karle, these proceedings.

IceTop/IceCube coincidences

XINHUA BAI, THOMAS GAISSER, TODOR STANEV, & TILO WALDENMAIER FOR THE ICECUBE COL-
LABORATION *
Bartol research Institute, Department of Physics and Astronomy, University of Delaware, Newark, DE 19716, U.S.A.
*bai@bartol.udel.edu; * see special section of these proceedings*

Abstract: Atmospheric muons in IceCube are often accompanied by air showers seen in IceTop when their trajectories pass near the surface detectors. By selecting events in which only a single IceTop station on the surface is hit, we can identify a class of events with high probability of having a single muon in the deep detector. In this work we use this tagged sample of atmospheric muons as a calibration beam for IceCube.

1. Introduction

In 2006 IceCube collected data with sixteen IceTop stations and nine in-ice strings, as shown in Fig. 1. Ten more stations and thirteen more strings were deployed in 2006-07 austral summer [1]. IceTop runs with a simple multiplicity trigger that requires 6 or more digital optical modules (DOMs) to have signals above threshold. The configuration of gain settings and DOMs in tanks is such that IceTop triggers normally involve three or more stations separated from each other by 125 m. Such showers typically have energies of several hundred TeV and higher. The deep IceCube strings also have a simple multiplicity trigger of 8 or more DOMs within 5 μsec. The 8 DOMs need not be on the same IceCube string. Whenever there is an in-ice trigger, all IceTop DOMs are read out for the previous 8 μsec. This allows the possibility of identifying small, sub-threshold showers on the surface in coincidence with muons in deep IceCube.

Events that trigger both the surface array and deep IceCube can be reconstructed independently by the air shower array on the surface and by the in-ice detector. Such events can be used to verify the system timing and to survey the relative position of all active detection units, i.e. IceTop tanks or in-ice DOMs. The concept has been demonstrated in the SPASE2-AMANDA experiment [2]. Verification of timing with coincident events is now a rou-
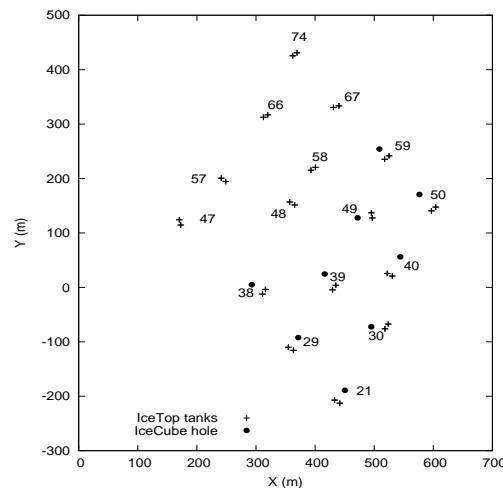
Figure 1: Surface map of IceCube in 2006. Two tanks (+) are separated from each other by 10 m at each station. Each tank has one high-gain and one low-gain DOM.

tine component of IceCube monitoring. One can also compare the two independently determined directions for the same events. Showers big enough to trigger IceTop, however, typically have several muons in the deep detector. One would also like to be able to tag single muons in IceCube to have a set of events similar to the ν_μ-induced muons that are the principal target of IceCube. In this paper we

describe how a sample enriched in single muons can be tagged with IceTop, and we illustrate the use of this sample for verification of IceCube.
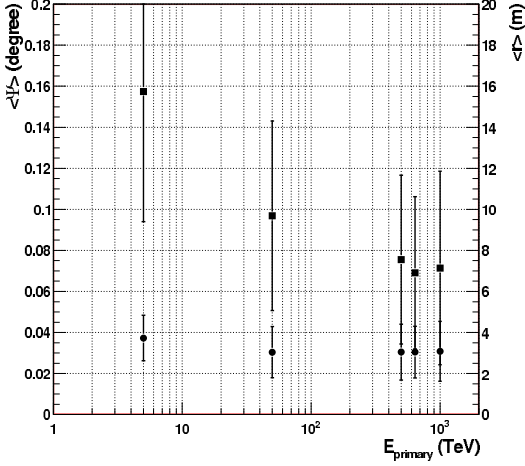
Figure 2: The average space angle Ψ between muons and air shower axis (solid circle, left vertical scale), the mean distance r of muons from air shower core (solid square, right vertical scale) as function of primary proton energy. The error bars represent the rms of Ψ and r. Only muons with energy above 460 GeV on the surface are counted. Proton showers were produced at the South-Pole altitude by CORSIKA [4] with QGSJET as the high energy hadronic model.

2. Muons in air showers and their energy loss in the ice

The average number of high energy muons in an air shower can be parameterized as [3]

$$N_{\mu,>E_\mu} = A\frac{0.0145 TeV}{E_\mu cos(\theta)}(\frac{E_0}{AE_\mu})^{0.757}(1-\frac{AE_\mu}{E_0})^{5.25}$$

in which A, E_0 and θ are the mass, total energy and zenith angle of the primary nucleus. Muons with energy high enough to trigger the in-ice detector are also nearly parallel with the air shower axis as shown in Fig. 2.

The mean muon energy loss in matter is customarily expressed as

$$\frac{dE}{dx} = -a(E) - b(E) \cdot E,$$

where $a(E)$ stands for ionization loss and $b(E)$ for stochastic energy loss due to pair production, photo-nuclear interactions and bremsstrahlung. As an approximation, $a(E)$ and $b(E)$ can be treated as constants. For ice at the South-Pole, $a = 0.26\ GeV\,mwe^{-1}$ and $b = 3.57 \cdot 10^{-4}\,mwe^{-1}$, which are claimed with the systematic error of $\sim 3.7\%$. [5]. The least mean energy required for a muon to reach the top (1450 m) and the bottom (2450 m) of the in-ice detector is about 460 GeV and 930 GeV. For cosmic-ray protons of 500 TeV, typical of showers that trigger IceTop, $\langle N_\mu \rangle \approx 6$ at 1450 m and ≈ 2 at 2450 m.
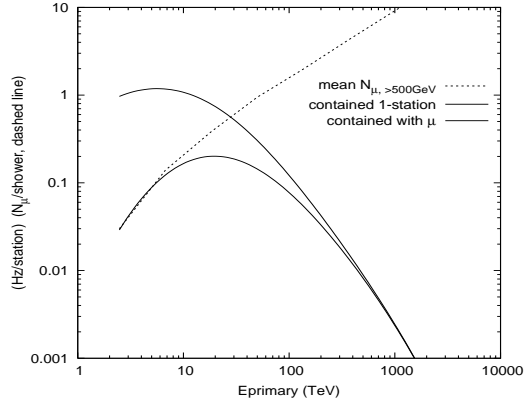
Figure 3: Response function for single station events in IceTop. Only four contained stations (39, 48, 49 and 58) were considered. The dashed line represents the number of muons above 500 GeV at production in a proton shower. The lower curve shows the response function for events with one muon in the deep detector.

We can select a sample of lower energy events by choosing in-ice triggers with both tanks hit at exactly one IceTop station. We also require the single station is not on the periphery so that events with energy high enough to hit both tanks at two or more IceTop stations are excluded from the sample. The concept is illustrated in Fig. 3 where we show an estimate of the distribution of primary cosmic-ray proton energies that give single station hits above 30MeV threshold in each tank. The lower curve shows the convolution of this response function with the probability of producing a muon with $E_\mu > 500$ GeV. This corresponds to the distribution of primary energy that gives rise to the single station coincident event sample. About ninety

percent of this sample are generated by primaries with $E < 100$ TeV, and about three quarters have only a single muon with $E_\mu > 500$ GeV at production.

3. Verification of time synchronization and depth of the DOMs

A critical requirement for doing physics with Ice-Cube is good time synchronization among the individual DOMs in IceCube, including IceTop together with accurate positions for the DOMs. Calibration with flashers and survey by hole logging during deployment shows that timing synchronization is at the level of 3 ns for a whole In-Ice string while the depth of individual DOMs are known with an accuracy of 50 cm [6]. By using tagged, vertical muons we can make a global check on the combination of time synchronization and depth of the DOMs over a 2.5 km baseline, from the surface to the deepest module on an IceCube string. To ensure that the single station events are not caused by tails of big air showers outside the array, only the inner stations of the IceTop array are used together with the in-ice strings directly below them. With the 16 IceTop station and 9 in-ice string array in 2006, only stations 39 and 49 fulfill this requirement.

For these two strings the muon speed has been individually calculated for each DOM relative to the time t_0 at the surface according to $v_i = d_i/(t_i - t_0)$ where d_i is the distance between the station and the ith in-ice DOM. Because of scattering in the ice, there is a distribution of arrival times of photons at each DOM relative to the arrival time in the ideal case with no scattering. We represent the distribution of delays by an exponential with a characteristic delay τ. We then convolve this exponential distribution with a Gaussian resolution function to represent other uncertainties in the system. The result is a Gaussian-convoluted exponential function as shown bellow. By fitting the distribution of arrival times at each DOM, we extract a fitted value of the arrival time t_i at the ith DOM in the absence of scattering.

$$\frac{dN}{dt} = \frac{1}{2}\frac{N}{\tau}e^{-\frac{t-t_i}{\tau}}e^{\frac{\sigma^2}{2\tau^2}} \cdot \mathrm{erfc}\left(\frac{t_i - t + \frac{\sigma^2}{\tau}}{\sqrt{2}\sigma}\right)$$
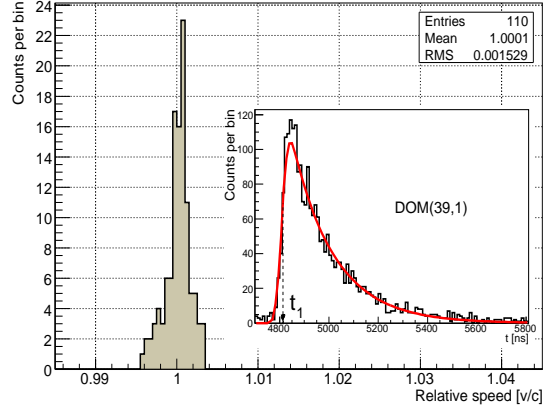
Figure 4: The distribution of muon speed (v) relative to the speed of light (c). The cut-in entry shows the time delay on one in-ice DOM and the fit. See text for details.

Other parameters here are the effective time resolution, σ, and the mean number of hits N. The expression erfc represents the complementary error function [7].

The distribution of the relative muon speed to the speed of light, v_i/c, is shown in Fig. 4, where we use the surveyed values of d_i to calculate the velocity. There are 60 DOMs on each string, 10 of which are not fitted because of insufficient data, so there are 110 entries in Fig. 4. The rms of 0.0015 of the distribution of v_i/c in Fig. 4 reflects the uncertainties in the system timing, the location of DOMs and the true muon position on the surface. This corresponds to upper limits on the uncertainty of 12 ns or 4 m over 2.5 km. Thus, although this method at present is not as precise as the standard survey and calibration techniques, it is useful to show by a complementary and independent method that there are no significant deviation from expectation.

4. Muons in the in-ice detector

4.1 Muon direction

Small air showers trigger a single IceTop station efficiently only when the shower core is close to the station. Since high energy muons are nearly parallel to the shower axis, the line connecting the station on the surface and the center of gravity (COG) of triggered in-ice DOMs approximates the muon trajectory closely. If we use half the string spac-
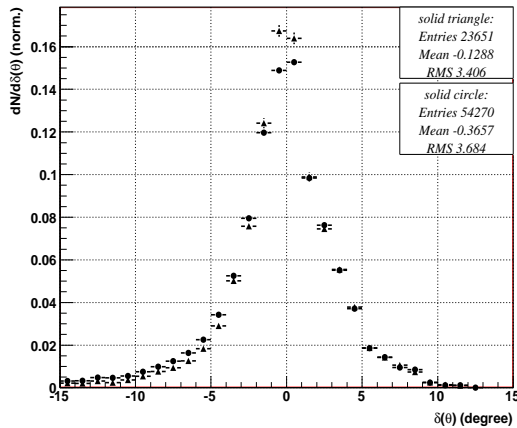
Figure 5: The difference between the zenith angle defined by the line connecting triggered IceTop station and the COG of triggered in-ice DOMs and that by the in-ice reconstruction. See text for details.

ing to estimate the accuracy of the location of the track at the surface and at 1500 m, we find that the direction of the track should be determined to an accuracy of about $3°$. Fig. 5 shows a comparison between the zenith angle defined by this line and by an independent in-ice reconstruction. The events in the solid-circle histogram have charge more than 5 photo-electrons in the triggered IceTop station. Those under the solid-triangle histogram have charge more than 400 photo-electrons, indicating a core closer to the station and/or slightly higher primary energy. The mean of $\delta(\theta)$ decreased from 0.37 degree in the low-density sample to 0.13 degrees in the high density sample.The rms are about 3.7 degrees and 3.4 degrees respectively for the two groups. Given the estimated $3°$ uncertainty in the estimation of the direction by this method, the good agreement indicates that the in-ice reconstruction algorithm has an accuracy of $2°$ or better for events near the vertical. Nevertheless, further investigation is needed to understand these events with zenith offset larger than 6 degrees.

4.2 Uncorrelated, coincident atmospheric muons in IceCube

An important source of background for upward-moving neutrino-induced muons in IceCube is the subset of events in which two uncorrelated atmospheric muons pass through the detector in the same trigger window. Such events, which are estimated to constitute about 3% of the trigger rate in the full cubic kilometer IceCube [8], are of concern because the time sequence of hits in the combined event can easily have an upward component. It will be useful to tag a subset of such events with IceTop for study and to check that they are efficiently filtered. At present, however, with the smaller detector the fraction of accidental coincidences is much smaller, and IceTop can only tag a very small fraction of them. The rate of identified single station coincidences in 2006 was about 0.075 Hz per station, so 1.2 Hz over the sixteen station array. An estimate of the rate of tagged double uncorrelated events is therefore $\sim 10^{-5}$ Hz, somewhat about one per day. For comparison, the trigger rate of the 9-string IceCube in 2006 was 146 Hz.

References

[1] T. Gaisser et al., "Performance of IceTop array", this conference.

[2] J. Ahrens et al., NIM A 522 (2004) 347.

[3] T. Gaisser, *Cosmic Rays and Particles Physics* (Cambridge University Press, 1990).

[4] *CORSIKA: an Air Shower Simulation Program*, http://www-ik.fzk.de/corsika/

[5] P. Miocinovic, *Muon energy reconstruction in the Antarctic Muon and Neutrino Detector Array*, PhD thesis, UCLA at Berkeley, 2001.

[6] A. Achterberg et al., Astropart. Phys. 26 (2006) 155.

[7] William H. Press, Saul A. Teukolsky, William T. Vetterling, Brian P. Flannery, *Numerical Recipes*, 2nd edition. (Cambridge University Press, 1992).

[8] J. Ahrens et al., Astropart. Phys. 20 (2004) 507.

Lateral Distribution of Air Shower Signals and Initial Energy Spectrum above 1 PeV from IceTop

S. KLEPSER[1], F. KISLAT[2], H. KOLANOSKI[2], P. NIESSEN[3], A. VAN OVERLOOP[4] FOR THE ICECUBE COLLABORATION[5]

[1] *DESY, D-15735 Zeuthen, Germany*

[2] *Institut für Physik, Humboldt-Universität zu Berlin, D-12489 Berlin, Germany*

[3] *Bartol Research Institute, University of Delaware, Newark, DE 19716, U.S.A.*

[4] *Dept. of Subatomic and Radiation Physics, University of Gent, B-9000 Gent, Belgium*

[5] *see special section of these proceedings*

stefan.klepser@desy.de

Abstract: The IceTop surface detector array is part of the IceCube Neutrino Observatory that is presently being built at the South Pole. In a triangular grid with a spacing of $125\,\mathrm{m}$, up to 80 pairs of ice Cherenkov tanks will be set up, 16 of which were already in operation in 2006. The data from this array allows the reconstruction of a first preliminary energy spectrum in the range of about $1\,\mathrm{PeV}$ to $100\,\mathrm{PeV}$. To reconstruct the primary energy of a cosmic ray particle, a fit to the lateral distribution of the air shower signals has to be performed. We have developed a functional description of expected lateral distributions and of the corresponding fluctuations of the measured signals. The function and its parameters have been tuned in a CORSIKA simulation study with parametrised particle responses. From a detailed detector simulation, the fluctuations could be extracted and qualitatively compared with experimental data. Some performance tests and an initial energy spectrum, uncorrected for efficiency near threshold, are presented.

Introduction

When a high energy cosmic ray hits the earth's atmosphere, it induces an extensive air shower (EAS) whose axis and energy can be reconstructed by detector arrays at ground level. In general, the arrival times of the particles deliver the direction information while the signal strength distribution is used to reconstruct the core and size of the shower. The shower size is usually represented by the signal S_R at a certain perpendicular distance R from the shower axis ("core radius"). With the spacing of IceTop, S_{100} at $R = 100\,\mathrm{m}$ proved to be a stable and reliable quantity in the fit procedure.

The signal S of an IceTop tank is derived from the charge of two photomultipliers that are operated at different gains ($5 \cdot 10^4$ and $5 \cdot 10^6$ in 2006) to enhance the dynamic range of the detector well above 10^5. They collect the Cherenkov photons produced by the shower particles in the $2.45\,\mathrm{m}^3$ of ice in each tank. The total signal is proportional to the deposited energy in the tank since the Cherenkov light and the deposited energy are both approximately proportional to the track lengths of the charged particles. Using atmospheric muons for calibration, the signals can thus be converted to the detector-independent unit VEM (vertical equivalent muon), which is equivalent to about $200\,\mathrm{MeV}$ of deposited energy [3].

To estimate the energy of the primary particle and determine the shower core, a log-likelihood fit is applied to the measured signals. This requires a lateral distribution function (LDF) $S(r)$ at a given core radius, and a parametrisation of the signal fluctuations. The likelihood also includes a term for stations without trigger.

LDF and Fluctuation Parametrisation

To find an appropriate LDF for IceTop, lateral distributions of CORSIKA shower simulations [6] were analysed. The hadronic interaction mod-
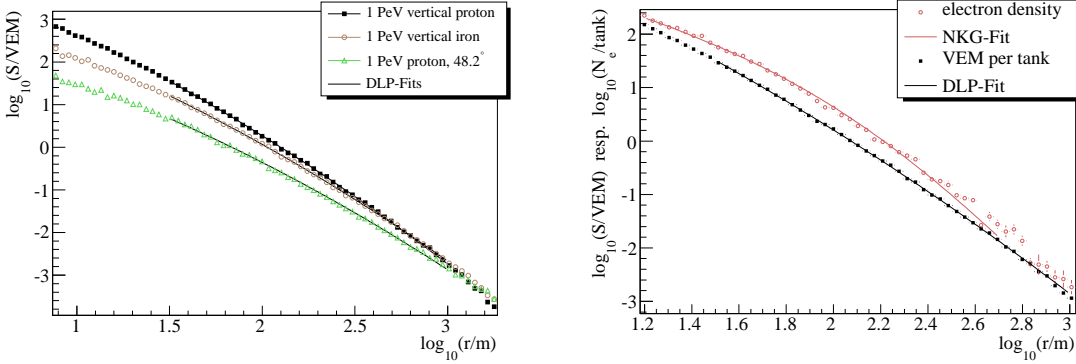
Figure 1: Left: Derived lateral signal distributions of IceTop tanks for three different simulated showers, fitted with the DLP function described in the text. Right: Comparison between lateral electron density and tank signal distribution, fitted with NKG and DLP respectively.

els used in all simulations are Sibyll 2.1 [4] for energies above $80\,\mathrm{GeV}$ and Fluka [5] below that. Each shower particle was weighted with an average response function $S_j(E)$ derived from single particle simulations that were carried out with a Geant4-based detector simulation [1]. The particle types considered are $j = \{\gamma, e^\pm, \mu^\pm, p, \bar{p}, n, \bar{n}, \pi^\pm, K^{\pm,0}\}$, which are the most abundant in air showers. Three examples of the distributions that were found, and a comparison to the electron density distribution described by the NKG function [8] are given in Fig. 1. It is remarkable that the main feature of the NKG function in double logarithmic representation, which is a bend with a maximal curvature approximately at the Molière Radius ($128\,\mathrm{m}$ at the South Pole [2]), cannot be seen in the tank signal lateral distributions. This is presumably a consequence of the fact that the energy deposition is not proportional to the particle number.

The function found to fit these distributions well in a range between 30 and $1000\,\mathrm{m}$ is a parabola in a double logarithmic representation (DLP), which can be written as

$$S(R) = S_{R_0} \left(\frac{R}{R_0} \right)^{-\beta - \kappa\,\log_{10}\left(\frac{R}{R_0} \right)} \qquad (3)$$

with $R_0 = 100\,\mathrm{m}$ being the reference core radius, β the slope at R_0, and $\kappa \approx 0.303$ the curvature of the parabola. This curvature is approx-

imately a constant for all hadronic showers and thus a fixed parameter for all fits on real data. The parameter β is roughly linearly connected to the shower age parameter of the NKG function via $s_{NKG} = -0.94\,\beta + 3.4$ for all simulated angles, energies and nuclei.

To study the fluctuations σ_S of the approximately log-normally distributed tank signals, two analyses were done. Figure 2 shows the comparison of the dependencies of σ_S on S that were found. The points designated with "tank-to-tank" indicate the outcome of a study of signal differences between the two tanks separated by $10\,\mathrm{m}$ at each detector station. Shower fluctuations were thus measured directly in data and the result is compared to simulated data that was produced with CORSIKA showers processed with a Geant4 detector simulation of the array. The lower points are taken from a similar simulation with tanks set up in a ring-like structure. Since the former is biased by uncertainties in reconstruction and shower intrinsic correlations, and the latter depends on the quality of the detector simulation, the two methods are not fully comparable but should yield results in the same order of magnitude. This could roughly be verified, although the tank-to-tank fluctuations have some features at higher amplitudes that are most likely an artefact from misreconstructed cores that are very close to one of the tanks. In the full array simulations described below, the parametrisa-

44
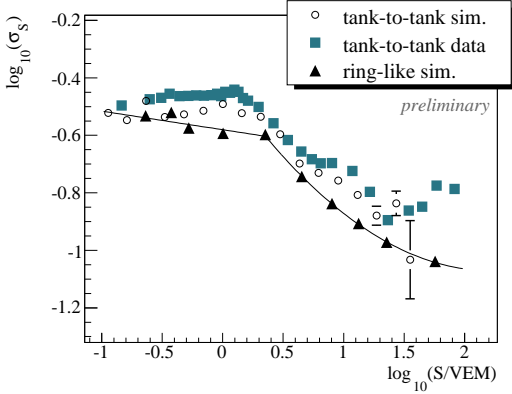
Figure 2: Dependency of the signal fluctuation σ_S on the signal S in data and different simulations (the error bars are partly smaller than the markers). σ_S designates the standard deviation of $\log_{10}(S)$. The differences between the methods are discussed in the text. The solid line indicates the parametrisation that was extracted for the lateral fit.

Figure 3: CORSIKA simulations of $\log_{10}(S_{100})$ as a function of $\sec\theta$ for various energies. The lines are projections of the fit that was performed on all data points simultaneously ($\chi^2/\mathrm{ndf} = 41.2/32$).

tion taken from the ring-like simulation delivers a better core and energy resolution and is therefore used in the fit. The dependence of σ_S on the core radius was found to be in the order of $15\,\%$ for radii above $30\,\mathrm{m}$ and is therefore negligible.

With the parametrised CORSIKA simulations described above, it was found that for zenith angles $\theta < 50°$, the dependence of S_R on $x = \sec\theta$ can be described by parabolas (Fig. 3). Assuming that the maximum of $\log_{10} S_R$ and its position x_{max} linearly depend on $\log_{10} E$, a function $S_R(\theta, E)$ was found that fits all data points and can be inverted analytically to $E(S_R, \theta)$. For several R between 50 and $1000\,\mathrm{m}$, the parameters of $E(S_R, \theta)$ were interpolated such that the conversion from S_R to the primary energy can be done at any radius R_{opt} that might be regarded optimal for physical or numerical reasons. Presently, to be as independent as possible from the quality of the LDF, R_{opt} is chosen event by event in a way that $\log_{10} R_{opt}$ is the mean logarithmic core radius of all tanks that were actually used in the fit.

This energy conversion does not yet take into account the influence of the primary mass. From the shower size differences observed between proton

and iron showers in the simulations ($\Delta \log_{10} S_R \approx 0.1$), the systematic uncertainty on the spectral index of the following spectrum can be estimated to be $\sigma_\gamma \approx 0.1$.

Performance and Results

To benchmark the performance of the LDF, CORSIKA simulations of $1\,\mathrm{PeV}$ vertical showers were carried out on the 2006 array configuration, using the tank intersects of the shower particles and the above $S_j(E)$ tank response parametrisations to scale the responses of the particles. The simulation also includes the generation of PMT responses, digitisation and the behaviour of the IceCube trigger devices. Thus the simulated raw data completely resembles the level and format of experimental raw data. The quantities that serve to estimate the quality of the LDF are the core position resolution σ_{core}, the energy resolution $\sigma_{\log_{10} E}$, the

45
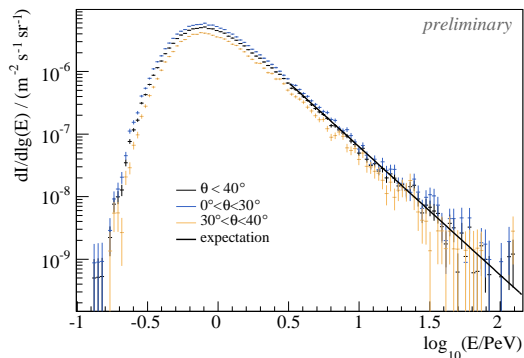
Figure 4: Preliminary, raw energy spectrum without acceptance correction. The difference between high and low zenith range indicates the systematic uncertainty. Though not deconvoluted yet, the high-energetic part is compared to the expected spectrum and agrees well with it (solid line, [7]).

reconstruction efficiency ϵ and the mean of the χ^2 distribution.

Compared to a simple power law and the NKG function, the numbers found indicate a slight preference for the DLP function, especially concerning the reconstruction efficiency. For vertical 1 PeV showers, the core and energy resolution are $\sigma_{core} = 12.8$ m and $\sigma_{\log_{10} E} = 0.094$. However, once a bigger array is available in the coming years, this has to be reevaluated.

With the energy extracted as described above, a dataset with an effective lifetime of $0.692 \cdot 10^6$ s was analysed. Requiring 5 triggered stations, the reconstructed core to be 50 m inside the array and the zenith angle to be $\theta < 40°$, an exposure of $0.67 \cdot 10^{11}$ m²sr s is achieved. In this dataset, 192507 shower events were detected. From the known energy spectrum [7] of charged cosmic rays, one can estimate an effective reconstruction threshold of ~ 500 TeV and expect approximately 1000 events above 10 PeV and 10 events above 100 PeV. In the dataset, 800 and 5 events were found respectively.

The raw distribution of energy estimates without acceptance correction is shown in Fig. 4. The high energy part, where the efficiency can be assumed to be constant and close to 1, the slope of the spec-trum agrees well with the slope of $\gamma \approx 3.05$ that is expected from other experiments, drawn as a solid line for comparison. The absolute scale of the raw spectrum is lower than the expectation, which indicates the need for more simulations to tune the energy extraction and correct for efficiencies.

Conclusion

With the 2006 array configuration, we will be able to measure the cosmic ray energy spectrum from 0.5 to 100 PeV. The signal distributions are well understood, and applying advanced log-likelihood fits we are able to reconstruct the cores and sizes of the measured showers with good precision. Since February 2007, already 26 stations are in operation, which covers a third of the total planned area. This and the development of an unfolding procedure will enable IceTop to measure an energy spectrum well above 100 PeV at the end of 2007.

References

[1] J. Allison et al. Geant4 developments and applications. *IEEE Trans. Nucl. Sci.*, 53:270–278, 2006.

[2] L. Anchordoqui et al. High energy physics in the atmosphere: Phenomenology of cosmic ray air showers. *Ann. Phys.*, 314:145–207, 2004.

[3] L. Demirörs et al. Icetop tank response to muons. In *Proc. 30th ICRC*, Mérida, Mexico, 2007.

[4] R. Engel, T.K. Gaisser, P. Lipari, and T. Stanev. Air shower calculations with the new version of sibyll. In *Proc. 26th ICRC*, Salt Lake City, 1999.

[5] A. Ferrari, P. R. Sala, A. Fasso, and J. Ranft. Fluka: A multi-particle transport code (program version 2005). 2005. CERN-2005-010.

[6] D. Heck et al. Corsika: A monte carlo code to simulate extensive air showers. 1998. FZKA-6019.

[7] Joerg R. Hoerandel. On the knee in the energy spectrum of cosmic rays. *Astropart. Phys.*, 19:193–220, 2003.

[8] K. Kamata and J. Nishimura. *Progr. Theor. Phys. Suppl.*, 6:93, 1958.

IceTop tank response to muons

L. DEMIRÖRS[3], M. BEIMFORDE[1], J. EISCH[2], J. MADSEN[4], P. NIESSEN[3], G. M. SPICZAK[4], S. STOYANOV[3], S. TILAV[3] FOR THE ICECUBE COLLABORATION[5]

[1]*Institut für Physik, Humboldt-Universität zu Berlin, D-12489 Berlin, Germany*

[2]*Dept. of Physics, University of Wisconsin, Madison, WI 53706, USA*

[3]*Bartol Research Inst., Dept. of Physics & Astronomy, University of Delaware, Newark, DE 19716, USA*

[4]*Dept. of Physics, University of Wisconsin, River Falls, WI 54022, USA*

[5]*see special section of these proceedings*

levent@udel.edu

Abstract: Each digital optical module (DOM) of the IceTop air shower array is calibrated by identifying and understanding its muon response, which is measured in vertical equivalent muon (VEM). Special calibration runs and austral season measurements with a tagging telescope provide the basis for determining the VEM and monitoring its variation with time and temperature. We also study muons that stop and decay in the tank. The energy spectrum of the electrons from muon decay is well known (Michel spectrum) and can also be used as a calibration tool. Both spectra are compared to a GEANT4 based Monte Carlo simulation to gain a better understanding of the tank properties.

Introduction

IceTop is an air shower array of ice–Cherenkov counters [1, 2]. Each of its current 26 stations is made up of two IceTop tanks. The tank shell is black, cross–linked polyethelyne, 6 mm thick, 1.1 m high, and 1.9 m in diameter. A second layer of 4 mm thickness, made out of zirconium fused polyethylene, is molded on the inner surface to act as a diffusely reflective liner (eight tanks deployed in 2005 have Tyvek linings). Each tank is filled with 90 cm of frozen water and then covered with 47 g/cm^2 of perlite to provide insulation and a barrier to light leaks around the fitted wooden tank cover.

The tank ice is viewed by two standard IceCube digital optical modules (DOMs). They consist of a 10" Hamamatsu R7081–02 photo multiplier tube (PMT) and processing and readout electronics. Two different types of digitizers are used to process the PMT signal: a fast pipelined ADC (FADC) with 255 samples of 25 ns each, and two Analog Transient Wave Digitizer (ATWD) chips, with three channels of up to 128 samples of about 3.6 ns each. The three channels are configured with different pre–amplification factors to extend the DOM's dynamic range (for details, cf. [3]).

IceTop setup for calibration runs

Periodic special IceTop calibration runs are carried out to serve two purposes: one, to calibrate the conversion from integrated waveform to vertical equivalent muon (VEM) for each DOM in a tank, and two, to monitor the DOMs response's time dependence.

The calibration run configuration differs from the regular one used for air shower data runs. In this so–called singles mode, the local coincidence between DOMs and the simple majority trigger are disabled. All DOMs are set to the same nominal gain of $5 \cdot 10^6$, while in the air shower mode, the two DOMs in the same tank are set to different gains (in 2006, $5 \cdot 10^6$ and $5 \cdot 10^4$, resp.) to extend the dynamic range of a tank. For the DOMs that are operated at the lower gain, the VEM might differ due to changes in the collection efficiency of the PMT. Currently, that effect is not taken into account.
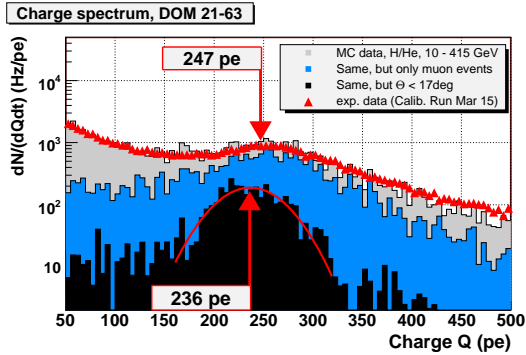
Figure 1: MC simulated charge spectrum for DOM 21–63. See text for further explanations.

Figure 2: Distribution of VEMs for all DOMs.

The data files are analyzed with an IceTop specific waveform processing module written for the official offline software suite. Each raw waveform, given in ATWD channel counts, is corrected for the specific, ATWD chip–dependent pedestal pattern, and calibrated to give charge. Further corrections include the (optional) adjustment of any residual baseline offset and a droop correction. Finally, the charge, given in units of photo electrons (pe), is calculated by summing up all the waveform bins.

Calibration using through-going muons

A DOM's response to a vertical muon passing an IceTop tank is defined to be one VEM. The energy deposit of such a muon is around 200 MeV in the tank [4]. By finding the vertical muon signal in the measured total charge spectrum, the DOM–dependent charge–to–VEM conversion factor is determined. However, single IceTop tanks cannot discriminate between different particles or incident angles. Therefore, the relation between the measured peak position of the total charge spectrum and the VEM must be determined with simulations and the tagging telescope.

This is illustrated in Fig. 1. The measured total charge spectrum is shown in triangles. The simulated total charge spectrum (light grey) is obtained with GEANT4 based simulations. Using Corsika [5] generated hydrogen and helium air showers with primary energies between 10 and 415 GeV and angles up to 70 deg as input, the DOM response is simulated by generating and tracking the

Cherenkov light in a tank. Several tank and DOM properties, e.g. the reflectivities of the sides and top, ice quality, PMT quantum efficiency, are taken into account [6].

Superimposed on the simulated total charge spectrum is the contribution from only muons. Choosing a cut on the muons' incident zenith angle that correponds to the angular acceptance of the tagging telescope (< 17 deg), the black histogram is obtained. It gives the best estimate for the VEM, which is determined as the mean of a Gaussian fit, 236 pe for this particular DOM.

Comparing this to the peak position of the simulated total charge spectrum, 247 pe, gives a correction factor of about five percent. This is the amount by which the measured total charge spectra's peak positions have to be corrected to determine the VEM. Currently, it is assumed that this correction factor is the same for all IceTop tanks.

The spread in VEM is shown in Fig. 2 for a run taken on March 15, 2007. The fluctuations in the response, even between DOMs in the same tank, are the main reason to introduce the VEM as a uniform, array–wide unit.

The VEM response per DOM is tracked with regular calibration runs. In Fig. 3, the VEM response over time is shown for both DOMs in Tank 21b. Both DOMs exhibit a rather stable VEM response, except for a sharp drop in DOM 21-64 around July 2006. In total, about half of all DOMs of the oldest tanks, deployed in 2005, show a significant drop in their VEM response in mid–2006. Though the specific cause of these changes in the DOM response is unknown, evidence points to seasonal effects,
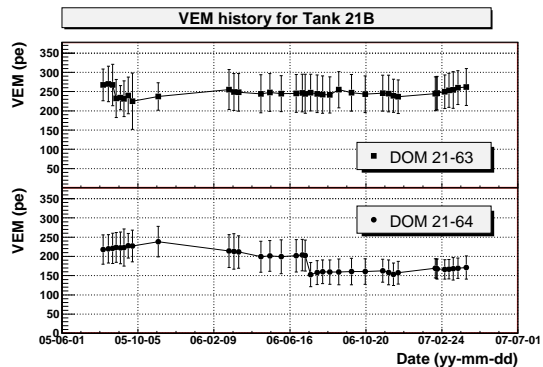
Figure 3: History of charge to VEM conversion for DOMs 21-63/64

i.e. the change in temperature during the Antarctic winter.

Muon Telescope Measurements

A portable, solar–powered muon telescope was developed to tag muons that have angles close to vertical (< 17 deg) and pass through the center of the tank. With this device the VEM charge can be determined independently from simulation.

The muon telescope is a completely autonomous device, having its own data acquisition system and power supply. It measures signals in coincidence between two scintillator slabs 70 cm apart and records the GPS clock time stamp on a Flash Media drive.

Measurements were taken during the polar season 2005/2006 on tanks deployed one year ear-
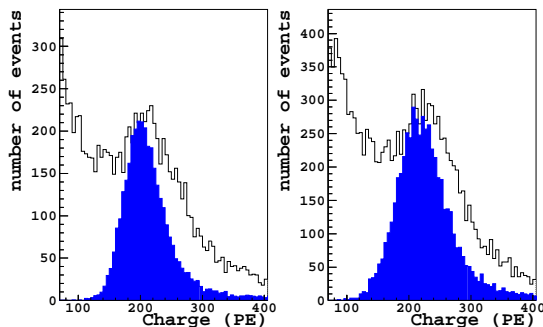
Figure 4: Total charge spectra (black) for tank 39b with tagged muon spectrum (blue) superimposed. See text for further explanation.
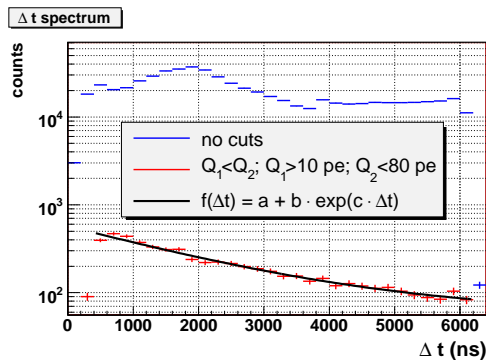
Figure 5: Time difference distributions between the two signals in a FADC trace. The exponential fit yields a lifetime of $\tau = 2.06 \pm 0.16\,\mu$s.

lier. Configuring the DOMs in a tank to singles mode, data were taken for six hours. Matching the GPS time stamps from both the muon telescope and the DOMs was done using a $[-2, 2]\,\mu$s time window. Thus, a tagged quasi–vertical muon data set is obtained. Figure 4 shows the charge spectra for DOMs 63 and 64 in Tank 39b and superimposed the tagged muon charge spectra. If compared to Fig. 1, the tagged spectra show some differences. This is mainly due to the fact that in the simulation muons over the whole tank surface are accepted, while the tagging telescope is positioned in the tank center. When the statistics in simulation are improved, more realistic cuts can be applied. Still, the qualitative difference between the tagged and the full spectrum is well reproduced in the simulated spectrum.

Calibration using stopping muons

An IceTop tank stops muons of kinetic energies up to 210 MeV (vertical muons) and 430 MeV (muon crossing through the tank diagonally from an upper to a lower corner). After stopping, the muon decays with its characteristic mean lifetime of $2.19703\,\mu$s into an electron and an antineutrino–neutrino pair (neglecting muon capture). The resulting energy distribution of the electron is the well–known Michel spectrum. The maximum electron energy is 53 MeV, which corresponds to a range of less than 25 cm in the tank ice. Thus, most of the decay electrons are well contained within the

49
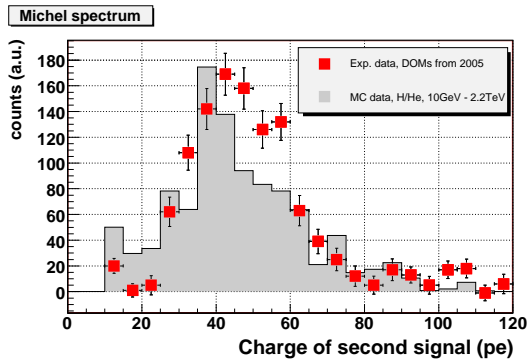
Figure 6: Measured Michel spectrum (symbols) in comparison with a simulated one.

tank volume, making them a suitable calibration sample.

A feasibility study was carried out by applying the method outlined in [7] to the IceTop configuration. First, calibration data from 2005 were analyzed to find FADC traces with two distinct signals. The time difference of those two signals is shown in Fig. 5 as the upper histogram. To suppress background, stringent cuts were applied on the integrated charges Q_1 and Q_2 of the primary and secondary signal, respectively. The cuts were adjusted by using the GEANT4 based simulation from [6].

Fitting the remaining time difference spectrum yields a lifetime of $\tau = 2.06 \pm 0.16\,\mu$s, which is comparable to the muon mean lifetime of $2.2\,\mu$s.

To extract the Michel spectrum from the background, a difference method is chosen that does not require the cuts imposed above. First, two time windows are chosen, a "decay" window between 1 and $2\,\mu$s, and a "crossing" window between 5 and $6\,\mu$s. For both time windows, the integrated charge of the second signal is calculated. By subtracting them from each other, the Michel spectrum is obtained, which is compared to a simulated spectrum in Fig. 6. Though the simulation lacks statistics, it qualitatively describes the measured spectrum rather well.

Conclusion

The VEM calibration of the IceTop air shower array with through–going muons is a well established and well understood procedure. The VEM is measured and calibrated on a weekly to monthly basis and provides, in conjunction with the single DOM rate and temperature, a basic set of observables for monitoring the detector hardware. GEANT4 based simulations agree well with the measured charge spectra and the muon telescope data, showing that the input parameters describe the actual tank properties rather well.

The stopping muon analysis has shown the feasibility of using the muon decay signal as a supplementary calibration source. Already at this stage, the GEANT4 based simulation shows a promising agreement with the measured spectra. However, further improvements in both the analysis and the simulation are needed to establish it as a standard calibration method.

Acknowledgments

References

[1] T. Gaisser et al. Performance of the IceTop array. In *Proc. 30th Int. Cosmic Ray Conf.*, Mérida, Mexico, 2007.

[2] Todor Stanev and Ralf Ulrich. *Nucl. Phys. Proc. Suppl.*, 145:327–330, 2005.

[3] A. Achterberg et al. *Astropart. Phys.*, 26:155–173, 2006.

[4] M. Beimforde. Diploma Thesis, Humboldt–Universität zu Berlin, 2006. (http://www-zeuthen.desy.de/nuastro/publications/diploma/arbeiten/ThesisBeimforde.pdf).

[5] D. Heck, G. Schatz, T. Thouw, J. Knapp, and J. N. Capdevielle. FZKA-6019.

[6] J. Clem and P. Nießen. Response of IceTop tanks to low-energy particles. In *Proc. 30th Int. Cosmic Ray Conf.*, Mérida, Mexico, 2007.

[7] P. Allison et al. *Proc. 29th Int. Cosmic Ray Conf.*, 8:299, 2005.

Response of IceTop tanks to low-energy particles

J. M. CLEM[1], P. NIESSEN[1], AND S. STOYANOV[1] FOR THE ICECUBE COLLABORATION[2]

[1]*University of Delaware, Dept. of Physics and Astronomy, DE-19716 Newark, US of America*

[2]*see special section of these proceedings*

levent@udel.edu

Abstract: Solar activity can cause variations in the cosmic-ray particle flux measured at the Earth's surface. This manifests mostly in the low-energy electromagnetic component of cosmic ray induced cascades. The IceTop experiment detects these particles by their emission of Cherenkov light in a contained ice volume through photo-multipliers. We give the prediction of the response to the low-energy part of cascades and compare to experiment.

Introduction

The IceTop Air Shower Array, located close to the geographical South Pole (altitude 2835 m, 700g/cm^2), consists of tanks with reflective liners using clear ice as a Cherenkov medium. Light generated in the ice is observed by digital optical modules (DOMs) which consist of a photo multiplier tube (PMT) and digitising electronics assembled in a glass pressure sphere. Thus, energy deposition of particles can be measured through the observed light yield. Each tank has two DOMs running at different gain settings to increase the dynamic range of the observations. Two tanks, placed at 10 metres from each other, are combined into a station. Currently, 26 stations, separated by typically 125 metres, forming a diamond shaped triangular grid are deployed. In normal operation, the high gain DOMs are run in coincidence to reject events not associated with air showers. For this work, we use data from tanks run in "single mode", in which the coincidence condition is disabled.

Simulations

Two separate simulations are utilised in this analysis, one based on CORSIKA[1] and another on FLUKA/AIR[2, 3].

In the AIR model, primary protons, alphas, carbon, silicon and iron are generated within the rigidity range of 0.5GV-20TV uniform in $\cos^2(\theta)$, θ being the zenith angle. The atmosphere density profile (23.3% oxygen, 75.4% nitrogen and 1.3% argon) was based on the US Standard Atmosphere 1976 model. The primary cosmic ray spectrum used in this calculation was determined through an analysis of simultaneous proton and helium measurements made on high altitude balloon flights (see refs. in [3, 4]). The outer air-space boundary is radially separated by 65 kilometres from the inner ground-air boundary and a single 1 cm^2 element on the air-space boundary is illuminated with primaries. Particle intensity at various depths is determined by superimposing all elements on the spherical boundary defining the depth. Due to rotational invariance this process is equivalent to illuminating the entire sky and recording the flux in a single element at ground level. Although this approach provides a quick result, it ignores the effects of multiple particle tracks entering the IceTop tanks simultaneously.

In the CORSIKA simulation, the hadronic interaction model for energies above 80 GeV is SIBYLL v2.1[5], for lower energies FLUKA is applied. The electromagnetic interactions are treated with EGS4[6]. Hydrogen as well as helium primaries are simulated with angles between 0 and 70 degrees. The angular spectrum is constant in $\cos^2(\theta)$, like for the AIR simulation. The cascades are generated with primary energies between 10 GeV and 468 GeV with a power-law $\sim$

51

$(E/E_0)^{-1}$ and are re-weighted later to the fluxes averaged from various experiments[4]. Two atmospheres for the austral winter and summer (1st of July/31st of December) parametrised by the MSIS-90-E model[7] are used. We find that the counting rate in the austral winter is approx. 6% higher compared to the summer. In a second step, the cascade particles are inserted into the detector simulation to generate the light yield in the photo multiplier. The simulation is based on GEANT4[8] and takes into account the interactions of particles and the tracking of the Cherenkov photons. This requires input of the optical parameters of the inside of the tank. The reflectivity of the tank liner was measured as a function of wavelength in the laboratory. The first eight tanks of the experiment are lined with Tyvek[TM], while the later tanks have an integrated coating using zirconium as reflective agent. The simulations are done using the optical properties of the Tyvek[TM] liner.

The tank is then modelled as a cylindrical polyethylene vessel of 0.93 metre radius and 1.00 metre height, filled with ice to a level of 0.90 metres. The tank is embedded in 0.3 metres of snow, simulated as water of density 0.4 g/cm^3. Regarding the optics of the ice, a refractive index of 1.33 is assumed and the absorption length is set to 200 metres, based on measurements in the deep glacial ice and on comparisons of the simulations to the experimental data. The ice is covered with 47 g/cm^2 of Perlite[TM] which is modelled as opaque to light but reflective at the ice interface. The light propagation in the DOM itself is simulated using the geometry and optical properties of the pressure sphere, the PMT glass and the optical gel coupling the two. The quantum efficiency of the photo cathode is applied to yield individual photo electrons. However, neither the amplification stages nor the signal processing electronics are simulated. The final result of the simulation is the number of photo electrons (npe).

Secondary particle spectra

The resulting secondary particle spectra from simulation and experiments[9] are shown in Fig. 1. All measurements of the electrons, muons and gammas took place at solar minimum and a low geo-
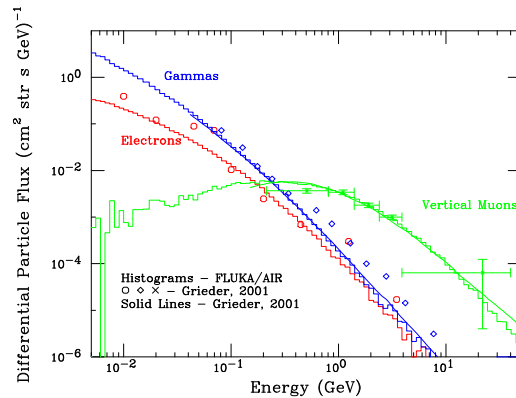
Figure 1: Fluxes of secondary electrons, muons and gammas from simulation for solar minimum, compared to experiments compiled in[9].

magnetic cutoff, comparable to South Pole conditions. The muon and electron measurements were made by a balloon instrument while the gamma rays were measured from a mountain top. The agreement with the simulations is reasonable, however the differences will be investigated.

Response to electrons, muons and gammas

The particles entering the tank are detected by the DOM either by their own Cherenkov light (if they are charged) or by the light emitted in stochastic processes (pair production, delta electrons, etc.). The number of photo electrons seen per particle
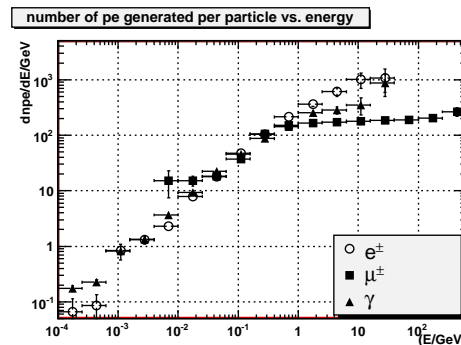
Figure 2: Number of photons per particle vs. particle energy.

as a function of the particle energy in the tank is shown in Fig. 2. It is averaged over all angles and
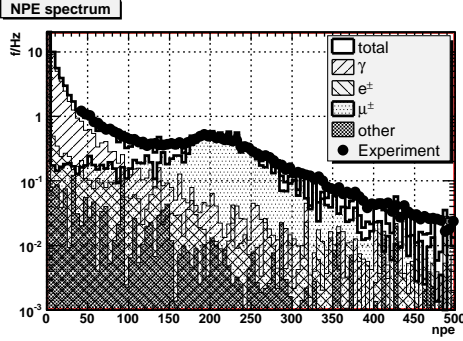
Figure 3: Contribution of secondary particles to the overall npe signal. The experimental data for DOM 63 of station 29's Tyvek^{TM}lined tank is shown as well.

impact parameters. The light yield of the muons turns flat at around 1 GeV, where the muons become minimal ionising plus a logarithmically rising stochastic contribution. For all three particle types, the light generation threshold is around 1 MeV.

Contributions to the photon electron rate

The simulation allows one to study the contribution of the different cascade secondary particles to the photo electron response from the DOM. This is shown in Fig. 3. For different particles (gamma, electron, muon and other), the number of photons seen by the DOM is summed up and histogrammed.

The dominant contributions come from gammas, electrons and muons, however the neutron component is significant at low primary energy. Other particles contribute at the 1% level.

The simulation is compared to measurements. There are some variations in the position of the muon peak from tank to tank and a tank fitting the simulation is shown. Since the purpose of these data is to determine the position of the muon peak, a threshold of about 40 npe is applied. There is good agreement between experiment and simulation.

Primary Cosmic Ray Single Mode Ice-Top Yield Function

The yield function $S(P, z)$ describes the primary cosmic ray detection efficiency of a full sky illumination of particles averaged over all arriving angles (uniform in $\cos^2(\theta)$). It is related to the count-rate $N(P_C, z, t)$ by

$$N(P_C, z, t) = \int_{P_C}^{\infty} (S(P, z)\, j(P, t))dP.$$
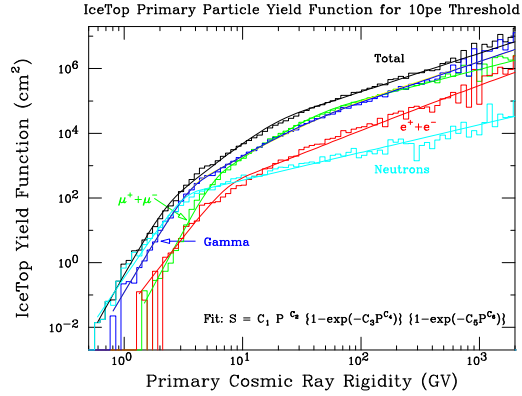
Figure 4: Primary cosmic ray yield function $S(P, z = 700\mathrm{g/cm}^2)$ for IceTop tank in singles mode. The individual contributions made by secondary components to the yield function are separated into different curves.

where P is the particle's rigidity (momentum/charge), z is the atmospheric depth and t represents time. P_C, the geomagnetic cutoff, is effectively 0 at the South Pole. Using $S_i(P, z)$, the single mode IceTop yield function, and $j_i(P, t)$, the primary rigidity spectrum for primaries of particle type i, one can decompose the product of yield function and rigidity spectrum, $S(P, z)\, j(P, z)$ into $\sum S_i(P, z)\, j_i(P, z)$. Utilising the FLUKA/AIR model and a FLUKA Cherenkov optical model assuming a zirconium lined IceTop tank, the IceTop yield function was calculated for a 10pe threshold (Fig. 4). The data are fit using a variation of the Dorman Function[10]

$$S(P) = C_1 P^{C_2} \quad \times \quad (1 - \exp\{-C_3 P^{C_4}\})$$
$$\times \quad (1 - \exp\{-C_5 P^{C_6}\}),$$

typically used to model Neutron Monitor latitude survey data. The fit parameters extracted from the simulations in Fig. 4 for the total count rate as function of PE threshold are shown in Tab. 1.

C	5pe	10pe	25pe	50pe
1	32.81	30.18	21.79	15.20
2	4.8075	4.8032	4.7731	4.7408
3	0.0341	0.0150	.00534	.00232
4	1.1849	1.4696	1.8457	2.270
5	30.588	28.323	30.874	33.54
6	-3.6117	-3.6184	-3.6070	-3.584

Table 1: Fit values for the yield function

Integral count rates

The above information can now be used to predict counting rates above a given threshold (Fig. 5). The agreement between experiment and simulation is reasonably good for the solar minimum and
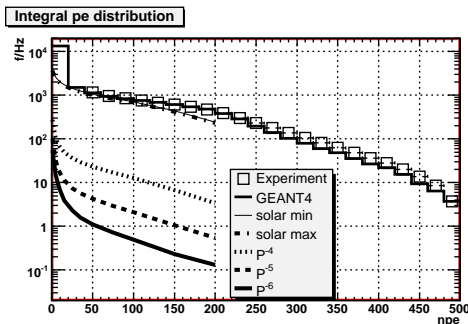
Figure 5: Integrated photon counting rates for various primary spectra, including $P^{-4,-5,-6}$ as expected for solar activity. Note that solar minimum and maximum give approximately the same rates.

maximum periods. The addition of $P^{-4,-5,-6}$ spectra, which are typical for solar flares, to the galactic cosmic ray background is expected to yield a count rate enhancement by a few percent depending on the IceTop tank photo-electron threshold setting and solar particle intensity.

Conclusion

The IceTop tanks are sensitive to low energy particles produced in cascades by cosmic radiation.

The response of the IceTop detectors is understood reasonably well in terms of the simulation, as shown by comparison to experimental measurements. This allows predictions of rate changes induced by changes in the primary particle spectrum. Furthermore these prediction suggest variations greater than that induced by atmospheric variations, leading to good detectability of solar events.

This analysis ignores the effects of multiple particle tracks entering the IceTop tanks simultaneously as each particle track reaching the ground is treated as an uncorrelated event regardless of arrival time. For low energy primaries this is a valid approach, however at high energies this could be a source of systematic errors. This effect will be investigated in order to quantify it.

Acknowledgements

References

[1] D. Heck et al., Report FZKA 6019, Forschungszentrum Karlsruhe

[2] A. Fasso, A. Ferrari, J. Ranft, and P.R. Sala, CERN-2005-10 (2005), INFN/TC_05/11, SLAC-R-773

[3] J. M. Clem, G. De Angelis, P. Goldhagen, and J. W. Wilson, Radiat. Prot. Dosimetry, 110: 423-428, 2004.

[4] T.K. Gaisser, M. Honda, P. Lipari, and T. Stanev, Proceedings of ICRC (2001) 1643

[5] R.S. Fletcher, T.K. Gaisser, P. Lipari, and T. Stanev, Phys. Rev. D50 (1994) 5710

[6] W.R. Nelson, H. Hirayama, and D.W.O. Rogers, Report SLAC 265 (1985), Stanford Linear Accelerator Centre

[7] http://nssdc.gsfc.nasa.gov/space/model/atmos/msise.html

[8] Geant4 Collaboration, NIM A 506 (2003), 250-303

[9] Peter K.F. Grieder, Cosmic Rays at Earth, Elsevier, 2001

[10] J. M. Clem, and Lev I. Dorman, Space Science Rev., Vol 93., p. 335-359, 2000

Testing alternative oscillation scenarios with atmospheric neutrinos using AMANDA-II data from 2000 to 2003

J. AHRENS[1] AND J.L. KELLEY[2] FOR THE ICECUBE COLLABORATION[A]

[1] *Institute of Physics, Mainz University, Staudinger Weg 7, D-55099 Mainz, Germany*

[2] *Department of Physics, University of Wisconsin, Madison, WI 53706, U.S.A.*

[A] *See special section of these proceedings*

jens.ahrens@lycos.de, jkelley@icecube.wisc.edu

Abstract: The AMANDA-II neutrino telescope detects upward-going atmospheric muon neutrinos penetrating the Earth from the Northern Hemisphere via the Cherenkov light of neutrino-induced muons, allowing the reconstruction of the original neutrino direction. Due to the high energy threshold of about $50\,\mathrm{GeV}$, the declination spectrum is minimally affected by standard neutrino oscillations; however, alternative oscillation models predicting subdominant effects can be tested and constrained. Of particular interest are models that allow one to test Lorentz invariance and the equivalence principle. Using the AMANDA-II data from the years 2000 to 2003, a sample of 3401 candidate neutrino-induced events was selected. No indication for alternative oscillation effects was found. For maximal mixing angles, an upper limit is set on both the Lorentz violation parameter $\delta c/c$ and the equivalence principle violation parameter $2|\phi|\delta\gamma$ of 5.3×10^{-27} at the 90% confidence level.

Introduction and detector description

Cosmic ray particles entering the Earth's atmosphere generate a steady flux of secondary particles, including muons and neutrinos. High energy muons pass through the atmosphere and can penetrate several kilometers of ice and rock, while atmospheric neutrinos of energies only above roughly $40\,\mathrm{TeV}$ start to be absorbed in the Earth. Lower energy muon neutrinos penetrating the diameter of the Earth can oscillate into tau neutrinos. However, the oscillation maxima at $30\,\mathrm{GeV}$ [1] and below are beneath the AMANDA-II threshold. Departures from conventional mass-induced oscillations could emerge at higher neutrino energies due to relativity-violating effects (see below). Such mechanisms would distort the expected angular distribution and energy spectrum of atmospheric neutrinos and could be detectable by AMANDA-II.

The AMANDA-II neutrino telescope is embedded $1500-2000\,\mathrm{m}$ deep in the transparent and inert ice of the Antarctic ice sheet, close to the geographic South Pole. AMANDA-II consists of 677 optical modules (OMs) on 19 vertical strings, which are arranged in three approximately concentric circles of $60\,\mathrm{m}, 120\,\mathrm{m}$ and $200\,\mathrm{m}$ diameter. Muons produced in ν_μ-nucleon interactions can be directionally reconstructed by observing the Cherenkov radiation that propagates through the ice to the array of photosensors. To ensure that the observed muon is due to a neutrino interaction, the Earth is used as a filter against atmospheric muons, and only tracks from the Northern Hemisphere (declination $\delta > 0°$) are selected.

Phenomenology of standard and alternative neutrino oscillations

It is commonly accepted that standard (mass-induced) $\nu_\mu \rightarrow \nu_\tau$ oscillations[1] are responsible for the measured deficit of atmospheric muon neutrinos (see *e.g.* [1]). Atmospheric neutrino data can also be used to test non-standard oscillation mechanisms that lead to observable differences at higher

---

1. In the regime of atmospheric neutrino oscillations, it suffices to consider a two-flavor system of eigenstates (ν_μ, ν_τ).

neutrino energies. Various new physics scenarios can result in neutrino flavor mixing. Two of these scenarios, which can be described in a mathematically analogous way, have been tested in this analysis. The underlying theories assume small deviations from the principles of the theory of relativity and lead to measurable neutrino oscillations:

- In theories predicting violation of Lorentz invariance (VLI), a set of additional neutrino eigenstates with different maximal attainable velocities (MAV) c_n/c is introduced, violating special relativity [2].

- In theories predicting violation of the weak equivalence principle (VEP), gravitational neutrino eigenstates are introduced which couple with distinct strengths γ_n to a gravitational potential ϕ, conflicting with the universal coupling assumed in general relativity [3, 4].

The main difference between these oscillation scenarios and standard oscillations is the linear energy dependence of the oscillation frequency, shifting observable oscillation effects into the energy range of AMANDA-II. For the sake of simplicity, we will focus on the VLI scenario. As both theories are mathematically equivalent, the results can be transferred to the VEP case by simply exchanging the relativity-violating oscillation parameters $\delta c/c \to 2|\phi|\delta\gamma$ and mixing angles $\Theta_c \to \Theta_\gamma$.

Combining standard and VLI oscillations, one obtains three systems of neutrino eigenstates (flavor, mass, and MAV eigenstates), resulting in a total of 5 oscillation parameters: the mass-squared difference Δm^2, two mixing angles Θ_m and Θ_c, the VLI parameter $\delta c/c$, and a complex phase η. Fixing $\Delta m^2 = 2.3 \times 10^{-3}\,\mathrm{eV}^2$ and $\Theta_m = 45°$, the survival probability may then be written as:

$$P(\nu_\mu \to \nu_\mu) = 1 - \sin^2 2\Theta \, \sin^2 (\Omega L) \quad (4)$$

$$2\Theta = \arctan(s/t) \qquad \Omega = \sqrt{s^2 + t^2} \quad (5)$$

$$\begin{aligned} s &= 2.92 \times 10^{-3} \, | \, 1/E_\nu + \\ & \quad 8.70 \times 10^{20} \, \delta c/c \, \sin 2\Theta_c \, E_\nu \, \mathrm{e}^{i\eta} | \, , \\ t &= 2.54 \times 10^{18} \, \delta c/c \, \cos 2\Theta_c \, E_\nu \, . \quad (6) \end{aligned}$$

Here the the muon neutrino path length L is expressed in km and the neutrino energy E_ν in

GeV. For the given set of parameters, one can observe a significant effect within the analyzed energy range $(100\,\mathrm{GeV} - 10\,\mathrm{TeV})$ and declination range $(\delta \geq 20°)$, for certain values of Θ_c and $\delta c/c$.

Data selection

The data analyzed in this analysis are selected from 7.9×10^9 events recorded from 2000 to 2003. Detector signals are recorded when 24 or more OMs report signals within a sliding window of $2.5\,\mu$s. Signals from unstable OMs, electronic and OM noise or cross-talk, as well as hits due to uncorrelated muons coincident within the trigger time, are rejected. Also, data periods with reduced data quality are discarded, corresponding to 87.8 days. The 17.3% deadtime of the data acquisition system results in a total livetime of 807.2 days used for the analysis.

The events are processed with a fast pattern recognition algorithm (A) to select tracks that are likely to be upgoing ($\delta_A > -20°$). The calculated track direction serves as a first guess for 16-fold iterative maximum likelihood reconstruction algorithms (B), restricted to upgoing tracks with $\delta > 0°$. The alternative hypothesis of a downgoing track is tested with a two-fold iterative fit requiring $\delta < -10°$. In order to reduce the probability of wrongly reconstructed tracks due to spurious hits, both fits are repeated after rejecting hits with timing residuals larger than two standard deviations. Background rejection and angular resolution are further improved by a 10-fold iterative fit (C) incorporating the probabilities that modules registered hits for the given track. From an examination of the likelihood contours in declination and right ascension [5], an estimate of the median space angle resolution σ_Ψ is obtained for individual tracks. The following selection criteria are applied, with $L_{\mathrm{diff}} \equiv \Delta \ln L$ being the difference of up- and downgoing likelihood minima: (1) declinations $\delta_A > -20°$, $\delta_B > 0°$ and $\delta_C > 20°$; (2) space angle differences $\Psi(A, B) < 30°$, $\Psi(B, C) < 7.5°$; (3) space angle resolutions $\sigma_{\Psi(B)} < 6°$ and $\sigma_{\Psi(C)} < 3.0°$; (4) likelihood difference $L_{\mathrm{diff}}(B, C) > 32.5$.

The oscillation probability depends on the neutrino flight length (*i.e.* declination) and the neutrino energy. As an energy estimator, we use a correlated observable, the number of OMs triggered in an event (N_{ch}). Using Monte Carlo simulations, declination- and N_{ch}-dependent selection criteria have been developed by dividing the distribution of the angular resolution into equal declination and N_{ch} bins. For each of these bins, a fixed, optimized percentage (8%) of the events with poor angular resolution is rejected. The same was done for the likelihood difference distributions. These criteria improved the efficiency of the data selection by 30% compared to simple selections in the angular resolution and the likelihood difference. The resulting number of selected neutrino candidate events is 3401. From a study of the distribution of space angle difference, the background of wrongly reconstructed atmospheric muons is estimated to be 4%.

A full simulation chain, including neutrino absorption in the Earth, neutral current regeneration, muon propagation, and detector response is used to simulate the response of AMANDA-II to atmospheric neutrinos [6, 7]. The expected atmospheric muon neutrino flux before oscillations is taken from Lipari [8].

Analysis method and systematic errors

The analysis method uses a χ^2-test to compare the declination and N_{ch} distributions of data with Monte Carlo simulations including VLI oscillation effects. The systematic uncertainties affecting the Monte Carlo prediction are integrated into the χ^2 expression:

$$\chi^2 \left(\delta c/c, \Theta_c, \cos\eta \right) =$$

$$\sum_{i=1}^{N_{Bins}} \frac{\left(N_i^D - N_i^{BG} - F \cdot N_i^{MC} \left(\delta c/c, \Theta_c, \cos\eta \right) \right)^2}{N_i^D + N_i^{BG} + \left(\sigma_i^{MC} \right)^2}$$

$$+ \left(\frac{\alpha}{\sigma_\alpha} \right)^2 + \left(\frac{\kappa}{\sigma_\kappa} \right)^2 + \left(\frac{\epsilon}{\sigma_\epsilon} \right)^2 \quad , \quad (7)$$

where N_i^x denotes the number events in bin i and x denotes data (D), background (BG) and Monte
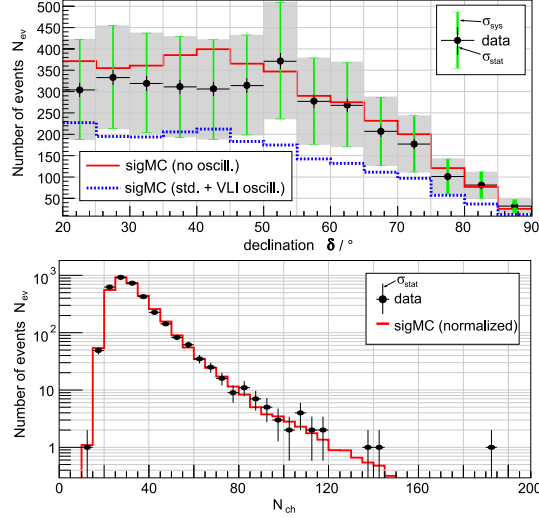
Figure 1: Top: Measured atmospheric neutrino declination distribution with statistical and systematic errors. Also shown are the predicted distributions without oscillation and with $\delta c/c = 10^{-24}$, $\Theta_c = \pi/4$ and $\cos\eta = 0$. Bottom: N_{ch} distributions of data (statistical errors only) and the predicted distribution without oscillations, normalized to the data.

Carlo (MC). The function F represents the product of functions $f_\alpha \cdot f_\kappa^i \cdot f_\epsilon^i$ which are defined as:

$$f_\alpha = 1 + \alpha, \qquad f_\kappa^i = c_i \cdot \kappa + 1,$$
$$f_\epsilon^i = 1 + 2\epsilon \left(0.5 - \sin\delta_i \right) . \qquad (8)$$

α parametrizes the systematic uncertainty in the overall normalization due to uncertainties in the detector response and theoretical uncertainties of the atmospheric neutrino flux ($\sigma_\alpha = 30\%$). The uncertainty due to the relative production rate between kaons and pions, which affects the shape of the declination distribution, is parametrized by ϵ and is estimated as $\sigma_\epsilon = 6\%$ in total [9]. The uncertainty in the sensitivity of the optical modules is parametrized by κ ($\kappa = 0$ for 100% sensitivity) and was measured to be $\sigma_\kappa = 11.5\%$. The function f_κ^i was derived from the changes in the declination distribution generated by Monte Carlo distributions with different OM sensitivities. In order to determine the optimal number of declination and N_{ch} bins and their optimal range, toy Monte Carlo samples of 10000 events have been generated re-

flecting the simulated flux and systematic uncertainties as assumed above. The mathematical properties of expression (4) were checked, and belts for 90%, 95% and 99% confidence level were derived from a high statistics toy Monte Carlo sample.

The results of the toy Monte Carlo studies favor an analysis using the following 4 bins: ($N_{ch} \leq 49$, $\delta \leq 55°$), ($N_{ch} \leq 49$, $\delta > 55°$), ($N_{ch} > 49$, $\delta \leq 55°$), and ($N_{ch} > 49$, $\delta > 55°$).

The exclusion regions for alternative oscillation effects are obtained by scanning through the oscillation parameter space. For each point $[\delta c/c, \sin(2\Theta_c), \cos(\eta)]$ the χ^2 expression is minimized in the error variables α, ϵ and κ.

Results and Outlook

The analysis of the final atmospheric neutrino sample finds no evidence for alternative oscillations, and a preliminary upper limit on the VLI parameter $\delta c/c$ is set of 5.3×10^{-27} at the 90% confidence level, for nearly maximal mixing angles $\Theta_c \approx \pm\pi/4$. The dependence on the unconstrained phase η is found to be small (see figure 2); the most conservative limit is obtained for $\cos\eta = 0$. The limit can also be interpreted in the context of VEP theories, leading to an upper limit of $2|\phi|\delta\gamma \leq 5.3 \times 10^{-27}$. This result improves the limits obtained using data from Super-Kamiokande [10] and MACRO [11]. However, AMANDA is not sensitive to small mixing angles due to the systematic errors and its higher energy threshold. A likelihood analysis of the 2000-2005 AMANDA-II data sample is in progress, with improved systematic error estimation and increased sensitivity [12]. This analysis will also extend the technique to search for evidence of quantum decoherence resulting from interaction of neutrinos with the background space-time foam [13]. The next-generation IceCube detector, when completed in 2010, will be able to extend the sensitivity to VLI effects by about one order of magnitude [14].

Acknowledgments
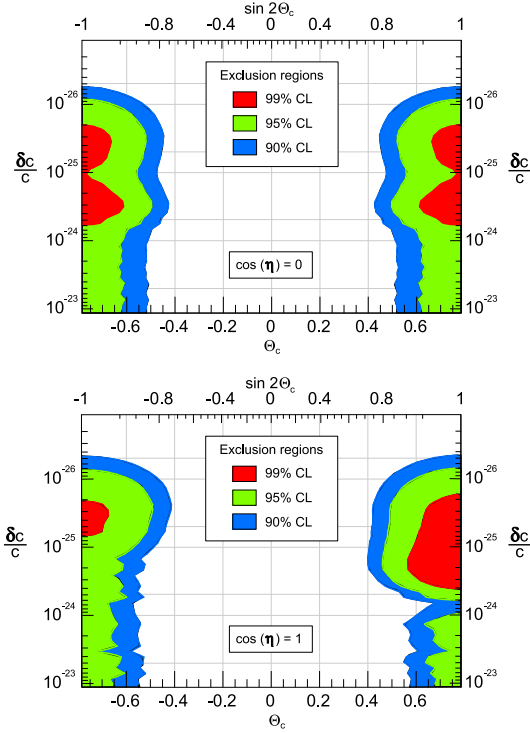
Figure 2: Shown are preliminary exclusion regions for VLI (VEP) oscillation effects, top for $\cos\eta = 0$, bottom for $\cos\eta = 1$.

References

[1] Y. Ashie *et al.*, *Phys. Rev. D* 71, 112005 (2005); E. Aliu *et al.*, *Phys. Rev. Lett.* 94, 081802 (2005).

[2] S. Coleman and S.L. Glashow, *Phys. Lett. B* 405, 249 (1997).

[3] M. Gasperini, *Phys. Rev. D* 38, 2635 (1988).

[4] A. Halprin and C.N. Leung, *Phys. Rev. Lett.* 67, 14 (1991).

[5] T. Neunhöffer, *Astropart. Phys.* 25, 220 (2006).

[6] G. C. Hill, *Astropart. Phys.* 6, 215 (1997).

[7] D. Chirkin and W. Rhode, hep-ph/0407075 (2004).

[8] P. Lipari, *Astropart. Phys.* 1, 195 (1993).

[9] K. Nitto, Ph.D. thesis, University of Osaka (2003).

[10] M.C. González-García and M. Maltoni, *Phys. Rev. D* 70, 033010 (2004).

[11] G. Battistoni *et al.*, *Phys. Lett. B* 615, 14 (2005).

[12] J.L. Kelley for the IceCube Collaboration, *Proc. of the First Workshop on Exotic Physics with Neutrino Telescopes*, astro-ph/0701333 (2007).

[13] D. Morgan *et al.*, *Astropart. Phys.* 25, 311 (2006).

[14] M.C. González-García, F. Halzen, and M. Maltoni, *Phys. Rev. D* 71, 093010 (2005).

Atmospheric muon neutrino analysis with IceCube

J. PRETZ[1] FOR THE ICECUBE COLLABORATION[2]

[1]*Dept. of Physics, University of Maryland, College Park, MD 20742, USA*

[2] *see special section of these proceedings*

pretz@icecube.umd.edu

Abstract: The heart of the IceCube neutrino observatory is a cubic kilometer Cherenkov detector being constructed in the deep ice under the geographic South Pole. IceCube is sensitive to high-energy muon neutrinos and muon anti-neutrinos by detecting the secondary muon produced when the neutrino interacts in or near the instrumented volume. The principal source of muon neutrinos are neutrinos from the decay of hadrons in cosmic-ray air showers. IceCube operated during 2006 with 9 out of 80 anticipated strings in the ice. I will demonstrate that IceCube can find and reconstruct atmospheric neutrinos with high efficiency.

Introduction

The IceCube neutrino detector [1] is partially deployed at the geographic South Pole. In 2006, the deep-ice detector consisted of 540 light-sensitive Digital Optical Modules (DOMs), arranged 17 meters apart on 9 strings of 60 DOMs each. The detector in this configuration is termed IC-9. The strings are arranged on a hexagonal grid and spaced 125 meters apart. DOMs are deployed in the deep ice between 1.5 and 2.5 kilometers below the surface. Figure 1 shows the location of strings making up the IC-9 array along with the relative position of the AMANDA detector.

IceCube is sensitive to muon neutrinos (and anti-neutrinos) by observing the Cherenkov light from the secondary muon produced when the neutrino interacts near the detector volume. Atmospheric neutrinos, formed in the decay of mesons resulting from a cosmic ray striking the atmosphere, dominate. Since atmospheric neutrinos are relatively well-understood [2], they serve as a verification and calibration tool for the new detector. Muons from neutrino interactions are separated from muons produced in cosmic rays by selecting muons moving upward through the detector. These muons must be the result of a neutrino interaction since neutrinos are the only particle that can traverse the Earth without interacting.
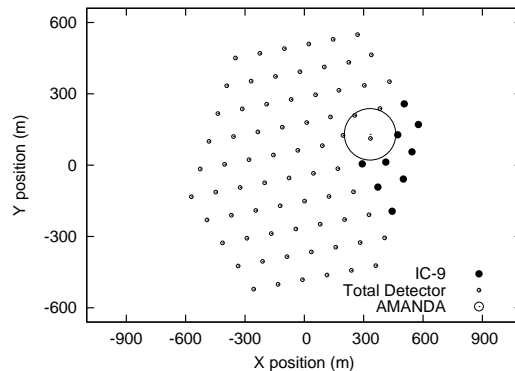
Figure 1: Shown are the locations of strings for the 2006 IC-9 detector, and the location of the strings in the completed detector. The location of the AMANDA detector is also indicated.

Data Acquisition and Filtering

In 2006, we acquired 137.4 days of livetime with IC-9 suitable for analysis. The waveform capture in a DOM was triggered whenever the DOM detected a signal above a threshold of about 0.3 photoelectrons. The DOMs were operated in Local Coincidence (LC) with their neighbors, meaning that a triggered DOM's waveform was only transmitted to the surface if an adjacent DOM on the string also triggered within ± 1000 ns. The surface data acquisition system set off a trigger if 8 or more DOMs were read out in 5 μs. When an event is formed, all DOM hits were read out within $\pm 8\mu s$ around the trigger window.

Because of limited bandwidth between the South Pole and the data center in the North, the data is filtered in real time, and only candidates for up-going events are sent North.

Hit cleaning algorithms were applied to the triggered events to remove light from additional suprious muons, and to remove noise hits. The photon arrival times are determined by a fit to the DOM waveform, with a variable number of photon arrivals. The hit cleaning isolated the 4 μs window in which the most hits occur, and remaining DOM hits are kept only if another DOM hit occured within a radius of 100 meters and within a time of 500 ns. At the pole, simple first-guess algorithms were used to reject events that were down-going. In addition, events with fewer than 11 DOMs hit were rejected to limit the data volume. This filter reduced the data rate by approximately 95%. The remaining events were transmitted to the data center via satellite for further study.

Reconstruction and Event Selection

In the North, we reconstructed the direction of events using a maximum-likelihood technique similar to the AMANDA muon reconstruction [3]. Only the earliest arrival times were used for reconstruction and no amplitude information was included in this analysis. The likelihood function is based on a parametrization of the photon arrival time distribution without any prior assumption of the relative likelihood of a cosmic ray muon or neutrino event. The likelihood function is formed with an analytic approximation to the photon arrival time probability density function, accounting for the short (~ 20 meter) scattering length of light in IceCube. Events that reconstruct as down-going are discarded. Despite the fact that remaining events appear up-going, they are in fact dominated by mis-reconstructed down-going events. These mis-reconstructed events are removed with quality cuts and the remaining events constitute the neutrino candidate dataset.

The quality cuts are based on direct hits in the detector. Direct hits are those which arrive between $-15ns$ and $+75ns$ from the time expected from unscattered Cherenkov photons radiated from the reconstructed muon. We cut both on the number of recorded direct hits N_{dir} and the largest distance of such hits along the track, L_{dir}. An event with a large N_{dir} and a large L_{dir} is a better quality event because the long lever arm of many unscattered photon arrivals increases confidence in the event reconstruction.

We can fold these two cuts together into one dimensionless number, the cut strength S_{cut} which corresponds to cuts of $N_{dir} \geq S_{cut}$ and $L_{dir} > 25 \cdot S_{cut}$ meters.

Table 1 shows the rates of events passing to the different levels of the analysis, for both experimental data and simulated events. Simulated events fall into three categories. 'Single shower' events are events from single air-shower events in the atmosphere above the detector. 'Double shower' events come from two uncorrelated air showers. Finally 'atmospheric neutrino' events come from π and K decay in the air showers in the Northern hemisphere. The CORSIKA air-shower [4] simulation was used to model down-going air shower events. An extension to high energies [5] for the atmospheric neutrino model of [2] with the cross-section parametrization of [6] was used to determine the expected up-going muon rate. In estimating the systematic error, we have included a 30% uncertainty in the atmospheric neutrino flux modeling [7], and a 20% uncertainty due to uncertainties introduced in the modeling of the depth-dependent ice properties and the DOM detection efficiency.

Criterion Satisfied	Experimental Data	Single Shower	Double Shower	Atmospheric Neutrinos
Trigger Level	124.5	124.5	1.5	6.6×10^{-4}
Filter Level	6.56	4.96	0.45	3.7×10^{-4}
Up-going ($S_{cut} = 0$)	0.80	0.49	0.21	3.3×10^{-4}
Up-going ($S_{cut} = 10$)	$(1.97 \pm 0.12) \cdot 10^{-5}$	-	-	$(1.77 \cdot \pm 0.63) \cdot 10^{-5}$
Up-going ($S_{cut} = 10$ and $\theta > 120$)	$(1.19 \pm 0.10) \cdot 10^{-5}$	-	-	$(1.42 \cdot 0.51) \cdot 10^{-5}$

Table 1: Event Passing Rates (Hz). Shown are the event passing rates through different processing levels for the simulated event categories and for experimental data. The trigger level comprises the events triggering the detector after hit cleaning and re-triggering. The filter level comprises events which passed the online filtering conditions. Rates are also shown for events which reconstruct as up-going with and without the final quality cuts applied (see the text for cut definition). Note that the rates from air-shower events have been multiplied by 0.90 so that the simulation and data agree at trigger level. This is consistent with an approximately 20% uncertainty in the absolute cosmic-ray flux. For the final sample, statistical errors are given for the data and systematic errors are given for the atmospheric neutrino simulation.

Results

Figure 2 shows the number of up-going events remaining as we tighten cuts. The contribution of the data is shown together with the expectation for atmospheric neutrinos and the total simulation prediction. Below a cut strength of about $S_{cut} = 10$, the data is dominated by mis-reconstructed down-going cosmic-ray shower muons. For higher cut strengths, we have removed most of these mis-reconstructed events and are dominated by atmospheric neutrinos. The accurate simulation of the mis-reconstructed muon population requires excellent modeling of the depth-dependent ice properties and DOM sensitivity. In this initial study, we observe a 60%-80% discrepancy between data and simulation for mis-reconstructed muons. Nevertheless, over four orders of magnitude, the background simulation tracks the data, and we see a clear transition to a population dominated by atmospheric neutrinos.

Figure 3 shows the expected energy distribution of simulated atmospheric neutrino events surviving to $S_{cut} = 10$. The lower threshold of about 100 GeV is set by the range of the secondary muons, and the dropoff at high energies is due to the decreasing flux of atmospheric neutrinos.

Figure 4 shows the zenith angle distribution for events which survive at $S_{cut} = 10$. Above 120 degrees, for vertical events, we have good agreement
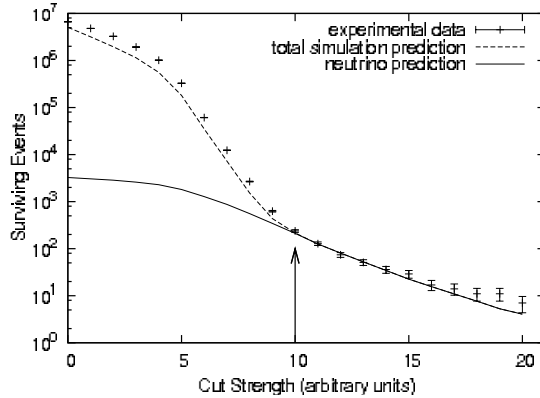
Figure 2: Data vs Cut Strength. Shown is the remaining number of events as the cut strength S_{cut} (defined in the text) is varied. Curves are shown for the data and the total simulation prediction. Also shown is the prediction due to atmospheric neutrinos alone. The selection from the text corresponds to a cuts strength of $S_{cut} = 10$, and is denoted by an arrow. At this point, the data are dominated by atmospheric neutrinos.
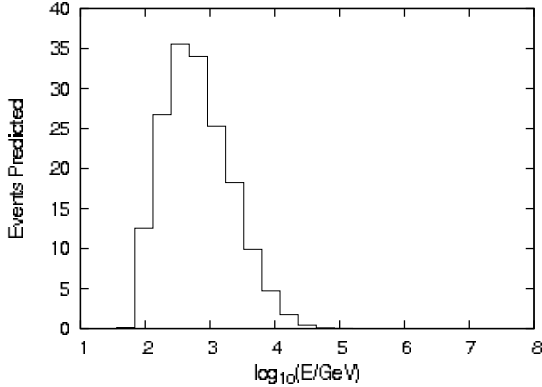
Figure 3: The distribution of neutrino energy for events surviving the analysis cuts, as determined by the atmospheric neutrino simulation.

Figure 4: Distribution of the reconstructed zenith angle θ of the final event sample. A zenith angle of 90 degrees indicates a horizontal event, and a zenith of 180 degrees is a directly up-going event. The band shown for the atmospheric neutrino simulation includes the systematic errors; the error bars on the data are statistical only.

between experimental data and atmospheric neutrino simulation. The excess at the horizon is believed to be residual air-shower muon events. This belief is reinforced by the fact that excess data at the horizon is typically of lower quality (as measured by N_{dir}, L_{dir} and the number of hit DOMs) than expected from atmospheric neutrino simulation. The data above the horizon agrees well in these variables with a pure atmospheric neutrino expectation.

In the recorded 137.4 days of livetime we measure 234 events surviving to $S_{cut} = 10$, compared to an expectation of $211 \pm 76(syst.) \pm 14(stat.)$ events from a pure atmospheric neutrino signal. Above a zenith of 120 degrees, where the background contamination is small, we measure 142 events with an expectation of $169 \pm 60(syst.) \pm 13(stat)$ events.

Conclusions

IceCube is partially deployed and acquiring physics-quality data. During the 2006 season, we accumulated 137.4 days of livetime and observe an atmospheric neutrino signal consistent with expectation. We have identified 234 neutrino candidate events. For zenith angles above 120 degrees, the background from misreconstructed muons is small and the sample is dominated by atmospheric neutrinos. The selection of events was done within six months of the beginning of data acquisition,

demonstrating the viability of the full data acquisition chain, from PMT waveform capture at the DOM with nanosecond timing, to event selection at the South Pole and transmission of that selected data via satellite to the North.

References

[1] A. Karle et al. *These proceedings.*

[2] G. D. Barr, T. K. Gaisser, P. Lipari, Simon Robbins, and T. Stanev. *Phys. Rev.*, D70:023006, 2004.

[3] J. Ahrens et al. *Nucl. Inst. Meth.*, A524:169–194, 2004.

[4] D. Heck et al. *Proceedings of the 27th International Cosmic Ray Conference*, pages 233–236, 2001.

[5] G. Barr. private communication.

[6] H. L. Lai et al. *Eur. Phys. J.*, C12:375–392, 2000.

[7] G. D. Barr, S. Robbins, T. K. Gaisser, and T. Stanev. *Phys. Rev.*, D74:094009, 2006.

ICRC'07
Merida, México

Muon energy reconstruction and atmospheric neutrino spectrum unfolding with the IceCube detector

JUAN-DE-DIOS ZORNOZA[1,2], DMITRY CHIRKIN[3] ON BEHALF OF THE ICECUBE COLLABORATION[4]

[1]*Department of Physics, University of Wisconsin, Madison, Wisconsin, 53703, USA*

[2]*IFIC (CISC-University of Valencia), Ed. de Investigación de Paterna, AC 22085, 46071, Valencia, Spain*

[3] *Lawrence Berkeley National Laboratory, Berkeley, California 94720, USA*

[4] *See special section of these proceedings*

zornoza@icecube.wisc.edu

Abstract: Data collected during the year 2006 by the first 9 strings of IceCube can be used to measure the energy spectrum of the atmospheric muon neutrino flux. Atmospheric neutrinos, an important scientific output by itself (for instance, to understand the high-energy hadronic interaction models), are also fundamental in order to check the performance of the detector and to estimate the background for the extraterrestrial high-energy neutrinos searches. A full reconstruction of the neutrino-induced muon tracks provides both directional and energy information. The reconstructed energy-correlated parameter, the photon density emitted by the muon along its track, can be used to calculate the energy spectrum, which is reconstructed by using unfolding techniques. We will discuss the unfolding procedure to be applied to data from the 9-string configuration of IceCube.

Motivation

The IceCube collaboration is building a cubic kilometer neutrino telescope in the Antarctic ice. Since neutrinos are neutral, stable and weakly interacting, they are a unique probe to study the Universe at high energies and IceCube will be the most powerful tool available for observing them. The detector will be completed by 2011 and the construction goal is 80 strings with 4800 photomultipliers, which will detect the Cherenkov light emitted by the relativistic muons produced in the CC interactions of high-energy neutrinos. IceCube can also observe the cascades produced by CC ν_e and ν_τ interactions and NC interactions of any flavor.

During the Austral summer 2006-07, a total of 22 strings were deployed and the detector is working smoothly. In this paper we will study the data corresponding to the previous season, when 9 strings were installed.

The scientific output of neutrino astronomy is very wide, including the search of dark matter and the observation of astrophysical neutrinos from a large variety of sources (gamma-ray bursts, active galac-

tic nuclei, microquasars, etc.) Therefore, it is very important to study the background due to neutrinos from decay of pions and kaons produced by the interaction of cosmic rays in the atmosphere. Experiments like AMANDA [1] have measured the neutrino atmospheric spectrum up to ~100 TeV and IceCube will be able to explore the region where the prompt neutrino component (due to charmed meson decays) will dominate. The atmospheric muon background can be severely reduced by selecting only up-going events and imposing restrictive constrains in the quality of the reconstructed track. On the other hand, atmospheric neutrinos cannot be rejected in this way, so it is important to understand well the rates and spectrum of this background.

A detailed study of the rates of the 9-string configuration of IceCube can be found in [2]. In this paper, we will focus on the reconstruction of the energy spectrum. This spectrum cannot be reconstructed by just piling-up the energy of individual events because of two factors. First, the energy resolution is limited because we only see part of the muon energy (which in turn is only part of the neu-

trino energy) and because the muon energy loss is stochastic. Second, the spectrum falls very quickly with energy (as $E^{-3.7}$), so the events for which the energy is overestimated would bury the events at higher energy, distorting the resulting spectrum. In order to overcome this problem, a different approach is needed: the unfolding techniques.

The structure of this paper is as follows. In the next section, we will describe the calculation of the variable used for the unfolding. This variable has to be correlated with the neutrino energy with the lowest possible spread. Among the different variables that have been studied (number of hit optical sensors, total charge, photon density along the track, etc.) the best results are obtained when reconstructing the energy from the photon density along the track at the point of closest approach to the center of gravity of hits in the event. In the following section we make a brief description of the unfolding procedure and test the robustness of the method. Finally, we show the resulting unfolded spectrum.

Energy reconstruction technique

As a muon travels through ice, it emits about $3 \cdot 10^4$ Cherenkov photons in the spectral range visible to the detector per meter along its track, just from electromagnetic interaction of the bare muon. In addition, the knock-on electrons, bremsstrahlung, electron pairs, and photonuclear interactions caused by the muon traveling through ice, generate short cascades along the muon track [3]. Particles created in such cascades also emit Cherenkov radiation, increasing the "effective length" of the muon (which determines the total number of Cherenkov photons using the above factor) by the amount proportional to the energy of the cascade, on average by about 4 m· E/GeV [4]. The number of additional Cherenkov photons emitted by the passing muon due to cascades created along its path is therefore proportional to the total energy deposited in form of such cascades. In a well-known approximation of the muon energy losses, $dE/dx = a + b \cdot E$, the second term is largely due to just such energy deposits. Above the critical energy ($\sim$ 1 TeV), the second term begins to dominate the energy losses, and the total number of Cherenkov photons left by a muon per unit

length of the muon track becomes proportional to its energy:

$$N_c = 3 \cdot 10^4 \text{m}^{-1}(1.22 + 1.36 \cdot 10^{-3} E/[\text{GeV}]) \quad (9)$$

This "photon density" along the muon track enters naturally into the muon track reconstruction through a term in a log likelihood function, which describes how well the number of photons observed at a distance d from the track is described by the flux function (defined as the lateral distribution of Cherenkov photons around the muon track given as a function of the distance from the track). The flux function is easily computed in the vicinity of the track, before the scattering of light alters the original direction of photons in the Cherenkov cone around the track. At large distances one may use the diffusive approximation since the photons observed there have sustained many direction-altering scattering events. In the intermediate distance region these approximations are stitched together with a function, chosen to describe all 3 regions. The shape of the function was inspired by the eikonal small-angle scattering approximation of light that may be used in low-scattering media, e.g., water. The chosen flux function was verified against data and was found to perform extremely well.

The photon density along the muon track thus becomes the 6th parameter in addition to two angles and 3 parameters describing a point in space and time along the muon track, against which the likelihood function is minimized. One may then calculate the energy by either inverting equation (1) or performing a Monte Carlo study of the correlation of the calculated photon density and energy (see Figure 1). The second approach additionally results in a smearing matrix, which can then be used for spectra unfolding (next section). In all cases the energy of the muon is taken at the point of closest approach to the center of gravity of hits left by the muon in the detector (which yields better energy estimates than alternatives).

Figure 2 shows the resolution of the energy reconstructed with the method described here and with methods based on the calculation of the number of hit optical channels (N_{ch}) and total charge (Q_{tot}). For the isotropic fluxes in the energy range of $10^{4.4} - 10^{7.4}$ GeV a reconstruction precision of
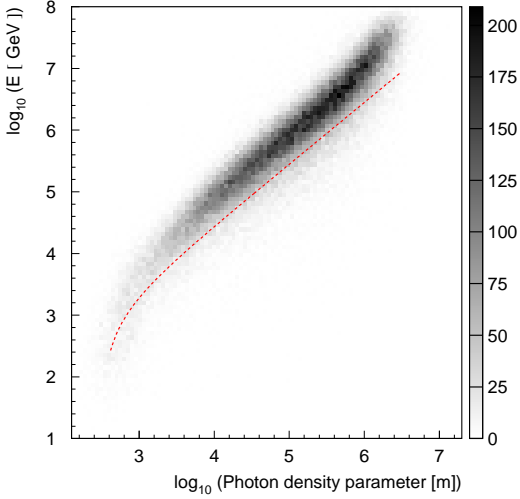
Figure 1: Correlation of true muon energy and reconstructed photon density parameter (photon density N_c times optical sensor effective PMT area). The red line corresponds to the application of eq. (1). It overestimates the value of the photon density parameter somewhat when compared to the detailed simulation.

Figure 2: Energy reconstruction precision: blue (lowest curve) for the photon-density-based approach of this paper, red for the Q_{tot} and green (highest curve) for the N_{ch}-based calculations.

0.3 in $\log_{10}$(E [GeV]) is achieved. This is close to the theoretically achievable (determined by the uncertainty related to stochastic nature of energy losses). For the atmospheric neutrino fluxes this energy range increases to $10^{3.6} - 10^{7.6}$ GeV (this may also be due to somewhat reduced statistics at lower energies). At low energies the resolution worsens due to a reduced dependence of muon energy losses on muon energy below the critical energy. This may potentially be improved by using the observed muon track length as an additional energy-correlated parameter. At high energies one expects the nearby optical sensors to be saturated, leading to increased systematic uncertainties and, in turn, to reduced energy reconstruction precision. This will likely improve with more detailed corrections of the saturated behavior taken in the account.

Unfolding procedure

There are different unfolding methods used in high energy physics. Previous studies of the atmospheric neutrino unfolding have been done both for AMANDA data [5, 6] and ANTARES simu-

lation [7]. For this analysis we have chosen the Singular Value Decomposition algorithm [8], since it is robust, efficient and easy to implement. The problem of unfolding can be expressed, in matrix notation, by the expression $\hat{A}y = b$, where $\hat{A}$ is the so-called smearing matrix (which has to be generated by Monte Carlo), y is the spectrum we want to measure (in this case, the neutrino energy spectrum), and b is the experimental observable (reconstructed muon energy). Inverting the smearing matrix does not give a useful solution because of the effect of statistical fluctuations, which completely spoils the result. The SVD algorithm is based on the decomposition of $\hat{A}$ as $\hat{A} = USV^T$, where U and V are orthogonal matrices and S is a nonnegative diagonal matrix whose diagonal elements are called "singular values". It can be shown that this decomposition allows one to easily identify the elements of the system that contribute to the statistical fluctuations but provide useful information. Thus, these elements can be filtered out in order to obtain a smoother solution.

Another interesting point of this method is that in practice we do not try to solve directly the spectrum, but the deviations from a reasonable assumption. This also helps to reduce the effect of statistical fluctuations.
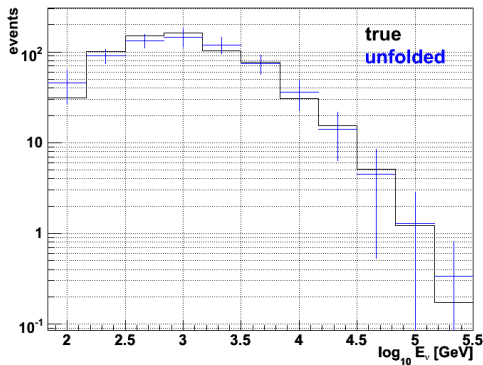
Figure 3: True (black line) and unfolded (blue crosses) Monte Carlo spectra (preliminary). It can be seen that the agreement between both distributions is good. Errors include global unfolding uncertainties.

Results and discussion

The event selection used in this work is guided by one applied in the atmospheric neutrino rates analysis [2]. The variables to perform such a selection are the same but the values have been somewhat relaxed in order to increase the statistics: N_{dir} (number of unscattered photons) ≥ 8, L_{dir} (length of the track) > 200 m and θ (zenith angle) > 92 deg. These cuts should still reject most of the background contamination, which is still under study. In order to check that the simulation is under control, we have compared simulated and measured distribution of several variables, finding good agreement.

We have checked the robustness of the unfolded results as function of the spectral index used when creating the smearing matrix and the initial assumption made for the solution of the system. As a spectral index of $\gamma = -2$ is far from $\gamma = -3.7$, the dependence on the uncertainty of the smearing matrix is small. We used rather different shapes for the initial assumption on the solution and could show that the algorithm coverges towards the expected solution. Figure 3 compares the true (generated by Monte Carlo) and unfolded distributions, showing a good agreement between both (preliminary result).

Conclusions

The atmospheric neutrino spectrum is an important result both for its intrinsic physics interest and because atmospheric neutrinos are the main source of background in most of the analysis in neutrino telescopes. In order to reconstruct this spectrum we have to use unfolding techniques. In this paper we have described how to reconstruct the muon energy (at the point of closest approach to the center of gravity hits in the event), which is the variable found to best correlate with the neutrino energy. Finally, the unfolded spectrum is obtained, showing also that the algorithm works properly when compared with Monte Carlo.

References

[1] J.D. Zornoza, Nucl. Phys. Proc. Suppl. **165**, 196-199, 2007.

[2] "Detection of atmospheric muon neutrinos with the IceCube 9-string detector", A. Achterberg *et al.* (IceCube collaboration), submitted to PRD (2007), arXiv:0705.1781v1.

[3] "Muon Monte Carlo: a high-precision tool for muon propagation through matter", D. Chirkin, hep-ph/0407075.

[4] Ph.D. thesis, C.H.Wiebusch, Physicalische Institute, RWTH Aachen, 1995

[5] H. Geenen for the AMANDA collaboration, Proceedings of 28th ICRC, Tsukuba, Japan, 2003.

[6] "Search for a diffuse flux of non-terrestrial muon neutrinos with the AMANDA detector" K. Muenich for the IceCube collaboration, Proceedings of 29th ICRC, Pune, India, 2005.

[7] "Sensitivity to diffuse fluxes and energy spectrum reconstruction in the ANTARES neutrino telescope", J.D. Zornoza, Ph.D. Thesis, University of Valencia, 2005.

[8] A. Hoecker and V. Kartvelishvili, Nucl. Inst. & Meth. in Phys. Res. **A372**, 469-481, 1996.

Searches for a diffuse flux of extra-terrestrial muon neutrinos with AMANDA-II and IceCube

KOTOYO HOSHINA[1], JESSICA HODGES[1], GARY C. HILL[1] FOR THE ICECUBE COLLABORATION[2]
[1]*Dept. of Physics, University of Wisconsin, Madison, WI 53706, USA*
[2]*See special section of these proceedings.*
kotoyo.hoshina@icecube.wisc.edu

Abstract: The AMANDA-II data collected during the period 2000–2003 have been analysed in a search for a diffuse flux of high-energy extra-terrestrial muon neutrinos from the sum of all sources in the Universe. With no excess of events seen, an upper limit of $E_\nu^2 \times dN_\nu/dE_\nu < 7.4 \times 10^{-8}$ GeV cm^{-2} s^{-1} sr^{-1} was obtained. The astrophysical implications of this upper bound are discussed, in addition to results from the search for signals with other energy spectra. The sensitivity of the diffuse analysis of IceCube 9-string is presented.

Introduction

High energy photons have been used to paint a picture of the non-thermal Universe, but a more complete image of the hot and dense regions of space can potentially be obtained by studying astrophysical neutrinos. Neutrinos can provide valuable information because they are undeflected by magnetic fields and hence their paths point back to the particle's source. Unlike photons, neutrinos are only rarely absorbed when traveling through matter. However, their low interaction cross section also makes their detection more challenging. The observation of astrophysical neutrinos would confirm predictions that hadrons are accelerated in objects such as active galactic nuclei or gamma-ray bursts [1, 2].

Instead of searching for neutrinos from either a specific time or location in the sky, diffuse analyses search for extra-terrestrial neutrinos from unresolved sources. If the neutrino flux from an individual source is too small to be detected by point source search techniques, it is nevertheless possible that many sources, isotropically distributed throughout the Universe, could combine to make a detectable signal. This search method assumes that the signal has a harder energy spectrum than atmospheric neutrinos. When examining an energy-related parameter, an excess of events over the ex-

pected atmospheric neutrino background would be indicative of an extra-terrestrial neutrino flux.

Search Method

Cosmic ray interactions in the atmosphere create pions, kaons and charmed hadrons which can later decay into muons and neutrinos. The main background for this analysis consists of atmospheric muons traveling downward through the ice. Diffuse analyses use the Earth as a filter to search for upgoing astrophysical neutrino-induced events. Once the background muons have been rejected, the data set mainly consists of neutrino-induced upward events. To separate atmospheric neutrinos from extra-terrestrial neutrinos, we use an energy-related observable as a final filter. This procedure is based on the assumption that the signal neutrinos follow a $\Phi \propto E^{-2}$ energy spectrum resulting from shock acceleration processes. The atmospheric neutrino flux has a much softer energy spectrum (typically $\Phi \propto E^{-3.7}$ for light meson induced, $\Phi \propto E^{-2.7}$ for charmed hadron induced).

AMANDA-II diffuse muon searches

Searches for a diffuse flux have been performed with through-going muon events from

1997 AMANDA-B10 data [3] and 2000–2003 AMANDA-II data (807 days livetime) [4]. A search based on a regularized unfolding of the energy spectrum is also reported in these proceedings [5]. The energy estimator used by the 2000–2003 muon analysis was the number of optical modules (channels) that reported at least one Cherenkov photon during an event (N_{ch}). Due to their harder energy spectrum, extraterrestrial neutrinos are expected to produce a flatter N_{ch} distribution than atmospheric neutrinos (see Figure 1).

The search for an extra-terrestrial neutrino component used the number of events above an N_{ch} cut, after subtracting a calculated contribution from atmospheric neutrinos. The cut was optimized to produce the best limit setting sensitivity [6]. In order not to bias the analysis, data above the resulting cut ($N_{ch} > 100$) were kept hidden from the analyzer while the lower N_{ch} events were compared to atmospheric neutrino expectations from Bartol [7] and Honda [8]. The various atmospheric neutrino calculations (Bartol and Honda models, with and without systematic uncertainties) were normalized to the low N_{ch} data, and the resulting spread in the number of events predicted with $N_{ch} > 100$ was figured as an uncertainty in the limit calculation.

The observed N_{ch} distribution is compared to the atmospheric neutrino background calculations in Figure 1. For the $N_{ch} > 100$ region, 6 events were seen, while 7.0 were expected. Using the range of atmospheric uncertainty (shaded band in Figure 1) in the limit calculation [9] leads to an upper limit on a $\Phi \propto E^{-2}$ flux of muon neutrinos at Earth of $E_\nu^2 \times dN_\nu/dE_\nu = 7.4 \times 10^{-8}$ GeV cm^{-2} s^{-1} sr^{-1}. This upper limit is valid in the energy range 16–2500 TeV. In comparison, an unfolding of the atmospheric neutrino spectrum with this same data set leads to an upper limit of $E_\nu^2 \times dN_\nu/dE_\nu = 2.6 \times 10^{-8}$ GeV cm^{-2} s^{-1} sr^{-1} for the energy range 300–1000 TeV [5]. With this analysis, limits were also placed on specific extra-terrestrial models and on the flux of prompt, charmed hadron neutrinos from Earth's atmosphere [4].

Figure 4 shows the upper limit on the ν_μ flux from sources with an E^{-2} energy spectrum. The limit from the AMANDA-II 4-year analysis is a factor of four above the Waxman-Bahcall upper bound [1].
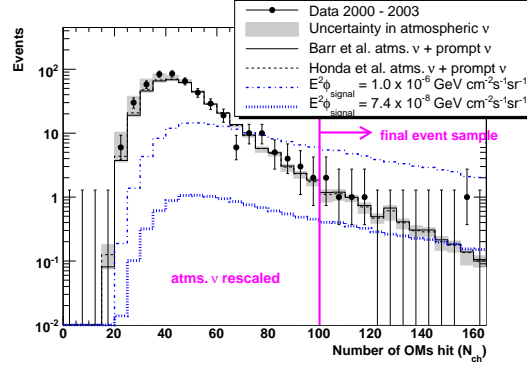
Figure 1: N_{ch}, the number of OMs triggered, for the AMANDA-II 2000–2003 diffuse muon neutrino analysis. The data is compared to atmospheric neutrino expectations [7, 8]. The signal prediction for a $\Phi \propto E^{-2}$ flux is rescaled to reflect the upper limit derived from this analysis.

IceCube 9 String

The IceCube neutrino observatory is under construction and will be completed within the next four years. In 2006, the first nine IceCube strings were operated as a physics detector for 137 days. The IceCube 9-string detector (IC9) has an instrumented volume four times larger than AMANDA-II. Each string contains 60 digital optical modules (DOMs) in ice, spaced in 17 m intervals between depths of 1450 to 2450 m. The distance between strings is 125 m, approximately three times greater than in AMANDA-II.

Muon Background Rejection

Like the 2000–2003 AMANDA-II analysis, the IC9 analysis uses the number of hit DOMs (N_{ch}) as an energy-related observable to distinguish atmospheric neutrinos from extra-terrestrial neutrinos. This method requires atmospheric muon backgrounds to be removed first. For IC9, the atmospheric muon rejection has been re-optimized to preserve more near-horizontal signal events (now covering 80–180 degrees in zenith) and accommodate the new detector geometry.

For the background study, atmospheric muons were simulated using CORSIKA. In addition, coincident muon events were generated, in which
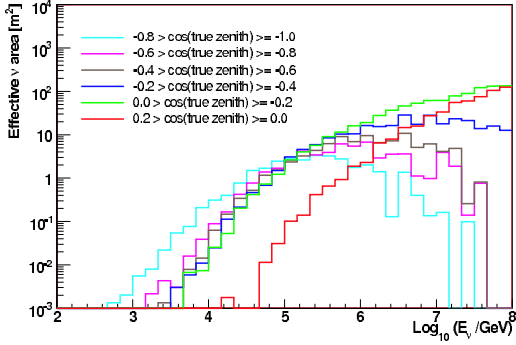
Figure 2: Effective area after final background-rejection. The curve for $\cos(\text{zenith}) > 0$ shows an increased energy threshold because of the cut on average hit distance.

Figure 3: N_{ch} distribution in IC9 after background atmospheric muon rejection. The IC9 cuts raise the energy threshold relative to AMANDA-II, leading to a lower atmospheric neutrino rate compared to Figure 1. The signal curve corresponds to a test flux of $1\times10^{-6}\text{E}^{-2}$ GeV cm^{-2} s^{-1} sr^{-1}.

muons from two independent atmospheric showers are detected during the same trigger window. For atmospheric neutrinos, 1.6×10^7 ν_μ events were generated and re-weighted with the Bartol flux [7].

Atmospheric muons can enter the sample when they are mis-reconstructed as upgoing or when they arrive from near the horizon. One of the most effective parameters for rejecting mis-reconstructed events is the number of direct hits (N_{dir}). These are hits close to the reconstructed track so they are assumed to result mostly from unscattered Cherenkov photons. The AMANDA-II analysis selected well-reconstructed tracks based on an N_{dir} cut and the distribution of hits along the length of the track. With its larger string spacing, the IC9 analysis uses a relaxed N_{dir} cut complemented by new requirements on the calculated precision of the zenith angle reconstruction and the number of strings hit. Besides rejecting mis-reconstructed muons, these cuts lead to the energy threshold behavior visible in Figure 2. Therefore lower energy atmospheric muons as well as atmospheric neutrinos are further suppressed.

Preserving signal events near the horizon is important because the effective area for high energy ν_μ is greatest there (Figure 2). This enhancement is strengthened in IC9 by the large height to width ratio. However, atmospheric muon tracks at these zenith angles are generally well-reconstructed and often survive the other cuts. Therefore another energy-related parameter was introduced, namely

the average perpendicular distance between all hit DOMs and the reconstructed track. The higher light yield for energetic tracks means light can reach far away DOMs, so a cut on the average hit distance distinguishes strongly against the lower energy atmospheric muon events. This cut is applied only for events above the horizon.

Sensitivity

After the atmospheric muon rejection cuts, simulated events are dominated by atmospheric and extra-terrestrial neutrinos. Figure 3 shows the N_{ch} distribution for these events. The best N_{ch} cut was determined to be 60 for IC9 (137 days) by optimizing the Model Rejection Factor [6]. Assuming no extra-terrestrial signal, the expected upper limit was calculated using the Feldman-Cousins method [9], giving a sensitivity of 1.4×10^{-7}GeV cm^{-2} s^{-1} sr^{-1}. Figure 4 shows the IC9 sensitivity in relation to sources with an E^{-2} energy spectrum and the AMANDA-II search. The IC9 sensitivity is only a factor 2 above AMANDA-II 4-year, despite its much lower integrated livetime. Further improvements may be expected, both from longer term operation of the full IceCube detector and refinements of the analysis such as new energy reconstruction methods.
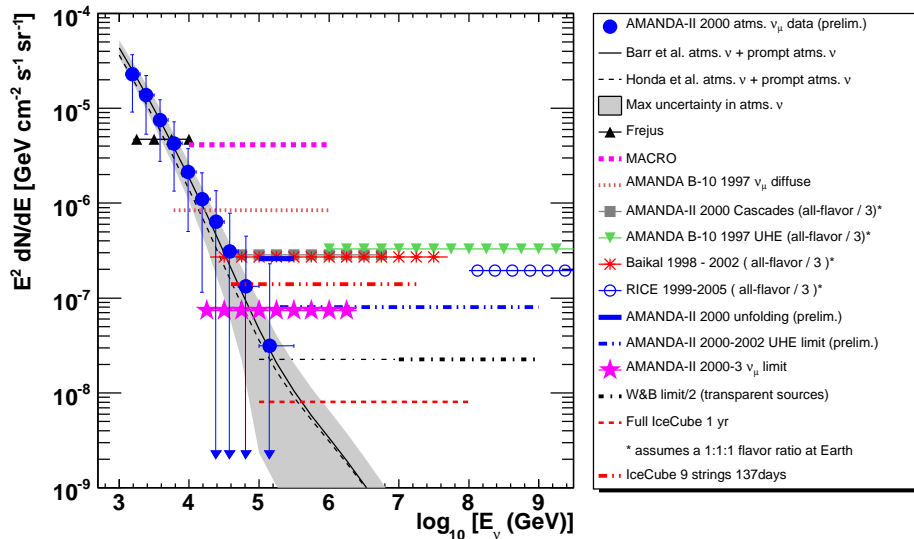
Figure 4: Upper limit on the ν_μ flux from sources with an E^{-2} energy spectrum for the 2000–2003 AMANDA-II data, and expected sensitivity of IC9 for 137 days.

Conclusion

The AMANDA-II data collected during the period 2000–2003 have been analysed in a search for a diffuse flux of high-energy extra-terrestrial muon neutrinos. With no excess of events seen, an upper limit of $E_\nu^2 \times dN_\nu/dE_\nu < 7.4 \times 10^{-8}$ GeV cm^{-2} s^{-1} sr^{-1} was obtained. The sensitivity of 9 IceCube strings for 137 days livetime was studied with simulated data, making use of new cuts to improve acceptance near the horizon. The expected sensitivity is 1.4×10^{-7} GeV cm^{-2} s^{-1} sr^{-1}. This analysis is ongoing and will be unblinded in the near future.

Acknowledgements

References

[1] E. Waxman and J. Bahcall, *Phys. Rev.* D **59**, 023002 (1998).

[2] K. Mannheim, R.J. Protheroe, and J.P. Rachen, *Phys. Rev.* D **63**, 023003 (2000).

[3] J. Ahrens et al. *Phys. Rev.* D **66**, 012005 (2002)

[4] A. Achterberg et al., *Phys. Rev.* D, submitted, arXiv:0705.1315 (2007).

[5] K. Münich for the IceCube Collaboration, these proceedings

[6] G.C. Hill and K. Rawlins, *Astropart. Phys.* **19**, 393 (2003).

[7] G.D. Barr, T.K. Gaisser, P. Lipari, S. Robbins, and T. Stanev, *Phys. Rev.* D **70**, 023006 (2004).

[8] M. Honda, T. Kajita, K. Kasahara, and S. Midorikawa, *Phys. Rev.* D **70**, 043008 (2004).

[9] Cousins R D and Highland V L 1992 *Nucl. Ins. Meth. Phys. Res.* **A320** 331, Feldman G and Cousins R 1998 *Phys. Rev.* D **57** 3873, Conrad J, Botner O, Hallgren A and de los Heros C 2003 *Phys. Rev.* D **67** 012002, Hill G C 2003 *Phys. Rev.* D 118101

Measurement of the atmospheric lepton energy spectra with AMANDA-II

K. MÜNICH[1], J. LÜNEMANN[1] FOR THE ICECUBE COLLABORATION
[1] *Inst. of Physics, University of Dortmund, Dortmund, Germany*
kirsten.muenich@udo.edu

Abstract: Extragalactic objects such as active galactic nuclei (AGN) and gamma-ray bursts (GRB) are potential sources for the ultra-high energy cosmic ray flux. Assuming hadronic processes in these sources, a diffuse neutrino flux might be produced together with the charged cosmic ray component. To measure this diffuse extraterrestrial neutrino flux is one of the main goals of the Antarctic Muon and Neutrino Detector Array (AMANDA-II). The neutrino spectrum, based on a four year data set (2000-2003), is presented. The spectrum agrees with the atmospheric neutrino flux predictions. Upper limits to isotropic extraterrestrial contributions are derived.

Introduction

The search for extraterrestrial neutrino sources is the driving force behind the construction of large neutrino telescopes. Though all three neutrino species should arrive at Earth in equal number, muons from muon neutrinos have a distinct signature in the detector (a long path emitting Cherenkov light) that makes them a desirable focus for this analysis. The drawback of this signature is the existence of a large background of atmospheric muons entering the detector from the upper hemisphere. Atmospheric muons are suppressed by selecting only upgoing events as potential signal candidates. Muons from neutrinos produced in the atmosphere dominate even in this sample.

The search for extraterrestrial muon neutrinos within the data sample can be performed by multiple approaches, for instance by selecting local coincidences with proposed steady neutrino sources (AGN) or local and temporal coincidences with GRBs. Since the energy spectrum of extraterrestrial neutrinos is expected to be significantly harder than the atmospheric neutrino spectrum, another approach relies directly on the reduction of the atmospheric neutrino background by energy selection [2]. The analysis described here is based on the reconstruction of the energy spectrum of atmospheric muon neutrinos. Data taken with the AMANDA-II detector between 2000 and 2003

provide 2972 upgoing muons with a lifetime of 807 days. The criteria used for the selection of events are described in [3]. In addition a zenith angle veto at 10 degrees below the horizon is applied.

Unfolding of the energy spectrum

In this analysis, the problem of determining the energy spectrum from the observed detector response is solved by applying a regularized unfolding method. The underlying Fredholm integral equation of first kind is reduced to a matrix equation system. The kernel is determined with Monte Carlo methods. Statistically insignificant contributions to the kernel are suppressed by regularization [4, 5]. The observables used must be correlated to the neutrino energy. In total, eight observables are found to satisfy these conditions. Because the unfolding algorithm used for this calculation, RUN [4], allows only three input variables, six observables are combined into one energy-sensitive variable by a neural network application [5, 6]. In Figure 1, the Gaussian response of this variable to mono-energetic muons from the simulation is shown. The unfolded neutrino energy spectrum is compared to the flux expectations from [7, 1] in Figure 2. The error bars in the plot comprise both statistical and systematic uncertainties. The theoretical uncertainty of the atmospheric neutrino flux contributes with 25% to the total systematic error
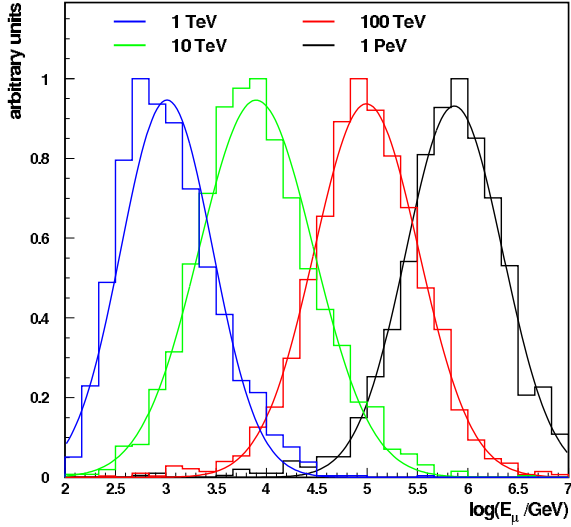
Figure 1: Neural network output for simulated mono-energetic muons fitted with Gaussian distributions.

of 30%. For a detailed error discussion see [6]. Good agreement is observed when the unfolded four-year neutrino spectrum is compared to the unfolded data from 2000 analysed in [5, 6] (Figure 3).

Figure 2: Comparison of the unfolded energy spectrum with flux expectations according to Ref.[7, 8]. The shaded bands show the range between the horizontal (upper border) and vertical flux (lower border).

Upper limits to additional contributions to the neutrino flux

Two properties of the unfolded spectrum in Figure 2 should be noted. First, the variable binning with a width of about half of the resolution was optimized by Monte Carlo to obtain the best sensitivity to an E^{-2} contribution of extraterrestrial neutrinos. The bins are statistically correlated to each other. This is taken into account in the error calculation. However, it is not obvious which kind of probability density function (pdf) the flux errors obey and how upper limits to additional contributions to the atmospheric neutrino flux have to be derived. Therefore, a confidence belt construction [8] has been applied to the unfolding problem. The second remark concerns the 2000-2003 data quality. During this period, small changes in the detector properties, such as the photomultiplier high voltage, resulted in different detector response in the observables used in this analysis. Since only the logarithm of these variables enters

Figure 3: Comparison of the unfolded energy spectrum for 2000 and 2000-2003.
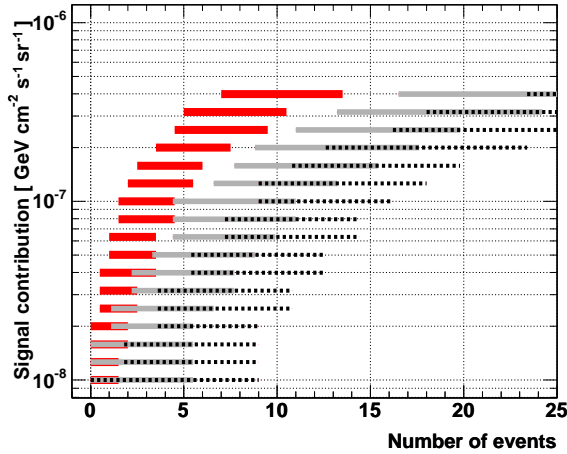
Figure 4: The unified approach of Feldman and Cousins has been applied to the unfolding problem by calculating individual probability density functions. 90% Feldman-Cousins confidence belts of three unfolding energy bins: 50 to 100 TeV (black dotted), 100 to 300 TeV (gray) and 300 TeV to 1 PeV (red) are displayed.

the unfolding procedure, these systematic effects concern only the low energy portion of the spectrum ($E < 2$ TeV).

Assuming a diffuse signal energy spectrum with an energy dependence of E^{-2}, the unfolded response for 17 different signal contributions between 10^{-8} GeV cm^{-2} s^{-1} sr^{-1} and $4 \cdot 10^{-7}$ GeV cm^{-2} s^{-1} sr^{-1} has been calculated. For each signal contribution, the complete Monte Carlo and analysis chain has been applied. Finally, 1,000 Monte Carlo experiments each containing the equivalent of four years of AMANDA-II data have been used for each of the 17 signal contributions. The energy distributions of all 17,000 Monte Carlo experiments have been reconstructed. After applying an energy cut, the statistical weights, which corresponds to the weighted number of events, for a fixed signal distribution are summed, histogrammed and normalized to get the individual pdf. Using the pdfs for each signal contribution the Feldman-Cousins approach is applied. The resulting confidence belts are shown in Figure 4. The upper limit is obtained from the confidence belt by reading off the flux value that corresponds to the statistical weight of the unfolded data (Figure 5).
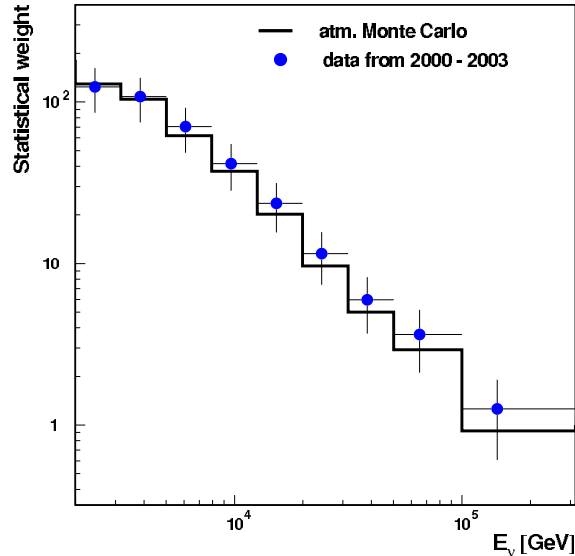
Figure 5: Statistical weight of the unfolded data.

The statistical weight between 300 TeV and 1 PeV is 0.005. The error bars can be used to calculate an upper limit. Assuming normal distribution for the pdfs, the 90% upper limit on the sum of atmospheric plus extraterrestrial flux is given by 1.28 times the standard deviation. By subtracting the atmospheric portion (gained by fitting the Volkova prediction [9] to the unfolded spectrum) from the total upper limit, an upper limit on the extraterrestrial contribution can be calculated, see [5]. In Figure 6 the unfolded neutrino spectrum (blue circles) for data from 2000-2003 as well as the resulting upper limits are shown. The upper limits obtained by the Feldman-Cousins procedure (blue lines) are compared to those upper limits (pink lines) obtained by using the normal distributed pdf and the atmospheric fit. Since the upper limits obtained from the two different methods are in agreement, this is a good indication that the statistic errors in the procedure have been treated properly. The upper limits derived by calculating the individual pdfs in combination with the Feldman-Cousins approach deliver slightly more restrictive bounds. The resulting limits are compared with different flux models (see Figure 6). MPR-max represents the maximum neutrino flux from blazars in photohadronic interactions. An upper bound on the flux from AGN was estimated in [10], which is indi-
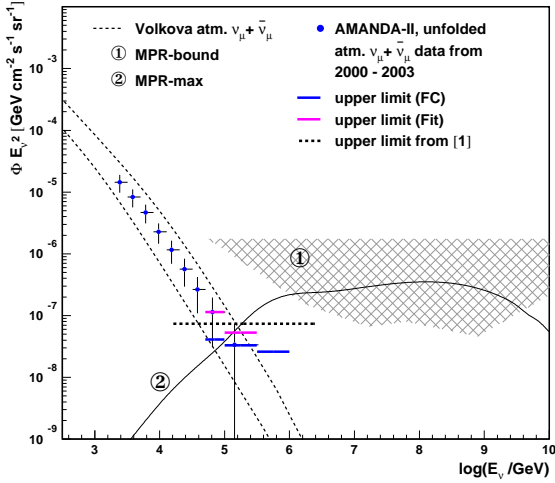
Figure 6: Reconstructed neutrino spectrum and resulting upper limits (blue and pink lines) for data from 2000-2003. The results are compared with different flux models [10] and the result from [2]. For the FC upper limit we added a bin from 300 TeV to 1 PeV which is not shown in Figures 2, 3 and 5 as only 0.005 events were observed in this range and the corresponding flux value is out of the displayed flux range.

cated in the figure as shaded region (MPR-bound). The upper border of that region represents the limit for sources that are optically thick to $n\gamma$ interactions, $\tau_{n\gamma} \gg 1$. The bound for optically thin sources ($\tau_{n\gamma} < 1$) is given by the lower bound of the shaded region.

Conclusion

The energy spectrum of atmospheric muon neutrinos has been reconstructed with a regularized unfolding method in the energy range between 1 TeV and 300 TeV. In this energy range, no flattening of the spectrum is observed, as would be expected if a significant extraterrestrial neutrino contribution was presented. Upper limits to additional contributions of $\phi \cdot E^2 = 4.1 \cdot 10^{-8}\,\mathrm{GeV\,cm^{-2}\,s^{-1}\,sr^{-1}}$ to the energy bin between 50 TeV and 100 TeV, $\phi \cdot E^2 = 3.3 \cdot 10^{-8}\,\mathrm{GeV\,cm^{-2}\,s^{-1}\,sr^{-1}}$ between 100 TeV and 300 TeV and $\phi \cdot E^2 = 2.6 \cdot 10^{-8}\,\mathrm{GeV\,cm^{-2}\,s^{-1}\,sr^{-1}}$ be-

tween 300 TeV and 1 PeV are obtained. This is presently the most restrictive upper limit in this energy range and at the given energies well below the theoretical upper bound by Mannheim et al. [10]. This upper limit restricts the parameter range of the source models for AGN classes with flat luminosity distributions (FRII) [11]. A comparison of these upper limits to the upper limits obtained with independent methods in AMANDA-II [2] shows good agreement. All results shown here are preliminary.

Acknowledgements

References

[1] G. D. Barr *et al.* *Physical Review D*, 70(2):023006, 2004.

[2] A. Achterberg *et al.* 2007. arXiv:0705.1315.

[3] A. Achterberg *et al. accepted by Physical Review D*, 2007. astro-ph/0611063.

[4] V. Blobel. In *Proc. of the 1984 CERN School of Computing*, CERN 85-09, page 88, 1985.

[5] K. Münich. PhD thesis, Universität Dortmund, 2007.

[6] K. Münich for the IceCube Collaboration. In *Proc. of the 29. ICRC, Pune, India*, 2005. astro-ph/0509330.

[7] M. Honda *et al.* *Physical Review D*, 70(4):043008, 2004.

[8] G. J. Feldman and R. D. Cousins. *Physical Review D*, 57:3873, 1998.

[9] L. V. Volkova. *Soviet Journal of Nuclear Physics*, 31:784–790, 1980.

[10] K. Mannheim *et al.* *Physical Review D*, 63:23003, 2001.

[11] J. K. Becker *et al. accepted by Astroparticle Physics*, 2007. astro-ph/0607427.

Multi-year Search for UHE Diffuse Neutrino Flux with AMANDA-II

L. GERHARDT[1] FOR THE ICECUBE COLLABORATION[2]

[1] *University of California, Irvine, Irvine, CA, USA*

[2] *See special section of these proceedings*

gerhardt@hep.ps.uci.edu

Abstract: AMANDA-II is a high volume neutrino telescope designed to search for astrophysical neutrinos. Data from 2000 - 2002 has been searched for a diffuse flux of ultra-high energy (UHE) neutrinos with energies in excess of 10^5 GeV. Due to absorption of UHE neutrinos in the earth, the UHE signal is concentrated at the horizon and has to be separated from the background of large muon-bundles induced by cosmic ray air showers. No statistically significant excess above the expected background is seen in the data, and a preliminary upper limit is set on the diffuse all-flavor neutrino flux of $E^2 \Phi_{90\%\text{CL}} < 2.4 \times 10^{-7}$ GeV cm^{-2} s^{-1} sr^{-1} valid over the energy range of 2×10^5 GeV to 10^9 GeV. A number of models which predict neutrino fluxes from active galactic nuclei are preliminarily excluded at the 90% confidence level.

Introduction

AMANDA-II is a large volume neutrino telescope with the capability to search for neutrinos from astrophysical sources [2]. In a previous publication [3] it was shown that AMANDA-II is able to search for UHE neutrinos (neutrinos with energy greater than 10^5 GeV). UHE neutrinos are of interest because they are associated with the potential acceleration of hadrons by AGNs [4, 5], are produced by the interactions of exotic phenomena such as topological defects [6] or Z-bursts [7], and are guaranteed by-products of the interaction of high energy cosmic rays with the cosmic microwave background [8, 9].

Above 10^7 GeV the Earth is essentially opaque to neutrinos [10]. This, combined with the limited overburden above AMANDA-II (approximately 1.5 km, for a description of the AMANDA-II detector see [2]), means that UHE neutrinos will be concentrated at the horizon. The background for this analysis consists of bundles of down-going, high-energy muons from atmospheric cosmic ray showers. The muons from these bundles can spread over cross-sectional areas as large as 200 m^2.

Experimental and Simulated Data

This analysis used AMANDA-II data collected between February 2000 and November 2002, with an integrated lifetime of 571 days after offline re-triggering and correcting for dead time and periods where the detector was unstable. Of this data 20% from each year was used to develop selection criteria, while the rest, with a lifetime of 456.8 days, was set aside for the final analysis. Cosmic ray air shower background events were generated using CORSIKA [1]. The UHE neutrinos were generated with energies between 10^3 GeV and 10^{12} GeV using ANIS [11]. For more details on AMANDA simulation procedures see [2, 3].

Method

This analysis exploits the differences in light deposition from the background of bundles of many low energy muons and single UHE muons or cascades from UHE neutrinos. A muon bundle with the same total energy as a UHE neutrino spreads its light over a larger volume, leading to a lower light density in the array. Both types of events have a large number of hits, but for the same number of hit optical modules (OMs), the muon bundle

has a lower total number of hits (each OM may have multiple, separate hits in one event). Background muon bundles also have a higher fraction of OMs with a single hit, while the UHE neutrino generates more multiple hits. In addition to selecting on variables which correlate with energy, selecting on the reconstructed direction of the lepton track separates the primarily horizontal UHE neutrinos from down-going muon bundles (Fig. 1). Reconstruction algorithms optimized for cascade
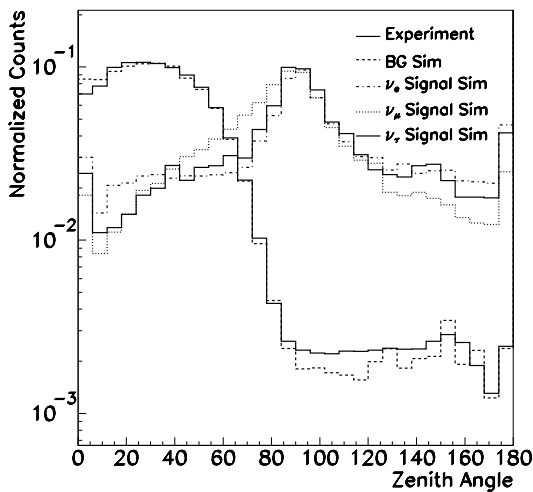
Figure 1: Reconstructed zenith angle for the experiment, background muon bundle and E^{-2} electron, muon, and tau neutrino signal simulations. The majority of signal events are expected at the horizon, while the background is primarily downgoing.

light deposition [2] are also used to select UHE neutrinos with an energy deposit from stochastic process (i.e. bremsstrahlung or e^+/e^- pair creation) many orders of magnitude brighter than the depositions from background muon bundles.

Systematic and Statistical Uncertainties

The sensitivity of AMANDA-II is determined from simulation. The dominant sources of uncertainty in this calculation are listed below.

Normalization of Cosmic Ray Flux: The average energy of simulated cosmic ray pri-

maries at the penultimate selection level is 4.4×10^7 GeV. Estimates of the error in the normalization of the cosmic ray flux range from 20% [12] to a factor of two [13]. This analysis uses the more conservative uncertainty of a factor of two.

Cosmic Ray Composition: There is considerable uncertainty in the cosmic ray composition above the knee [13]. The difference between background passing rates at the penultimate selection level for iron- and proton-dominated spectra is 30%; this is taken as the uncertainty due to cosmic ray composition.

Detector Sensitivity The optical properties of the refrozen ice around each OM, the absolute sensitivity of individual OMs, and obscuration of OMs by nearby power cables can effect the detector sensitivity. Variations of these parameters can cause a 15% variation in the background and E^{-2} signal passing rate.

Neutrino Cross Section: The uncertainty in the standard model neutrino cross section is as large as a factor of two at high energies depending on the model assumed for the proton structure [14]. This causes a maximum variation in number of expected signal events for an E^{-2} spectrum of 8%.

Statistical: Due to the very demanding computational requirements, background simulation statistics are somewhat limited. A statistical error of 1σ for a Poissonian distribution with $\mu = 0$ is assumed for each year at the final selection level. The signal simulation has an average statistical error of 5% for each neutrino flavor.

Summing the systematic errors of the signal simulation in quadrature gives a systematic uncertainty of 17%. Combining this with the statistical uncertainty of 5% per neutrino flavor gives a total uncertainty of 18%. Following a similar method for the background simulation, the systematic uncertainty is 105%, and the maximum background expectation is fewer than 2.1 events for three years. These uncertainties are included in the final limit using a method outlined in [15].

eliminated at the 90% confidence level (see Table 1).
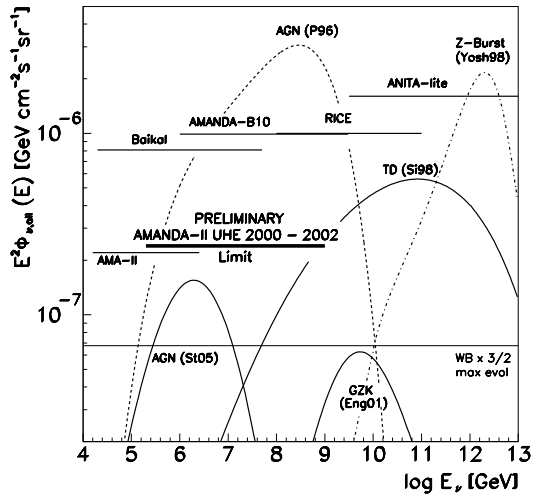
Figure 2: Preliminary all-flavor neutrino flux limit and sensitivity for 2000 - 2002 over the range which contains 90% of the expected signal with an E^{-2} spectrum. Also shown are several representative models: St05 from [5], P96 from [4], Eng01 from [8], Si98 from [6], Yosh98 from [7] and the Waxman-Bahcall upper bound [16]. Existing experimental limits shown are from RICE [17], ANITA-lite [18], Baikal [19], AMANDA-B10 [3] and AMANDA-II lower energy diffuse search [20].

Figure 3: Angle-averaged neutrino effective area for 2000 - 2002 after application of all selection criteria. The peak at $\sim 10^7$ GeV in the ν_e effective area is due to the Glashow resonance.

Results

The effective area after applying all selection criteria is shown in Fig. 3. After applying all selection criteria two events were found in the 456.8 days of data between 2000 - 2002. The background expectation for the same time period is fewer than 2.1 events, after including simulation uncertainties. This yields a 90% confidence level average event upper limit [21] of 4.74 and a preliminary upper limit on the all-flavor neutrino flux of

$$E^2\Phi_{90\%\text{CL}} \leq 2.4 \times 10^{-7}\text{GeV cm}^{-2}\text{ s}^{-1}\text{ sr}^{-1}$$
(10)

with 90% of the E^{-2} signal found between the energies of 2×10^5 GeV and 10^9 GeV. This is the most stringent limit at these energy ranges to date (Fig. 2). A number of neutrino flux predictions are

Future Prospects

AMANDA-II hardware upgrades which were completed in 2003 should lead to an improvement of the sensitivity at ultra-high energies [22]. AMANDA-II is now surrounded by the next-generation IceCube detector which is currently under construction. The sensitivity to UHE neutrinos will further increase as the IceCube detector approaches its final size of 1 km^3 [23].

Acknowledgements

Table 1: Flux models, the number of neutrinos of all flavors expected at the Earth at the final selection level and the preliminary MRFs for 456.8 days of livetime. A MRF of less than one indicates that the model is excluded with 90% confidence.

Model	ν_{all}	MRF
AGN [4]	20.6	0.23
AGN [24]	17.4	0.27
AGN [25]	8.8	0.54
AGN [26]	5.9	0.80
AGN RL B [27]	4.5	1.05
Z-Burst [28]	2.0	2.37
AGN [5]	1.8	2.63
GZK ν norm AGASA [29]	1.8	2.63
GZK ν mono-energetic [9]	1.2	3.95
GZK ν a=2 [9]	1.1	4.31
GZK ν norm HiRes [29]	1.0	4.74
TD [6]	0.9	5.27
AGN RL A [27]	0.3	15.8
Z-Burst [7]	0.1	57.4
GZK ν [8]	0.06	79.0

References

[1] D. Heck. (DESY-PROC-1999-01):227, 1999.

[2] M. Ackermann et al. *Astroparticle Physics*, 22:127–138, 2004.

[3] M. Ackermann et al. *Astroparticle Physics*, 22:339–353, 2005.

[4] R. Protheroe. (astro-ph/9607165), 1996.

[5] F. Stecker. *Physics Review D*, 72:107301, 2005.

[6] G. Sigl, S. Lee, P. Bhattacharjee, and S. Yoshida. *Physics Review D*, 59:043504, 1998.

[7] S. Yoshida, G. Sigl, and Lee S. *Physics Review Letters*, 81:5505–5508, 1998.

[8] R. Engel, D. Secker, and T. Stanev. *Physics Review D*, 64:093010, 2001.

[9] O. Kalashev, V. Kuzmin, D. Semikoz, and G. Sigl. *Physical Review D*, 66:063004, 2002.

[10] J. Klein and A. Mann. *Astroparticle Physics*, 10:321–329, 1999.

[11] M. Kowalski and A. Gazizov. *Computer Physics Communications*, 171:203–213, 2005.

[12] J. Hörandel. *Astroparticle Physics*, 19:193–230, 2003.

[13] Particle Data Group. *Physics Letters B*, 592:186–234, 2004.

[14] R. Gandhi, C. Quigg, M. Reno, and I. Sarcevic. *Astroparticle Physics*, 5:81–110, 1996.

[15] F. Tegenfeldt and J. Conrad. *Nuclear Instruments and Methods in Physics Research A*, 539:407–413, 2005.

[16] J. Bahcall and E. Waxman. *Physics Review D*, 59:023002, 1998.

[17] I. Kravchenko et al. *Physics Review D*, 73:082002, 2006.

[18] S. Barwick et al. *Physics Review Letters*, 96:171101, 2006.

[19] V. Aynutdinov et al. *Astroparticle Physics*, 25:140–150, 2006.

[20] A. Achterberg et al. *submitted to Physics Review D*, 2007.

[21] G. Feldman and F. Cousins. *Physical Review D*, 57:3873, 1998.

[22] A. Silvestri. *Proceedings 29th International Cosmic Ray Conference, Pune, India*, pages 431–434, 2005.

[23] J. Ahrens et al. *Astroparticle Physics*, 20:507, 2004.

[24] F. Stecker, C. Done, M. Salamon, and P. Sommers. *Physics Review Letters*, 69:2738, 1991.

[25] F. Halzen and E. Zas. *The Astrophysical Journal*, 488:669–674, 1997.

[26] K. Mannheim, R. Protheroe, and J. Rachen. *Physical Review D*, 63:023003, 2000.

[27] K. Mannheim. *Astroparticle Physics*, 3:295–302, 1995.

[28] O. Kalashev, V. Kuzmin, D. Semikoz, and G. Sigl. *Physical Review D*, 65:103003, 2002.

[29] M. Ahlers et al. *Physics Review D*, 72:023001, 2005.

Likelihood deconvolution of diffuse prompt and extra-terrestrial neutrino fluxes in the AMANDA-II detector

GARY C. HILL FOR THE ICECUBE COLLABORATION
Department of Physics, University of Wisconsin, Madison, WI 53706, U.S.A.
ghill@icecube.wisc.edu

Abstract: The AMANDA-II detector at the South Pole station, Antarctica, has been used in several searches for a flux of extra-terrestrial neutrinos from the sum of all sources in the universe. These searches are complicated by uncertainties in the expected fluxes of background neutrinos, both those from cosmic-ray pion and kaon meson production (conventional atmospheric neutrinos) and those from charm-containing mesons (prompt atmospheric neutrinos). In this work, we explore the use of a full likelihood analysis on flux sensitive distributions in order to account for the uncertainties and place simultaneous constraints on the fluxes of interest. The method is illustrated using simulated data sets, with application to the real AMANDA-II data to come.

Introduction

The search for an extra-terrestrial diffuse flux is one of the most challenging tasks of a neutrino detector. In contrast to a point source search, where backgrounds are measured from off-source data, a diffuse search requires a good understanding and prediction of the expected backgrounds. In the case of a diffuse neutrino search, the backgrounds are atmospheric neutrinos. There are two components to this flux, one thought to be well understood, and another less certain. The conventional atmospheric neutrinos[1, 2] are due to decay of pions and kaons produced by cosmic radiation interacting with the earth's atmosphere. Prompt atmospheric neutrinos[3, 4, 5, 6, 7], from the production and decay of mesons containing charm quarks, have never been identified and predictions of this flux span orders of magnitude. The prompt component should follow the spectral index of the primary cosmic rays, whilst the conventional component has a spectrum about one power steeper. The expected flux of extra-terrestrial neutrinos from, for example, the sum of all active galaxies in the universe, is expected to have a harder spectrum ($\sim E^{-2}$) than either of the atmospheric neutrino components. The low expected event rates and similarity of the spectra of prompt and extra-terrestrial

neutrinos will make their independent identification difficult[8]. The AMANDA-II detector data from the years 2000-03 have been searched for prompt and extra-terrestrial components[13, 14]. Spectral differences in the neutrino fluxes would manifest themselves in different expected energy distributions of detected events in the AMANDA-II neutrino detector. The number of optical modules (N_{ch}) registering at least one photon was used as an energy estimator. A diffuse extra-terrestrial signal would appear as an excess of events at higher values of the N_{ch} parameter. In order not to bias the analysis, a blind analysis, and a simulation based unbiased optimum limit setting technique were used to choose the best cut appropriate for each signal spectrum. The atmospheric neutrino background simulation was normalised to observed data below the cut in order to constrain some of the uncertainties. The prompt neutrinos were treated in two ways, firstly, they were included as a background for the extra-terrestrial searches, and secondly, they were treated as an unknown signal, to be constrained by the observed data. The final limit on an E^{-2} flux was set at a level of $E_\nu^2 \times dN_\nu/dE_\nu = 7.4 \times 10^{-8}$ GeV cm^{-2} s^{-1} sr^{-1}, valid over an energy range 16-2500 TeV. This is the best limit to date on extra-terrestrial neutrino fluxes. Despite this success, the

cut and count method does suffer from some drawbacks. Primarily, the shape of the N_{ch} distribution is not used in the analysis, only the integrated number of events above the cut value. A likelihood analysis can be used to take advantage of the full shape of the N_{ch} distribution. In addition, such an analysis can simultaneously constrain all the parameters, both those of direct interest (the numbers of prompt and extraterrestrial neutrinos) and those of indirect interest - known as "nuisance parameters" (normalisation and shape of the conventional atmospheric neutrinos). Another key point is that if an entire distribution is used in a likelihood analysis, then there is no need to optimise a selection cut on that parameter, removing discussion of what is the optimal cut criterion. These likelihood methods with nuisance parameters are standard for neutrino oscillation analyses[9], and for "unbinned" astrophysical point source searches[10, 11, 12].

Methodology

The likelihood function in this analysis is the product over a binned version of the N_{ch} distribution of the bin-by-bin Poisson probabilities of events observed given events expected.

$$P(\{n_i\} \mid \{\mu_i\}) = \Pi_i \frac{(\mu_i)^{n_i}}{n_i!} \exp(-\mu_i) + \frac{\Delta\epsilon^2}{\sigma_\epsilon} \tag{11}$$

For each bin, the expectation μ_i is the sum of conventional and prompt atmospheric neutrinos, and extra-terrestrial neutrinos

$$\mu_i = \epsilon(A_c \mu_{ci}(\Delta\gamma) + A_p \mu_{pi} + A_e \mu_{ei}) \tag{12}$$

where subscripts c, p and e stand for conventional, prompt and extra-terrestrial neutrino fluxes respectively. As an example, the term $A_e \mu_{ei}$ is the number of events expected in bin i after convolving an extra-terrestrial flux, normalised to a total of A_e events, with the effective area of the detector (which includes absorption effects in the earth). The parameter $\Delta\gamma$ of the conventional atmospheric flux allows for changes in the spectral shape relative to the prediction. Full calculations[1, 2] of the angular and spectral dependence of the flux have been made, here we allow for deviations away from the exact form $\Phi_0(E, \theta)$ by using $\Phi(E, \theta) =$ $\Phi_0(E, \theta)E^{\Delta\gamma}$. Since the spectrum only approximately follows a power-law (and this varies with angle) we choose to fit for deviations away from the actual spectrum, rather than fit for a simple power law γ. Fitting for $\Delta\gamma$ would allow statements to made such as "the data favour a similar/harder/steeper spectral form than that calculated theoretically," rather than simply fitting for a single value of γ. The parameter ϵ is an efficiency term reflecting uncertainties in the effective area of the detector. While this is strictly energy- and thus bin-dependent, with strong bin-to-bin correlations, here we simplify to a constant form for this initial illustration of the method. Epsilon is constrained to a Gaussian form with width σ_ϵ by the penalty term in the likelihood function, with $\Delta\epsilon$ being the difference between the tested value of the efficiency, ϵ, and the notional best fit value for the efficiency, $\epsilon_0 = 1$. To test a given hypothesis, e.g. that $A_p = 20.0$ and $A_e = 10.0$, the likelihood is maximised, fixing A_p and A_e to the desired values and allowing ϵ, A_c and $\Delta\gamma$ to float. This likelihood, denoted $\mathcal{L}$, is then compared to the likelihood $\hat{\mathcal{L}}$ where all parameters are free to float in the fit. The tested hypothesis is then rejected at a confidence level set by the probability of observing a greater likelihood ratio, given the truth of the null hypothesis A_p and A_e, than the specific one that was observed. The distribution of the likelihood ratio statistic under the null hypothesis is known approximately from Wilks' theorem. Asymptotically, the likelihood ratio defined by $-2\log\mathcal{L}/\hat{\mathcal{L}}$ follows a chi-square distribution with degrees of freedom equal to the number of fixed parameters in the $\mathcal{L}$ fit. The confidence level at which the hypothesis is then rejected is found from checking the ratio $-2\log\mathcal{L}/\hat{\mathcal{L}}$ against the appropriate chi-square value (e.g. a 90% c.l. corresponds to a chi-square of 4.6 for two degrees of freedom). In order to compute the exact confidence level for each null hypothesis, the likelihood ratio may be compared to its expected distribution, generated from many random event distributions drawn from the null hypothesis[15]. In this paper, we use the chi-square approximation for simplicity, leaving the full interval constuction for final analysis.

Having written down the form of the likelihood function, the details of the components must be determined. Here, we take the shape of the con-

ventional atmospheric neutrino detector response, $\mu_c(\Delta\gamma)$ as the convolution of the Bartol flux[1], with the detector effective area, multiplied by the factor $E^{\Delta\gamma}$. There are two primary sources of uncertainty in the prediction of the atmospheric neutrino flux - the cosmic ray primary spectrum and the interaction model. Together, these manifest themselves as overall uncertainties in the normalisation (fitted by A_c), and as an increasing uncertainty in the flux as a function of energy (see figure 12 of [13]). This energy dependent uncertainty can be approximately parameterised as a change of slope in the neutrino spectrum. The prompt flux is the "Charm D" model[7], an older prediction, but with a spectral shape similar to more recent preditions. The extra-terrestrial flux follows an E^{-2} power law. The value of the effective area uncertainty, σ_ϵ, is taken as 10%, effectively bounding (95% region) it to extrema of plus/minus 20%.

Example fitting of a test data set

To demonstrate the power of the likelihood method, we derive a random test data set by sampling 450 events from the Bartol N_{ch} distribution. These event are then treated as though they are the real data set. Figure 1 shows the result of the fitting procedure, where the data set is best fit by 446.5 atmospheric neutrinos and 3.6 extra-terrestrial neutrinos. The normalisation and $\Delta\gamma$ of the atmospheric neutrinos, and the effective area parameter ϵ, were allowed to float during this fit. The potential to constrain the atmospheric neutrino parameters is shown in figure 2, where an acceptance region was found while allowing the effective area uncertainty to float. The size of this experimentally determined allowed region is similar to the theoretical uncertainties of flux. This simple N_{ch} fitting procedure is not powerful enough to constrain the theory with only AMANDA-II. However, with increased exposure (more AMANDA-II data and the larger IceCube detector) the experimental observations will begin to constrain the theory, allowing for proper measurements of the flux. In figure 3 the allowed regions for prompt and extra-terrestrial fluxes are shown. Since there is only background in the test data set, the allowed region includes the background only corner of the plane. The upper bounds of the allowed regions

define combinations of allowed amounts of the two components. The 90% confidence level count on the extra-terrestrial axis (25 events) corresponds to a flux level of $E_\nu^2 \times dN_\nu/dE_\nu = 1.2 \times 10^{-7}$ GeV cm^{-2} s^{-1} sr^{-1}. Since this result is just for one specific test data set, a meaningful comparison to the standard analysis[13] cannot be made, without determining a sensitivity over many repeated random experiments. It is expected that the likelihood method will lead to an improvement in the sensitivity. The actual predicted level of the CharmD prompt flux corresponds to 8 events in this acceptance region.

Future work

To properly estimate the sensitivity and discovery potential, many test sets, drawn from mixtures of backgrounds and signals must be processed and the acceptance regions combined. This will be done using the median likelihood ratios at each point in the plane. Required signal combinations for definite discovery of either or both of the signal fluxes could also be determined.

The nature of the parameterisations of the fluxes can be further developed and improved. In principle, the atmospheric neutrinos could be parameterised in ways more directly connected to the physics of the cosmic ray fluxes and interaction models, for instance to fit for the charm production cross-sections, and to allow for the charm spectral index to float. Instead of using an E^{-2} extra-terrestrial spectrum, the spectral index of this additional component flux could be a fit parameter. The uncertainties on the detector response could be treated in a proper bin-to-bin correlated manner.

Conclusions

A likelihood ratio fitting method, incorporating nuisance parameters, has been developed for application to a neutrino search with the AMANDA-II detector. This method allows for the simultaneous constraint of background and signal flux parameters. The use of an entire distribution in the analysis removes the need for optimisation of a selection cut, and allows all the available information to be
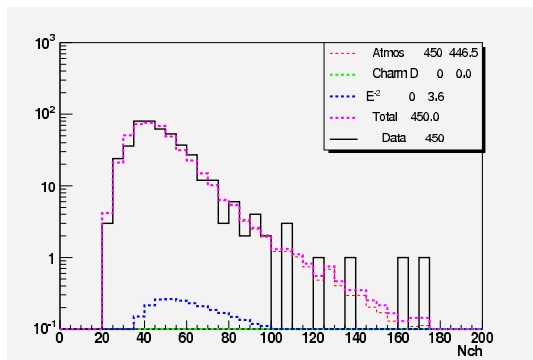
Figure 1: Fitting of a test data set with the likelihood procedure. The data set, drawn from the Bartol atmospheric neutrino distribution, is best fit by a near pure atmospheric neutrino contribution, plus 3.6 extra-terrestrial events. The allowed regions for the additional components are shown in figure 3.

Figure 2: Test data set allowed regions of the atmospheric neutrino total event count, and spectral slope difference $\Delta\gamma$. The confidence level contours correspond to one-sigma, 90%, two and three sigma, moving outward from the best fit point.

incorporated into the confidence interval construction.

References

[1] G.D. Barr, T.K. Gaisser, P. Lipari, S. Robbins, and T. Stanev, Phys. Rev. D **70**, 023006 (2004).

Figure 3: Allowed regions of the prompt and extra-terrestrial neutrino contributions for the test data set, allowing the atmospheric neutrino and detector effective area parameters to float. The 90% confidence level count on the extra-terrestrial axis (25 events) corresponds to a flux level of $E_\nu^2 \times dN_\nu/dE_\nu = 1.2 \times 10^{-7}$ GeV cm^{-2} s^{-1} sr^{-1}.

[2] M. Honda, T. Kajita, K. Kasahara, and S. Midorikawa, Phys. Rev. D **70**, 043008 (2004).

[3] A.D. Martin, M.G. Ryskin, and A.M. Stasto, Acta Phys. Polon. **B34**, 3273 (2003).

[4] G. Fiorentini, A. Naumov, and F.L. Villante, Phys. Lett. B **510**, 173 (2001).

[5] E.V. Bugaev *et al.*, Il Nuovo Cimento **12C**, No. 1, 41 (1989).

[6] C.G.S. Costa, Astropart. Phys. **16**, 193 (2001).

[7] E. Zas, F. Halzen, and R.A. Vázquez, Astropart. Phys. **1**, 297 (1993).

[8] G.C. Hill, Astropart. Phys. **6**, 215 (1997).

[9] see J Kelley, J. Ahrens, these proceedings, for an application to searches for non-standard oscillation physics in atmospheric neutrinos

[10] T. Neunhoffer and L. Koepke, Nucl. Inst. Meth. A **558** 561 (2006)

[11] J. Braun, these proceedings

[12] C. Finley, these proceeding

[13] A. Achterberg, et al, Phys. Rev. D, submitted, arXiv:0705.1315 (2007)

[14] K. Hoshina, J.Hodges, G.C. Hill, these proceedings

[15] G. Feldman and R. Cousins, Phys. Rev. D **57**, 3873 (1998).

Search for Neutrino-Induced Cascades with AMANDA data taken in 2000-2004

O. TARASOVA[a], M. KOWALSKI[b], M. WALTER[a] FOR THE ICECUBE COLLABORATION[c]

[a]*DESY, D-15735, Zeuthen, Germany*
[b]*Institut für Physik, Humboldt Universität zu Berlin, D-12489 Berlin, Germany*
[c]*see special section of these proceedings*
tarasova@ifh.de,marek.kowalski@physik.hu-berlin.de,walter@ifh.de

Abstract: The Antarctic Muon And Neutrino Detector Array (AMANDA) is a Cherenkov detector deployed in the Antarctic ice cap at the South Pole [1]. The charged-current interaction of high-energy electron or tau neutrinos, as well as neutral-current interactions of neutrinos of any flavor, can produce isolated electromagnetic or hadronic cascades. There are several advantages associated with the cascade channel in the search for a "diffuse" flux of astrophysical neutrinos. The energy resolution of AMANDA allows us to distinguish between a hard astrophysical spectrum and a soft atmospheric spectrum. In addition, the flux of atmospheric electron neutrinos is lower by an order of magnitude relative to atmospheric muon neutrinos, while the background from downward-going atmospheric muons can be suppressed due to their track-like topology. The low background in this channel allows us to attain 4π acceptance above energies of $\sim 50\,\mathrm{TeV}$. We present the analysis of AMANDA data collected during 2000-2004. Compared to our previous analysis, this data set is a factor of five larger, resulting in a correspondingly improved sensitivity for the flux of astrophysical neutrinos.

Introduction

There are several theoretical predictions that cosmic neutrinos are produced by accelerated protons within high-energy astrophysical objects such as Active Galactic Nuclei (AGN) and Gamma Ray Bursts (GRB). Neutrinos can propagate in straight lines through the universe as they are not effected by magnetic fields of the galaxy and essentially do not interact with particles on the way to the earth. They are expected to be produced in the source with a ratio $\nu_e : \nu_\mu : \nu_\tau \sim 1 : 2 : 0$ but due to flavor-mixing during propagation a $1 : 1 : 1$ ratio is expected at the detector. However, due to the very small cross-section neutrinos are also difficult to detect. In order to perform a search for galactic and extragalactic neutrinos, the AMANDA telescope was installed in the antarctic ice cap at the geographical South Pole and has been operating since 2000. It consists of 677 optical modules (OM) which are attached to 19 strings and buried at depths from $1500\,\mathrm{m}$ to $2000\,\mathrm{m}$ under the ice surface. Each optical module contains a photomultiplier suited to register Cherenkov light emit-ted by a charged particle which is produced in the neutrino interaction. The signature of a charged-current interaction of ν_e and ν_τ is an electromagnetic and a mainly lower energetic hadronic cascade. Via neutral-current interaction, neutrinos of any flavor can produce isolated hadronic showers. This analysis is focused on a search for neutrinos from unresolved sources (diffuse flux) which have a cascade-like signature in the AMANDA detector. The muon-like events are the main background for this analysis. In the cascade channel the direction of the incoming neutrino is poorly reconstructed, however, the energy resolution of the detector for cascade reconstruction is $\mathcal{O}(\log(\mathrm{E}_\nu)) = 0.18$. By removing track-like events, one can eliminate most of the background from atmospheric muons. In addition, the flux of atmospheric electron neutrinos is much lower than the flux of muon neutrinos.

Experimental data and MC simulation

The experimental data used in this analysis were collected between 2000 and 2004. After exclud-

ing bad and unstable runs from the analysis we end up with a lifetime of 1000.1 days, where in total 8.8×10^9 triggered events were recorded. The main contribution are muons from meson decays in the atmosphere.

The atmospheric muon background was simulated with CORSIKA [2]. To reach large statistics for the high energy part of the background spectrum with acceptable computing time, about 5000 days of downgoing atmospheric muons were generated with energies above 5 TeV. For comparison a smaller sample of standard CORSIKA events was produced.

The cascades were simulated with ANIS [3] generating all three neutrino flavors (ν_e, ν_τ and ν_μ) at energies between 100 GeV and 100 PeV assuming an E^{-1} energy spectrum. The resulting muons were further propagated using MMC (see [4] for details). The signal spectrum was reweighted afterwards to a hypothetical E^{-2} flux of ν_e. Atmospheric ν were simulated by reweighting the same neutrino events to a steeper $\sim E^{-3.7}$ spectrum [5].

Analysis Optimization

The analysis consists of several filter levels including reconstruction of the cascade vertex and energy as well as a few quality cuts to select high quality events. The reconstruction algorithms based on the likelihood minimization method are described in [3, 6]. The vertex resolution of cascade-like events is about 4 m. Quality cuts were performed using the likelihood values L_{vertex} and L_{energy}, given by reconstruction algorithms.

In order to reduce events with a mis-reconstructed vertex, the cut on the vertex likelihood function has been applied, $L_{\text{vertex}} < 7.1$. The cut on the energy likelihood L_{energy} was performed as function of the reconstructed energy. Another energy-dependent cut was applied on the radial distance of the reconstructed vertex position ρ_{xy}. For $E_{\text{reco}} < 1.25$ TeV this cut was set such that only events with the reconstructed vertex position within a 100 m radius from the detector center (fiducial volume of AMANDA) were used in the analysis. Taking into account that the higher energetic events are often reconstructed at distances outside of the detector and the fact that the antici-
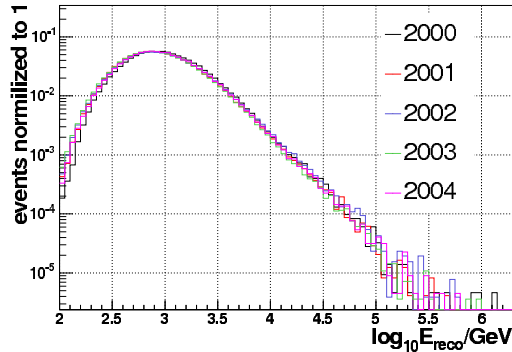
Figure 1: The reconstructed energy distribution of cascade candidate events for the five years (2000-2004) used in this analysis.

pated background is rather small for these energies, we allow an energy dependent increase of the volume above $E_{\text{reco}} > 1.25$ TeV.

By this filter, the set of experimental data is reduced by a factor of 10^5. Fig. 1 shows the reconstructed energy of cascade candidates for the different years. Small variations arise from slightly different hardware configuration for different periods.

At the final filter level, two additional cuts were performed and optimized for the analysis. In addition to a cut on E_{reco} we introduced a discriminating parameter Q_s that involves the following set of three variables:

- vertex likelihood value L_{vertex},

- $\cos(\theta_\mu)$ taken from muon track likelihood reconstruction,

- radial distance, ρ_{xy}^{60}, between the vertex position of two likelihood vertex fits; the second fit is thereby not using hits within a 60 m sphere around the vertex position determined by the first fit.

The method to construct the discriminating parameter Q_s is described in more detail in [7]. The three distributions are shown in Fig. 2 for signal and background Monte Carlo and for experimental data. All distributions for data and background MC are in a good agreement apart some discrepancy in
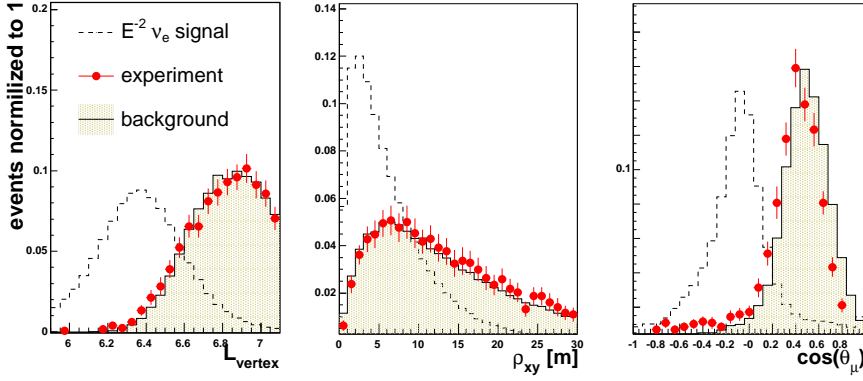
Figure 2: Distributions of the three variables used to construct the discriminating parameter Q_s for the experimental data, the background and the signal MC. Left: vertex likelihood distribution for signal and background. Middle: ρ_{xy}^{60} distributions (see text for details). Right: $\cos(\theta_\mu)$ distribution taken from the iterative muon likelihood reconstruction.

the $\cos(\theta_\mu)$ distribution. The reason for this could be an incorrect simulation of the ice properties and it needs to be taken into account in the systematic error. To maintain blindness we used only 20% of the experimental data to perform the final cut optimization. However, the optimization was done assuming the statistics of the full data sample i.e. the data were re-scaled by a factor of five. In Fig. 3 one sees the energy spectra for signal and background Monte Carlo and for experimental events which passed through the cascade filter. Here the background distribution was normalized to the experiment.

The final cuts on the reconstructed energy were applied following the optimization method described in [8]. This cut was performed in order to separate the potential signal from the background. Both cuts Q_s and E_{reco} were chosen to result in the highest sensitivity to an astrophysical neutrino flux. The sensitivity is defined here as the average upper limit [9] which was obtained in an ensemble of identical experiments in absence of the signal. In Fig. 4, the average upper limit $\bar{\phi}$ is shown as a function of E_{cut} for $Q_s > 0.92$. This procedure was repeated for a large range of Q_s values in order to obtain the optimal discriminating parameter and energy cut. To make a smooth background interpolation possible, the background distribution was fitted with a power-law function
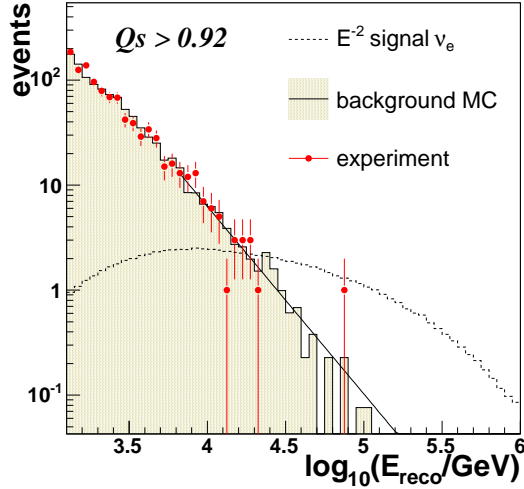
Figure 3: The reconstructed cascade energy distribution E_{reco}. Shown are experimental data as well as background and signal Monte Carlo simulation after application of all quality cuts and a cut on the discriminating parameter $Q > 0.92$. The smooth line is a result of the power-law fit to the background simulation.

(see Fig. 3). For the discriminating parameter the optimal cut is at $Q_s > 0.92$. The energy cut obtained from the optimization is $\log(E) > 4.65$. The corresponding sensitivity on the flux of ν_e is $2.7 \times 10^{-7}(E/GeV)^{-2}/(GeVs\ sr\ cm^2)$.

There is 1 event from the 20% experimental data subset passing this cut. We expect 1.3 background events from atmospheric muons. The expectation for the atmospheric ν_e and ν_μ which passed all cuts is 0.02 events for the 20% sample. No systematic uncertainties have been estimated yet, however, the uncertainties in the detector response and in the predictions of the atmospheric muon and neutrino fluxes are expected to be substantial.
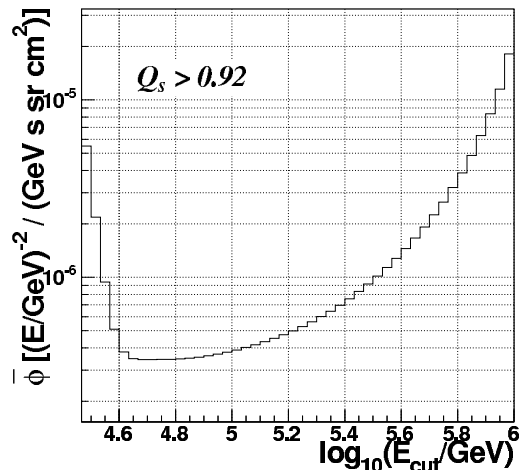
Figure 4: The average upper limit as a function of energy cut. The best sensitivity is reached for $\log(E_{cut}) = 4.65$.

Results

Analyzing a 20% sub-sample of the 5 years AMANDA data, a search for cascade-like events was performed. The observed events from experimental data are statistically consistent with the background expectation. The expected number of signal events from a diffuse flux assuming a E^{-2} spectra and a strength of $10^{-7}(E/GeV)^{-2}/(GeVs\ sr\ cm^2)$ is 2.1 ν_e events, leading to a preliminary sensitivity on the ν_e flux

of $2.7 \times 10^{-7}(E/GeV)^{-2}/(GeV\ s\ sr\ cm^2)$. Fig. 5 shows the effective areas after all selection cuts combined for neutrinos and anti-neutrinos. The effective area for tau neutrino is larger at high energy due to tau regeneration. Anti-electron neutrinos show a large increase in the effective area near 6.4 PeV due to the Glashow resonance.
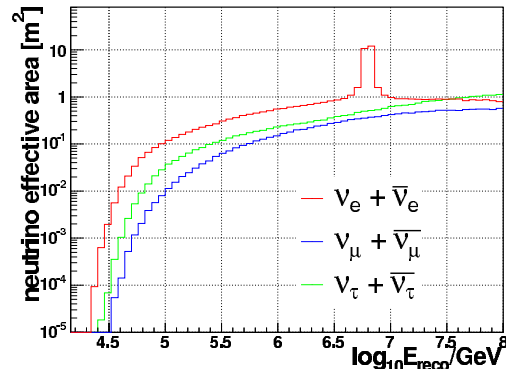
Figure 5: The effective neutrino areas for ν_e, ν_μ and ν_τ are shown as a function of neutrino energy after all selection criteria have been applied.

References

[1] J. Ahrens et al. *Nucl. Instr. Meth A*, 524:169, 2004.

[2] D.Heck. *Tech. Rep. FZKA*, 6019, 1998.

[3] A. Gazizov and M. Kowalski. *Comput. Phys. Commun.*, 172:203, 2005.

[4] J. Ahrens et al. High Energy Neutrino Generator for Neutrino Telescopes. *Phys. Rev.*, D67:012003, 2003.

[5] P. Lipari. Lepton Spectra In the Earth's Atmosphere. *Astropart. Phys.*, page 195, 1993.

[6] M. Kowalski and I. Taboada. In *2nd Workshop Methodical Aspects of Underwater/Underice Telescopes, Hamburg, Germany*, 2001.

[7] A. Ahrens et al. *Astropart. Phys.*, 22:127–138, 2004.

[8] G. Hill and K. Rawlins. *Astropart. Phys.*, 393, 2003.

[9] G. Feldman and R. Cousins. *Phys. Rev.*, D57:3873, 1998.

EHE Neutrino Search with the IceCube 9 String Array

AYA ISHIHARA[1] FOR THE ICECUBE COLLABORATION[2]

[1] *Department of Physics, Chiba University, Chiba 263-8522, Japan*

[2] *See special section of these proceedings*

aya@hepburn.s.chiba-u.ac.jp

Abstract: The performance of the partially ($\sim$10%) constructed IceCube neutrino detector on the search for extremely high energy (EHE) neutrino in data taken in 2006 is presented. Background event numbers are estimated based on an empirical model which reasonably describes a part of the same experimental sample. Following this background estimate an upper limit of the neutrino fluxes at 90% C.L. would be placed at $E^2 \phi_{\nu_e + \nu_\mu + \nu_\tau} \simeq 1.6 \times 10^{-6}$ GeV/cm^2 sec sr for neutrinos with an energy of 10^8 GeV in the absence of signals in the 2006 sample. The corresponding neutrino effective area is also presented.

Introduction

Extremely high energy (EHE) neutrinos are expected to fill a key role in connecting the observed EHE cosmic-rays to their birthplaces, which may shed light on the long standing puzzles of the origin of EHE cosmic-rays. Because of their low intensity, the detection of EHE neutrino requires a huge effective detection volume. The IceCube neutrino observatory [1], located at the geographic South Pole, will consist of a km^3 fiducial volume of clean glacier ice as a Cherenkov radiator and an array of photon detectors. The initial IceCube 9 string array (IC-9) was deployed by February 2006. Each string was positioned with a spacing of approximately 125 m and with 60 optical sensors attached to it at intervals of $\sim$17 m. The IC-9 detector was operational from June through November of 2006. The high energy events sample used in this analysis is a part of the full dataset taken with IC-9 satisfying the condition that a minimum of 80 out of 540 IC-9 optical sensors (DOMs) record Cherenkov pulses within 5 μsec. The effective livetime corresponding to this dataset is 124 days after rejecting events taken during times of unstable operation.

We report here for the first time on the expected sensitivity of this IC-9 detector configuration for neutrinos with energies 10^7 GeV and above.

EHE events in IceCube

At extremely high energies, neutrinos are mainly detected by secondary muons and taus generated during propagation of EHE neutrino in the Earth [2]. The propagation of particles has been simulated in detail by the JULIeT package [3]. Particles are seen in the detector as series of energetic cascades from radiative energy loss processes rather than bare tracks. These radiative energy losses are proportional to the energies of muons and taus and so is the Cherenkov light deposit in the IceCube detector. Figure 1 shows distributions of the total number of photoelectrons (NPE) detected by the 540 DOMs as function of muon and tau energies from the full IceCube Monte Carlo simulation. The trigger condition of 80 or more recorded DOM signals has been applied. A clear correlation between NPE and the energy of particles measured at 880 m from the IceCube center is observed. The IC-9 DOM response to a large NPE signal is limited mainly due to its readout configuration and PMT performance. Taking fully into account these effects in the simulation, the visible departure from linearity stems from the saturation of the detector during signal capture. Particles traversing far away from the detector leave low NPE signals regardless of their energy. From these observation, we use NPE as a robust estimator of the particle energy - together with the zenith angle - as main selection criterion.
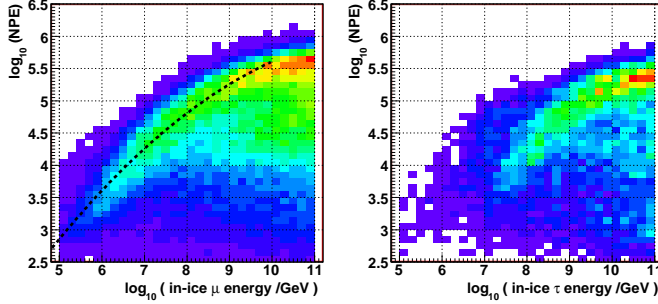
Figure 1: Event from the Monte Carlo simulation of the IC-9 detector in a plane of NPE and charged lepton energy measured at 880 meters from the IceCube center. Events passing within 880 m of the center of IceCube are considered in the plots and more distant events do not contribute to the data sample. The distribution in the left plot is for muons. The plot for taus on the right illustrates the suppression of energy loss compared to that of muons and the contributions from tau-decays. The charged lepton energy distribution is assumed to follow E^{-1} in these plots for illustrative purposes.

Background modeling

EHE neutrino induced muons and taus enter mostly from near or above the horizon with downgoing geometry because of the increase of neutrino cross section with energy. Therefore, atmospheric muon bundles, penetrating the detector from above, constitute a major background. However, the estimation of the atmospheric muon event rate in the relevant energy range is highly uncertain, as it involves poorly characterized hadronic interactions and a knowledge on the primary comic ray composition at energies where there is no direct measurement available. In the present analysis, we fit a part of the experimental IC-9 high energy event sample by an empirical formula to build the atmospheric muon background model. The model is then extrapolated to higher energies to estimate background intensity in the signal region.

This study used an event sample with $10^4 \leq$ NPE $\leq 10^5$ in which the bias in the high energy event dataset from the filter requirement of 80 DOMs is minimal. Events are dominated by atmospheric muons over possible cosmic neutrino events by more than 2 orders of magnitude as shown in Ref. [4]. The empirical model is based on the Elbert formula [5] that describes the number of muons with energies greater than a energy threshold initiated in a cosmic ray air shower cascade. The energy weighed integration of the formula relates the total energy carried by a muon bundle to the primary cosmic ray energy. The relation associates muon bundle event rate to given primary
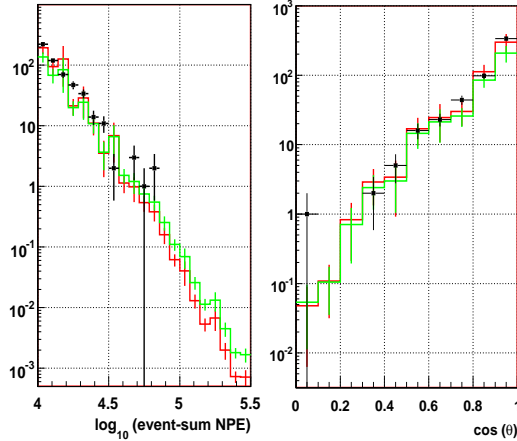
Figure 2: Event distributions of data as a function of NPE (left) and zenith angle θ (right). Black dots with error bars denote the IC-9 high energy event sample in $4.0 \leq log_{10}$ NPE ≤ 5.0. Red and green histograms are from the Monte Carlo simulation of the empirical atmospheric muon bundle model with two sets of parameters that gives similarly good agreement with experimental data.

cosmic-ray flux which was taken from the compilation in Ref. [6]. In other words, the background muon event rate is governed by the intensity of the cosmic ray flux and depends on the fraction of energy that goes to a muon bundle in an air shower. The two parameters of the model, the coefficient to determine multiplicity of muons in a bundle and the lowest energy of muons in a bundle to leave detectable signal in the IceCube detectors,

are estimated by comparing model simulation and experimental sample in the plane of NPE and reconstructed zenith angle for NPE below 10^5. The comparison of the model and experimental data is shown in Fig. 2. The black dots show a mid-NPE subsample of the data. Colored lines indicate the model simulation with two sets of parameters that give similar goodness in fits in terms of $\chi^2/d.o.f$ with respect to the experimental sample but with extreme cases of the low muon multiplicity coefficient (green line) and the low threshold energy coefficient (red line) in a bundle. Obviously, the models represent the experimental NPE and declination dependence well.

Results

Event distributions for signal and muon-bundle induced background are shown in Fig. 3. For the signal we chose a GZK cosmogenic neutrino model [7] as calculated in Ref. [8]. The plots show that the atmospheric muon bundle model has a steeper distribution in NPE compared with that of the signal GZK model. The number of muons and taus originating from the propagation of the signal neutrino in the earth exceeds that of atmospheric muon bundles at directions near the horizon as well as at the higher NPE. These observations suggest that the background can be rejected by excluding events with low NPE values and vertical reconstructed directions. The signal domain is defined by the following conditions:

$$\log_{10}\mathrm{NPE} \geq \log_{10}\mathrm{NPE}_{\mathrm{low}}, \qquad (13)$$

and if $\cos\theta \geq 0.1$,

$$\log_{10}\mathrm{NPE} \geq 4.7 + \frac{1.1}{0.9}(\cos\theta - 0.1). \qquad (14)$$

Summarized in Table 1 are the expected numbers of signal and background events above cut levels defined with different values of $\log_{10}\mathrm{NPE}_{low}$.

The resulting sensitivity to the all flavor EHE neutrinos is calculated independent of the neutrino flux models with the quasi-differential method based on the flux per energy decade. A similar approach is found in Ref. [9]. The first year IC-9 sensitivity curves at 90% confidence level are shown in the left plot of Fig. 4 for the four cut levels in Table 1 with an assumption of negligible background. It is also shown that this EHE neutrino

Table 1: Preliminary numbers of expected Ice-Cube EHE events of muons and taus produced from the GZK model [8] and from the background atmospheric muon model prediction. The predictions are normalized to a livetime of 124 days and presented for different $\log_{10}\mathrm{NPE}_{low}$ values in Eqs. (13) and (14). GZK $\mu + \tau$ indicates the number of events with muons and taus induced by the GZK neutrino outside the IceCube detector volume defined by a sphere of 880 m radius. GZK $\nu_{e+\mu+\tau}$ indicates contributions from charged particles created inside the sphere.

cut level	1	2	3	4
$\log_{10}\mathrm{NPE}_{low}$	4.4	4.6	4.8	5.0
GZK $\mu + \tau$	0.033	0.027	0.020	0.011
GZK $\nu_{e+\mu+\tau}$	0.028	0.024	0.020	0.015
atmospheric μ	0.003	$\leq 10^{-4}$	$\leq 10^{-4}$	$\leq 10^{-4}$

search is sensitive to the neutrinos with energies on the surface ranging between $\sim 10^7$ and $\sim 10^9$ GeV. Choosing cut level number 2, the 90% C.L. upper limit of EHE neutrino fluxes by the 2006 IC-9 observation would be placed at $E^2\phi_{\nu_e+\nu_\mu+\nu_\tau} \simeq 1.6 \times 10^{-6}$ GeV/cm^2 sec sr for neutrinos at an energy of 10^8 GeV; the corresponding neutrino effective area with our preferred cut level 2 is also shown on the right plot of Fig. 4.

Discussion

The sensitivity estimate has been obtained with the assumption of negligible background based on the empirical model prediction. The systematic uncertainties in the background estimation must be further considered, however. Possible contributions from fluctuations in the hadronic interaction processes in the air shower cascades and fluctuations in the muon bundle spatial distribution at IceCube detector depths (1450-2450 m) are disregarded in the current study. The estimation of these effects must be performed before the cuts are finalized. We would like to also remark that estimations of the contribution from the prompt muon in the present background model are uncertain. While the IC-9 high energy sample below 10^5 NPE (corresponding roughly to $E \leq 10^{7-8}$ GeV) shows no indication of a significant prompt muon contribution, a potential excess of events beyond the atmospheric muon bundle model could either be due to prompt muons, cosmic neutrinos or due to events of exotic physics origin.

89
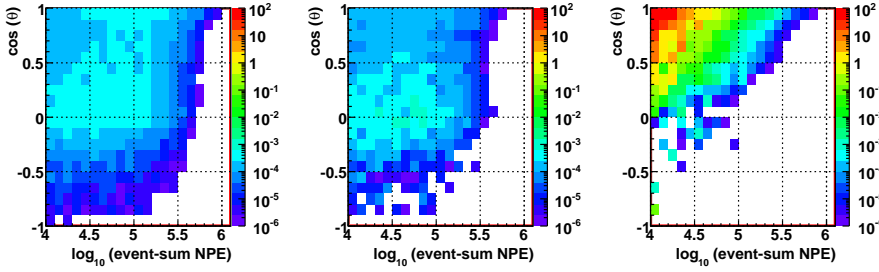
Figure 3: Event distribution in the plane of NPE and cosine of zenith angle obtained by Monte Carlo simulations. Plotted on the left and middle are those for GZK neutrino-induced muon and tau signals, respectively. The background atmospheric muon bundle model is shown on the right. Projections of the atmospheric muon bundle distribution is represented by green lines in Fig. 2.
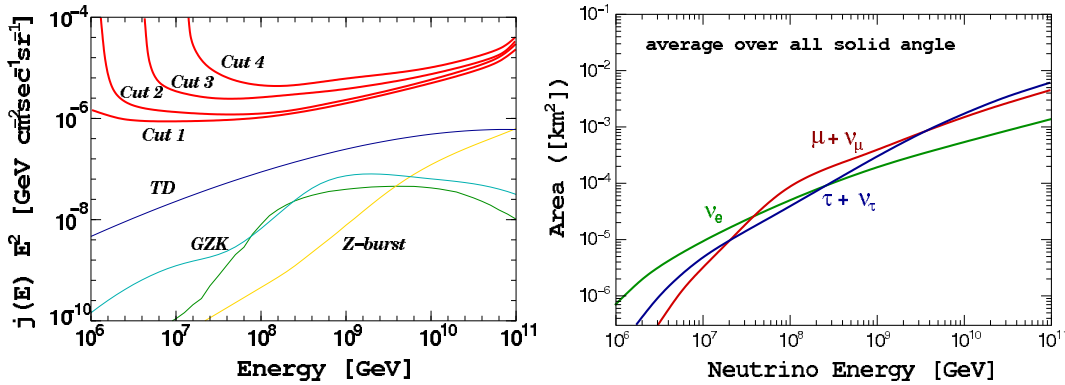
Figure 4: The 2006 IC-9 sensitivity curves at 90% C.L. on the EHE neutrino model fluxes is shown on the left. The fluxes of the three neutrino flavors ν_e, ν_μ, ν_τ are summed up. GZK refers to the GZK model from Ref. [8] for the lower curve and Ref. [10] for the upper curve. The TD and Z-burst predictions are from Ref. [11] and Ref. [12], respectively. Plotted on the right is the corresponding neutrino effective area of three neutrino flavors for cut level 2.

Acknowledgments

References

[1] J. Ahrens *et al.*, Astropart. Phys. **20** 507 (2004); http://icecube.wisc.edu/.

[2] S. Yoshida, R. Ishibashi, H. Miyamoto Phys. Rev. D **69** 103004 (2004).

[3] http://www.ppl.phys.chiba-u.jp/JULIeT/

[4] A. Ishihara, Nucl. Phys. **B** (Proc. Suppl.) 200-206 (2007); astro-ph/0611794 (2006).

[5] T. K. Gaisser, *Cosmic Rays and Particle Physics*, (Cambridge University Press, 1990).

[6] M. Nagano and A. A. Watson, Rev. Mod. Phys. **72**, 689 (2000).

[7] V. S. Beresinsky and G. T. Zatsepin, Phys. Lett. **28B**, 423 (1969).

[8] S. Yoshida and M. Teshima, Prog. Theor. Phys. **89**, 833 (1993).

[9] X. Bertou *et al.*, Astropart. Phys. **17** 183 (2002).

[10] O. E. Kalashev, V. A. Kuzmin, D. V. Semikoz, and G. Sigl, Phys. Rev. D **66**, 063004 (2002).

[11] G. Sigl, S. Lee, P. Bhattacharjee, and S. Yoshida, Phys. Rev. D **59**, 043504 (1999).

[12] S. Yoshida, G. Sigl, and S. Lee, Phys. Rev. Lett. **81**, 5505 (1998).

Very high energy electromagnetic cascades in the LPM regime with IceCube

J. BOLMONT[1], B. VOIGT[1] AND R. NAHNHAUER[1], FOR THE ICECUBE COLLABORATION[2].

[1] *DESY, D-15738 Zeuthen, Germany*

[2] *see special section of these proceedings*

julien.bolmont@desy.de

Abstract: With a volume of $\sim$1 km^3, IceCube will be able to detect very high energy neutrinos above $\sim$100 PeV. At these energies, bremsstrahlung and pair production are suppressed by the Landau-Pomeranchuk-Migdal (LPM) effect. Therefore, ν_e and ν_τ interactions in the ice can produce several hundred meter long cascades. We present an analysis of IceCube sensitivity to ν_e events. It includes cascade simulation in the LPM regime and makes use of preliminary algorithms for incident angle reconstruction. We give the obtained effective area for the 22 string configuration and discuss IceCube angular reconstruction precision.

Introduction

Different models predict a significant flux of high energy neutrinos above $\sim$100 PeV. Topological defects, superheavy relics of the Big-Bang, the GZK mechanism or gamma ray bursts could produce such high energy neutrinos (see [1] for a review).

The IceCube neutrino detector is under construction at the South Pole [2]. Currently, it is made of 22 strings each holding 60 optical detectors, instrumenting a volume of $\sim$0.3 km^3. Strings are separated by 125 m and modules on a string are separated by 17 m. By its completion in 2011, there will be up to 80 strings and the corresponding volume will be $\sim$1 km^3.

At low energies, $e^\pm$ produced by charged current interactions produce small cascades compared to the spacing between two optical modules. The produced light is emitted in the direction of the Cherenkov cone but it is scattered in the ice so that when observed from a distance, it can be considered to be emitted almost isotropically from the centre of the cascade. Therefore, the angular resolution for cascades is poor.

However, for a 100 PeV neutrino, the secondary particle energy is high enough for bremsstrahlung and pair-production to be supressed by the Landau-Pomeranchuck-Migdal (LPM) [3, 4] effect. This

leads to an elongation of the cascades, which in turn could result in better angular resolution for cascade events in IceCube.

Here, we focus on electromagnetic cascade analysis for ν_e events at energies above $\sim$100 PeV where the LPM effect has to be taken into acount. The LPM effect also affects hadronic cascades but as the input energy is distributed over a large number of secondary particles, their length does not increase as dramatically. Hadronic cascades will not be discussed in this paper.

In the next section, we describe two simulation tools for high energy cascades in the LPM regime. The longitudinal profiles obtained are used to estimate the Cherenkov light output in the ice. Following that, effective area is computed for the 22 string detector. Finally, the precision of incident angle reconstruction is evaluated.

The results shown are preliminary.

Simulation of high-energy cascades

To study high-energy cascades in ice, two simulation packages have been developed. One allows the rapid simulation of cascade profiles and uses a parameterisation of bremsstrahlung and pair-production cross sections in the LPM regime, and a parameterisation of energy deposition for the low
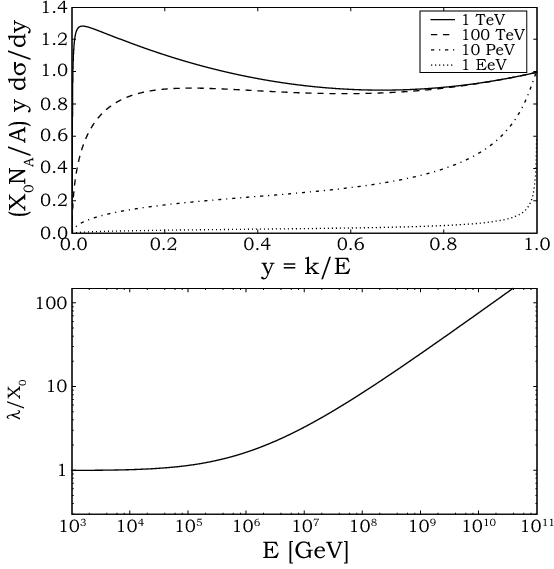
Figure 1: Top panel: differential energy cross section for bremsstrahlung as a function of $y = k/E$ where k is the energy of the photon and E the energy of the electron. Bottom panel: mean free path for bremsstrahlung as a function of energy.

energy products of the cascade. The other package is a full Monte Carlo simulation of cascades based on CORSIKA. It is devoted to fine studies of the development of cascades.

Hybrid approach

Following Niess and Bertin [5], a simulation of the cascade development has been implemented. This simulation takes into account bremsstrahlung and pair production interactions and works only in one dimension. The suppression of both processes by the LPM effect is included. Parameterisations of bremsstrahlung and pair production cross sections are taken from [6]. Fig. 1 shows the differential cross section and radiation length parameterisation for bremsstrahlung. The increase of the mean free path above 1 PeV is due to the LPM effect.

In the simulation, high energy particles are propagated until their energy falls below a cut-off energy on the order of 1 TeV and the energy loss profile of these particles is computed using a parameterisation. The individual energy loss profiles of these
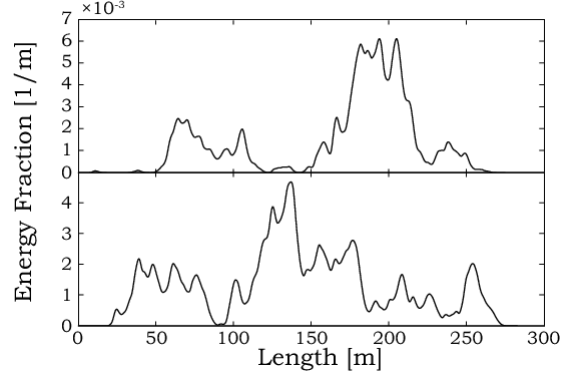
Figure 2: Longitudinal energy profiles of two 10 EeV electromagnetic cascades.
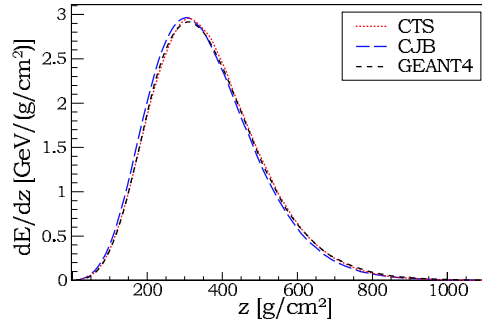
Figure 3: Average longitudinal profile of one hundred 1 TeV cascades. Comparison between CTS, CJB and GEANT4.

low energy particles are summed to obtain the total energy deposit profile of the full shower.

The fractional energy of the secondary particles is generated randomly from the differential cross section using a Metropolis-Hastings Algorithm [7]. This allows the quick generation of random samples. For instance, when the cut-off energy is on the order of 1 TeV, a single cascade with energies in the PeV range can be simulated in a few milliseconds. A 10 EeV cascade is simulated within less than 3 minutes when the cut-off is set to 50 TeV.

Fig. 2 shows longitudinal energy profiles of two 10 EeV cascades. Their length is about 200 m. Many different sub-cascades contribute to this profile. The figure also shows that the shape and length of the longitudinal profile can vary significantly from one cascade to another.

Monte Carlo approach

In addition to the simple hybrid approach presented in the previous section, we have also developed a more realistic simulation tool, able to provide more precise information on cascade development. This tool is based on the well-known atmospheric cascade simulation tool CORSIKA [8].

As CORSIKA is devoted to cascade simulations in the atmosphere, several modifications had to be made in order to adapt the code to a uniform density medium. This work was initially done by T. Sloan for the ACoRNE collaboration with CORSIKA 6204 [9]. Hereafter, this version will be denoted CTS.

We have used these modifications and taken them a step further to get more functionality and more flexibility. The new modifications allow us to:

- switch the medium from air to ice during the configuration step,

- use the different simulation packages (VENUS, QGSJET and others) available with CORSIKA,

- use all the other options available in CORSIKA, whenever they are relevant to a simulation in water/ice.

The changes were made starting from the most recent version of CORSIKA (CORSIKA 6502).

To check the validity of this software (denoted CJB), we simulated 1 TeV electrons using both versions CJB and CTS with the same input parameters and the same random generator seeds. The results were also compared with GEANT4 [10].

Fig. 3 shows the energy deposition profiles for the two versions of CORSIKA and GEANT4. The profiles are very similar. The small difference between CJB and CTS comes mainly from minor revisions in the EGS4 code [12] between CORSIKA releases 6204 and 6502.

A 10 EeV cascade can be simulated in less than 2 minutes for default values of cut-off energies, provided the thinning option is enabled.
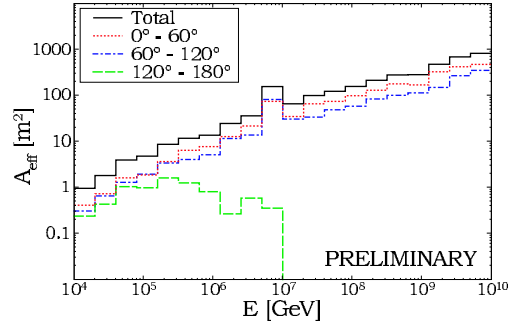
Figure 4: Effective area for different incident angles and for the 22 string configuration.

Reconstruction and effective areas

Electron neutrinos with energies between 10 TeV and 10 EeV were generated, propagated through the Earth and forced to interact in the vicinity of the instrumented detector volume using a software package based on the ANIS [11] neutrino generator. The development of the cascades in the ice has been done with the hybrid simulation tool described previously. The detector response includes the simulation of light propagation through the ice, optical module responses and a trigger simulation requiring 8 modules hit within a time window of $4\,\mu$s.

A basic analysis method typically used to reject muon background was applied to the pure ν_e sample in order to calculate the effective area, taking into account the reconstruction efficiency. The selection is done by computing the ratio between the longitudinal and lateral size of the light distribution, using the fact that cascades are more spherical than muon tracks.

The number of passing events was used to calculate the neutrino effective area for three different zenith angle (θ) bands for the 22 string configuration (Fig. 4). The effective area generally increases with energy due to the rising cross section of neutrino interactions. However, for neutrinos with energies above $\sim$1 PeV the earth becomes opaque and the effective area for neutrinos coming from below the horizon ($120^{\rm o} < \theta < 180^{\rm o}$) falls off. The peak between 5 PeV and 10 PeV is caused by resonant $\overline{\nu_e} + e^-$ scattering at energies around 6.3 PeV (the Glashow resonance).

Precision of incident angle reconstruction

Cascade-like events passing the trigger conditions are reconstructed using a simple *line-fit* algorithm [13] usually used for muon track reconstruction. It uses the hit times to produce a track defined by a vertex point and a direction.

The difference ϕ between generated and reconstructed directions is computed. Fig. 5 shows the cumulative fraction of events reconstructed with an arbitrary precision ϕ. At 1 EeV, the proportion of cascades reconstructed with a precision better than 20° is ∼5%. At 10 EeV, when the LPM effect is taken into account, this proportion is ∼20%.

Conclusions

At very high energies, the LPM effect can increase the length of cascades to several hundred meters. This could lead to better angular resolution for high energy cascades. We have developed two new tools in order to study these events.

A very simple *line-fit* method seems to indicate a significant improvement of angular reconstruction precision at high energies. However, this improvement, due to cascade lengthening, still leads to insufficient resolution for possible high energy neutrino source identification.

Achieving this goal will require dedicated algorithms to fully exploit the cascade lengthening and to obtain improved angular resolution. Such methods are under development.

Acknowledgements
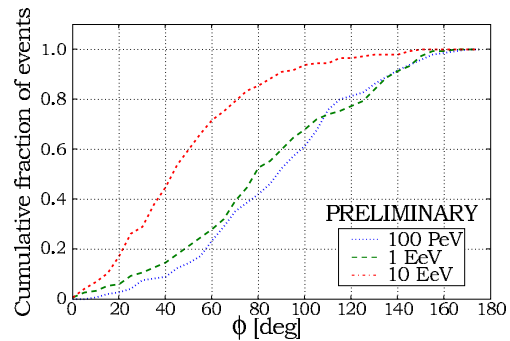
Figure 5: Cumulative fraction of events reconstructed with an arbitrary precision ϕ, for the 2007 22 string configuration.

References

[1] R. Gandhi, *Nucl. Phys. Proc. Suppl.*, 91, 453, 2000

[2] A. Karle, *ICRC 2007 Proceedings*, 2007

[3] L. D. Landau and I. J. Pomeranchuk, *Dokl. Akad. Nauk SSR*, 92, 535 & 735, 1953

[4] A. B. Migdal, *Phys. Rev.*, 103, 1811, 1956

[5] V. Niess and V. Bertin, *Astropart. Phys.*, 26, 243, 2006

[6] S. Klein, *Rev. Mod. Phys.*, 71, 1501, 1999

[7] W. K. Hastings, *Biometrika*, 57, 97, 1970

[8] D. Heck et al., Report FZKA 6019, 1998; available from http://www-ik.fzk.de/

[9] S. Bevan et al., arXiv:0704.1025, 2007

[10] S. Agostinelli et al., *Nucl. Inst. Meth. A*, 506, 250, 2003

[11] A. Gazizov and M. P. Kowalski, *Computer Physics Communications*, 172, 203, 2005

[12] W.R. Nelson et al., Report SLAC 265, 1985

[13] J. Ahrens et al., NIM A 524, 169, 2004

IceCube Performance with Artificial Light Sources: the Road to Cascade Analyses

J. KIRYLUK[1], M.V. D'AGOSTINO[2], S.R. KLEIN[1], C. SONG[3], AND D.R. WILLIAMS[4] FOR THE ICE-
CUBE COLLABORATION[5]

[1]*Lawrence Berkeley National Laboratory, Berkeley, CA 94720, USA*

[2] *Dept. of Physics, University of California, Berkeley, CA 94720, USA*

[3] *Dept. of Physics, University of Wisconsin, Madison, WI 53706, USA*

[4] *Dept. of Physics, Pennsylvania State University, University Park, PA 16802, USA*

[5] *see special section of these proceedings*

JKiryluk@lbl.gov

Abstract: The IceCube one km^3 neutrino observatory will collect large samples of neutrino interactions, allowing for observations with small statistical errors. To make maximum use of this statistical power, it is also being designed to minimize systematic errors, via a variety of different calibration techniques. LED and laser light sources are a key part of many of these calibration techniques. To a significant extent, they mimic cascade (ν_e) interactions, allowing fairly direct tests of cascade reconstruction techniques. This contribution will survey the light sources and discuss selected calibration studies.

Introduction

The main goal of IceCube [1] is to detect cosmic neutrinos of all flavors in a wide energy range, from $\sim$100 GeV to $\sim$100 EeV and search for their sources. When complete, the IceCube detector will be composed of up to 4800 Digital Optical Modules (DOMs) on 80 strings spaced by 125 m. The array covers an area of one km^2 from 1.45 to 2.45 km below the surface [2].

High energy neutrinos are detected by observing the Cherenkov radiation from secondary particles produced in neutrino interactions inside or near the detector. Muon neutrinos in charged current (CC) interactions are identified by the final state muon track [3]. Electron and tau neutrinos in CC interactions, as well as all flavor neutrinos initiating neutral current (NC) interactions are identified by observing electromagnetic or hadronic showers (cascades). For example, up to $\sim$10 PeV, electromagnetic showers initiated by the final state electron can be approximated as expanding light spheres originating from a point source. A 10 TeV cascade triggers IceCube optical modules out to a radius of about 130 m [4]. Cascade reconstruction is expected to have limited pointing capability but good

energy resolution, 0.11 in $\log_{10}(E)$ [5]. The good energy resolution and low background from atmospheric neutrinos makes cascades attractive for diffuse extraterrestrial neutrino searches [6].

Artificial light sources are of particular importance in IceCube. Each DOM includes 12 LEDs (flashers) as a calibration source. As shown in Fig.1, one string also holds a nitrogen laser with absolute calibration that serves as a "standard candle". The flashers and standard candle (SC) are used for a wide variety of purposes: timing, charge amplitude and geometry calibrations, to measure the optical properties of the ice (a key problem for IceCube), and to mimic cascades. The flasher light output is comparable to cascades with energies up to about 500 TeV, while the standard candle output is comparable to cascades with energies up to about 30 PeV. For the ice studies, the availability of flashers at different depths is critical, allowing comparisons of ice properties at different depths. These studies build on the lessons learned from AMANDA, which pioneered the use of artificial light sources [7].

In this report we present the results of a few selected studies performed with the flashers and standard candle: geometry and timing calibrations, and
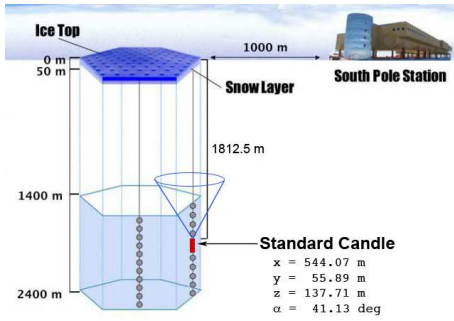
Figure 1: Schematic of the IceCube detector showing the location of the Standard Candle. For clarity, only two out of 80 strings are shown.
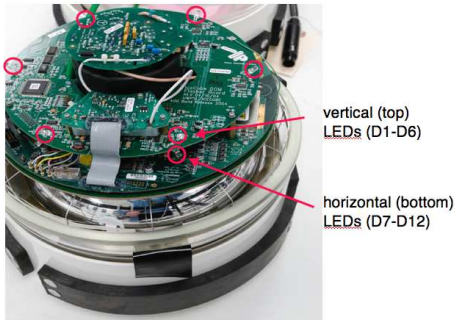
Figure 2: Digital Optical Module with six horizontal and six vertical LED flashers.

the position resolution of cascade algorithms. This work uses data collected during 2006 with 9 strings that had been deployed in IceCube at that time.

LED Flashers

Each DOM contains a flasher board which holds twelve 405 nm LEDs. Six of them point horizontally outward and six point upwards at ~48 degrees. They are mounted on the top and the bottom of the flasher board respectively, cf. Fig.2. The LEDs are individually flashed with a programmable pulse width and amplitude. Typical flasher runs last 500 s with the LEDs firing at 10 Hz at full brightness, with nominal width of 10 ns.
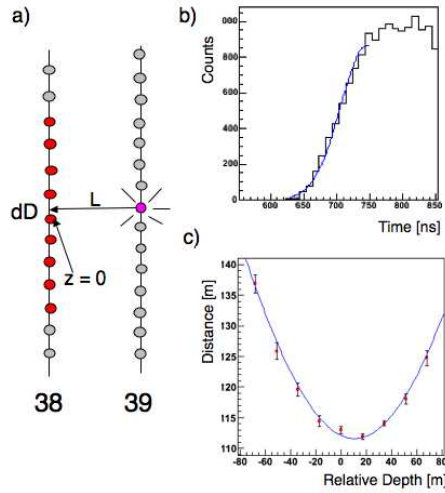
Figure 3: a) Schematics of the interstring detector geometry measurement. The flasher light from LEDs on DOM 39-15 is seen on a neighboring string. b) The earliest hit time distribution for light detected at DOM 38-10. c) The earliest hit time observed at DOMs on string 38 shown as a function of the relative depth between the observing DOMs and the flashing DOM.

Geometry Calibration

The LED flashers were used to calibrate the position of the DOMs. Figure 3a) shows a schematic of one study that was used to measure the relative depth of DOMs on different strings. The LEDs in a DOM on one string were pulsed and arrival times for nine nearby DOMs on a neighboring string were analyzed. The time of the earliest hit t_0 was derived from the photon arrival time distribution, cf. Fig. 3b), by fitting a Gaussian in the turn-on region: $t_0 = \mu - 3\sigma$, where μ and σ are the mean and sigma of the Gaussian. The uncertainty is determined by propagating the errors on the fit parameters. The arrival times of the earliest hits are converted to distances (assuming that there is no scattering, appropriate for the first photon seen). Figure 3c) shows these distances versus the relative depth from the deployment records. This distribution was fitted with a hyperbola to determine the relative depth and lateral separation between the two strings. The position of the minimum gives the relative depth and is used to correct the string
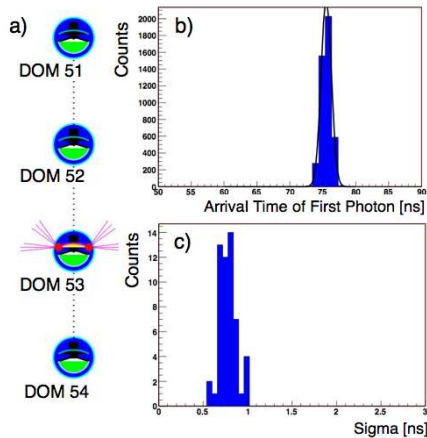
Figure 4: a) DOM 53 is flashing. b) Photon arrival time delay at DOM 52 when DOM 53 is flashing. c) RMS variation of time delay measured with flashers for 59 DOM pairs on an IceCube string.

position determined from deployment and survey data. Systematic uncertainties in the determination of the lateral separation are under study.

Timing Calibration

Flasher data are used also to verify the system timing resolution. The method is to flash an LED on a DOM and measure the arrival time of light reaching a nearby DOM, as shown in Fig. 4a). The earliest photons are likely not scattered, hence the difference in timing between the two DOMs reflects the time in ice. The distance between DOMs on the same string ($\sim$17m) is smaller than the light scattering length in ice ($\sim$25m) and the light intensity is high enough so that direct light is seen on neighboring DOMs. The resolution is dominated by electronics and timing uncertainties. A distribution of the first photon arrival time for a single receiving DOM is shown in Fig. 4b). The resolution for most DOMs was found better than 2 ns, as shown in Fig. 4c), confirming the precision of the time synchronization procedure. The results are consistent with an alternative method which uses muon tracks [2].

Standard Candle

The Standard Candle (SC) is an in-situ calibrated N_2 pulsed laser, which emits light with a wavelength of 337 nm. It is used to study cascade reconstruction, and to provide a method for calibrating the cascade energy scale which is independent of Monte Carlo simulations. At 100 % intensity, the SC generates $(4.0 \pm 0.4) \times 10^{12}$ photons which are emitted at an angle of $41°$ with respect to the candle axis, as is shown in Fig. 1. The $41°$ angle was chosen to approximately match the Cherenkov radiation from a cascade. Although the light distribution initially matches that of a cascade, the wavelength of 337 nm is shorter than most of the Cherenkov radiation observed in IceCube. This results in $\sim$10 % shorter absorption and scattering lengths, and requires adjustments to the amplitude calibrations. Pre-deployment calibration and internal power measurement contribute to 10% uncertainty in light output. The light intensity is determined on a pulse-by-pulse basis.

The SC is equipped with an adjustable attenuator that can reduce the light output down to 0.5% of the full scale. This is used to study detector (especially photo-multiplier tubes) non-linearities. We plan to deploy one additional standard candle, which will point downwards or to the side, allowing different cascade geometries to be studied in future.

Reconstruction Results

Figure 5 shows an event with the SC at full laser intensity. Results from the SC laser events reconstruction as cascades are shown in Fig. 6. The dashed histogram shows the center-of-gravity (COG) x position. The COG is calculated for each event as the signal amplitude weighted mean of all hit DOM positions. The mean COG x position, about 512 m, is about 30 meters from the actual SC x position of 544 m (shown as a dashed-dotted line). The reason for this discrepancy is that the SC is on a string at the edge of the 9 string array, and the COG is pulled toward the center of the array. The COG is used as a first approximation for a full maximum-likelihood reconstruction algorithm [8]. This algorithm considers the photon arrival times at all of the other DOMs. It finds an x position (continuous histogram) within 10 m of the actual
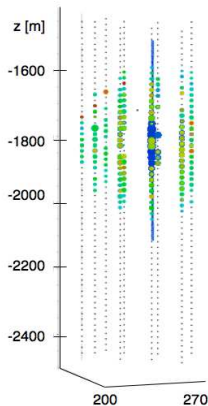
Figure 5: Standard Candle event display with 162 DOMs hit. The size of the circles is proportional to the signal amplitude, while the color distinguishes between relative photon arrival times in the DOMs.

Figure 6: The reconstructed x-vertex position of 'cascades' from SC events. The dashed histogram shows the center-of-gravity (COG) position, and the continuous histogram shows the reconstructed vertex position. The dashed-dotted line is the 'true' SC laser position in the detector ($x = 544.1$ m).

SC position for about 99% of the events. Similar results have been obtained for y and z vertex positions. The fact that the algorithm can find the position so well for asymmetric events (with DOMs on only one side of the SC) gives us confidence in the reconstruction algorithm accuracy.

Summary

The IceCube flasher LEDs and standard candle laser are used for a variety of calibration and verification studies, including geometry and timing calibrations, and studies of ice properties. It has been demonstrated that for most DOMs the timing resolutions is better than 2 ns and the DOM positions are known to 1 m. These studies will help IceCube reduce the systematic errors for various physics analyses. Artificial light sources have also been used to study the position reconstruction performance of cascade reconstruction algorithms, and to study the absolute energy scale of the detector. In future, they will be used to study also the energy and directional reconstruction of more advanced algorithms.

References

[1] IceCube, http://icecube.wisc.edu
[2] IceCube, A. Achterberg *et al.*, Astropart. Phys. **26**, 155 (2006); A. Achterberg *et al.*, to be submitted to Nucl. Instrum. Meth.
[3] AMANDA, J. Ahrens *et al.*, Nucl. Instrum. Meth. **A524** (2004) 169.
[4] F. Halzen, Eur. Phys. J. **C46** (2006) 669.
[5] IceCube, J. Ahrens *et al.*, *IceCube Preliminary Design Document* (2001).
[6] M. Kowalski, JCAP 05 (2005) 010.
[7] AMANDA, M. Ackermann *et al.*, J. Geophys. Res. **111** (2006) D13203.
[8] D. Chirkin, these proceedings.

Neutrino Point Source Search Strategies for AMANDA-II and Results from 2005

J. BRAUN, A. KARLE, AND T. MONTARULI FOR THE ICECUBE COLLABORATION
Physics Department, University of Wisconsin, Madison, WI 53706, USA
jbraun@icecube.wisc.edu For a full authorlist, see the special section in these proceedings.

Abstract: Current point source searches mostly utilize only direction and time of the reconstructed event; furthermore, they reduce available information by grouping events into sky bins. In this analysis we use a search based on maximum likelihood techniques, utilizing both event angular resolution and energy, to enhance our ability to detect point sources. Especially, use of energy information allows us to fit the spectral index of a hypothetical source simultaneously with flux. This method improves both sensitivity and discovery potential of the AMANDA-II array by greater than 30%. The method can naturally be applied to IceCube and allows superposition of data from detectors with different sensitivity and angular resolution, such as the IceCube array which changes and improves with each season of construction.

Introduction

Pinpointing the origin of high energy cosmic rays is one of the most important goals of neutrino astrophysics. Observation of a high energy neutrino source would provide clear indication of hadronic processes associated with cosmic rays. Neutrinos are neither deflected by magnetic fields nor significantly attenuated on transit to Earth, making them excellent astronomical messengers in the $>$TeV universe.

The Antarctic Muon And Neutrino Detector Array (AMANDA), a subdetector of the IceCube Observatory, is composed of 19 strings with 677 total optical modules located 1500 m – 2000 m below the ice surface at the Geographic South Pole. Muons produced by charged-current ν_μ and $\bar{\nu}_\mu$ interactions produce tracks of Čerenkov light and are reconstructed with 1.5^o–2.5^o median angular resolution [2]. The large background of muons from cosmic ray interactions in the atmosphere precludes ν_μ and $\bar{\nu}_\mu$ searches in half of the sky, but for $\delta > 0$ cosmic ray muons are attenuated by Earth leaving a relatively pure atmospheric neutrino background.

Detection of an extraterrestrial high energy neutrino source has so far eluded the neutrino telescope community. To probe lower fluxes, either larger neutrino telescopes must be built, more sophisticated point source analysis techniques [8] [5]

must be developed to better utilize data from existing experiments, or both [1].

Method

An unbinned maximum likelihood search method is used in contrast to previous AMANDA point source analyses [2]. The past binned search method makes use of a single statistic, namely "How many events are within bin radius 'b'" and a background estimation to make a statement about the existence of a source at any particular position in the sky. It is reasonable to think the use of additional information must enhance ability to search for point sources. Additional information includes:

- Events outside the search bin

- The distribution of events within the search bin

- Event energy estimation.

The energy distribution of a hypothetical E^{-2} source is drastically different from that of the atmospheric neutrino background. If high energy events are observed, such events are not very compatible with atmospheric neutrino background and enhance discovery potential. Conversely, if high energy events are not observed, the method is able
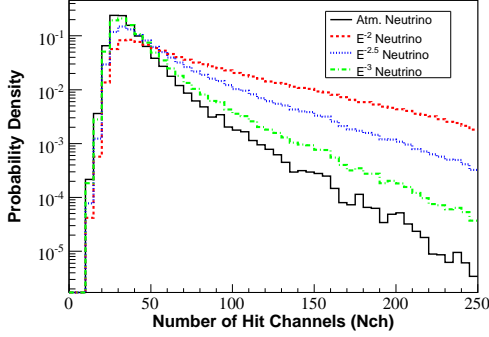
Figure 1: Number of hit channels (Nch) PDF for simulated atmospheric neutrinos and various signal spectra

to reject the signal hypothesis with higher confidence. In AMANDA, the number of optical modules, or channels, hit by at least one photon during an event correlates with event energy. By using the difference in the distribution of number of hit channels, shown in figure 1 for various energy spectra, events are more accurately classified as signal or background.

At a hypothetical source position x_o, the data is modeled as an unknown mixture of background and events produced by the source. Each event near the source declination is assigned a likelihood of belonging to the source. This source PDF is the product of probability functions describing the detector point spread, which is zenith dependent, and number of channels hit (Nch):

$$S_i(x_i, x_o, \theta, N_{ch}, \gamma) = P(x_i|x_o, \theta)P(N_{ch}|\gamma),$$

where γ is the source spectral index. The detector point spread is modeled as a two dimensional Gaussian:

$$P(x_i|x_o, \theta) = \frac{e^{-\frac{|x_i - x_o|^2}{2\sigma^2(\theta)}}}{2\pi\sigma^2(\theta)}.$$

The Gaussian width σ is fitted to simulation. The background PDF depends on $P(N_{ch}|Atmos.\nu)$, the probability of obtaining the observed Nch value from atmospheric neutrinos, and event density within the band. The full likelihood function is a

combination of signal and background probabilities S and B over all events in the declination band ranging $\pm 5^o$ of the source position x_o and containing N total events:

$$\mathcal{L} = \prod_i^N \left(\frac{n_s}{N} \cdot S_i(x_i, x_o, \theta, N_{ch}, \gamma) + (1 - \frac{n_s}{N}) \cdot B_i(N_{ch}) \right).$$

The signal and background PDF are normalized such that the free parameter n_s describes the number of signal events present. The quantity $-log(\mathcal{L})$ is minimized with respect to n_s and γ, obtaining best estimates of signal strength $\hat{n}_s$ and spectral index $\hat{\gamma}$. The logarithm of the likelihood ratio

$$\lambda = log \frac{\mathcal{L}(\hat{n}_s, \hat{\gamma})}{\mathcal{L}(n_s = 0, Atmos.\nu)}$$

is used to determine significance and flux limits for each observation.

Significance is calculated by comparing the observed value of λ to the distribution obtained from randomized data. Adding a simulated signal flux shifts the distribution of λ to higher values, corresponding to higher significance. Discovery potential is measured by calculating the signal flux necessary to increase λ such that a given significance is exceeded in a given percentage of trials. Feldman-Cousins confidence intervals [4] are constructed knowing the response of λ to increasing signal flux and are used to calculate sensitivity and flux upper limits. A 30% improvement in sensitivity and discovery potential using the unbinned maximum likelihood method is shown in both sensitivity and discovery potential in figure 3.

Since signal spectral index is estimated simultaneously with flux, the obtained value of $\hat{\gamma}$ serves as an estimate of spectral index. The value -2log$\mathcal{L}/\hat{\mathcal{L}}$ approximately follows a chi-square distribution with two degrees of freedom when signal strength n_s and spectral index γ are simultaneously varied. Using this approximation, confidence contours in signal strength and spectral index are shown in figure 2. The signal strength n_s is typically overestimated by approximately 10% due to mismatch between the true point spread function and the Gaussian approximation used in this analysis. This effect is measured using detector signal Monte Carlo
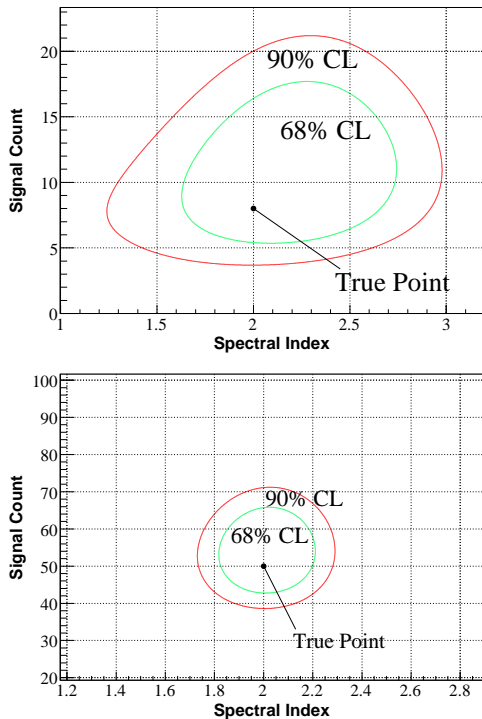
Figure 2: Confidence estimates in source strength and spectral index for a case of 8 E^{-2} signal events (top) and 50 E^{-2} signal events (bottom)

and is calibrated away. As an example, suppose Markarian 421 ($\delta = 38.2^o$) produces 8 events in the detector with an E^{-2} energy spectrum. Application of this method to the coordinates of Markarian 421 would yield a 53% chance of discovery at 5σ confidence level. Preliminarily, 1σ spectral index confidence bounds for this source would be better than ± 0.5 around $\hat{\gamma}$ for an energy spectrum near E^{-2}.

Another benefit is the ability to combine data from detectors with different angular resolution. A binned search regards each event equally and bin radius must be optimized given the combination of datasets; however, this method can recognize which dataset the event is from and use the appropriate point spread distribution to more accurately describe the event. This benefit is particulary important during the construction phase of IceCube, as detector resolution will improve each year.

Data Sample

Data are taken during the austral winter from mid-February 2005 through October 2005. Accounting for the time the detector is down and a brief time the detector is dead following each event yields 199.3 days of detector livetime and $1.8 \cdot 10^9$ events. Most events are recorded from a multiplicity trigger requiring at least 24 optical modules register photon hits within 2.5 μs. False hits produced by crosstalk, isolated hits caused by PMT dark noise, and hits from 154 modules with either an abnormal dark noise rate or position outside the main detector volume are removed. Remaining hits from 523 optical modules are reconstructed as muon tracks with increasing accuracy and cpu requirements [3], and zenith filters are applied to remove the majority of cosmic ray muon background. Filtering is divided into levels to maximize CPU efficiency while retaining the vast majority of neutrino events [2]. 5.2 million events remain in the final filtered sample, mostly misreconstructed muons. Neutrino events are chosen from this sample to minimize average flux upper limit [6] based on reconstruction and topological criteria including a track angular resolution estimate [7], the ratio of upgoing reconstruction likelihood to downgoing likelihood, the distribution of hits along the track, and track length. Events are divided into 5° declination bands, and optimization is performed simultaneously on all parameters for E^{-2} and $E^{-2.5}$ source spectra. A compromise cut is applied between the $E^{-2} – E^{-2.5}$ optimization. Optimized point source sensitivity (figure 3) shows a $\sim$30% improvement against the binned method uniform over the sky. Discovery potential is similarly improved. After the cut, 887 events remain above $\delta = 10^o$, with any 10° declination band containing 50-150 events. A large number of misreconstructed muons add to atmospheric neutrinos in the final sample below $\delta = 10^o$.

Results

The method is applied to a catalog of candidate neutrino sources including microquasars, supernova remnants, TeV blasars, and other objects of interest. Results for a selected subset of objects are summarized in table 1. A scan of the entire sky at points spaced by 0.25^o is also performed using
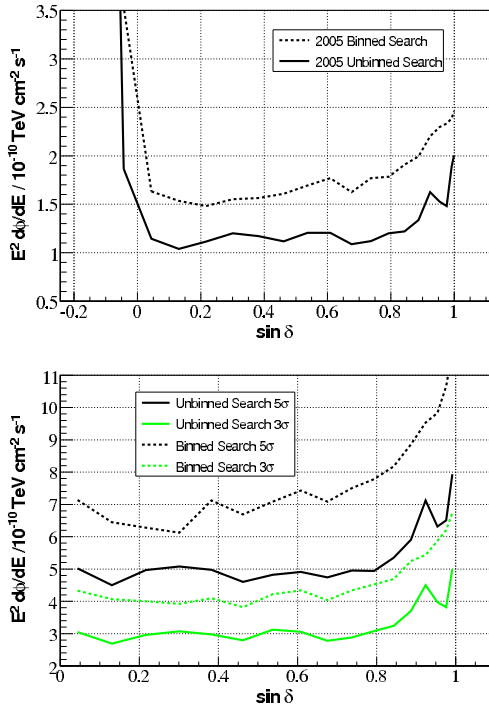
Figure 3: Preliminary point source sensitivity to E^{-2} energy spectra (top), and discovery flux for E^{-2} energy spectra (bottom). 90% of sources with this flux are detected at the stated significance, excluding trial factors.
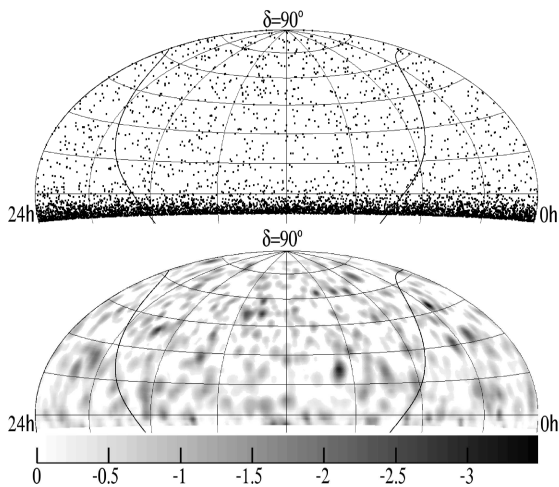
Figure 4: Preliminary sky map of neutrino candidate events (top), and of $\log_{10}$(p-value) (bottom)

Candidate	$\delta(^o)$	μ_{90}	p
Markarian 421	38.2	5.87	~ 1
Markarian 501	39.8	18.1	0.184
Cygnus X-1	35.2	12.9	0.414
Cygnus X-3	41.0	11.0	0.458
LS I +61 303	61.2	3.81	~ 1
Crab Nebula	22.0	9.24	~ 1
MGRO J2109+37	36.8	20.1	0.152

Table 1: Preliminary flux upper limits for selected neutrino source candidates over 199.3 days livetime: source declination δ in degrees, flux 90% confidence level upper limits for E^{-2} spectra ($E^2 \cdot \phi < \mu_{90} \cdot 10^{-11} \, \mathrm{TeV\,cm^{-2}\,s^{-1}}$), probability of observed or higher likelihood given random chance

this method. The resulting p-value map is shown in figure 4. The highest obtained p-value corresponds to 3.6σ. The probability of this deviation due to background alone is evaluated by comparing against 100 simulated experiments with randomized right ascension, and is found to be 69%.

References

[1] "One Year IceCube Point Source Analysis". This conference.

[2] A. Achterberg et al. *Phys. Rev. D*, 75:102001, 2007.

[3] J. Ahrens et al. *Nucl. Instr. Meth. A*, 524:169, 2004.

[4] G. Feldman and R. Cousins. *Phys. Rev. D*, 57:3873, 1998.

[5] A. Heijboer. 2004. Ph.D. Thesis, Universiteit van Amsterdam, Amsterdam, The Netherlands.

[6] G. C. Hill and K. Rawlins. *Astropart. Phys.*, 19:393, 2003.

[7] T. Neunhöffer. *Astropart. Phys.*, 25:220–225, 2006.

[8] T. Neunhöffer and L. Köpke. *Nucl. Instr. Meth. A*, 558:561, 2006.

Point source analysis for cosmic neutrinos beyond PeV energies with AMANDA and IceCube

R. FRANKE[1], R. LAUER[1], M. ACKERMANN[1,2], E. BERNARDINI[1] FOR THE ICECUBE COLLABORATION[3]

[1] *DESY, D-15735 Zeuthen, Germany*

[2] *Now at Stanford Linear Accelerator Center, Stanford, California 94305-4060, USA*

[3] *For a complete authorlist see special section in these proceedings.*

robert.franke@desy.de

Abstract: The Antarctic neutrino telescope AMANDA-II, part of the IceCube observatory, can be used for searches for cosmic point sources of neutrinos with a wide range of energy. The highest of these energy bands spans from about 10^5 to 10^{10} GeV. Several source models predict a significant neutrino flux in this part of the spectrum, for example from active galactic nuclei. Since the interaction length of neutrinos with energies above $5 \cdot 10^4$ GeV is smaller than the diameter of the Earth, the observable area lies mainly in the southern sky, in contrast to point source searches at lower energies. Nonetheless, the low atmospheric muon background at these energies makes such an analysis feasible, and it would comprise some interesting source candidates. We present the methods and sensitivity of this analysis as applied to data collected with the AMANDA-II detector during the year 2004. We comment also on the status of an equivalent analysis being developed for data from IceCube in its nine string configuration of 2006.

Introduction

Active galactic nuclei (AGN), and blazars in particular, are promising sources of high energy neutrinos detectable with the Antarctic Neutrino Telescope AMANDA-II, part of the IceCube observatory. Being candidates for the production of an observed flux of charged particles with energies up to a few hundred EeV, there is reason to expect a measurable neutrino flux beyond PeV energies from this class of objects. Additionally, theoretical models for several of these extra-galactic sources predict their neutrino spectra to be peaked in the PeV to EeV energy range, as for example presented in [7], [8].

An analysis with the aim to find neutrino point sources in this very high energy range is different from other point source analyses, as for example [1]. The usual approach to reduce the background of atmospheric muons is by selecting up-going neutrinos only, i.e. neutrinos which have traversed the Earth before interacting in the ice or bedrock near the detector. This effectively lim-

its the accessible neutrino spectrum due to the increase of neutrino cross section with energy. For multi-PeV neutrinos, the interaction length is much smaller than the diameter of the Earth and thus prevents most of the up-going neutrinos in this energy range from reaching the detector. On the other hand, down-going neutrinos from the southern sky high above the horizon have only the ice above the detector as target material and hence a significantly reduced interaction probability. Thus, a dedicated ultra high energy neutrino analysis must utilize a zenith angle band around the horizon, where the sensitivity of a standard search is limited by atmospheric muons. At higher energies, these muons form a much smaller background due to their soft spectrum. Bringing part of the sky in the southern hemisphere into the field of view also gives the possibility to observe candidate objects not included in other neutrino searches, thus enlarging the angular window where AMANDA-II is sensitive to point source signals.

Source Candidates

The main class of objects which are expected to emit a comparatively large flux of neutrinos at ultra high energies are blazars, particularly the GeV-blazars detected by EGRET and the TeV-blazars discovered by various air Čerenkov telescopes. The analysis is also sensitive to the galactic center as a possible source, lying in a region less than $30°$ above the horizon. The third EGRET catalog contains 39 confirmed AGN gamma ray sources with declinations between $+20°$ and $-30°$ [6]. The strongest sources have gamma ray fluxes of the order of 10^{-6} photons cm^{-2} s^{-1}, integrated for energies above 100 MeV.

In the final analysis, we will select a subset of these objects to avoid reducing the statistical significance by trial factors. As a first approach to find a suitable classification and identify the blazars with the highest potential as neutrino point sources, we extrapolate each gamma ray flux distribution to higher energies. The flux distribution is approximated with a power law $F(E) = F_0 \cdot E^{-\Gamma}$ where E is the photon energy and F_0 the flux normalization, making use of the spectral index Γ as measured by EGRET. For our current purposes of comparing the candidates, we assume a direct correlation between photons and neutrinos. We calculate the integrated photon flux $F_I = \int_{E_{th}}^{\infty} F(E)\,dE$ with $E_{th} = 100\,\text{TeV}$ as the lower energy threshold for this analysis. The resulting maximum values for individual sources lie in the order of 10^{-10} photons cm^{-2} s^{-1}.

We work on improving this first classification by using the parametrization of spectral energy distributions for blazars as presented in [4], with the plan to perform a more detailed study of flux predictions by individually fitting the observed EGRET spectra to the hadronic model used in [2]. In addition to the GeV blazars, the source list will include the galactic center and a sample chosen from 20 objects, located in the chosen zenith band, from which TeV gamma rays have been observed.

Reconstruction Methods

The point source analysis for neutrinos beyond PeV energies we present here is developed for data from the AMANDA-II detector taken during the year 2004. The detector consists of 677 optical modules (OMs) on 19 strings, most of which are deployed at depths between 1.5 and 2 km in the deep ice located at the Gepgraphic South Pole. For this analysis we use 540 OMs that show a stable performance. The analysis strategy is based on identifying tracks from neutrino-induced muons passing through the detector and emitting Čerenkov radiation.

To account for photon scattering in the ice, it is necessary to use likelihood algorithms to reconstruct particle tracks. An iterative maximum likelihood fit of the photon arrival times in the OMs finds the most probable muon track [3]. As a parametrization of the light propagation in ice we use an empirical model of the ice properties. The standard version of this likelihood approach includes only the timing information of the first photon hit in each photomultiplier. Monte Carlo simulations show, however, that the angular resolution of AMANDA-II with this reconstruction method degrades for higher energies. A high energy muon emits more photons per track length than one at lower energies. As photons are scattered independently in the ice, the order of arrival of multiple photons in one OM is not identical to their sequence of emission from the track. As a remedy for this we use an improved version of the likelihood fit. The likelihood is given by the probability that any of the detected photons in an OM arrives at the time of the first hit recorded in that OM and all other photons arrive at a later time [3]. This requires a numerical integration over the probability density function which is computationally expensive. For this reason, it is not possible to run the improved fit iteratively for each event, but instead the track result of the standard likelihood fit is taken as the initial hypothesis for the improved likelihood maximization.

In Monte Carlo simulations of a signal neutrino flux between 10^5 and 10^{10} GeV this method shows an improvement in median angular resolution. For an E^{-2} spectrum the angular resolution obtained with the improved fit is $3.87°$, compared to $6.9°$ for the standard approach. The resolution as a function of primary neutrino energy for the standard fit and improved fit method is shown in Fig. 1. The whole analysis was performed using the IceCube
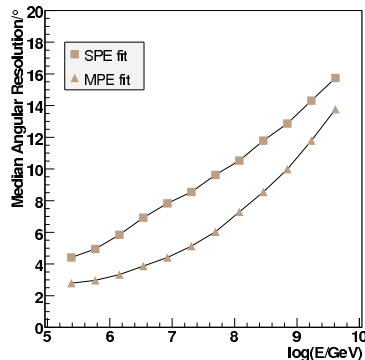
Figure 1: Median angular resolution in degrees as a function of primary neutrino energy from Monte Carlo simulation, reconstructed with the simple (SPE) and improved fit (MPE) accounting for multiple scattered photons. These resolutions are based on the discussed event sample with more than 140 hits and a one-photoelectron fraction smaller than 0.72.

software framework to simplify the use and exchange of tools and method implementations [5].

Event Selection

From the data collected with AMANDA-II in ca. 195 days of lifetime during 2004 we select events with a large light output that is likely to be caused by high energy events. We require at least 140 hits in the detector and a fraction of one-photoelectron hits smaller than 0.72. This results in a data sample of approximately $1.5 \cdot 10^7$ events. Standard cleaning procedures are applied to the sample to eliminate isolated hits and reduce electronically induced cross-talk.

The main background dominating the data sample after this first selection is intense muon bundles from energetic cosmic ray air showers, which can fake the signature of a single muon of higher energy. However, the light from intense muon bundles is expected to be distributed more evenly through the detector as it is emitted from multiple tracks instead of a single one as in the case of a signal event. A multi-PeV neutrino-induced muon emits significantly more photons through stochastic energy losses and Monte Carlo simula-
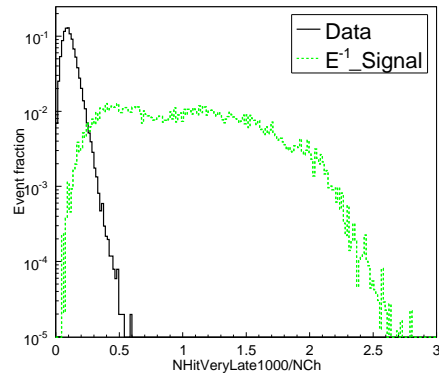
Figure 2: Ratio of late hits (hits ocurring more than 1000 ns after the first hit in that OM) to the number of hit OMs for an E^{-1} signal spectrum and experimental data.

tions show that this leads to a higher fraction of very late hits. We define very late hits as hits occurring more than 1000 ns after the first hit in the same OM. These can be caused by scattered photons or afterpulses in the photomultipliers. Normalizing the number of OMs with very late hits to the number of hit OMs yields a useful basic discrimination variable between expected signal and background, see Fig. 2.

Due to the long computation time of the improved likelihood method, this selection is also motivated by reducing the number of events before reconstruction. Hence, choosing a cut value for the afterpulse fraction is based on the aim to keep approximately 20 % of the (background dominated) data. Monte Carlo simulations of signal and background show that this implies a signal passing rate of 94 % for an E^{-1} spectrum and 98 % for an E^{-2} muon-neutrino spectrum. Therefore we select events with a fraction of OMs with very late hits larger than 0.15.

To estimate a sensitivity for this analysis, a number of background-signal discrimination variables have been examined. In a first iteration three variables sensitive to the light distribution in the detector and with respect to the track fit were chosen. These variables are the number of photons registered outside a 50 m cylinder around the track fit, the ratio of hit channels to the total number of hits and the ratio of late hits to the total number of hits. The cuts on these variables were optimized for sen-
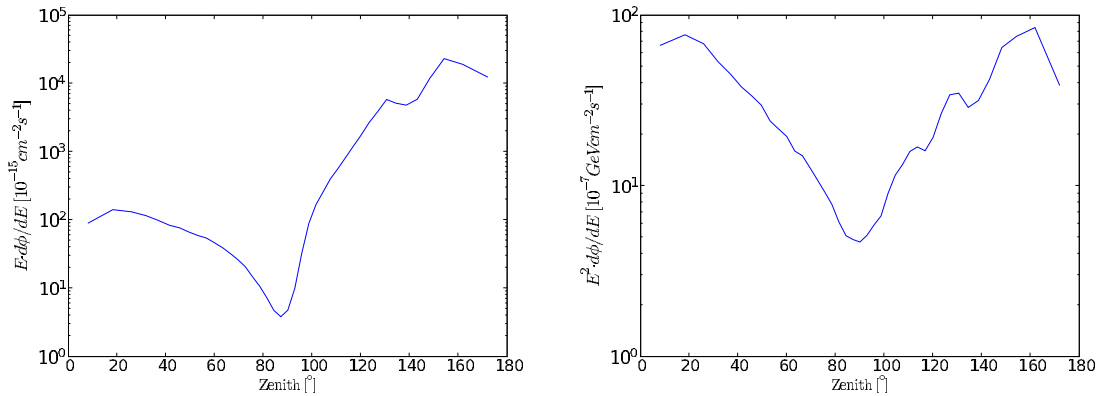
Figure 3: Preliminary sensitivities for this analysis for an E^{-1} (left) and E^{-2} (right) flux of muon neutrinos in the energy range from 10^5 GeV to 10^{10} GeV vs. zenith angle. The upper limit is shown as a limit to the normalization constant Φ_0 of the differential flux $d\Phi/dE = \Phi_0 E^{-\gamma}$, $\gamma = 1, 2$.

sitivity in different zenith bands, using the data as a background estimate. The achieved preliminary sensitivity versus zenith angle for this analysis can be seen in Fig. 3. For the E^{-1} signal spectrum 90% of the events over the whole zenith range have an energy between $3.6 \cdot 10^7$ GeV and $8.9 \cdot 10^9$ GeV after the cuts. At the horizon this energy range is $5.9 \cdot 10^7$ GeV to $9.0 \cdot 10^9$ GeV. For the E^{-2} spectrum the energy range which contains 90% of the events extends from $1.4 \cdot 10^5$ GeV to $1.2 \cdot 10^8$ GeV over the whole sky and from $2.0 \cdot 10^5$ GeV to $4.0 \cdot 10^8$ GeV at the horizon.

Conclusions and Outlook

Presented here is a dedicated analysis for the search for point-like sources of cosmic neutrinos beyond PeV energies. Our strategy enlarges the window for potential discoveries with AMANDA-II to parts of the southern sky and improves the methods for detecting neutrino events at the highest energies.

The concept of this analysis is currently being developed further with the aim to be applied to the data taken with IceCube in the nine string configuration of 2006. A preliminary study of reconstruction methods after a basic selection of high multiplicity hits shows an angular resolution of approximately $2°$. Due to the asymmetric detector configuration the sensitivity of the analysis is not ex-

pected to improve much compared to the results presented here for AMANDA-II. A significant improvement of the sensitivity for point-like neutrino sources with extremely high energies can be expected with the 22-string configuration of IceCube in 2007.

References

[1] A. Achterberg et al. *Phys. Rev. D*, 75:102001, 2007.

[2] F. Aharonian et al. *Astron. Astroph.*, 454:775–779, 2006.

[3] J. Ahrens et al. *Nucl. Instrum. Meth.*, A524:169–194, 2004.

[4] G. Fossati, L. Maraschi, A. Celotti, A. Comastri, and G. Ghisellini. *Mon. Not. Roy. Astron. Soc.*, 299:433–448, 1998.

[5] R. Franke. Diploma thesis, 2007. Humboldt University, Berlin.

[6] R. C. Hartman et al. *Astrophys. J. Suppl.*, 123:79, 1999.

[7] A. Yu. Neronov and D. V. Semikoz. *Phys. Rev.*, D66:123003, 2002.

[8] R. J. Protheroe, A. C. Donea, and A. Reimer. *Astropart. Phys.*, 19:559–568, 2003.

Nine-String IceCube Point Source Analysis

C. FINLEY[1], J. DUMM[1], T. MONTARULI[1,2], FOR THE ICECUBE COLLABORATION[3].

[1]*Dept. of Physics, Universtiy of Wisconsin, Madison, WI, 53706, USA*
[2]*on leave from Università di Bari, Dipartimento di Fisica, I-70126, Bari, Italy*
[3]*see special section of these proceedings*
chad.finley@icecube.wisc.edu

Abstract: The construction of the IceCube Neutrino Observatory began during the austral summer of 2004-05, and is expected to continue through 2011. During 2006, nine of the projected 80 strings were already deployed and taking data, making IceCube an operational neutrino observatory while still at about 10% of its final size. We present the first results of a point-source search based on the analysis of this year of data, and characterize the angular resolution and effective area of the nine string configuration. With 137.4 days of detector livetime, 233 neutrino candidate events were selected in the analysis; the sky-averaged point-source sensitivity for an E^{-2} spectrum is $\frac{d\Phi}{dE} = 12 \times 10^{-11}$ TeV^{-1} cm^{-2} s^{-1} $(E/\text{TeV})^{-2}$. No significant point-source is found. We also discuss how the performance is expected to improve as the detector moves toward completion.

Introduction

The IceCube Neutrino Observatory is a cubic kilometer-scale detector under construction at the geographic South Pole. Its primary mission is the search for high energy extraterrestrial neutrinos, which may reveal the origin of cosmic rays and offer insight into the most energetic phenomena in the universe. The detector consists of an array of digital optical modules: 60 modules are connected on one string, and a planned total of up to 80 strings are to be deployed in the Antarctic ice at depths between 1.5 and 2.5 kilometers beneath the ice surface. Construction is limited to the austral summer time, and therefore is spread over a number of years. As the detector grows, commissioning of the new strings and data-taking occur during the rest of the year.

Nine strings were in operation during 2006, shown in Figure 1. At about 10% of its completed size, the partial detector configuration is not optimal: muon tracks which traverse the long axis of the detector can be reconstructed much more accurately than those which pass through from other directions. Nevertheless, high-quality data was obtained between June and November, providing the
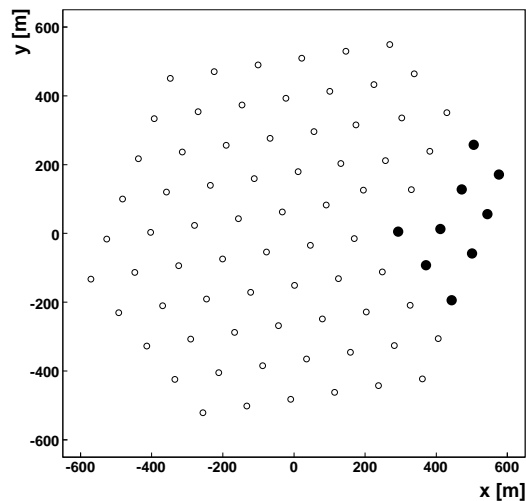
Figure 1: Configuration of IceCube strings; filled markers indicate the location of the nine strings already deployed and taking data in 2006.

first opportunity to perform a search for extraterrestrial neutrinos with the IceCube detector. Point source searches like the one presented here are the simplest and most direct way to distinguish an extraterrestrial neutrino signal from the experimental backgrounds. Discovery of point sources would also directly indicate the sites of cosmic ray acceleration.

Method

An unbinned maximum likelihood method is used to search for point sources. For a specified, hypothetical source location x_s and total number of events n_{tot}, the source hypothesis is that the data set is a mixture of n_s signal events (distributed around the source according to their individual angular uncertainty) and $n_{tot} - n_s$ background events (distributed over the sky according to the detector background distributions). This can be expressed as the partial probability P_i of each event:

$$P_i(x, x_s, n_s) = \frac{n_s}{n_{tot}} S_i(x, x_s) + \left(1 - \frac{n_s}{n_{tot}}\right) B_i(x)$$

where $S_i(x, x_s)$ is the source pdf of the event (determined by its angular uncertainty) and $B_i(x)$ is the background pdf. The background pdf is determined by using the declination distribution of the real data set.

The likelihood $\mathcal{L}$ is defined as the product of all individual event pdf's evaluated at the event and source coordinates:

$$\mathcal{L}(x_s, n_s) = \prod P_i(x_i, x_s, n_s)$$

The best estimate for the number of signal events $\hat{n}_s$ is found by maximizing the log likelihood ratio λ with respect to the null hypothesis $n_s = 0$:

$$\log \lambda = \log \frac{\mathcal{L}(x_s, \hat{n}_s)}{\mathcal{L}(x_s, n_s = 0)}.$$

log λ is the test statistic which determines the significance of an observed deviation from the null hypothesis.
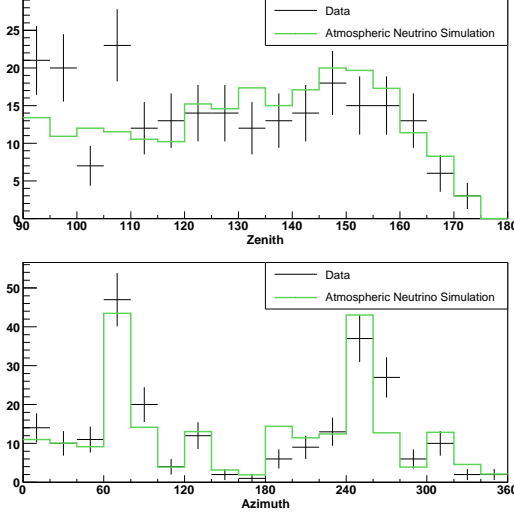
Figure 2: Distribution of data events in zenith and azimuth after analysis cuts have been applied, compared with simulated atmospheric neutrino events. (Note: declination $\delta = \theta_{zen} - 90°$.)

Event Selection

Data in this analysis first passed two levels of filtering to reject down-going muon events; these filter levels are described in [1]. The remaining events were reconstructed using a likelihood algorithm that also provides an angular uncertainty estimate by evaluation of the likelihood function around the direction of the best fit. After filtering, the main background is still mis-reconstructed down-going muons and muon bundles from cosmic ray showers. To reduce this mis-reconstructed background, a tight cut on each track's angular uncertainty was used, and only tracks which reconstructed as up-going (zenith angle greater than $90°$) are kept in the analysis. A second cut on the minimum number of modules which were hit by direct Cherenkov photons (as estimated for the reconstructed track, using a time window of -15 to $+75$ ns around the expected arrival time) provides additional background rejection, primarily of down-going muons from two different cosmic ray showers which trigger the detector in coincidence and reconstruct as a single upward-going event. What remains after tight cuts on both of these parameters is the "irreducible" background of well-
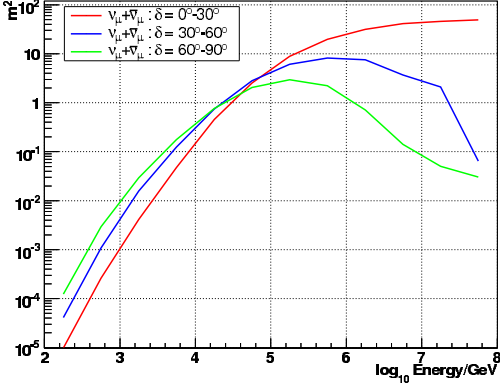
Figure 3: IC-9 effective area to a flux of $\nu_\mu + \bar{\nu}_\mu$, averaged over different declination ranges.

reconstructed upward-going atmospheric neutrino events, the product of cosmic ray showers in the northern hemisphere.

To determine the final cut values, the point source analysis was performed on simulated data sets, consisting of simulated source events added to real data scrambled in right ascension. The cuts were optimized for discovery potential: the combination of cuts which could detect the smallest source flux at 5σ significance in 50% of the trials. For most possible source declinations and a range of spectra ($\frac{d\Phi}{dE} \propto E^{-\gamma}$ for the range $\gamma = 2$ to $\gamma = 3$) the optimal cuts were the same.

Data Sample

Data taking occurred between June and November 2006. The detector livetime was 137.4 days. The zenith distribution of data events is shown after final cuts and compared with simulated atmospheric neutrino events (using the spectrum predicted by the Bartol group[2]) in Figure 2. The final sample is restricted to events with declination less than $85°$, because the right-ascension scrambling technique for estimating background does not work near the pole, where statistics are low and the events cannot be scrambled. After cuts, there are 233 events in the data sample, and 227 predicted atmospheric neutrino events. The excess of data events at low zenith angles is most likely misreconstructed down-going muons, which are in-
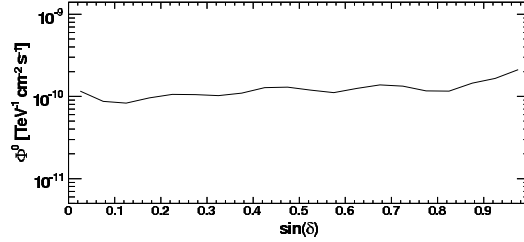
Figure 4: IC-9 sensitivity as a function of declination to a point source with differential flux $\frac{d\Phi}{dE} = \Phi^0 (E/\text{TeV})^{-2}$. Specifically, Φ^0 is the minimum source flux normalization (assuming E^{-2} spectrum) such that 90% of simulated trials result in a log likelihood ratio $\log\lambda$ greater than the median log likelihood ratio in background-only trials ($\log\lambda = 0$).

creasingly hard to reject near the horizon. Because the cut optimization was performed using scrambled real data, this residue of mis-reconstructed events indicates that harder cuts, which could eliminate these events entirely, would ultimately decrease the discovery potential.

The azimuth distribution of data and simulation is also shown in Figure 2. The two directions corresponding to the long axis of the nine-string detector are clearly visible. For other directions, it is more difficult to reconstruct tracks with high accuracy and to reject background.

The effective area to an equal-ratio flux of $\nu_\mu + \bar{\nu}_\mu$ is shown in Figure 3. In Figure 4, the sensitivity (median flux upper limit) is shown as a function of declination. The sky-averaged point-source sensitivity to an E^{-2} source spectrum is $\frac{d\Phi}{dE} = 12 \times 10^{-11} \text{ TeV}^{-1} \text{ cm}^{-2} \text{ s}^{-1} (E/\text{TeV})^{-2}$. The median angular reconstruction error is $2.0°$.

Results

The analysis consists of an all-sky point source search, and individual point source searches using a pre-defined source list. The result of the all-sky search is shown in Figure 5. The maximum upward deviation from background is at r.a. $= 276.6°$, dec $= 20.4°$, with 3.35σ significance. This is consistent with random fluctuations: in simulations of
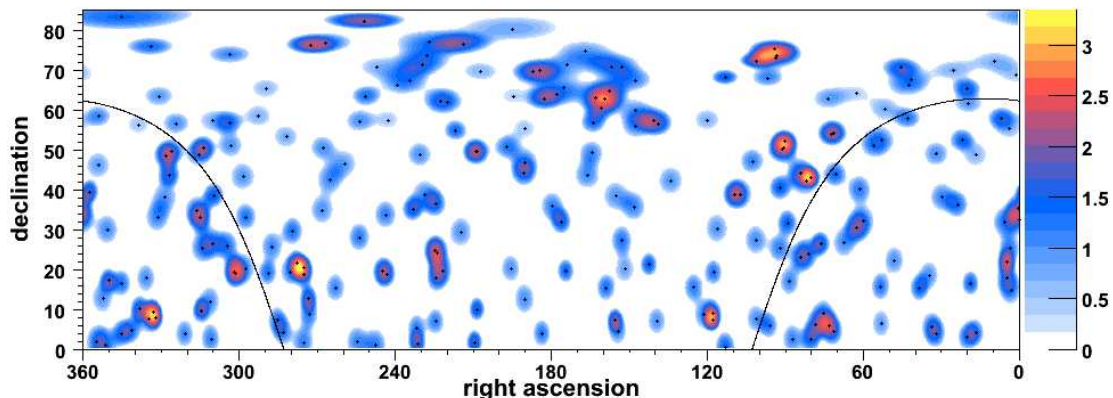
Figure 5: Sky map of the significance $[\sigma]$ of deviations from background, estimated from the maximum likelihood point-source search. (Black points are reconstructed event directions.)

background-only data sets (data scrambled in right ascension), 60% have a maximum deviation (anywhere) of $3.35\,\sigma$ or greater.

Twenty-six galactic and extragalactic objects were included in the pre-defined source list. Of these, the most significant excess over background was $1.77\,\sigma$, found for the Crab Nebula. This is also consistent with random fluctuations: the probability for at least one out of 26 source directions to have an excess of $1.77\,\sigma$ or greater is 65%. The 90% confidence level flux upper limit for the Crab Nebula is $\frac{d\Phi}{dE} = 22 \times 10^{-11}\,\mathrm{TeV^{-1}\,cm^{-2}\,s^{-1}}\,(E/\mathrm{TeV})^{-2}$.

Discussion

Nine IceCube strings (out of a projected total of 80) were operating and taking data in 2006. Analysis of this first year of data indicates that the point-source sensitivity of the nine string detector is comparable to an equivalent livetime of the AMANDA-II detector. This is a promising result, given that the configuration of the nine-string detector is far from optimal. For example, as seen in Fig. 2, more than half of the well-reconstructed events arrive from less than 10% of the full range of azimuth. Therefore as construction continues, enlarging the array will not only increase the detector volume, but also greatly improve the angular resolution in all directions. This should become

apparent with the 22-string configuration which began operating this year. Continued software development should also deliver more advanced track reconstruction algorithms and background rejection techniques. The current analysis can serve as a benchmark for evaluating the performance of these new tools. Extrapolating the present rate of growth, the IceCube Neutrino Observatory will begin to deliver results of unsurpassed sensitivity well before detector construction is completed.

Acknowledgments

References

[1] A. Achterberg et al. Detection of atmospheric muon neutrinos with the IceCube 9-string detector. *Phys. Rev.*, D76:027101, 2007.

[2] G. D. Barr, T. K. Gaisser, P. Lipari, Simon Robbins, and T. Stanev. A three-dimensional calculation of atmospheric neutrinos. *Phys. Rev.*, D70:023006, 2004.

Search for Signatures of Extra-Terrestrial Neutrinos with a Multipole Analysis of the AMANDA-II Sky-map

J.-P. HÜLSS[1], CH. WIEBUSCH[1] FOR THE ICECUBE COLLABORATION[a]

[1] *RWTH Aachen University, Aachen, Germany;* [a] *see special section of these proceedings*

huelss@physik.rwth-aachen.de

Abstract: In this analysis 3329 neutrino events detected by AMANDA-II during the years 2000-2003 are analysed for anisotropies or unexpected structures in their arrival direction. The structures could arise due to the presence of a signal from many weak and therefore unresolved cosmic neutrino sources, a few brighter sources or extended sources (e.g. a diffuse flux from the galactic plane). The sky-distribution of arrival directions (sky-map) is expanded in a series of spherical harmonics and the power in each multipole moment is calculated. Compared to previous AMANDA-II analyses, it provides a new complementary approach, in particular in the search for very weak individual astro-physical sources. No excess from extra-terrestrial sources is found. Statistical errors as well as systematic errors related to the uncertainty of the angular distribution of the atmospheric neutrinos are quantified using the Feldman-Cousins unified approach. Limits for contributions from extra-terrestrial sources to the sky-map are derived as function of the average source strength and the spectral index of the energy spectrum for different sky-distributions: weak sources isotropically distributed in the northern sky, sources located in the galactic and super-galactic plane. The tested average flux per source varies between $\phi_{low} = 5 \cdot 10^{-13}$ cm^{-2}s^{-1} and $\phi_{high} = 5 \cdot 10^{-11}$ cm^{-2}s^{-1} at the earth, assuming an E^{-2} power spectrum in the sensitive energy range between 1.6 TeV and 1.6 PeV. The number of sources in the sky can be limited at 90% C.L. to be less than 3524 for the assumed ϕ_{low} and less than 28 for ϕ_{high}.

Introduction

There are several proposed candidate objects which could be neutrino sources in the universe, e.g. Active Galactic Nuclei, Supernova Remnants or Micro Quasars.

A direct measurement of these neutrinos is not possible. However, they produce high energetic muons in charged current interactions. Which points into the initial neutrino direction. The charged muons produce Cherenkov-Light passing through the deep ice at the South Pole. The emitted light is measured with the AMANDA-II detector [1] using photomultipliers and the direction and energy of the muon is reconstructed.

The AMANDA-II detector was completed in 2000 and is taking data since then. This analysis uses 4 years of AMANDA-II data (2000 to 2003, 807 days lifetime). The main background are muons produced in the atmosphere. To reject these events only up-going events are included in this sample.

This reduces the field of view to the northern sky. The final event sample consists of $N = 3329$ muon neutrino events. The measured data is reconstructed and filtered as described in [1]. The background of miss-reconstructed down-going muons in this sample is below 5%.

Angular Power Spectrum

This analysis compares the angular power spectrum of the measured data to the background expectation of neutrinos produced in the atmosphere. The data is expanded by means of spherical harmonics $Y_l^m(\theta, \phi)$. The multipole index l characterises the angular scale ($\delta \approx \pi/l$) and m the orientation of the angular structures. Small l correspond to large angular scales (e.g. overall sky-distribution). Small structures appear at large l (e.g. angle between sources). Orientation averaged observables are the multipole moments C_l (power

components):

$$C_l = \frac{1}{2l+1} \sum_{m=-l}^{l} |a_l^m|^2,$$

$$a_l^m = \int_\Omega \sum_{i=1}^{N} \delta(\theta_i, \phi_i) \bar{Y}_l^m(\theta, \phi) d\Omega.$$

Ω stands for the integration over the unit sphere. The software GLESP [3] is used to calculate the integral.

The accuracy of the calculated C_l values from GLESP is limited by the event statistics. The obtained values for C_l which are expected to be zero are found to be non-zero but to scale about as $C_l \sim C_0/N$ and C_0 is normalised to π. The AMANDA-II point source resolution is about $3°$ corresponding to $l \approx 60$. An estimate for the maximum l is provided by the mean angle between the data points: 29 mrad corresponding to $l \approx 116$. A limitation for the maximum l is derived from the degrees of freedom. This is $l = 57$ for 3329 events.

Correlations between the multipole moments due to the limited aperture are taken into account in the statistical analysis.

Data and Background Simulation

The angular power spectrum for the background (atmospheric neutrinos) and different signals is estimated by simulations. Each simulated data set has 3329 events (same as the experimental sample) and contains atmospheric background as well as signal events. The neutrinos are distributed according to the angular acceptance of AMANDA-II. This acceptance is energy dependant. The directions of all simulated neutrinos are varied randomly according to the angular resolution function of AMANDA-II.

The simulation of the atmospheric neutrinos is done according to their angular zenith distribution. Theoretical uncertainties are considered by varying the assumed distribution randomly within it's uncertainties for each simulated data set. For the azimuth angle a flat distribution is assumed due to the rotation of the detector.

Source neutrinos are simulated with a Poisson-distributed number of events per source at the earth

and an power law energy spectrum. The mean number of events varies between $\mu = 0.1$ (corresponding to $\phi \approx 5 \cdot 10^{-13}$ cm^{-2}s^{-1}) and $\mu = 10$ (corresponding to $\phi \approx 5 \cdot 10^{-11}$ cm^{-2}s^{-1}). ϕ is the integrated flux per source at the earth in the sensitive range between 1.6 TeV and 1.6 PeV assuming an E^{-2} energy spectrum. Source locations are simulated isotropically distributed in the northern hemisphere or located in the (super) galactic plane.

Figure 1 shows the angular power spectrum for atmospheric neutrinos compared with an example spectrum for extra-terrestrial neutrinos. The steep falling of the spectrum for $l < 6$ appears due to the restriction to the northern sky while the flat tail corresponds to the statistical limitation of GLESP (see above). Error bars are derived from the RMS spread found for 1000 simulated and analysed data sets. The tested multipole moments C_l for the analysis are chosen by simulation according to their sensitivity for a certain signal [2]: $C_{2/3/5}$ for isotropic distributed sources with a flux below $\phi = 5 \cdot 10^{-12}$ cm^{-2}s^{-1}, C_{1-40} for a higher flux and C_{1-15} for the (super) galactic plane. For weak sources ($\mu \leq 1$) using only $C_{2/3/5}$ restricts the sensitivity to the overall distribution of the neutrinos.

Experimental Result

The analysis steps have been optimised using simulation without referring to the data (blind analysis). The angular power spectrum of the experimental data is calculated in the same way as for the simulated data. Figure 1 shows the result. The experimental moments are generally within the errors of the background expectation and no general deviation is observed. For further analysis

$$d_l \equiv (C_l^{exp.} - C_l^{sim.})/\sigma_l$$

is defined as the difference between measurement and simulation normalised to the combined uncertainty from statistics and the model dependence. The average $< d_l >$ over l for the experimental data and the purely atmospheric expectation is $< d_l >= 0.2 \pm 0.14$ with a $RMS = 1.0 \pm 0.3$. The value $D^2 = \sum_{l=1}^{40} d_l^2 = 57.2$ is calculated. The probability to obtain a larger D^2 is 7% (from
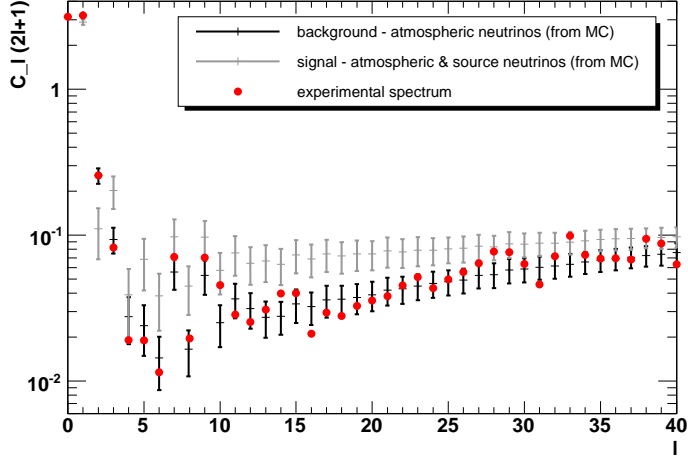
Figure 1: Expected angular power spectrum for atmospheric neutrinos (black) and one signal example (gray) (both from Monte Carlo Data) compared to the experimental spectrum (red dots). The example data is simulated for 110 sources in the northern sky with a flux per source $\phi = 5.23 \cdot 10^{-11}$ cm^{-2}s^{-1}. The error bars include systematic errors as described in the text.

the simulations). This is the probability for consistency of experimental data and the purely atmospheric expectation. It does not show a good agreement. However, this probability does not reject the purly atmospheric assumption.

Limits on Cosmic Contributions

The contribution of signal events in the experimental sample is tested by means of the observable $D^2 = \sum d_l^2$. Upper limits on these are derived by constructing confident belts according to [4] as a function of the number of signal neutrinos in the data sample.

The derived upper limits for an energy range from 1.6 TeV to 1.6 PeV and an E^{-2} energy spectrum are shown in table 1 and in figure 2. The limit on the total number of signal neutrinos in the data sample is almost independent of the source strength. We limit the contribution from isotropically distributed sources to be less than about 300 events total and less than about 200 events for the (super) galactic plane. As expected the results for the galactic and super galactic plane are nearly identical. The step in the limits for the isotropically distributed sources corresponds to the change in the used l (see above).

The limits on the number of neutrinos can be converted to limits on the number of sources (fig. 2). The number of sources is decreasing with increasing strength. The tested flux per source in this analysis is chosen to be below the flux limit for resolved sources $\phi = 4.38 \cdot 10^{-11}$ cm^{-2}s^{-1} derived by [1]. However, limits on the number of sources presented here depend on the assumed sky distribution of the sources and the equal source strength.

With this analysis further limits are derived [2]. Table 1 shows limits for other power law energy spectra.The limit on a diffuse neutrino flux (E^{-2}) is about $5 \cdot 10^{-7}$ GeV^{-1}cm^{-2}s^{-1}sr^{-1}. This is a factor 2 to 3 worse compared to the actual limit set by AMANDA-II. A diffuse flux ($E^{-2.7}$) from the galactic plane is limited to be below $E^{2.7} \cdot d\phi/dE < 3.4 \cdot 10^{-3}$ GeV$^{1.7}$cm^{-2}s^{-1}sr^{-1} with 90% C.L.. $C_{2,3}$ are sensitive to atmospheric neutrino oscillation. Figure 1 shows no difference between the expectation and the experimental result. We derive a limit $\Delta m^2_{atms.} < 5 \cdot 10^{-3}$ eV^2 (90% C.L.) for maximum mixing.

Conclusion

For the first time the technique of a multipole analysis, well known from CMBR, is applied to the
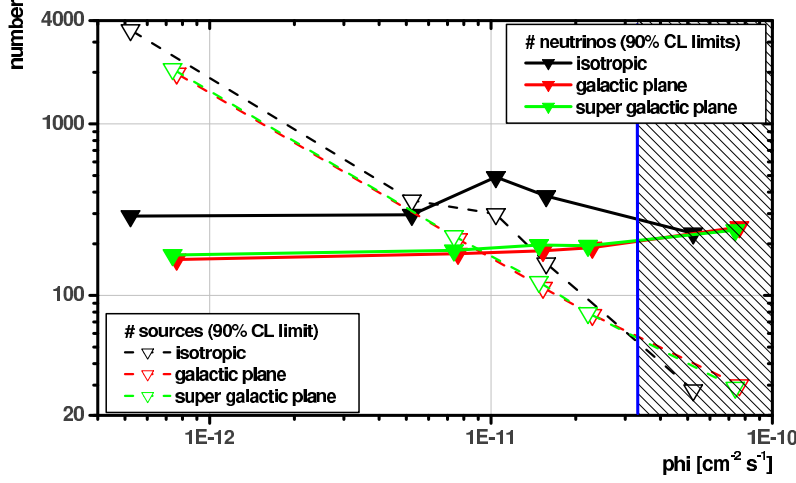
Figure 2: 90% CL upper limits on the number of neutrinos from extra terrestrial sources in the data sample (full lines) and on the number of sources in the northern sky (dashed lines) for different distributions assuming an E^{-2} energy spectrum. Complementary to this analysis the direct search for point sources excludes any source above a flux of $\phi = 4.38 \cdot 10^{-11}$ cm^{-2}s^{-1} [1]. This restriction is indicated as the shaded region in the graph.

AMANDA-II data. It is found suitable to search for a signal of extra-terrestrial neutrinos. The analysis is not well optimised yet. For the future with increased statistics and improved analysis we expect a substantially increasing sensitivity.

References

[1] A. Achterberg et al. (The IceCube Collaboration): Five years of searches for point sources of astrophysical neutrinos with the AMANDA-II neutrino telescope; astro-ph/06 11063, 2006, accepted for publication in Phys. Rev. D, 2007.

[2] J.-P. Hülß: Search for Signatures of Extra-Terrestrial Neutrinos with a Multipole Analysis of the AMANDA-II Sky Map; diploma thesis, WU D 06-04, University Wuppertal, Germany, 2006.

[3] A.G. Doroshkevick et al.: Gauss-Legendre Sky Pixelation (GLESP) for CMB maps; astro-ph/0305537 v4, 2005.

[4] G. Feldman, R. Cousins: A Unified Approach to the Classical Statistical Analysis of Small Signals; Phys. Rev. D57:3873-3889, 1998.

	μ	0.1	1	2	3	10
isotropically distributed sources						
E^{-2}	ϕ	0.52	5.2	10	16	52
	N_ν	290	295	490	380	230
	N_S	3524	358	298	154	28
$E^{-2.5}$	ϕ			29	43	
	N_ν			775	625	
	N_S			625	298	
sources in the galactic plane						
E^{-2}	ϕ	0.76	7.6	15	23	76
	N_ν	162	175	182	190	250
	N_S	1968	213	111	77	30
$E^{-2.4}$	ϕ			36	53	
	N_ν			168	172	
	N_S			115	78	
sources in the super galactic plane						
E^{-2}	ϕ	0.74	7.4	15	22	74
	N_ν	172	183	197	195	240
	N_S	2090	222	120	79	29
$E^{-2.4}$	ϕ			33	49	
	N_ν			175	178	
	N_S			119	81	

Table 1: Derived 90% CL limits on the number of measured extra terrestrial neutrinos N_ν and the number of sources in the northern hemisphere N_S depending on the source flux ϕ (in 10^{-12}cm^{-2}s^{-1}) and the energy spectrum.

Cluster Search for neutrino flares from pre-defined directions

K.SATALECKA[1], E.BERNARDINI[1], M.ACKERMANN[12], M.TLUCZYKONT[1] FOR THE ICECUBE COLLABORATION[3]

[1] *DESY Zeuthen, Plataneneallee 6, D-15738, Germany*

[2] *Stanford Linear Accelerator Center, Stanford, California 94305-4060, USA*

[3] *see special section of these proceedings*

elisa.bernardini@desy.de

Abstract: We present here a method to search for clusters of high energy neutrinos from pre-defined directions, a study of the background rate over short time scales, and report novel results obtained from AMANDA data from years 2004 to 2006. The time structures we search for must indicate an occasional deviation from the background hypothesis while not contradicting observations from time-integrated searches. In the context of the multi-messenger approach, where the information from high energy neutrinos and different electromagnetic wavelengths (e.g., high energy gamma-rays) is combined, we look for correlations between the high energy neutrinos and high states of γ-ray emission of selected sources. This test is performed before the cluster search in order to prevent a posteriori findings of coincidences of neutrino events with γ-ray flares once a significant cluster is found.

Introduction

Different observations of some candidate neutrino sources indicate that their electromagnetic emission is very variable and often shows a flare-like behavior. According to several models one can expect that the neutrino emission from those sources have a similar character. Time integrated analyses [1] [4] [3] are not always sensitive to this behavior: if signal events are emitted in flares, for an equivalent signal efficiency the integrated background is higher over longer exposures. We therefore developed a dedicated time variability analysis with the goal of improving the discovery chance.

Using a time-clustering algorithm, we look for time structures (clusters) in the time distribution of the neutrino events from certain directions. This approach has the advantage of being independent of any a priori assumption on the time structure of the potential signal, but is affected by a high trial factor. An issue for this type of analysis is the reliability of the background estimation over short time scales. So far the background was estimated from the event density as a function of the declination (similar to the ON/OFF-source approach of

γ-ray astronomy) [1]. This method however fails when applied to short time scales due to the limited event statistics. To address this problem we developed a parametrization of the background which reduces its statistical uncertainty. In the next section we describe in more detail the principle of this analysis, discuss its performance in comparison to previous analyses and give results obtained on data collected with AMANDA-II in 2004 to 2006.

The analysis presented here is realized in two steps. In order to prevent a posteriori observations of coincidences with γ-rays we first test the event sample for a coincident γ-ray emission for those sources and periods when the γ-ray data is available. The outcome of this test is declared positive if an excess significance equal or higher than 5σ is found. If in the first step none of the observations shows a significance of 5σ or higher (or if there are not enough γ-ray data for a coincidence study) we apply the time-clustering algorithm to the whole analysis period for a set of selected sources. Three types of sources were chosen for this analysis: blazars, XRBs and radio laud AGNs [2]. The selection criteria required: a variable character of the source in one or more wavelengths and indications of non-termal emission.

Time-clustered search for neutrino bursts

For each preselected direction all combinations (clusters) of the arrival time of events within a certain angular bin are constructed. For each cluster its multiplicity (m) is compared to the expected background (μ_{bg}^{loc}) and the significance of the cluster (S_{bg}) is calculated. The cluster with the highest significance (S_{bg}^{best}) is chosen as the "best". The overall probability (P, trial factor corrected) to observe a cluster of significance S_{bg}^{best} or higher is calculated based on 10,000 Monte Carlo (MC) experiments. The main difference between this analysis and what was presented in [2] is that in this work no assumption is made on the duration of signal flares. Moreover, a correct background estimation over short time scales is necessary, in order to properly calculate the cluster's significance and its compatibility with the background hypothesis. The method used previously in the time integrated analysis [1] is simple and fast. However due to the low statistics it is affected by large uncertainties in a case of short time scales (e.g. $\Delta t < 10$ days).

A different approach for a background estimation has been developed for this work. We first tabularise the detector up-time development. This takes into account the inefficiency periods and data gaps after the data quality selection. Once corrected for the detector exposure we calculate the expected neutrino rate from the whole northern sky[1] by fitting the event rate versus time. We obtained 4.13±0.13/3.7±0.13/4.30±0.13 events per day (μ_{bg}^{year}) for 2004/2005/2006 respectively. For each sky angular bin the number of expected events in the whole data period (i.e year 2004, 2005 or 2006) is then calculated as:

$$\mu_{bg}^{loc} = \mu_{bg}^{year} \times \frac{N_{band} \times A_{bin}}{N_{all} \times A_{band}} \qquad (15)$$

where: N_{band} the number of events in the declination band in the sky defined by the bin size, N_{all} the number of all events in the sample for the analysed year, A_{bin} the area of the angular search bin, and A_{band} the area of the declination band defined by the size of the angular search bin. The ratio N_{band}/N_{all} allows to account for the different background density at different declinations.

The result of equation (1) is what we expect when we neglect the variation of the efficiency with the azimuth angle caused by the asymmetrical shape of the detector, (shown in 1) and assume a continuous up-time. The variability averages out for long
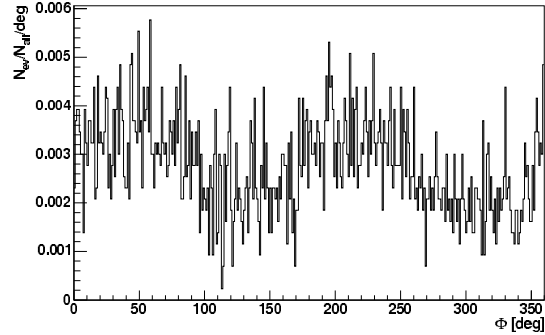
Figure 1: The normalized azimuth distribution of the data sample reported in [1].

periods of data. However, it plays a role for very short periods of integration. We therefore correct the value estimated in equation (1) for the effective azimuth exposure, calculated for each individual time cluster. The correction applied is given by the integral of the azimuth efficiency over the time period of a cluster, taking into account the effective time coverage (up-time) of the azimuth bin. The overall error in the background estimation is a combination of a statistical uncertainty, the error of the fit and the uncertainty introduced by the azimuth corrections.

A comparison of the outcome of this method to previous results shows that for short time scales the new method yields much smaller uncertainties while for longer time periods they are in very good agreement. For example for $\Delta t = 3$ days, we could achieve in this analysis an error of 20% compared to 30% in previous works.

Fig. 2 shows a study of the neutrino flare detection chance depending on the strength and duration of the signal. We produced about 10,000 MC experiments simulating a variable neutrino point-source of different signal strengths and durations,

---

1. We did not observe any dependency of the results for different choices in the binning of the event rates or angular regions of the sky (e.g. estimating the expected rate for different declination regions).

116

on a background μ_{bg}, characteristic for a chosen region of the sky. Positions in the sky of the on-source events were generated randomly, corresponding to the Point Spread Function, while the number of signal and background events were generated using corresponding Poisson averages. We performed this study for the cases of fixed and variable angular search bin size (chosen among the set of angular distances of the events relative to the sky positions of the pre-selected sources). We found that the best detection chance is obtained with a variable bin size.

The results of the cluster search for neutrino flare for 2004 to 2006 are reported in Table 2.
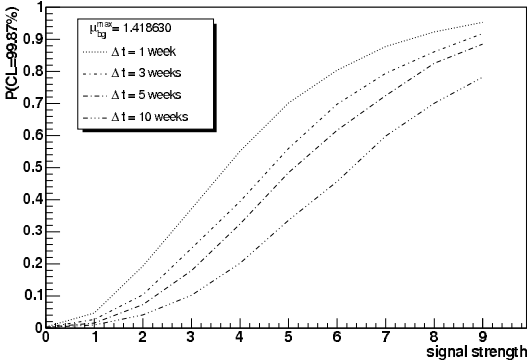
Figure 2: Probability of detecting a neutrino flare with a significance of 99.87% or higher in one year of data (2004 in this example). The X-axis shows the signal strength (mean number of signal events). The curves indicate different time duration of the signal (1, 3, 5 or 10 weeks).

Search for neutrino events in coincidence with γ-ray flares

Observations of strong variability in the high energy (TeV) γ-ray emission exist for various TeV neutrino candidate sources. However, often there is no long coverage of their flux and also a very limited knowledge exists on the frequency of γ-ray flares, as well as on their eventual time correlation with neutrino flares. Nevertheless, a search for coincidences between high energy neutrinos and γ-rays can possibly increase the discovery chance. Here we present the results of a test for correla-

tion of neutrinos with high state of γ-ray emission for a sub-sample of objects for which γ-ray data for the years 2004 to 2006 are published. For each selected source we established a flux threshold for the selection of periods of interest. The number of neutrino events observed - n_{obs} - in the whole period was compared to the expected background - μ_{bg} - and the significance of this observation was calculated.

The threshold to the gamma-ray flux was chosen based on an analysis of combined light-curves [5]. For each source we considered the integral flux above variable thresholds (S) and optimized the latter for the best S/sqrt(B), where B is proportional to the time coverage of the periods above threshold. We exclude periods of measurement gaps longer than one week as well as periods with upper limits on the flux only. In a case of Cygnus X-1 only one day of significant measurement was available so we took the sensitivity of the experiment as the flux threshold.

The results of the search for neutrino events in coincidence with γ-ray flares are reported in Table 1. No significant excess was found.

Table 1: Results of the search for neutrino events in coincidence with γ-ray flares. Column "Selected periods" give the year and integrated up-time of the detector in days.

Source	Sel. periods	n_{obs} / μ_{bg}
Mkn421	2004 (7.6)	0 / 0.057±0.007
	2005 (1.0)	0 / 0.0067±0.0008
	2006 (10.8)	0 / 0.078±0.009
Mkn501	2005 (21.1)	1 / 0.13±0.02
1ES1959+650	2005 (0.95)	0 / 0.0040±0.0007
BL Lac	2005 (2.0)	0 / 0.008±0.001
H1426+428	2006 (3.0)	0 / 0.018±0.002
Cyg X-1	2006 (1.0)	0 / 0.0070±0.0008
M87	2005 (4.7)	0 / 0.033±0.004

Results

The input data sample for this analysis for 2004 and 2005 was taken from [1] and [3] respectively. For 2006 we used the results of the AMANDA online event reconstruction and filtering chain, which was implemented following the scheme reported in

[1]. After excluding periods of IceCube calibration with an artificial light source and selecting high quality data we used 247.5/199.9/239.5 effective days of data taking for the year 2004/2005/2006. Table 2 reports the results of the cluster search for neutrino flares for combined data sets of 2004, 2005 and 2006. The highest excess observed (for Cygnus X-3) corresponds to 3.56σ. The overall probability to observe a cluster of this significance or higher at any time in the whole periods analyzed equals 5.9% (not including the trial factors due to looking on several sources) and is well compatible with the background hypothesis.

Table 2: Results of the search for neutrino clusters: duration Δt [days], angular bin size $\Delta\psi$ [deg], significance of the best cluster found S_{bg}^{best} [σ] and the overall probability to observe a cluster of this significance or higher at any time in the whole periods analyzed P [%] .

Source	Δt	$\Delta\psi$	S_{bg}^{best}	P
Mkn 421	3.9	5.2	1.6	95.0
Mkn 501	26.5	4.8	3.2	14.5
Mkn 180	0.35	2.2	2.92	30.0
1ES 1959+650	11.2	2.8	2.82	29.0
1ES 2234+514	42.2	3.4	2.7	35.0
1ES 1218+30.4	5.0	6.0	1.4	95.0
BL Lac	51.6	4.6	2.45	46.0
H1426+428	4.4	5.2	1.5	92.0
3C 66A	7.7	5.0	2.45	44.0
3C 454.3	8.1	4.8	2.7	33.0
GRO J0422+32	19.5	5.8	1.75	90.0
GRS 1915+150	94.4	2.0	3.2	8.4
LSI+61 303	0.2	4.5	2.9	31.0
Cyg X-1	27.5	6.37	3.2	15.0
Cyg X-3	**8.8**	**4.3**	**3.56**	**5.9**
XTE J1118+480	31.1	4.5	2.25	64.0
3C 273	194.5	6.1	2.88	9.1
M87	11.1	6.6	2.0	69.0

Summary

We have presented the first search for neutrino flares from pre-selected sources in AMANDA-II with no a priori assumption on the time structure of the signal. In order to prevent a posteriori findings of coincidences with γ-ray flares a pre-test was performed, to look for correlations between the high energy neutrinos and high states of γ-ray emission of selected sources. In both cases no significant excess was found above the expected background. To accomplish the time-clustered search we have developed a new background estimation method which allows to reduce the statistical uncertainties as compared to the classical ON/OFF-source approach. The method here presented also properly takes into account the effects due to the detector asymmetries arising from a non-homogeneous detector. This approach becomes relevant when analysing data for IceCube, a detector under construction with a non-homogeneous distribution of the strings before completion.

References

[1] A. Achterberg for the IceCube Collaboration. *Phys. Rev. D accepted for publication*, 2007. arXiv:astro-ph/0611063.

[2] M. Ackerman et al. for the IceCube Collaboration: Contributions to the ICRC, Pune, India, Aug. 3-10. pages 24–27, 2005.

[3] J. Braun et al. for the IceCube Collaboration: Contributions to the ICRC, Merida, Mexico, Jul. 3-11. 2007.

[4] C. Finley et al. for the IceCube Collaboration: Contributions to the ICRC, Merida, Mexico, Jul. 3-11. 2007.

[5] M. Tluczykont et al. *J. Phys.: Conf. Ser.*, 60:318–320, 2007.

All-Sky Search for Transient Sources of Neutrinos Using Five Years of AMANDA-II Data

RODÍN PORRATA[1] FOR THE ICECUBE COLLABORATION

[1]*University of California at Berkeley, Department of Physics, Berkeley, CA 94270, USA*

porrata@berkeley.edu

Abstract: Up to now, analyses of AMANDA data have been limited to searches for diffuse astrophysical sources, time-integrated searches for point sources, and searches for flares and bursts from preselected sources (AGN and GRB) over very limited timescales. However, multi-wavelength studies have shown that AGN and GRB emissions generally occur in exponential flares or bursts with strengths that can be much greater than that of the corresponding quiescent emission, and that the timescales for these violent outbursts can vary from milliseconds to months. Therefore, we are performing an all-sky search for transient sources of neutrinos with AMANDA data taken from the years 2000 to 2004 [1], surveying the largest range of timescales for which an improved signal to noise ratio can be obtained. In this report we describe a new analysis technique that utilizes an unbinned two-point correlation function which separates pairs of signal events from the atmospheric neutrino background by taking into account the probabilities for observing the given spatial separation, time separation, and total number of hit channels (NCH) of the events given both signal and background hypotheses. At the shortest timescales probed, this analysis achieves a differential fluence sensitivity, $\bar{\mathcal{F}}^0 = \left(\frac{E}{1\text{TeV}}\right)^\gamma \frac{d\mathcal{F}}{dE}$, to flaring FR-I galaxies that is almost a factor of three better than the 5-year stacked point source sensitivity, assuming a spectral index, $\gamma = 2$, and a $\mathcal{F}_{\nu_\mu + \bar{\nu}_\mu} / \mathcal{F}_{\nu_\tau + \bar{\nu}_\tau}$ flavor ratio of one. If they produce events in the detector at all, fluences from such sources must be critically close to the detection threshold to avoid having been observed in other surveys, thus a pair search could provide the earliest detection of astrophysical neutrinos.

Introduction

Studying the space-time-energy properties of pairs of neutrinos has several advantages over other methods of searching for astrophysical sources. 1. We can search the whole sky for astrophysical sources in disregard of the scarcity of multi-wavelength information that could potentially aid such a search, allowing the possible detection of source classes that are dark at other wavelengths. 2. Since the search utilizes the energetic information that can be inferred from NCH data, it uses the same advantage that a diffuse search does to observe a faint astrophysical signal, however, unlike a diffuse analysis, correlated event searches are unaffected by a charm component. 3. If the number is sufficient, a pair search has the greatest sensitivity to detect very weak classes of astrophysical point sources, and is more powerful than searching for other multiplicities, e.g., pairs probe 84 % more space than triplets, while if present, a neu-

trino triplet will be counted as 3 pairs, with comparable significance.[1]

The Time Variability of AGN and GRB

In summary, the activity of AGN and GRB [2][3][4][5][6][7][8], the primary astrophysical candidates associated with theorized hadronic processes inducing neutrino emission, suggests that we could observe astrophysical neutrinos arriving in bursts with almost any imaginable time difference. We assume that on a logarithmic scale, flare timescales are uniform.

---

1. Classes of point sources with N_e events per source and N_s objects will be expressed in this analysis as $N_p = N_s N_e (N_e - 1)/2$ pairs, e.g., if a source like Mrk 421, for which there is 7 events observed in the integrated point source analysis, emits those neutrinos on a timescale less than one day, then it will appear in this analysis as 21 pairs – a situation that has a chance better than 50 % of producing a 5-σ discovery.

However, considering the differences in the astrophysical processes over different timescales, the pair search is separated into searches over several different timescales based upon the classes of objects that might be observed. Tab. 1 lists a possible way to construct the search categories. Optimization of the search strategy and calculation of the significance of the search results is conducted separately for each search timescale.

Flare Category	T_l / T_u	L
GRB / TeV SN / TeV AGN	1 s / 2 hr	A
GRB afterglow / TeV AGN	2 hr / 3 dy	B
Large scale AGN flare	3 / 30 dy	C

Table 1: Timescales over which we will search for various astrophysical categories: (1) category of objects, (2) minimum/maximum time between events (T_l/T_u), (3) label for this discussion.

Constraints and Background

The diffuse analysis [9] imposes the most stringent limit on the total number of neutrinos from all astrophysical sources integrated over the entire sky that could possibly be observed. For the 2000-2004 point source dataset, this translates to ~ 80 neutrinos assuming an E^{-2} source spectrum. We have used this number as the maximum number of neutrinos that we simulate for any of the source classes we consider.

While studying the response of the detector to background and potential astrophysical sources, the time-integrated point source analyses are able to average the detector efficiencies over time and right ascension (RA). However, this analysis probes the detector down to timescales of a second or less, so it can be strongly affected by the asymmetries of the detector. A new method of randomizing the data was developed that properly takes into account the asymmetries in the combined zenith (ZEN) and azimuth (AZ) distribution of events, the preferential occurrence of NCH values from certain AZ and ZEN directions, and the granularity of the detector on-periods. The ZEN and AZ of background events are sampled from the data itself and a smearing function is applied. The smearing function, determined by MC, is the point spread function of the detector given an at-mospheric neutrino spectrum. Times are sampled from a list of all possible detector on-periods for the entire 5 year analysis. Having obtained a map of the ZEN, AZ, and time of the events according to the efficiencies of the detector, the RA is calculated using the transformation

$$RA = (MJD \cdot 24.06571 \cdot 15 - AZ)\%360$$

which is valid for a pair analysis performed on data obtained at South Pole. MJD is the Modified Julian Date. This method, comparable to *direct integration* [10], keeps all detector efficiencies intact, while producing a randomized sky-map of the data that is complete.

Search Technique

All pairs of neutrino events are compared. For each pair that falls within the minimum and maximum time differences given by the search class (see Tab. 1), ζ is calculated and if its value surpasses a predetermined threshold, ζ_c, the count of observed events is incremented. Once the tally is complete, the significance of the observation is determined using the Poisson p-value. To derive ζ, consider the likelihood ratio for the ith pair of events:

$$\mathcal{LR}_i = \frac{P(NCH_i|S) \, P(\log_{10}[\Delta t_i]|S) \, P(\psi_i|S)}{P(NCH_i|B) \, P(\log_{10}[\Delta t_i]|B) \, P(\psi_i|B)}$$

where:

$P(NCH_i|B)$ - The probability distribution for NCH, given a pair of background events. This is obtained by calculating the distribution of all combinations of NCH values from the data itself. Before this distribution is calculated, the values are standardized across 8 different declination bands by subtracting the median of the distribution and dividing by the inter-quartile difference, both declination dependent quantities. The standardization process removes to first order the geometric component of the variation of NCH values as a function of ZEN, leaving the spectral energy dependence intact.

$P(\log_{10}\Delta t_i|B)$ - The distribution of the logarithm of time differences of background pairs of events. This is obtained by fitting time differences of the data from 0.001 to 30 days with a power law. The

result of the fit gives $P(\log_{10}[\Delta T]|B) \propto \Delta T^{0.98}$. This is in agreement with expectations that it should increase proportionally with the time difference. The fit is used to obtain the probability of observing pairs of events that occur 0.01 days apart or less. For longer timescales the randomized time distribution is used directly.

$\mathbf{P}(\psi_\mathbf{i}|\mathbf{B})$ - The probability of observing a given spatial separation of background events is $\sim \rho_{bg} \sin \psi/2$, where ρ_{bg} is the local spatial density of background events. Since the background does not vary too quickly, and since an average over all directions is obtained when moving away from the point in question, this approximation is good enough.

$\mathbf{P}(\mathbf{NCH_i}|\mathbf{S})$ - The probability distribution for NCH given a pair of signal events. This is obtained from source MC, weighted according to an E^{-2} spectrum. This probability distribution is standardized using the same quantities used to standardize $P(NCH_i|B)$.

$\mathbf{P}(\log_{10}\Delta \mathbf{t_i}|\mathbf{S})$ - Based upon reviews of AGN and GRB activity, the central assumption of this work is that the distribution of flare/burst timescales is the scale invariant Jeffrey's prior [11], i.e., a *constant* for logarithmically sized bins.

$\mathbf{P}(\psi_\mathbf{i}|\mathbf{S})$ - The probability of observing a given separation in space of a pair of signal events from the same source. This is obtained from source MC data, weighted according to an E^{-2} spectrum. The PSF takes into account both the intrinsic $\nu_\mu \rightarrow \mu$ mismatch angle and the mismatch angle between the reconstructed muon and its true direction. Note that the PSF is evaluated at an angle, Ψ, which is half the separation angle, ψ, between the events.

According to the Neyman-Pearson Lemma, the quantity, $\zeta_i = \log_{10}(\mathcal{LR}_i)$, represents one of the best possible ways of utilizing all the information we have discussed in order to provide evidence to decide whether the ith pair of events is an observation of signal or background. The choice of the value of ζ_c is optimized in the following manner: The analysis is run on 10,000 simulated experiments with pure background and 1000 simulated experiments that contain a small amount of simulated signal. For each experiment, the background and signal pairs are counted as a function of the cut on ζ and the significance of the observation is cal-
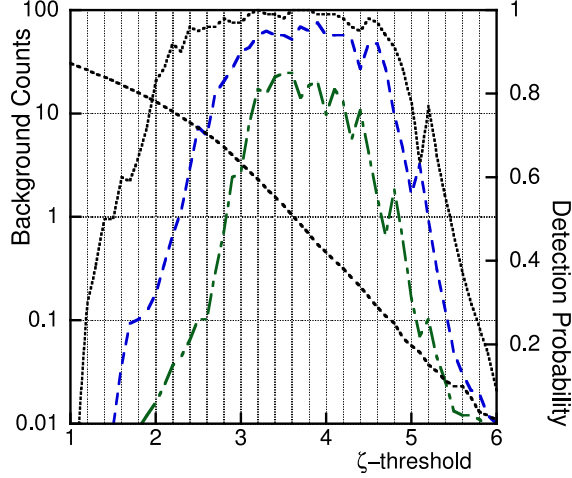
Figure 1: **Preliminary** probabilities for (from top to bottom) 3, 4, and 5-σ detections are plotted (units on r.h.s.) for a 2 hour search as a function of cut on ζ. The monotonically decreasing curve is the expected counts from background only. The time distribution of the signal is logarithmically uniform, 5.5 source pairs per $\log_{10}(\Delta T/\text{Days})$ extending from 10 seconds to 2 hours.

culated. Then the median signficance is calculated from the set of experiments and this is used to determine the best evidence threshold. For a search for GRB-timescale flares (A in Tab. 1), where the signal consists of $\sim$16 sources distributed isotropically on the sky and distributed log-uniformly from 10 seconds to two hours, each source contributing two events to the dataset, the expected background is plotted in Fig. 1, as are the 3, 4, and 5-σ detection probabilities. Here it is seen that the 5-σ detection probability is maximal at $\zeta_c = 3.6$ where its value is better than 80%.

Results and Conclusions

The fluence sensitivity is given by

$$\bar{\mathcal{F}}_L^0 = \frac{\bar{\mu}_{90}}{n_s} \mathcal{F}_s^0$$

where $\mathcal{F}_s^0$ is the normalization constant on the differential fluence (the differential flux integrated over the duration of flaring events) of the signal model studied, n_s is the number of neutrino

121

events that would be observed given such a flu-ence, and $\bar{\mu}_{90}$ is the Feldman-Cousins average upper limit given the background and no source events [12]. For classes of objects with more than one member, n_s is the sum of contributions from each. Preliminary differential fluence sen-sitivities, as well as detection probabilities, are presented in Tab. 2 for two classes of objects that meet the requirements of the diffuse anal-ysis. In Fig. 2 we plot the differential fluence

Cat.	N_s	$N_{\nu ps}$	ε_T	$\mathcal{F}_L^0$	$P_{5-\sigma}$
A	20	2	0.78	2.70	99.6
B	27	3	0.44	8.2	86

Table 2: **Preliminary** differential fluence sensitiv-ities and detection probabilities for representative source classes: (1) Category of objects, (2) no. of sources, (3) no. of neutrinos per source, (4) signal efficiency, (5) $\nu_\mu + \nu_\tau$ fluence sensitivity in units of 10^{-4} TeV^{-1} cm^{-2}, (6) 5-σ detection probabil-ity (%), excluding our $N_T = 4$ trials factor.

sensitivities of GRB-timescale source classes for which the nth source has a relative strength given by [13] $\mu_n = \mu_0 n^{-\alpha} e^{-n/n_c}$. Our sensitivity to FR-I-like objects [14] (not including the brightest source, which is 3C-274, $\alpha = 0.65$) that produce Cat. A flares is 1.3×10^{-3} TeV^{-1}cm^{-2} compared to the integrated stacking analysis [13] result of 3.4×10^{-3} TeV^{-1}cm^{-2}. The results of this survey are presented in Tab. 3. Although none of the ob-

Cat.	ζ_c	μ_{bg}	n_{obs}	p-value
A	3.885	0.573	1	0.44
B	1.94	31.5	37	0.19
C	0.63	431	457	0.11

Table 3: **Preliminary** results of survey. (1) Cate-gory of objects, (2) optimized evidence threshold, (3) no. background pairs expected, (4) no. pairs observed, (5) significance, excluding $N_T = 4$.

servations were significant, the results of the sen-sitivity study show the potential of this technique to search for weak astrophysical sources that flare. This study will serve as the starting point for all-sky transient searches performed with the full Ice-Cube detector.
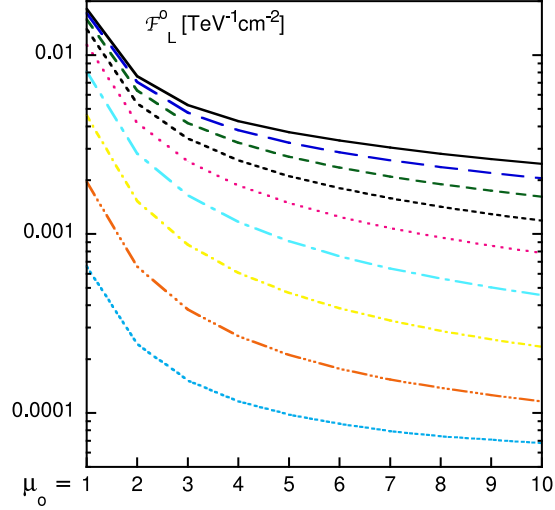
Figure 2: **Preliminary** fluence sensitivities for Cat. A objects characterized by α and μ_o. The curves, from top to bottom, are for $\alpha = 2$ to $\alpha = 0$ in steps of 0.25, assuming $n_c = 50$.

References

[1] A. Achterberg et al., Phys. Rev. D (accepted 2007).

[2] J. A. Galdos et al., Nature, **38** 319 (1996).

[3] D. Kniffen et al., ApJ **540** 184 (2000).

[4] K. Hurley et al., Nature, **372** 652 (1994).

[5] D. J. Thompson et al., ApJ. Supp. Ser., **157** 324 (2005).

[6] P. L. Nolan, ApJ, **597** 615-627, (2003).

[7] Valtaoja et al., ApJ Supp. Ser., **120** 95-99, (1999).

[8] J. Albert et al., submitted to ApJ, (2007).

[9] J. Hodges et al., Proc. 29th ICRC, Pune, India (2005).

[10] R. Atkins et al., ApJ, **595**, 803-811 (2003).

[11] P. Gregory, Cambridge Univ. Press 2005.

[12] G. Feldman and R. Cousins, Phys. Rev. D, **57** 3873 (1998).

[13] A. Achterberg et al., Astropart. Phys., **26** 282 (2006).

[14] B. Fanaroff and J. Riley, MNRAS **167** (1974).

ICRC'07
Merida, México

Neutrino Triggered Target of Opportunity (NToO) test run with AMANDA-II and MAGIC

M. ACKERMANN[1],[5], E. BERNARDINI[1], N. GALANTE[2], F. GOEBEL[2], M. HAYASHIDA[2], K. SATALECKA[1], M. TLUCZYKONT[1], R. M. WAGNER[2], FOR THE ICECUBE[3] AND MAGIC COLLABORATIONS[4]

[1]*DESY, Platanenallee 6, 15738 Zeuthen*

[2]*MPPMU, Föhringer Ring 6, 80805 München*

[3]*See special section of these proceedings*

[4]`http://magic.mppmu.mpg.de/collaboration/members`

[5]*Now at SLAC, Stanford University, USA*

elisa.bernardini@desy.de

Abstract: Kilometer scale neutrino telescopes are now being constructed (IceCube) and designed (KM3NeT). While no neutrino flux of cosmic origin has been discovered so far, the first weak signals are expected to be discerned in the next few years. Multi-messenger (observations combining different kinds of emission) investigations can enhance the discovery chance for neutrinos in case of correlations. One possible application is the search for time correlations of high energy neutrinos and established signals. We show the first adaptation of a Target of Opportunity strategy to collect simultaneous data of high energy neutrinos and gamma-rays. Neutrino events with coordinates close to preselected candidate sources are used to alert gamma-ray observations. The detection of a positive coincidence can enhance the neutrino discovery chance. More generally, this scheme of operation can increase the availability of simultaneous observations. If cosmic neutrino signals can be established, the combined observations will allow time correlation studies and therefore constraints on the source modeling. A first technical implementation of this scheme involving AMANDA-II and MAGIC has been realized for few pre-selected sources in a short test run (Sept. to Dec. 2006), showing the feasability of the concept. Results from this test run are shown.

Introduction

The major aim of neutrino astrophysics is to contribute to the understanding of the origin of high energy cosmic rays. A point-like neutrino signal of cosmic origin would be an unambiguous signature of hadronic processes, unlike γ-rays which can also be created in leptonic processes. Neutrino telescopes are ideal instruments to monitor the sky and look for the origin of cosmic rays because they can be continuously operated. The detection of cosmic neutrinos is however very challenging because of their small interaction cross-section and because of a large atmospheric background. Parallel measurements using neutrino and electromagnetic observations (multi-messenger) can increase the chance to discover the first signals by

reducing the trial factor penalty arising from observation of multiple sky bins and over different time periods. In a longer term perspective, the multi-messenger approach also aims at providing a scheme for the phenomenological interpretation of the first possible detections. The Antarctic Muon and Neutrino Detector Array (AMANDA) was built with the aim to search for extraterrestrial high energy neutrinos [2]. The Major Atmospheric Gamma Imaging Cherenkov telescope (MAGIC) is a current generation γ-ray telescope that operates in the northern hemisphere at a trigger energy threshold of 60 GeV [5].

Neutrino Target of Opportunity test run

The neutrino target of opportunity (NToO) test run described here was defined as a cooperation be-

tween the AMANDA (neutrinos) and MAGIC (γ-rays) collaborations [3]. Each time a neutrino event was detected from the direction of a predefined list of objects, a trigger was sent to the γ-ray telescope. MAGIC then tried to observe the object within a predefined time window after the neutrino trigger. The primary goal of the NToO approach is to achieve simultaneous neutrino/γ-ray observations. This can be realized by triggering follow-up observations of interesting neutrino events, such as multiplets within a short time window or very high energy events, therewith assuring γ-ray coverage for these neutrino events. Multiplets are very seldom in AMANDA-II observations (low statistics). We therefore implemented a test run based on single high energy neutrino events from pre-defined directions. These events are most likely due to atmospheric neutrino background. The test run took place between 27th of September and 27th of November 2006 and its purpose was to test the technical feasability of the NToO strategy. The AMANDA-II DAQ data at the South Pole passed through an online reconstruction filter that selected up-going muon tracks and provided a monitoring of the data quality. Whenever a neutrino event was reconstructed within a few degrees of one of the selected sources and passed the data quality criteria, a message was sent via e-mail to the MAGIC shift crew. The message contained the time of the event, the source name and the reconstructed angular distance from the source. If possible (day/night duty cycle), the object was then observed with the MAGIC telescope within 24 hours for a duration of 1 hour. A coincidence is counted when a γ-ray high state (flare) is measured in these observations. A γ-ray flare can be defined as an observation above a predefined threshold flux F_{thr}. The individual thresholds were chosen either based on the MAGIC sensitivity or in case of Mrk 421 to a conservatively low value for which the probability to observe a high state as defined above would be of the order of few percent.

An example analysis: Blazars

A stand-alone neutrino analysis can only yield a significant result if an excess above the expected atmospheric background is observed. In the multi-messenger framework, the observation of a number of neutrino events in coincidence with gamma-ray high states can be an indication for a neutrino/γ-ray correlation. If this correlation is incompatible with the chance probability for coincidence with atmospheric neutrinos such an observation would be evidence at the same time for a cosmic origin of the neutrino events and a hadronic nature of the gamma-ray signal. In this scheme for the interpretation of data a statistical test was defined before the measurements. Under the hypothesis that all the neutrinos detected from the direction of the source are atmospheric, the chance probability of detecting at least n_{obs} neutrinos and observing at least n_γ coincident gamma-ray flares is given by:

$$
P = \sum_{i=n_{obs}}^{+\infty} \frac{(n_{bck})^i}{i!} e^{-n_{bck}} \sum_{j=n_\gamma}^{i} \frac{i!}{j!(i-j)!} p_\gamma^j (1-p_\gamma)^{i-j},
$$
(16)

where the first term describes the Poisson probability of observing at least n_{obs} neutrinos with n_{bck} expected background events, and the second term describes the probability of observing at least n_γ coincident gamma-ray flares out of the $j \geq n_{obs}$ triggers. p_γ is the probability to observe a gamma-ray high state above a certain threshold F_{thr} within a given time window. P defines the post-trial significance of a set of coincidences observed from one source. Trial factors to account for the number of sources considered can be easily included using Binomial statistics. For illustration of Equation 16, let us assume that we observe $n_{obs} = 10$ neutrinos with a background expectation of $n_{bck} = 10$. In itself this measurement would not be significant. However, if coincidences with γ-ray high-states are observed the significance increases as shown in Figure 1 for different γ-ray probabilities. So far, limited knowledge is available on p_γ. Efforts are on-going to address the issue of estimating an upper limit on p_γ for a few interesting sources, from a compilation of gamma-ray observations [6] and from random or long term monitoring observations (e.g. performed by the VERITAS and the MAGIC telescopes). We notice that a compilation of existing data is likely biased from the availability of measurements triggered by high states of emission observed at different wavelengths, which would tend to give an overestimation of p_γ and therefore an underestimation of the significance of the coincidences. The probability
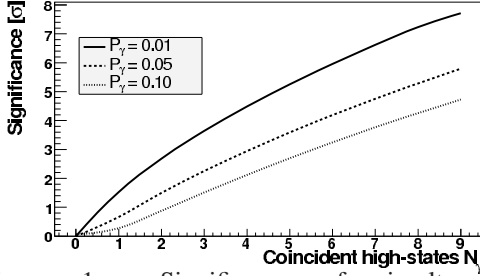
Figure 1: Significance of simultaneous neutrino/gamma-ray observations vs. the number of observed coincidences, given for different values of p_γ (Equation 16). Here, $n_{\rm obs} = n_{\rm bck} = 10$ was assumed.

p_γ is, on average, equal to the average high-state rate of an object. One method for the estimation of the high-state rate is based on the flux frequency distribution of the object, shown in Figure 2 for Mrk 421. This distribution can be interpreted as a stochastic flux-state distribution and can be well fit by an exponential. The high-state rate $R_{HS}(F_{thr})$ above a threshold F_{thr} is then given by

$$R_{HS}(F_{thr}) = \frac{\int_{F_{thr}}^{\infty} e^{bx}dx}{\int_{F_0}^{\infty} e^{bx}dx} = \frac{e^{bF_{thr}}}{e^{bF_0}} \qquad (17)$$

where F_0 is the baseline flux of the object and b is the slope of the flux distribution. The relative high-state rate of Mrk 421 as derived from this formula is shown in Figure 3 as a function of the chosen threshold F_{thr}. Due to the bias to high states of the available Mrk 421 observations, the high state rate is systematically overestimated here. These results will be described in detail in [6]. The estimation for p_γ can be used in Equation 16 in the case of Blazars, for which γ-ray data exist and long-term lightcurves have been compiled. The expected background rate is the rate of atmospheric neutrinos in the sky bins around the selected sources. Depending on the source declination and on the choice of the bin size, this rate ranges from about 1 to 4 events per year and per source based on the AMANDA-II event information and according to the current scheme of event reconstruction and selection [1].

List of selected sources

The first criterion for the selection of sources for the NToO test run is their variability. Only sources
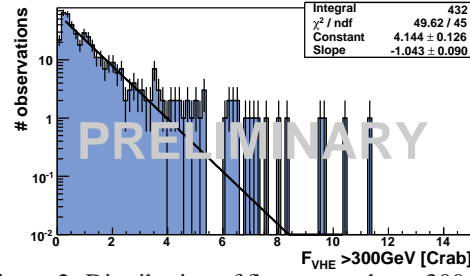
Figure 2: Distribution of flux states above 300 GeV of 15 years of VHE observations of Mrk 421 [6].
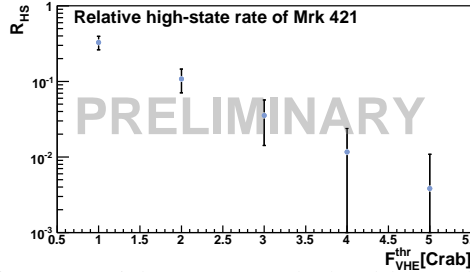
Figure 3: High-state rate calculated by applying equation 17 to the fit of the distribution of fluxstates in Figure 2.

known or expected to be variable were chosen for the test run. Other criteria are the minimal impact on the scientific plans of MAGIC and the possibility to efficiently organize the independent observation plans. Target sources are therefore preferably selected among those which are already included in the scheduled observation program (MAGIC). Further criteria are their potential for high-energy neutrino emission, good visibility for MAGIC during the time period of the test run (September–December) and previous detections at high-energy γ-rays or high probability for γ-ray emission. Sources meeting these requirements are Blazars and X-ray binaries. For these sources the level of correlation between high energy neutrinos and gamma-rays can be different under different scenarios (see for example the cases discussed in [7]).

Results and Interpretation

During the two months of data taking for the NToO program a total of 5 neutrino event triggers were initiated by AMANDA-II and sent to the MAGIC observatory. In two cases follow-up observations

	LSI+61 303	GRS 1915+105	IES 2344+514	IES 1959+650	Mrk 421
n_{bck}	0.86	1.26	0.99	0.92	1.51
n_{obs}	0	1	1	0	3
Follow ups	0	0	1	0	1
n_γ	–	–	0	–	0
F_{thr} [C.U.]	0.2	0.2	0.5	1.0	4.0
p_γ	–	–	–	< 0.15	< 0.05
P_ν	1.0	0.7	0.6	1.0	0.2

Table 1: List of selected sources for the NToO test run. Given are preliminary numbers for expected (n_{bck}) and observed (n_{obs}) neutrino triggers, the number of observed coincidences (n_γ), the γ-ray high-state probability and the probability P_ν for observing n_{obs} neutrinos or more. The error on n_{bck} is typically 0.1.

were performed with the MAGIC telescope lasting for 1 hour each. For the remaining 3 triggers, the source was not observable with MAGIC within 24 h following the trigger due to unfavourable astronomical, moon or weather conditions. In Table 1 the individual neutrino event counts n_{obs} are given along with the number of expected neutrino background events n_{bck}, the number of coincident observations with MAGIC, the number n_γ of observed coincident γ-ray flares (as defined above) and the γ-ray flare probability p_γ derived from Equation 17. The MAGIC follow up observation data has been analyzed with the standard MAGIC analysis chain [4]. The sensitivity of MAGIC is sufficient to detect a γ-ray flux level of 30% Crab Units (C.U.) with 5 sigma significance within 1 hour. It is therefore enough to determine whether the 2 triggered sources Mrk421 and 1ES2344 were in flaring state (according to the definition of flaring state in Table 1) during the NToO observations. The analysis yielded an upper limit for 1ES2344 (16% C.U.) and a low flux state for Mrk421 (30±10% C.U.). No coincident γ-ray flaring state has thus been observed.

Discussion and Perspectives

The NToO strategy was implemented in a test run involving the AMANDA-II and the MAGIC telescope for a time period of two-months. No coinci-

dent events have been observed during this test run. However, the technical feasibility of a NToO strategy was successfully tested. The neutrino trigger information sent via e-mail has initiated follow-up observations, whenever the sources were visible and the weather and astronomical (moon/sun) conditions allowed the operation of the MAGIC telescope. At the end of the test run, a different communication infrastructure was also implemented, based on a test client/server connection, which allows the queuing of follow-up observations using a similar pipeline as that already used by MAGIC to follow-up GRB alerts. Perspectively, different event selections will be developed for IceCube. A search for multiplets with pre-defined significances will provide a means for the selection of flare-like neutrino events. Furthermore, work is in progress for the analysis of high-energy neutrino events with the IceCube 22-string detector (2007) and with extensions in subsequent years. These analyzes will possibly be implemented in an IceCube NToO program in 2008.

References

[1] A. Achterberg et al. for the IceCube collaboration, 2006. arXiv:astro-ph/0611063, accepted for publication in Phys. Rev. D (2007).

[2] Andrés et al. *Astropart. Phys.*, 13:1, 2000.

[3] E. Bernardini for the IceCube collaboration. In *Towards a Major network of Atmospheric Cherenkov Telescopes*, 2005.

[4] T. Bretz and R. M. Wagner, 2003. in Proc. of the 28th ICRC, Tsukuba, Japan.

[5] E. Lorenz. *New Astron. Rev.*, 48:339, 2004.

[6] M. Tluczykont et al. In *2nd Workshop on TeV particle Astrophysics, Madison, WI, USA*, 2006.

[7] D.F. Torres and F. Halzen. 2006. arXiv:astro-ph/0607368, submitted to A&A.

Detecting GRBs with IceCube and optical follow-up observations

A. KAPPES[1,2], M. KOWALSKI[3], E. STRAHLER[1], I. TABOADA[4] FOR THE ICECUBE COLLABORATION[5]

[1]*Physics Dept. University of Wisconsin, Madison WI 53703. USA*

[2]*on leave of absence from Universität Erlangen-Nürnberg, D-91058 Erlangen. Germany*

[3]*Institute für Physik. Humboldt Universität zu Berlin, D-12489 Berlin. Germany*

[4]*Physics Dept. University of California, Berkeley CA 94720. USA*

[5]*see special section of these proceedings*

itaboada@berkeley.edu

Abstract: We present a summary of AMANDA results obtained in searches for neutrinos from Gamma-Ray Bursts (GRBs). Using simulations, we show how the IceCube detector, which is currently being constructed at the South Pole, will improve the sensitivity of the search. In order to improve the prospects for detections of gamma-ray dark bursts (e.g. choked bursts), as well as core collapse Supernovae (SNe), we discuss a novel follow-up scheme of high energy neutrino events from IceCube. Triggered by neutrino events from IceCube, a network of small optical telescopes is meant to monitor the sky for SNe rising lightcurves and GRB afterglows. The observing program is outlined and its status discussed.

Introduction

GRBs have been proposed as one of the most plausible sources of ultra-high energy cosmic rays [12] and high energy neutrinos [13]. In addition to being a major advance in astronomy, detection of high energy neutrinos from a burst would provide corroborating evidence for the acceleration of ultra-high energy cosmic rays within GRBs. It has been noticed that so-called long GRBs are often accompanied by SNe type Ib/Ic [6]. The prevalent interpretation is that the progenitors of these SNe and GRBs are very massive stars that undergo core collapse that leads to the formation of a black hole. The material accreted by the black hole can form highly relativistic jets which then produce the observed burst of γ-rays and accelerate particles to high energy. The connection between SNe and GRBs has inspired the speculation that a fraction of core collapse SNe which do not lead to GRBs may still be the source of TeV neutrinos [4].

For the purposes of establishing the sensitivity of IceCube to GRBs we will use the Waxman-Bahcall GRB [13] model as a benchmark. We will assume a flavor flux ratio of 1:1:1 at Earth motivated by neutrino oscillations. We use a flux nor-malization of 1.35×10^{-8} GeV cm^{-2} s^{-1} sr^{-1} at 1 PeV at the Earth for all neutrino flavors combined, a break energy of 100 TeV and a synchrotron break energy of 10 PeV. Finally, we assume that the Waxman-Bahcall GRB model corresponds to 670 GRBs per year over the full sky resulting in an average neutrino fluence per burst of $F_{\mathrm{burst}} = 1.3 \times 10^{-5}$ erg/cm^2 for all flavors combined. However, it should be noted that fluctuations in the characteristics of GRBs, notably redshift and γ-ray fluence, lead to significant fluctuations in the expected number of neutrinos from burst to burst [8].

IceCube is a high energy ($E > 1$ TeV) neutrino telescope currently under construction at the South Pole [9]. When completed, the deep ice component of IceCube will consist of 4800 digital optical modules (DOMs) arranged in up to 80 strings frozen into the ice, at depths ranging from 1450 m to 2450 m. Each DOM contains a photomultiplier tube and supporting hardware inside a glass pressure sphere. The total instrumented volume of IceCube will be ~ 1 km^3. The DOMs indirectly detect neutrinos by measuring the Cherenkov light from secondary charged particles produced in neutrino-nucleon interactions.

AMANDA-II [5], now integrated in IceCube as a sub-detector, was commissioned in the year 2000 and consists of a total of 677 optical modules. These are arranged on 19 strings with the sensors at depths ranging from $1500\,\mathrm{m}$ to $2000\,\mathrm{m}$ in a cylinder of $100\,\mathrm{m}$ radius. Its instrumented volume is about 70 times smaller than that of the deep ice component of IceCube.

The two main channels for detecting neutrinos with IceCube and AMANDA are the ν-induced muon and the ν-induced cascade channels. For the muon channel the detectors are mainly sensitive to up-going muons as the Earth can be used to shield against the much larger flux of down-going atmospheric muons. Searches for neutrinos from GRBs in the muon channel benefit from good angular resolution ($\sim 1°$ for $E_\nu > 1\,\mathrm{TeV}$) and from the long range of high energy muons. For cascade channels the detectors are sensitive to all neutrino flavors through various interaction channels. Here, analyses benefit from good energy resolution (~ 0.1 in $\log_{10} E$) and from 4π sr sensitivity to high energy neutrinos. The number of expected detected events can be calculated by convoluting the neutrino flux Φ with the corresponding effective neutrino area A_ν^{eff}:

$$ N_{\mathrm{evts}} = T \int \mathrm{d}\Omega \mathrm{d}E A_\nu^{\mathrm{eff}}(E,\theta) \frac{\mathrm{d}\Phi}{\mathrm{d}E}(E,\theta) \,, \quad (18) $$

where T is the observation time.

Searches for neutrinos in coincidence with GRBs have been conducted with the AMANDA detector in the muon and the cascade channels. The muon search was performed on over 400 bursts reported by BATSE and IPN3 between 1997 and 2003 [2]. Additionally, a dedicated search for neutrinos in coincidence with GRB030329 was performed [11]. Using the cascade channel, one analysis [3] focused on 73 bursts reported by BATSE in 2000 and another analysis searched for a statistical excess of cascade-like events during a rolling period of $1\,\mathrm{s}$ and $100\,\mathrm{s}$ for the years 2001-2003 [3]. So far no evidence for neutrinos from GRBs has been found. With the muon search the 90% c.l. limit set by AMANDA is 1.3 times higher than Waxman-Bahcall's prediction as defined above.

The main source of GRB data to be studied by IceCube will be GLAST, but also other satellites, e.g. Swift, will contribute. Since finding an unusually bright nearby GRB is key for the detection of neutrinos, the ideal satellite has a very large field of view (FoV). GLAST's FoV is ~ 9 sr and Swift's ~ 1.4 sr. In our calculations we assume a yearly detection rate of 200 GRBs by GLAST which are distributed uniformly over the sky. IceCube can be operated while being built. By the end of 2008 the accumulated exposure will be 0.75 km$^2 \cdot$yr; 1.3 km$^2 \cdot$yr by 2009 and 1.9 km$^2 \cdot$yr by 2010. IceCube is currently taking data with 22 strings.

IceCube sensitivity to muon neutrinos

In order to calculate the sensitivity of the IceCube detector to muon neutrinos from GRBs, bursts are simulated uniformly distributed over the northern sky. Each burst is assumed to produce a muon neutrino fluence of $1/3\, F_{\mathrm{burst}}$. The muon neutrino effective area as a function of neutrino energy and zenith angle is obtained from a full Monte Carlo simulation including a detailed ice and detector simulation. Displayed in Fig.1 is the effective area at trigger level as a function of energy averaged over zenith angles above $90°$ (up-going neutrinos). Past searches with AMANDA [2] have shown that 25–75% efficiency can be obtained with respect to trigger level once selection criteria are applied to data in order to remove the down-going muon background. IceCube has the potential of even higher efficiency. Thus we consider trigger level effective area representative (upper limit) of what the detector will be able to achieve.

The narrow constraints on the position and the timing of neutrinos from a GRB combined with the good angular and time resolution of IceCube lead to a very low expected background. For this first sensitivity estimate we therefore assume a background free observation.

In the following we estimate the number of GRBs required to reach the GRB flux predicted by Waxman-Bahcall and exclude it at 99.73% C.L. (3σ). With the observation of no events and a mean expected background of zero events the Feldman-Cousins method [7] yields an event upper limit of 6.0. In order to reach this number about 70 bursts in the northern hemisphere must be observed which can be expected after about 1 year of operation of the full detector.
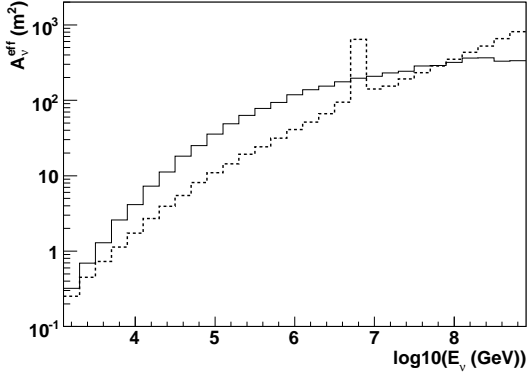
Figure 1: IceCube's effective neutrino area as a function of the neutrino energy at trigger level for ν_μ (solid) and ν_e (dashed). The ν_μ effective area is the average for neutrinos from the northern sky (2π sr) whereas that for ν_e is averaged over the whole sky (4π sr). The peak at 6.3 PeV is the Glashow resonance.

IceCube sensitivity to electron neutrinos

For ν_e-induced cascades the effective neutrino area $A_{\nu_e}^{\mathrm{eff}}$ is calculated for a uniform distribution of ν_e and $\bar\nu_e$ over 4π sr. We have taken into account charged current and neutral current interactions as well as the Glashow resonance. The effective area, averaged over an equal mixture of ν_e and $\bar\nu_e$, can be seen in Fig. 1. As with the muon channel, the effective area presented here is at trigger level.

The narrow constraints on the timing of neutrinos from a GRB combined with the good cascade energy and time resolution of IceCube lead to a very low expected background. We calculate the sensitivity supposing a background free search.

In the following we estimate the number of GRBs required to reach the GRB flux predicted by Waxman-Bahcall and exclude it at 99.73% c.l. (3σ). With the observation of no events and a mean expected background of zero events the Feldman-Cousins method yields an upper limit of 6.0. In order to reach this number about 560 bursts must be monitored. This can be expected after almost 3 yr of operation of IceCube in coincidence with GLAST. Including the contributions from ν_μ and ν_τ-induced cascades would roughly double the
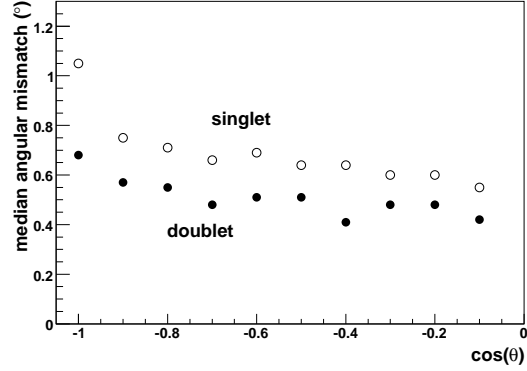
Figure 2: Median angular mismatch for single neutrino events and neutrino doublets (with $\Delta\Psi < 3°$). Quality cuts have been applied.

number of expected events [3] [1] Thus the number of bursts required is ~ 280 or 1.5 yr of satellite coincident observations.

An optical follow-up for neutrino events

So far we have discussed the search for a neutrino signal in coincidence with a GRB identified through satellites. For the future, we plan to complement this by performing an automated optical follow-up observations of selected neutrino events from IceCube [10]. First, the direction of neutrinos detected with IceCube is reconstructed online and if energy or multiplicity pass a certain threshold, a notice is sent to a network of optical telescopes. Then, within minutes after reception of the notice, automated optical telescopes monitor the corresponding part of the sky. Transient objects are thereby identified, e.g. through detection of GRB afterglows (on a timescale of minutes to hours) or rising SNe light-curves (on a timescale of days). These multi-messenger observations significantly improve the discovery potential of IceCube by providing a chance to detect and identify the source of the high-energy neutrinos. In what follows, we discuss the IceCube neutrino-burst trig-

---

1. Given the improved capabilities of IceCube it may be possible to treat high energy ν_τ-induced events as a separate channel.

ger and the corresponding telescope requirements for the optical follow-up observations.

The rate of atmospheric ν_μ events observed in the full IceCube detector is too high to perform individual follow-up observations: the trigger rate of neutrinos with zenith angle $> 80°$ will be $\sim 7 \times 10^5$ events per year. After imposing quality cuts similar to those used in Ref. [1], the rate is $\sim 7 \times 10^4$ per year but remains high. However, the background rate can be significantly reduced by triggering on multiplets, i.e. two or more neutrinos detected within a short time window, Δt, and within a spacial window, $\Delta\Omega$. Here Δt is determined by the typical burst duration. An adequate time scale which covers the duration of most GRBs and SNe models is 100 s. The optimal size $\Delta\Omega$ is determined by the pointing resolution of IceCube, which is of the order of one degree. Using simulation, the rate of doublets for a maximal angular separation of $3°$ as well as $\Delta t = 100$ s is 30 per year. This number is low enough that individual follow-up observations can be performed.

Once the alert will be issued, the corresponding part of the sky has to be searched for transient sources. By averaging the reconstructed directions of the neutrinos in a multiplet, one can improve the localization of the potential source. The median angular mismatch between the average and the true direction as a function of the declination band is shown in Fig. 2. The median angular mismatch is $0.5° - 0.6°$.

An optical telescope with a FoV of $2° \times 2°$ would cover more than 80 % of the IceCube's point spread function for doublets. Already now optical telescopes with such a FoV exist. For example, the ROTSE-III network consists of 4 fully automated telescopes, each with a 0.45 m diameter mirror and a $1.85° \times 1.85°$ FoV.

Conclusions

We have presented a preliminary summary of the capabilities of IceCube. With several search strategies in place, IceCube will be ready to discover a range of different phenomena related to GRBs, such as prompt emission of PeV neutrinos, precursor and afterglow neutrinos from GRBs and neutrinos from core-collapse SNe.

Within a few years IceCube will be able to detect the neutrino flux predicted by Waxman-Bahcall with high significance or set limits well below any current prediction. Follow-up observations with optical telescopes as suggested in this paper will further enhance and complement the satellite triggered searches by enabling IceCube to observe the potentially large fraction of bursts where no γ-ray signal is detected by satellites (dark GRBs). An optical follow-up program for IceCube will possibly be implemented in 2008.

Both in the case of detection or in the case of the derivation of an upper limit, the results from Ice-Cube will boost our understanding of GRBs, one of the most puzzling phenomena in our universe, and contribute to the resolution of the mystery of the origin of cosmic rays at the highest energies.

References

[1] A. Achterberg et al. *Astropart.Phys.*, 20:507, 2004.

[2] A. Achterberg et al. *arXiv:0705.1186. Submitted, ApJ*, 2007.

[3] A. Achterberg et al. *arXiv:astro-ph/0702265. In press, ApJ*, 2007.

[4] S. Ando and J. Beacom. *Phys.Rev.Lett.*, 061103, 2005.

[5] E. Andrés et al. *Nature*, 410:441, 2001.

[6] E. Berger. *Nature*, 426:154, 2003.

[7] G. Feldman and R. Cousins. *Phys.Rev.*, D57:3873, 1998.

[8] D. Guetta et al. *Astropart.Phys.*, 20:429, 2005.

[9] A. Karle. *Proc. of 30th ICRC*, 2007.

[10] M. Kowalski and A. Mohr. *Astropart.Phys.*, 27:533, 2007.

[11] M. Stamatikos. *Proc. of 29th ICRC. astro-ph:0510336*, 2005.

[12] E. Waxmann. *Phys.Rev.Lett.*, 75:386, 1995.

[13] E. Waxmann and J. Bahcall. *Phys.Rev.Lett.*, 78:2292, 1997.

Search for neutralino dark matter with the AMANDA neutrino telescope

D. HUBERT[1] AND A. DAVOUR[2] FOR THE ICECUBE COLLABORATION[3]
[1]*Dienst ELEM, Vrije Universiteit Brussel, B-1050 Brussels, Belgium*
[2]*Division of High Energy Physics, Uppsala University, S-75121 Uppsala, Sweden*
[3]*See special section of these proceedings*
dhubert@vub.ac.be

Abstract: If non-baryonic dark matter exists in the form of neutralinos, a neutrino flux is expected from the decay of neutralino pair annihilation products inside heavy celestial bodies. Data taken with the AMANDA neutrino telescope located at the South Pole can be used in a search for this indirect dark matter signal. We present the results from searches for neutralinos accumulated in the Sun using AMANDA data from 2001, and improved new limits on the flux of muons from 50–$250 GeV/c^2$ neutralino annihilations in the Earth obtained with data from 2001–2003.

Introduction

Cosmological observations have suggested the presence of non-baryonic dark matter on all distance scales. The WMAP results [1] confirmed our current understanding of the Universe, summarized in the concordance model. In this model the Universe contains about 23% non-baryonic cold dark matter, but nothing is predicted about the nature of this dark matter. A massive, weakly interacting and stable particle appears in Minimally Supersymmetric extensions to the Standard Model that assume R-parity conservation. Indeed, the supersymmetric partners of the neutral electroweak and Higgs bosons mix into a dark matter candidate, the neutralino, whose mass is expected in the GeV-TeV range [2]. On their trajectory through the Universe these particles will scatter weakly on normal matter and lose energy. Eventually, dark matter particles will be trapped in the gravitational field of heavy celestial objects, like the Earth and the Sun [3]. The particles accumulated in the center of these bodies will annihilate pairwise. The neutrinos produced in the decays of the Standard Model annihilation products can then be detected with a high energy neutrino detector as an excess over the atmospheric neutrino flux. In this paper we present the results of searches with the Antarctic Muon And Neutrino Detector Array (AMANDA) for neutralino dark matter accumulated in the Earth

(2001–2003 data set) and the Sun (2001 data set). We also discuss current improvements and preliminary results from ongoing analyses on higher statistics data samples accumulated during recent years.

The AMANDA detector [4] at the South Pole uses the polar ice cap as a Cherenkov medium for the detection of relativistic charged leptons produced in high energy neutrino interactions with nuclei. The $500 m$ high and $200 m$ wide detector was completed in 2000 and totals 677 light sensitive devices distributed on 19 strings. The detector is triggered when at least 24 detector modules are hit within a sliding $2.5 \mu s$ window. Since 2001 an additional, lower multiplicity, trigger (referred to as *string trigger*) is operational that exploits not only temporal information but also the space topology of the hit pattern. This lowers the energy threshold of the detector and is especially beneficial for the sensitivity to neutralinos with $m_\chi < 200 GeV/c^2$.

Reconstruction of muons, with their long range, offers the angular resolution required to reject the background produced by cosmic ray interactions with the atmosphere and search for a neutralino-induced signal, which, due to the geographic location of AMANDA, yields vertical upward-going (Earth) or near horizontal (Sun) tracks in the instrumented volume. Indeed, it is possible to eliminate the dominant background, downward-going atmo-

spheric muons. However, upward-going and horizontal atmospheric neutrinos will always contaminate the final, selected data sample.

Signal and background simulation

We have used the DARKSUSY program [5] to generate dark matter induced events for seven neutralino masses m_χ between $50 GeV/c^2$ and $5000 GeV/c^2$, and two annihilation channels for each mass: the W^+W^- channel produces a hard neutrino energy spectrum ($\tau^+\tau^-$ for $m_\chi < m_W$), while $b\bar{b}$ yields a soft spectrum. The cosmic ray showers in the atmosphere, in which downward-going muons are created, are generated with CORSIKA [6] with a primary spectral index of γ=2.7 and energies between $600 GeV$ and $10^{11} GeV$. The atmospheric neutrinos are produced with ANIS [7] with energies between $10 GeV$ and $325 TeV$ and zenith angles above $80°$.

Search for low mass neutralinos in the center of the Earth

A neutralino-induced signal from the center of the Earth is searched for in AMANDA data collected between 2001 and 2003, with a total effective livetime of 688.0 days. This search focuses on improving the sensitivity for low mass neutralinos, with $m_\chi \leq 250 GeV/c^2$, and includes events triggered with the string trigger. The complete data set of 5.3×10^9 events is divided in a 20% subsample, used for optimisation of the selection procedure, and a remaining 80% sample, on which the selection is applied and final results calculated. Detector data are used as background for the optimisation, and compared to simulated background events to verify the understanding of the background and the simulation. The simulated atmospheric muon sample contains 3.6×10^7 triggered events (equivalent to an effective livetime of 4.5 days). The sample of atmospheric neutrinos totals 2.4×10^5 events, which corresponds to 2.5×10^4 triggers when scaled to the livetime of the data sample used for calculation of the final results.

The characteristics of the signal differs depending on the neutralino model under study. Hence, the selection criteria are tuned separately for each neutralino model. Between 2001 and 2002 the detector was upgraded and the trigger settings changed slightly. The event selection is therefore developed separately for 2001.

First, we reduce the total background by selecting events with upward-going signature. Then the data are tested against reconstruction criteria to remove events unlikely to be correctly reconstructed. After this, the search is limited to the events with reconstructed angle differing less than $40°$ from straight upward-going. At this level (cut number 4 in Fig. 1a), the sample is still dominated by misreconstructed atmospheric muon events, more than 10^3 times more abundant than the atmospheric neutrino background. The background is then further reduced by a series of sequential cuts on reconstruction quality parameters and energy parameters.

After about ten cuts (depending on mass and annihilation channel), the data sample is dominated by atmospheric neutrinos. All of the data from the three years are combined at this analysis level, and the final selection is applied on the three years together. With no significant excess of vertical tracks observed, the final selection on reconstructed zenith angle is optimised for the average lowest possible 90% confidence level upper limit on the muon flux. From the number of observed events and the amount of estimated background in the final angular search bin, we infer the 90% confidence level upper limit on the number of signal events for each of the considered neutralino models. Combined with the effective volume at the final cut level and the livetime of the collected data, this yields an upper limit on the neutrino-to-muon conversion rate, which can then be related to the muon flux [8], see Fig. 1b.

Search for neutralino annihilations in the Sun

The data collected in 2001 is also used for the search for solar neutralinos and corresponds to 143.7 days of effective livetime. The total event sample contains 8.7×10^8 events, but does *not* include events triggered only by the string trigger. In contrast to the neutralino search in the Earth, the background level can be reliably obtained from randomization of the azimuthal angle. The advantage of this procedure is that it allows the use of the full data set for cut optimisation. The azimuthal angles are restored once the optimisation is finalised and results are calculated. The simulated atmospheric background sample at trigger level to-
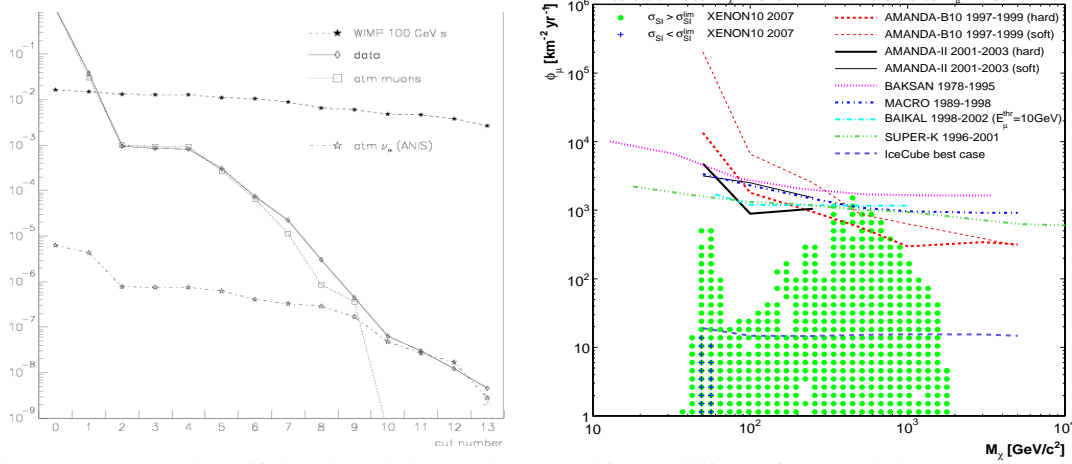
Figure 1: (a) Detection efficiencies relative to trigger level for the different filter levels in an Earth neutralino analysis ($m_\chi = 100 GeV/c^2$, soft spectrum) for 2001–2003 data. (b) As a function of neutralino mass, the 90% CL upper limit on the muon flux from hard (bottom) and soft (top) neutralino annihilations in the center of the Earth compared to the limits of other indirect experiments [9] and the sensitivity estimated for a best-case IceCube scenario [10]. Markers show predictions for cosmologically relevant MSSM models, the dots represent parameter space excluded by XENON10 [11].

tals 1.6×10^8 muons (equivalent to 32.5 days of effective livetime) and 1.9×10^4 neutrinos.

The solar neutralino analysis suffers the same backgrounds as the terrestrial neutralinos, but the signal is expected from a direction near the horizon, due to the trajectory of the Sun as seen from the South Pole. This analysis was only possible after completion of the full detector, whose $200m$ diameter size provides enough lever arm for robust reconstruction of horizontal tracks.

A similar analysis strategy as in previous section is adopted. First, events are selected with well-reconstructed horizontal or upward-going tracks. The remaining events are then passed through a neural network that was trained separately for the neutralino models under study and used data as background (filter level 4). Although a data reduction of $\sim 10^{-5}$ compared to trigger level is achieved, the data sample is still dominated by mis-reconstructed downward-going muons, see Fig. 2a. Finally, these are removed by cuts on observables related to reconstruction quality.

There is no sign of a significant excess of tracks from the direction of the Sun in the final data sample. The background in the final search bin around the Sun is estimated from off-source data in the same declination band, which eliminates the effects of uncertainties in background simula-

tion. Combining this with the number of observed events, the effective volume and the detector livetime, we obtain 90% confidence level upper limits on the muon flux coming from annihilations in the Sun for each considered neutralino mass [12], as shown in Fig. 2b.

Discussion and outlook

Figures 1b and 2b present the AMANDA upper limits on the muon flux from neutralino annihilations in the Earth and the Sun (only hard channel) respectively, together with the results from other indirect searches [9]. Limits have been rescaled to a common muon threshold of $1 GeV$ using the known energy spectrum of the neutralinos. Also shown are the cosmologically relevant MSSM models allowed (crosses) and disfavoured (dots) by the direct search from XENON10 [11].

Compared to the previously published AMANDA results from searches for neutralinos in the Earth [8] the analysis of 2001–2003 data benefits from the larger detector volume and the addition of the string trigger with its lower energy threshold. This makes it possible to improve the sensitivity especially for low energy Earth neutralino models; for masses above $250 GeV/c^2$ the effect is expected to be less pronounced. The new limits on the neutralino-induced muon flux are up to a factor 60 stronger than our earlier result.
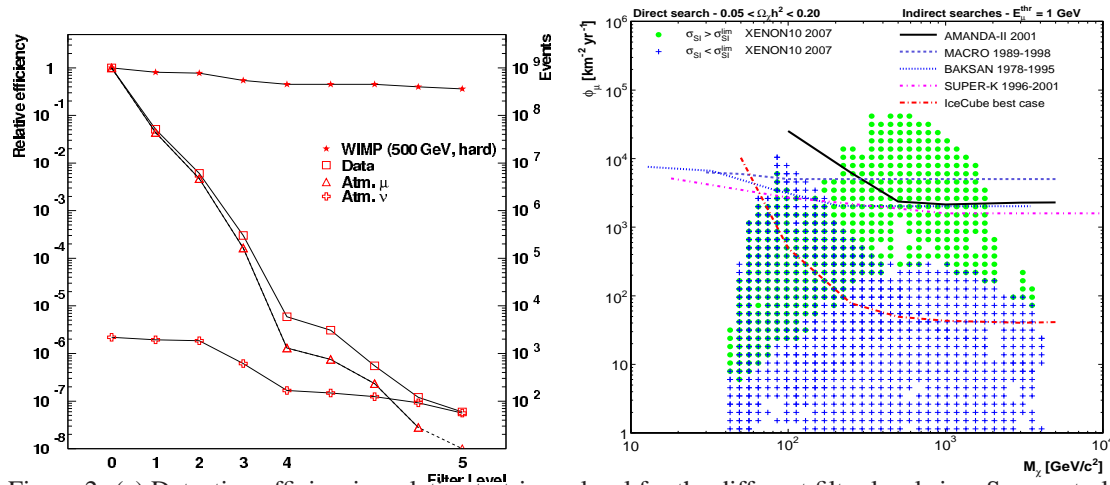
Figure 2: (a) Detection efficiencies relative to trigger level for the different filter levels in a Sun neutralino analysis ($m_\chi = 500 GeV/c^2$, hard spectrum) for 2001 data. (b) As a function of neutralino mass, the 90% CL upper limit on the muon flux from hard neutralino annihilations in the center of the Sun compared to limits of other indirect experiments [9] and the sensitivity estimated for a best-case IceCube scenario [10]. Markers show predictions for cosmologically relevant MSSM models, the dots represent parameter space excluded by XENON10 [11].

A similar improvement (with respect to [12]) is expected for the solar neutralino analysis of 2001–2003 data, thanks to the increased detector exposure, improved reconstruction techniques and the string trigger. A preliminary analysis shows a factor 10–100 improvement of the effective volume at early analysis level for low energy models, mainly due to the inclusion of the string triggered events.

The neutralino searches will be continued on a larger set of AMANDA data from 2000–2006. Since 2007 AMANDA is embedded as a high-granularity subdetector of the IceCube neutrino telescope, currently under construction. This offers additional opportunities for the dark matter searches, as described in [10].

References

[1] D. N. Spergel et al., Astrophys. J. Suppl. Ser. **170**, 377 (2007).

[2] G. Jungman, M. Kamionkowski and K. Griest, Phys. Rept. **267**, 195 (1996).

[3] A. Gould, Astrophys. J. **328**, 919 (1988); J. Lundberg and J. Edsjö, Phys. Rev. **D69**, 123505 (2004); W.H. Press and D.N. Spergel, Astrophys. J. **296**, 679 (1985).

[4] J. Ahrens et al. (the AMANDA Collaboration), Nucl. Instr. Meth. **A524**, 169 (2004).

[5] P. Gondolo et al., Journ. of Cosm. & Astrop. Phys. **0407**, 008 (2004).

[6] D. Heck et al., FZKA report 6019 (1998).

[7] A. Gazizov and M. Kowalski, Comput. Phys. Commun. **172**, 202 (2005).

[8] A. Achterberg et al. (the IceCube Collaboration), Astropart. Phys. **26**, 129 (2006).

[9] M. Boliev et al. (the BAKSAN Collaboration), in *Proc. of Dark Matter in Astro- and Particle Physics*, edited by H.V. Klapdor-Kleingrothaus and Y. Ramachers (World Scientific, 1997); M. Ambrosio et al. (the MACRO Collaboration), Phys. Rev. **D60**, 082002 (1999); S. Desai et al. (the Super-Kamiokande Collaboration), Phys. Rev. **D70**, 083523 (2004), erratum *ibid* **D70**, 109901 (2004); V. Aynutdinov et al. (the Baikal Collaboration), in *Proc. of First Workshop on Exotic Physics with Neutrino Telescopes (EPNT06)*, edited by C. de los Heros (Uppsala University, 2006).

[10] G. Wikström et al. (the IceCube Collaboration), these proceedings HE.3.3.

[11] J. Angle et al. (the XENON Collaboration), arXiv:0706.003 (2007).

[12] M. Ackermann et al. (the AMANDA Collaboration), Astropart. Phys. **24**, 459 (2006).

Prospects of dark matter detection in IceCube

G. WIKSTRÖM[1] FOR THE ICECUBE COLLABORATION[2]

[1]*Department of physics, Stockholm University, AlbaNova, S-10691 Stockholm, Sweden.*
[2] *See special section of these proceedings.*
wikstrom@physto.se

Abstract: The IceCube neutrino telescope, under construction at the South Pole, currently consists of 22 IceCube strings and 19 AMANDA strings. Combining the two arrays leads to a large instrumented volume with AMANDA as a dense core, an ideal situation for indirect detection of WIMP dark matter annihilations in the Sun. From simulations we calculate the current detector's sensitivity for solar WIMP neutrinos and find that it improves considerably compared to AMANDA-II. The improvement is due to a combination of reduced trigger thresholds and larger detector volume which permits the use of veto against muonic background.

Introduction

We investigated the possibilities of detecting a neutrino signal from neutralino WIMP dark matter annihilations in the Sun. The studied neutralino masses were $m_\chi = 50, 100, 250, 500$ and 1000 GeV and the annihilation channels were W^+W^- (*hard channel*) and $b\bar{b}$ (*soft channel*). For $m_\chi = 50$ GeV the $\tau^+\tau^-$ channel is defined as the hard channel. Neutrinos produced in the Sun from the decay and interactions of the neutralino annihilation products can reach the detector and produce muons in CC reactions $\nu_\mu(\overline{\nu}_\mu) + N \rightarrow \mu^-(\mu^+) + X$. These signal muons traversing the ice sheet produce Cherenkov light, detectable by the Optical Modules (OM) of the IceCube detector. The WIMP neutrino zenith angle will follow the Sun's position over the year, $\theta_\odot \in [67°, 113°]$, and the mean muon energy will be around $\langle E_\mu \rangle \sim m_\chi/3$ for hard channels and $\langle E_\mu \rangle \sim m_\chi/6$ for soft channels.

Muons produced in cosmic ray interactions in the atmosphere have a zenith angle range of $\theta_\mu \in [0°, 90°]$ since muons cannot traverse the whole Earth. These *atmospheric* μ constitute the main background. Another background is that of muon neutrinos produced in the atmosphere, *atmospheric* ν_μ, which have a near-isotropic angular distribution.

The 2007 IceCube detector [1] consists of 41 strings of which 19 constitute AMANDA [2]. The two arrays have separate trigger and data aquisition systems (DAQs) which record events autonomously. However, a trigger in AMANDA will force a readout of the IceCube strings, even if IceCube did not have a trigger.

To reject atmospheric μ background we searched for contained events, i.e. neutrino events with the CC vertex inside a fiducial volume, as defined in figure 1. We demanded the events to either have no OMs hit in the veto region or that the first OM hit in the veto region came later than the OM hits in the fiducial region. This aimed at ensuring that the muon was created inside the detector, and did not come from the atmosphere. To reduce the number of atmospheric μ events leaking in between veto strings, we also demand that the average downwards motion of hits should be less than 50 m. Events that did not fulfill these conditions were still accepted provided that they had track reconstructions with $\theta_{rec} \geq 70°$ and more than 10 hit OMs. These conditions together constitute the low-level filtering that will run at South Pole.
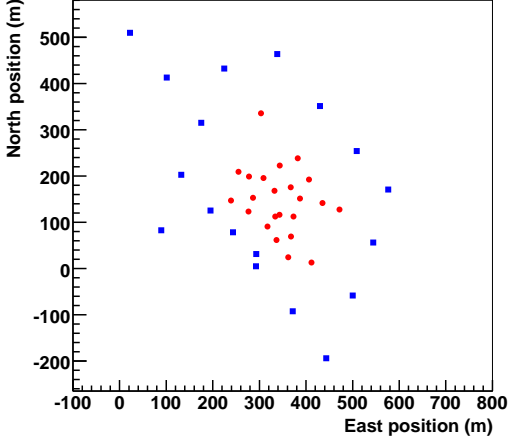
Figure 1: Top view of the 2007 IceCube detector consisting of 41 strings. The inner strings (dots) define the fiducial region, surrounded by veto strings (squares). Uppermost OMs of the fiducial strings belong to the veto region.

Simulations

A sample of atmospheric μ background events corresponding to ~ 1 hour of detector livetime ($2.3 \cdot 10^6$ events triggering) was simulated using `CORSIKA` [3] with the Hörandel CR composition model [4]. For the atmospheric ν_μ background, a sample corresponding to ~ 0.5 years of detector livetime ($4.2 \cdot 10^4$ events triggering) was generated according to the Bartol spectrum [5].

The solar WIMP signals were simulated with `WimpSim` [6], which uses `DarkSUSY` [7] and `PYTHIA` [8] to calculate annihilation rates and neutrino production. The neutrinos were propagated through the Sun and to the Earth with standard full flavour oscillations [9]. A charged lepton and a hadronic shower were then generated in the ice. For this analysis only simulated muon events with the Sun under the horizon, $\theta_\odot \in [90°, 113°]$, were used.

Muon propagation through the ice was simulated with `MMC` [10]. Cherenkov light propagation through the ice to the OMs, taking into account the ice properties [11], was done with `Photonics` [12]. The detector response was simulated with the IceCube simulation package `icesim`.

Filtering

Events were first selected based on a log-likelihood (LLH) reconstruction, by demanding $\theta_{LLH} \in [90°, 120°]$. Half of the atmospheric μ and the WIMP events passing this cut were then used to train and half to test a neural network (NN) using two hidden layers and eight event observables based on hit topology as well as the LLH reconstructed track parameters. A cut was made on the NN output value, the hit multiplicity and the reconstruction quality. This cut removed all simulated atmospheric μ background, and only WIMP events and atmospheric ν_μ background remained.

Among the remaining events we selected the neutrino candidates originating from the Sun's direction within a cone with half opening angle varying between $3°$ and $10°$ depending on m_χ and annihilation channel. At this final analysis stage V_{eff} for the observation of WIMP signals were calculated as

$$V_{eff} = \frac{N_{det} \cdot V_{gen}}{N_{gen}}, \qquad (19)$$

where N_{gen} is the number of generated CC interactions, V_{gen} is the generation volume, and N_{det} is the number of WIMP events in the search cone. Results are given in figure 2 (squares).

Sensitivity

From the expected number of surviving atmospheric ν_μ events μ_b we calculated the mean expected Feldman-Cousins $\mu_s^{90\%}(n_{obs}, \mu_b)$ [13] signal upper limit from all possible outcomes n_{obs} as the Poisson weighted sum

$$\bar{\mu}_s^{90\%} = \sum_{n_{obs}=0}^{\infty} \mu_s^{90\%}(n_{obs}, \mu_b) \frac{(\mu_b)^{n_{obs}}}{n_{obs}!} e^{-\mu_b}. \qquad (20)$$

From the WIMP V_{eff} and $\bar{\mu}_s^{90\%}$ we then calculated the mean expected upper limit on the neutrino to muon conversion rate

$$\bar{\Gamma}_{\nu \to \mu}^{90\%} = \frac{\bar{\mu}_s^{90\%}}{V_{eff} \cdot t}, \qquad (21)$$

where t is the analysis livetime, which here is 0.5 years. These values (one for each WIMP signal)
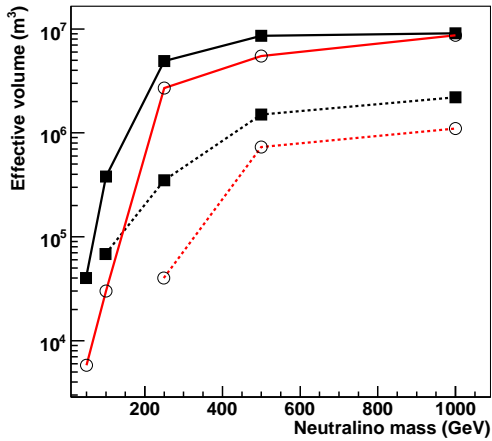
136

Figure 2: WIMP effective volume as a function of neutralino mass for hard (solid) and soft (dashed) annihilation channel, for analysis done on IceCube-22 + AMANDA (squares) and IceCube-22 only (circles).
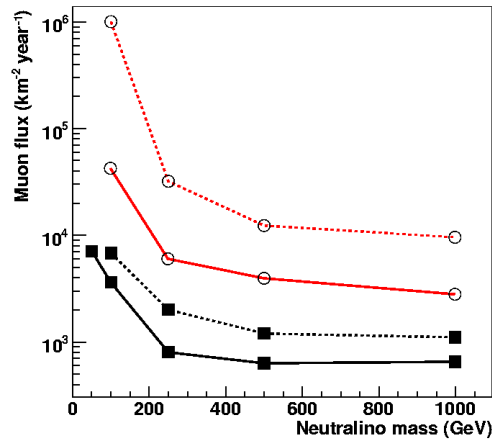

Figure 3: Expected sensitivity to muon flux from neutralino annihilations in the Sun as a function of neutralino mass for hard (solid) and soft (dashed) annihilation channel for this analysis using IceCube-22 and AMANDA (squares), compared to the 2001 AMANDA analysis [16, 17] (circles). Systematic uncertainties are not included.

were then used to calculate the mean expected upper limit on the muon flux from neutralino annihilations in the Sun, $\bar{\Phi}_\mu^{90\%}$ [14, 15], which is a measure of the detector's WIMP sensitivity. Comparing these values with the mean expected values from an earlier analysis with AMANDA-II [16, 17], we see improvements of an order of magnitude for lower WIMP masses, see figure 3.

Repeating the analysis with only the IceCube-22 array, we found that AMANDA stands for the major contribution to the sensitivity at lower m_χ and that the IceCube strings dominates for $m_\chi \geq 500$ GeV (see figure 2). The increase in sensitivity for the AMANDA array is due to lowered trigger multiplicity thresholds thanks to the new TWR-DAQ [18], whereas for higher m_χ the increased sensitivity comes from the increased detector volume in IceCube compared to AMANDA. The forced readout of IceCube when AMANDA has a trigger makes it much easier to distinguish a neutrino event from an atmospheric μ event.

Outlook

This sensitivity estimation demonstrates the feasibility of a WIMP analysis on experimental data from 2007 using the combined IceCube-22 and AMANDA detector.

References

[1] A. Achterberg *et al.* (the IceCube collaboration), *Astrop. Phys.* **26** (2006) 155.

[2] J. Ahrens *et al.* (the AMANDA collaboration), *Nucl. Instr. Meth.* **A524**, (2004) 169.

[3] D. Heck *et al.* FZKA Report 6019, Forschungszentrum Karlsruhe, 1998.

[4] J.Hörandel, *Astop. Phys.* **19** (2003) 193.

[5] G. D. Barr *et al.*, *Phys. Rev.* **D70** (2004) 023006.

[6] J. Edsjö, Simulation of WIMP annihilations in the Earth/Sun and propagation to a neutrino telescope, Stockholm University, 2006.

[7] P. Gondolo *et al.*, JCAP **0407** (2004) 008.

[8] T. Sjöstrand *et al.*, *Comp. Phys. Comm.* **135** (2001) 238.

[9] M. Maltoni *et al.*, *New J. Phys.* **6**, (2004) 122.

[10] D. A. Chirkin, Ph.D. thesis, University of California at Berkeley, 2003.

[11] M. Ackermann *et al.*, *J. Geophys. Res.* **111** (2006) D13203

[12] J. Lundberg, P. Miocinovic, T. Burgess, J. Adams, S. Hundertmark, P. Desiati, K. Woschnagg, & P. Niessen, arXiv:astro-ph/0702108, submitted to *Nucl. Instr. Meth.* **A**.

[13] G. Feldman, R. Cousins, *Phys. Rev.* **D57** (1998) 3873.

[14] J. Ahrens *et al.* (the AMANDA collaboration), *Phys. Rev.* **D66** (2002) 032006.

[15] L. Bergström, J. Edsjö and P. Gondolo, *Phys. Rev.* **D58** (1998) 103519.

[16] Y. S. Minaeva, Ph.D thesis, Stockholm University, 2004.

[17] M. Ackermann *et al.* (the AMANDA collaboration), *Astrop. Phys.* **24**, 459 (2006).

[18] W. Wagner, Ph.D thesis, Dortmund University, 2004.

![ICRC'07 Merida, México logo]

Search for Relativistic Magnetic Monopoles with the AMANDA-II Detector

H. Wissing[1] for the IceCube Collaboration[*]

[1]III Physikalisches Institut, RWTH Aachen University, D-52056 Aachen, Germany

[*]see special section of these proceedings

hwissing@physik.rwth-aachen.de

Abstract: Cherenkov emissions of magnetic charges moving through matter will exceed those of electric charges by several orders of magnitude. The AMANDA neutrino telescope is therefore capable of efficiently detecting relativistic magnetic monopoles that pass through its sensitive volume. We present the to date most stringent limit on the flux of relativistic magnetic monopoles based on the analysis of one year of data taken with AMANDA-II.

Introduction

The existence of magnetic monopoles is mandatory in a large class of Grand Unified Theories. Predicted monopole masses range from 10^8 to 10^{17} GeV, depending on the symmetry group and unification scale of the underlying theory [1]. The monopole magnetic charge will be an integer multiple of the *Dirac Charge* $g_D = e/(2\alpha)$, where e is the electric elementary charge and $\alpha = 1/137$ is the fine structure constant. Since magnetic monopoles are topologically stable, they should still be present in today's universe and can be searched for in cosmic radiation. Once created, monopoles can efficiently be accelerated by large scale magnetic fields. Monopoles with masses below $\sim 10^{14}$ GeV are expected be relativistic [2] and neutrino telescopes could detect their direct Cherenkov emissions. The number of Cherenkov photons N_γ emitted per path length dx and photon wavelength $d\lambda$ radiated from a monopole with magnetic charge g passing through matter with index of refraction n is [3]

$$\frac{dN_\gamma}{dxd\lambda} = \frac{2\pi\alpha}{\lambda^2} \left(\frac{gn}{e}\right)^2 \left(1 - \frac{1}{\beta^2 n^2}\right), \quad (22)$$

where β is the speed of the monopole as a fraction of the speed of light in vacuum. The Cherenkov light intensity in ice radiated from a relativistic magnetic monopole carrying one Dirac charge is enhanced by factor $(g_D \cdot n/e)^2 = 8300$ compared to the intensity radiated from a particle with electric charge e and the same speed.

Search Strategy

The AMANDA-II neutrino telescope consists of 677 light sensitive optical modules (OMs) embedded in the ice under the geographic South Pole at depths between 1500 and 2000 meters. Each OM contains a photomultiplier tube (PMT) and supporting electronics enclosed in a transparent pressure sphere. The OMs are deployed on 19 vertical strings arranged in three concentric circles (see Figure 1). The inner ten strings are read out electrically via coaxial or twisted-pair cables, while the outermost strings use optical fiber transmission. For each triggered event, leading and trailing edges of up to eight PMT pulses and one peak amplitude can be recorded per OM. AMANDA-II has been
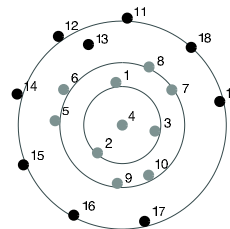

Figure 1: Arrangement of the 19 strings of the AMANDA-II detector in the horizontal plane.

taking data since the beginning of the year 2000. This analysis concerns data taken between February and November 2000.

We have simulated the detector response to relativistic magnetic monopoles carrying one Dirac Charge with four different speeds: $\beta = v/c = 0.76, 0.8, 0.9,$ and 1.0. Down-going atmospheric muons, which form the principal background to this search, were simulated with the air-shower simulation package CORSIKA [4]. Following a "blind" analysis procedure, the data selection chain is optimized on simulated data, and only a subset of 20% of the experimental data is used to verify the simulation of the detector response. This 20% is later discarded, and the developed selection criteria applied to the remaining 80% of the data. The blinded data comprise about 154 days of livetime, after correction for dead-time and rejection of periods of low data quality.

A relativistic magnetic monopole passing through the detector's sensitive volume will stand out as an extremely bright event relative to the atmospheric muon background. Observables that provide a measure of the light yield in the detector are the number of OMs hit during an event, the total number of pulses (or *hits*) recorded, the fraction of OMs which registered only a single hit (as opposed to those which recorded multiple hits), and the sum of the recorded PMT pulse amplitudes. These observables are used to reject the bulk of low energy atmospheric muons, either as one-dimensional cut parameters or as input to a discriminant analysis [5].

Up-going Monopoles

Magnetic monopoles with masses in excess of 10^{11} GeV can cross the entire earth and enter the detector from below [6]. The search for up-going relativistic magnetic monopoles is in principle background free, since up-going charged leptons induced by atmospheric neutrinos from the northern hemisphere will produce significantly less Cherenkov light than would magnetic monopoles. However, track reconstruction algorithms sometimes fail to identify large atmospheric muon bundles as down-going, and those misreconstructed events will remain as residual background. Fig-
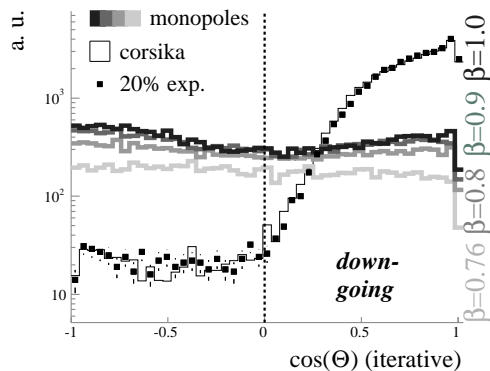

Figure 2: Cosine of the reconstructed zenith angle for simulated atmospheric muon background (light black histogram), 20% experimental data (black markers), and simulated monopole signal (heavy grey histograms). Each of the four grey histograms corresponds to one of the simulated monopole speeds from $\beta = 0.76$ (lightest grey) to $\beta = 1.0$ (darkest grey). A zenith angle of $\Theta = 0°$ corresponds to vertically down-going.

ure 2 shows the zenith angle distribution of reconstructed particle tracks obtained from an iterative likelihood reconstruction [7] for simulated signal and background as well as for 20% of the experimental data. For the up-going monopole search we reject all events for which the reconstructed zenith angle is smaller than 90 degrees. The background of misreconstructed atmospheric muon bundles is rejected by a final cut on the sum of PMT pulse amplitudes (ΣADC). At this level of the analysis, an excellent simulation of the OM response to large amounts of light is required. This involves an accurate modeling of the sensitivity of individual OMs as well as the probability with which OMs *"overflow"*, *i.e.*, record more than eight hits during one event (in which case a fraction of the hits is discarded by the data acquisition system). These requirements dictate that we use the amplitude sum of only a subset of OMs as final cut parameter, including only those OMs for which the detector simulation provides an exact description. This is the case for the OMs which are read out via fiber optics and which are located at depths below 1630 m. The fiber OMs have a substantially better time and double pulse resolution than the electronically read-out OMs. Thereby the simulation
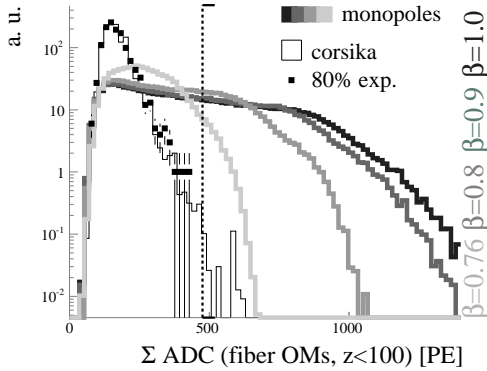
Figure 3: Sum of the PMT pulse amplitudes measured in the outer strings below a depth of 1630 m. The final cut (dashed line) requires the amplitude sum to be bigger than 476 photo electrons.

Figure 4: Expected background from atmospheric muons in the $\cos(\Theta) - \Sigma ADC$ plane before placing the final cut (dashed line).

of their response to multiple photons is more reliable. Using only this subset of OMs does not affect sensitivity, since the fiber OMs are attached to the outer nine strings of the array and define the surface area of the detector. Rather, the obtained flux limit improves as a result of the reduced systematic error.

Figure 3 shows the distribution of the final cut parameter. The exact value of the final cut is determined by optimizing the *sensitivity* of the analysis, *i.e.*, the cut is placed where we expect to obtain the most stringent flux limit. The background simulation predicts 0.23 events from misreconstructed atmospheric muons to remain in the 80% data set. After unblinding the data, no events are observed.

The 90% C. L. flux limits in units of $10^{-16} \text{cm}^{-2}\text{s}^{-1}\text{sr}^{-1}$ obtained for monopoles with various speeds β are listed in Table 1.

The limits are valid for monopoles with masses greater than 10^{11} GeV. A systematic uncertainty of 20% in both background rate and signal efficiency is incorporated into the calculation of the confidence belts according to [9].

β	0.76	0.8	0.9	1.0
$\Phi_{90\%C.L.}$	8.6	0.66	0.42	0.37

Table 1: 90% C. L. upper limits in units of $10^{-16} \text{cm}^{-2}\text{s}^{-1}\text{sr}^{-1}$ on the flux of relativistic magnetic monopoles with masses $> 10^{11}$ GeV.
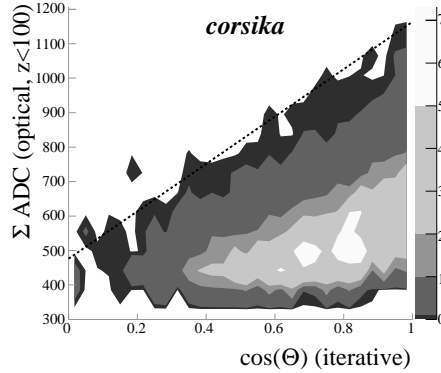
Down-going Monopoles

The search for down-going magnetic monopoles is subject to a much higher background rate. In order to preserve sensitivity over 4π sr, we use linear combinations of the reconstructed zenith angle and observables that are sensitive to the light deposition in the detector as cut parameters. The coefficients of each observable are found by a discriminant analysis. This optimization naturally results in cuts that require a greater light deposition for vertical tracks (smaller zenith angles), while the requirement is relaxed towards the horizon.

The final cut parameter for the down-going monopole search is a linear combination of the cosine of the reconstructed zenith angle ($\cos \Theta$) and the sum of pulse amplitudes recorded by the OMs on the outer strings at depths below 1630 m (ΣADC). Figure 4 shows the expected distribution of background events in the $\cos(\Theta) - \Sigma ADC$ plane. The final cut parameter is shown in Figure 5. Like in the up-going monopole search, the final cut is optimized such that we expect to obtain the most stringent limit. The background simulation predicts 2.6 events to remain in the experimental data set, and three events are observed after unblinding the data. The limits on relativistic monopoles with various speeds obtained from this observation are listed below (Table 2). The limits are valid for monopoles with masses greater than 10^8 GeV. Sys-
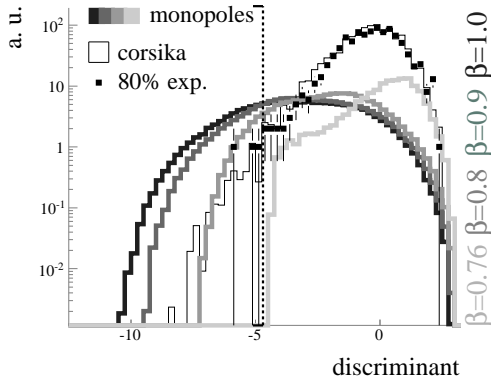
Figure 5: Final cut parameter (obtained from a discriminant analysis using $\cos(\Theta)$ and ΣADC as input observables) for the unblinded 80% experimental data (black markers), expected atmospheric muon background (black histogram), and simulated monopole signal (grey heavy histograms). The dashed black line marks the final cut.

tematic uncertainties are accounted for according to [9].

β	0.8	0.9	1.0
$\Phi_{90\%C.L.}$	16.33	4.1	2.8

Table 2: 90% C. L. upper limits in units of $10^{-16} \mathrm{cm}^{-2}\mathrm{s}^{-1}\mathrm{sr}^{-1}$ on the flux of relativistic magnetic monopoles with masses greater than 10^8 GeV.

Conclusions

The analysis of data taken with the AMANDA-II neutrino telescope during the year 2000 permits constraint of the flux of relativistic magnetic monopoles with speeds $\beta = v/c > 0.76$. For monopole speeds greater than $\beta = 0.8$ and monopole masses greater than $\sim 10^{11}$ GeV, the flux limit is presently the most stringent experimental limit. The search for lighter monopoles is possible, but less sensitive. With the analysis of one year of AMANDA data, the flux of magnetic monopoles with masses as low as 10^8 GeV and speeds close to $\beta = 0.8$ can be constrained to a level below the Parker Bound [10]. Figure 178

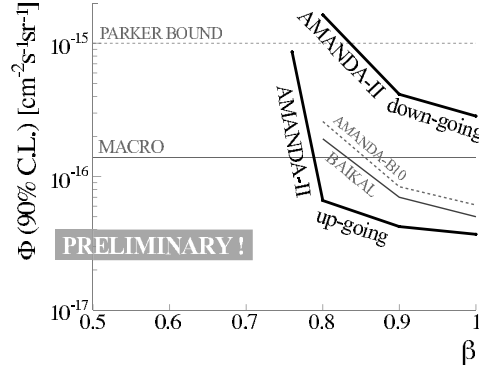shows the flux limits set by AMANDA compared to those set by some other experiments.

Figure 6: Limits on the flux of relativistic magnetic monopoles set AMANDA-II (this work), by MACRO [11], and by BAIKAL [12].

Acknowledgments

References

[1] G. 't Hooft, Nucl.Phys.B **79**, 276 (1974);

[2] S. D. Wick *et al.*, Astropart. Phys. **18**, 663 (2003).

[3] D. Tompkins, Phys.Rev. **B138**, 248 (1965).

[4] D. Heck and J. Knapp, Forschungszentrum Karlsruhe, Institut für Kernphysik (2000).

[5] R. A. Fisher, Annals Eugen. **7**, 179 (1936).

[6] J. Derkaoui *et al.* Astropart. Phys. **9**, 173 (1998).

[7] J. Ahrens *et al.*, Nucl. Instrum. Meth. **A524**, 169 (2004).

[8] G. C. Hill and K. Rawlins, Astropart. Phys. **19**, 393 (2003).

[9] J. Conrad *et.al*, Phys. Rev. **D67**, 12002 (2003).

[10] M. S. Turner, E. N. Parker, and T. J. Bogdan, Phys. Rev. **D26**, 1296 (1982).

[11] M. Ambrosio *et. al.*, Eur. Phys. J. **C25**, 511 (2002).

[12] The BAIKAL Collaboration, Proc. of 29th International Cosmic Ray Conference (2005).

Subrelativistic Particle Searches with the AMANDA-II detector

A. POHL[1,2], D. HARDTKE[3] FOR THE ICECUBE COLLABORATION[4]

[1]*Division of High Energy Physics, Uppsala University, S-75121 Uppsala, Sweden*

[2]*School of Pure and Applied Natural Sciences, University of Kalmar, S-39182 Kalmar, Sweden*

[3]*Department of Physics, University of California, Berkeley, CA 94720, USA*

[4]*see special section of these proceedings.*

arvid.pohl@hik.se

Abstract: Supermassive particles like magnetic monopoles, Q-balls and nuclearites may emit light at subrelativistic speeds through different suggested mechanisms. One of them is nucleon decay catalysis by magnetic monopoles, where the decay products would emit Cherenkov radiation along a monopole trajectory. The emitted secondary light from subrelativistic particles could make them visible to the AMANDA-II neutrino telescope, depending on the resulting luminosity. We present first experimental results from a search with AMANDA-II for events of this kind.

Introduction

The Grand Unified Theories (GUT) predict the existence of magnetic monopoles with expected mass of the order of $10^{16} - 10^{17}$ GeV[1]. These supermassive monopoles might become accelerated above virial velocities due to magnetic fields, but not relativistic [2].

Rubakov and Callan have indepentdtly proposed a mechanism by which SU(5) GUT monopoles are able to catalyse nucleon decay with a detectable cross section [3, 4]. The main decay channels would be $e^+\pi^0$, μ^+K^0 for protons and $e^+\pi^-$, μ^+K^- for neutrons, see [5] and refs. therein. The catalysis cross section has been suggested to be $\sigma = \sigma_0\beta^{-1}$ [3] or, at sufficiently low speeds, $\sigma = \sigma_0\beta^{-2}$ [6, 7], where σ_0 is a cross section typical of strong interactions. Nuclear attenuation factors have also been proposed, expressing nuclear spin effects on the decay catalysis [7]. The expected mean distance between nucleon decays catalysed along a monopole trajectory in ice, reaches down to submillimeter scales (following the cross sections above). Above the meter scale, the signal falls below our detector threshold.

In a neutrino telescope, the signature of these catalyzing monopoles would be a series of closely spaced light bursts produced along the monopole trajectory. Each burst would be Cherenkov radiation from an electromagnetic shower whose energy is close to the proton mass.

Other massive particles have also been hypothesized to exist in cosmic radiation. Two that might be detectable with neutrino telescopes are: Nuclearites (nuggets of strange dark matter) [8] and Q-balls (supersymmetric coherent states of squarks, sleptons and Higgs fields, predicted by supersymmetric generalizations of the standard model) [9].

Electrically neutral Q-balls would dissociate nucleons, emitting pions, which give them the same experimental signature in a neutrino telescope as catalyzing monopoles. Their cross section for nucleon dissociation is their geometric size. By limitations given in [10], it ranges from $\sim 10^{-26}\,\mathrm{cm}^2$ and many orders of magnitude upwards.

Nuclearites and charged Q-balls might also be detectable, as, travelling through matter, they would generate a thermal shock wave which emits black-body radiation at visible wavelengths [8, 11]. Their luminosity as given by [8] is determined by their geometric size, which is atomic or larger, and would exceed that of magnetic monopoles and neutral Q-balls by several orders of magnitude.

So far we have only considered magnetic monopoles.

The AMANDA-II Neutrino Telescope

AMANDA-II is a neutrino telescope located at a depth between 1500 m and 2000 m under the ice at the geographic South Pole. A cylindrical volume of roughly 200 m diameter of the Polar ice was instrumented with a total of 677 optical modules (OMs), consisting of a photomultiplier tube (PMT) and supporting electronics enclosed in a transparent pressure sphere. The OMs were deployed on 19 vertical strings.

A variety of triggers are used. First, the 24-fold multiplicity trigger requiring a minimum of 24 OMs hit within a fixed coincidence window of 2.5 μs, and second, a so-called correlation trigger, requiring n OMs to be hit in any group of m adjacent OMs on the same string (m, n typically $\sim 6, 9$). For each triggered event, PMT pulse data is recorded over a time window of $\sim 33\,\mu$s. The vast majority of triggers are due to down-going atmospheric muons, yielding an average event rate of roughly 90 Hz.

Simulation

The detection of slow particles builds on the fact that relativistic muons emit light during $\sim 3\,\mu$s, whereas slow particles emit during a large fraction of the 33 μs time window. A comparison is shown in Fig. 1. The upper picture shows a background event with the triggering muon at time 19 μs, and an accidental early non-triggering muon at 9 μs. The lower picture shows a simulated signal event. The signal separation from background is based on hits at times when no light from triggering muons is expected, the *early and late hits* outside the interval 16-24 μs.

In the simulation of sub-relativistic particles, all light output was expressed as Cherenkov radiation from electromagnetic showers arising from nucleon decay. All slow particles were simulated with isotropic directions and with speed $\beta = v/c = 10^{-2}$. In the simulations, the luminosity was expressed as the mean distance λ between two electromagnetic showers. So far, the simulated λ were in the range 2 mm - 60 cm.

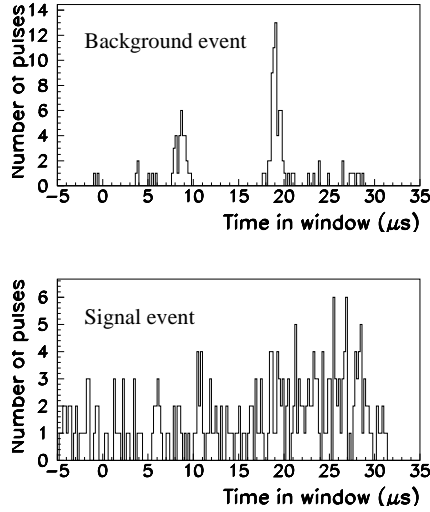For monopoles, only the decay of hydrogen protons was considered, and only the catalysis de-

Figure 1: Upper: a background event with a non-triggering muon (left) and a triggering muon (right). Lower: a simulated signal event from a particle traveling at speed $\beta = v/c = 0.01$.

cay channel $p \rightarrow e^+\pi^0$ (with a branching ratio of 0.9 or higher [12]). It creates an electromagnetic shower with energy close to the proton mass, whereas other channels lose some of their shower energy to neutrinos.

If a slow particle would approach the detector, atmospheric muons would cause contributing hits and possibly fire a trigger. These muons were included in the simulation.

The catalysis cross sections σ that correspond to the chosen λ are $3 \cdot 10^{-25}\,\text{cm}^2 - 9 \cdot 10^{-23}\,\text{cm}^2$. These are at the upper edge of what appears to be allowed by theoretical considerations.

Data analysis and results

A period of 113 days in 2001 when a constant correlation trigger definition was used, is considered here. It required a multiplicity of 6 within any 9 adjacent OMs in four strings and a multiplicity of 7 within any 11 adjacent OMs in the remaining strings. The simulations show that the correlation trigger was substantially more sensitive to this type of signal than the multiplicity trigger.
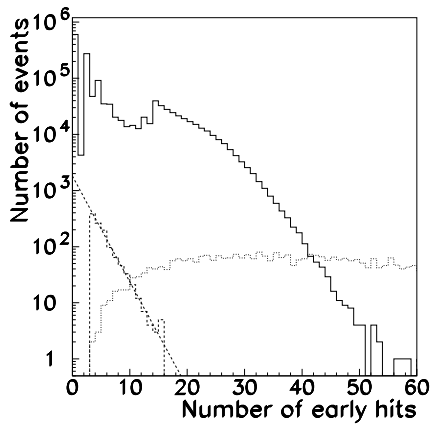
Figure 2: Number of early hits. *Solid*: Experimental data after first level filtering and cleaning. *Dashed*: Experimental data after second level filtering with an exponential fit. *Dotted*: Simulated signal after second level filtering ($\beta = 10^{-2}$, $\lambda = 2\,\mathrm{cm}$).

Figure 3: Flux limits (90% C.L.) and preliminary sensitivity (expected flux limit) at varying catalysis cross section.

The background properties and a preliminary expected sensitivity was determined using 20% of the data. A first filter reduced the data by 99%, requiring a total of at least 14 early and late hits.

Non-triggering muons contribute largely to early and late hits. The aim of the final filtering was to separate them from possible signal events. Hits from non-triggering muons arise within a short time span compared to hits from slow particles, as can be seen in Fig. 1. We defined hit clusters as collections of early hits that were separated by less than $2\,\mu$s. Each event was characterized by its cluster with most hits.

After trigger cleaning, we performed second level filtering using two cluster based cuts and one based on the events' geometries, as signal events are fairly well localized. The remaning events after filtering have an exponential distribution in the number of early hits. It is shown in Fig. 2, along with an exponential fit.

About 80% of signal events would be expected to have more than 20 early hits (cf. Fig. 2). Since none were found in the filtered data, the data must be almost signal free. Thus, the fit parameters are suitable for background estimation. They were used for calculating the expected number of background events at varying cuts in the number of early hits.
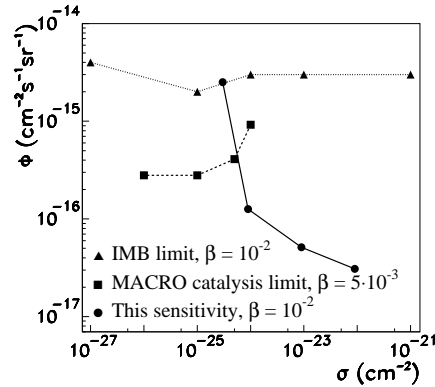
We optimized the final cut following the scheme described by [13] in order to achieve the optimum sensitivity, which is the 90% C.L. flux upper limit that we would obtain if no true signal were present.

The optimal final cut for the 80% sample requires > 27 early hits. The resulting sensitivities, without systematic uncertainties, are given in Fig. 3. For comparison, limits at similar particle speed are included: the MACRO limit based on nucleon catalysis from [5] and the IMB limit from [14]. Limits at lower velocities have been presented by Baikal and Kamiokande [15, 16].

Discussion and Outlook

The AMANDA neutrino telescope is an excellent instrument to search for several postulated super heavy exotic particles. In this document, we present first studies of the sensitivity of AMANDA to sub-relativistic particles. The given sensitivities are still preliminary. Specifically, systematic uncertainties are not yet included. So far, we have used relatively small sub-sets of the available AMANDA data in order to outline our analysis strategies. The sensitivity of the analysis will improve substantially with more data.

This analysis used data from the original AMANDA data acquisition system (DAQ). For each channel, the analog signal from the PMT is recorded using Time To Digital Converters (TDCs) and Peak Sensing Analog to Digital Converters (ADCs). The original AMANDA DAQ system is unable to precisely characterize multi photoelectron events. In addition, the DAQ suffers from a $\sim$ 1 millisecond dead time after each triggered event while the ADCs/ TDCs are read out. For events with slowly moving particles, this means that the DAQ system is unable to record the bulk of the signal.

Beginning in 2003, the AMANDA data acquisition system was upgraded to include full waveform readout and to reduce the detector deadtime. Each channel is now connected to a Transient Waveform Recorder (TWR), a flash ADC that samples at 100 MHz with 12 bit resolution. Although the readout window for the upgraded DAQ is shorter than for the original DAQ ($10.24\,\mu$s vs. $33\,\mu$s), the upgraded DAQ is able to record nearly continuously. In addition to the improved characterization of each event using the waveforms, the new DAQ allows for a reduction in the detector trigger threshold. Prior to 2004, AMANDA was generally run requiring a 24 channel coincidence in a $2.5\,\mu$s period, The upgraded DAQ can operate with a threshold of 18 optical modules. Additionally, events with between 13 and 17 hits are processed separately using a software trigger algorithm that looks for events where nearby optical modules are hit. The ability to almost continuously monitor the trajectory of a slowly moving particle, combined with the reduced trigger threshold, will greatly improve the sensitivity of AMANDA detector to such particle events.

AMANDA is now integrated with IceCube, and will continue to take data for several years. The analysis of the data from the integrated detector should give the best limits on the fluxes of slowly moving massive particles.

References

[1] G. 't Hooft, Nucl.Phys. **B79**, 276 (1974); A. M. Polyakov, JETP Lett. **20**, 194 (1974).

[2] S. D. Wick *et al.*, Astropart. Phys. **18**, 663-687 (2003).

[3] V. A. Rubakov, JETP Lett. **33**, 644 (1981);

[4] C. G. Callan, Phys. Rev. **D26**, 2058 (1982).

[5] M. Ambrosio, *et al.*, Eur. Phys. J. **C26** 163 (2002)

[6] V. A. Rubakov, M. S., Serebryakov, Nucl.Phys. **B218** 240 (1983)

[7] J. Arafune, M.Fukugita, Phys. Rev. Lett. **50** 1901 (1983)

[8] A. De Rújula and S. L. Glashow, Nature **312**, 734 (1984).

[9] J. Kusenko *et al.*, Phys. Rev. Lett. **80**, 3185 (1998).

[10] D. Bakari *et al.*, Astropart. Phys. **15**, 137 (2001).

[11] J. Arafune *et al.*, Phys. Rev. **D62**, 105013 (2000).

[12] F. A. Bais *et al.*, Nucl. Phys. **B219**, 189 (1983).

[13] G. C. Hill and K. Rawlins, Astropart. Phys. **19**, 393 (2003).

[14] R. Becker-Szendy *et al.*, Phys. Rev. **D49**, 2169 (1994).

[15] I. A. Belolaptikov *et al.*, Astropart. Phys. **7**, 263 (1997).

[16] D. Bakari *et al.*, J. Phys. Soc. Jap. **54**, 4065 (1985).

Exotic Particles Searches with IceCube

BRIAN CHRISTY[1], ALEX OLIVAS[1], AND DAVID HARDTKE[2] FOR THE ICECUBE COLLABORATION[3]
[1]*Dept. of Physics, University of Maryland, College Park, MD, 20742, USA*
[2]*Dept. of Physics, University of California, Berkeley, CA, 94720, USA*
[3]*see special section of these proceedings*

bchristy@icecube.umd.edu

Abstract: The IceCube neutrino observatory, currently under construction at the South Pole, offers a novel environment to search for particles beyond the Standard Model. With IceCube nearly 20% complete it is currently the largest operating neutrino telescope. The large instrumented volume and clear glacial ice allows for a big improvement of the sensitivity to many types of exotic cosmological relics. Exotic particles that IceCube is sensitive to include magnetic monopoles, nuclearites, and Q-balls. Estimated sensitivities for these particles will be presented.

Introduction

In 1931, Dirac [2] quantified the charge of a magnetic monopole by demonstrating that $g = Ne/2\alpha$, where α is the fine structure constant. Forty-three years later, t'Hooft and Polyakov independently found solutions to certain groups of Grand Unified Theories (GUTs) that matched the charge of the Dirac Monopole [10, 13]. This allowed estimates for the masses of magnetic monopoles to be $\sim \Lambda/\alpha$, where Λ is the symmetry breaking scale. This results in a mass range from 10^8 GeV to 10^{17} GeV for various GUT models. A lower limit is set by choosing Λ to be the electroweak unification scale, leading to a mass of 10^4 GeV. IceCube will expand the search for magnetic monopoles in two regimes. A magnetic monopole traveling through the detector above the Cherenkov threshold ($\beta > 0.76$) will emit radiation roughly 8300 times that of the bare muon [14].

At very large masses, monopoles may move with virial velocities ($\beta \sim 10^{-3}$). A slow-moving, super massive magnetic monopole will not emit Cherenkov radiation, but may be observed in other ways. Rubakov proposed that supermassive magnetic monopoles will catalyze nucleon decay. The nucleon decay products (primarily pions) will produce relativistic electrons that produce Cherenkov radiation. If the catalysis cross-section is sufficiently high, the supermassive magnetic monopole will appear as a slow moving track in the detector.

A similar signature would accompany the passage of a electrically neutral supersymmetric Q-ball though the IceCube array. A Q-ball is a soliton produced during the decay of the proposed Affleck-Dine condensate in the early universe. Sufficiently massive Q-balls would be absolutely stable and could account for some or all of the required dark matter in the universe. A neutral Q-ball passing near a nucleon will absorb the baryon number and emit $\sim$1GeV of energy in the form of pions [5]. The cross-section for this process is governed by the size of the Q-ball and can therefore be quite large [3].

It is also possible that novel forms of nuclear matter could be absolutely stable for very large baryon number [12]. Strangelets are a hypothetical state of nuclear matter with nearly equal up, down, and strange quark content. If such a state is the ground state of dense nuclear matter, cosmic-ray strangelets (aka nuclearites) could be produced in neutron star collisions. These heavy strangelets would have atomic sizes but nuclear densities. As they pass through the South Pole ice, they would produce a thermal shock emitting black-body radiation. This black-body radiation would register

in the IceCube photomultiplier tubes and cause the strangelet to appear as a slowly moving track.

Detector

IceCube is a kilometer-scale neutrino telescope currently being built between 1450 to 2450 meters below the Antarctic ice surface. It is designed for up to 80 strings of 60 Digital Optical Modules (DOMs), spaced out in a hexagonal pattern. For the data presented, we use the configuration of IceCube as of 2006, that is a total of 540 DOMs in 9 strings. The instrumented volume is $\sim$0.625 km^3, compared to the AMANDA instrumented volume of $\sim$0.016 km^3 The DOM is the cornerstone of the detector [4]. It is configured to detect photon signals via a Hamamatsu 10 inch Photomultiplier Tube(PMT). Onboard electronics contain two waveform digitizers, a fast Analog to Digital Converter (FADC) and an Analog Transient Waveform Digitizer (ATWD). The FADC has a nominal sampling rate of 25 ns/sample and can read up to 256 samples of the incoming waveform produced by the PMT. The ATWD digitizes the wavefrom across 3 channels representing different gain values. It runs with the nominal sampling rate of 3.3 ns/sample and can read up to 128 samples. In 2006, the number of samples was limited to reduce bandwidth. The highest gain ATWD channel was set to keep all 128 samples, while the two lower gains were only set to record the first 32 samples. Meanwhile, the FADC only kept the first 50 samples for a time window of 1.25μs. Since monopole events are extremely bright, their waveforms largely saturate the highest gain and hence information from the ATWD beyond 100 ns is greatly reduced. Though the FADC saturates before any ATWD channel, the longer time scale provides greater distinction between the signal and background. Hence, this study uses data provided by the FADC.

Signal and Background Simulations

Relativistic Magnetic Monopoles

The simulation of relativistic magnetic monopoles is done in three stages.

Magnetic monopoles are generated uniformly on a disk located 600m from the center of the detector pointing back towards it at various orientations. For this study, 10,000 monopole events were generated at binned angles theta and phi of 45 degrees, for a total of 260,000 events per dataset. A dataset was generated for four different speeds, β= 0.99, 0.9, 0.8, and 0.76.

Energy loss of the magnetic monopoles as they pass through the ice is modeled using the Bethe-Bloch formula as adapted by Ahlen [1]. Future plans are to extend this to include delta electrons, which will add to the overall light deposition in the detector.

The light output and propagation is modeled by a version of PHOTONICS [6] specifically generated to work with cone angles associated with the different speeds simulated. The light amplitude is scaled up using the formula of Tompkins [14].

Background

For this study, a 20% sample of the data for 2006 is used as the background. This sample consists of every fifth data event that passed the online high energy filter, in place to reduce the data rate over the satellite. The filter is set to accept events with the number of hit DOMs greater than 80. This filter reduced the number of triggered data events from $\sim 3.5 * 10^8$ to $\sim 3 * 10^5$.

Estimated Sensitvity to Relativistic Monopoles

The brightness of the magnetic monopole is the primary distinguishing feature. Therefore, we use parameters associated with the light yield in the first level of cuts. The two chosen are the number of hit DOMs (NDOM) and the total integrated FADC waveform (FCHARGE). The event rates are normalized to the expected rate for the 137.4 days of live time recorded by IceCube in 2006. For the monopole signal, a flux of $5 * 10^{-17} cm^{-2} s^{-1} str^{-1}$ is used, representing the lowest limit set by BAIKAL [7]. To get a conservative estimate on the sensitivity of the detector, a tight cut is made to eliminate all the 20% data sample. Figures 1 and 2 plot the signal and data for
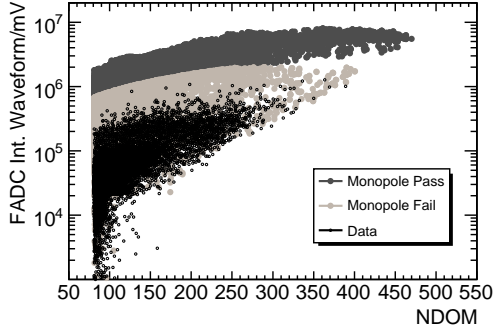
Figure 1: The effect of applying the linear cut to the integrated charge versus the number of hit DOMs distribution. Shown are the monopole signal simulation for $\beta = 0.99$ and data. The dark grey dots are signal events that pass the cut while the light grey signal dots and data (black) are rejected.

β	$A_{eff}(km^2)$	Exp Signal	Φ_{90}
0.99	0.3	19.05	$7*10^{-18}$
0.9	0.26	16.34	$7*10^{-18}$
0.8	0.08	4.92	$3*10^{-17}$
0.76	10^{-3}	0.09	$2*10^{-16}$

Table 1: Passing rates for linear cut. Expected signal and sensitivity for a full year of data.

FADC vs NDOM at the largest and smallest values of β studied. The following linear cut is chosen:

$$(FADC > 10^6 + 7500 * (NDOM - 125))$$

OR

$$(FADC > 3*10^6)$$

Table 1 shows the effective area of the signal resulting from this cut for each of the four monopole speeds. Assuming no events are seen, the flux sensitivity is calculated for the 90% C.L.

Estimated Sensitvity to Subrelativistic Particles

Slowly moving particles that traverse IceCube will appear as a connected series of small electromagnetic showers. The defining characteristic of the events is the length of time that photons remain in the detector. For a typical downgoing muon event,
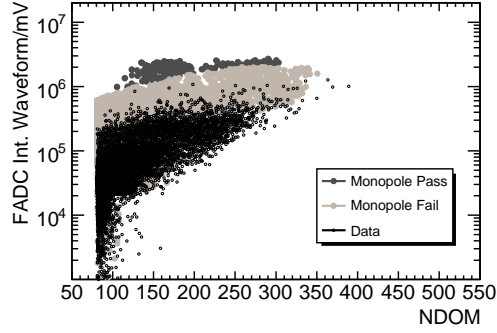

Figure 2: The effect of applying the linear cut to the integrated charge versus the number of hit DOMs distribution. Shown are the monopole signal simulation for $\beta = 0.76$ and data. The dark grey dots are signal events that pass the cut while the light grey signal dots and data (black) are rejected.

the mean event length is $\sim$1-2 μs, whereas a slowly moving particle will last hundreds of microseconds or even milliseconds. IceCube DOMs run as autonomous data collection devices and events are selected using a software trigger based on the individual DOM data. This makes IceCube very sensitive to slowly moving particle events. As long as the light output remains sufficient, the trigger will continue to add the DOM data to the triggered event. Currently, the IceCube sensitivity to Q-balls, Rubakov monopoles, and supermassive strangelets is limited by the high trigger threshold (8 DOMs in 5μs). Investigations are underway, however, of topological and tracking algorithms in the IceCube trigger system. Such a trigger will improve the sensitivity to slowly moving particles that produce less light.

Figure 3 shows the expected flux sensitivity to slowly moving massive particles ($\beta \sim 10^{-3}$) for the 2007 IceCube configuration (1320 DOMs in 22 strings) and the eventual full IceCube array. With the full IceCube array, we expect sensitivities more than two orders of magnitude better than the current experimental limits.
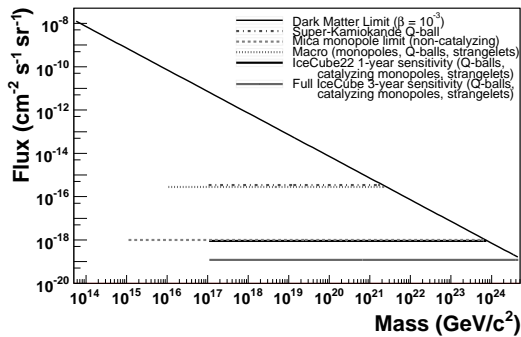
Figure 3: Current Limits [8, 9, 11] and Projected Sensitivities for Slowly Moving Massive Particles that may be seen by IceCube

Outlook and Conclusion

Each year, IceCube's capability to search for exotic particles will increase dramatically. With the 9 string detector alone, competitive limits on the flux of relativistic magnetic monopoles are achievable. However, these results are preliminary and will be refined. Background simulation will start with cosmic ray air showers produced by CORSIKA. Since only the high energy events are considered, weighting methods will be used. The asymmetry of the detector will require further analysis of the signatures produced at different angles. Finally, a log likelihood or neural network analysis may be employed to refine and optimize the cuts. With the additional analysis for slow moving exotics, IceCube will become a valuable tool in the search for these particles.

References

[1] S. Ahlen. Stopping Power Formula for Magnetic Monopoles. *Phys. Rev. D*, 17:229, 1978.

[2] P.A.M. Dirac. Quantized Singularities in the Electromagnetic Field. *Proc. Roy. Soc.A*, 133:60, 1931.

[3] D. Bakari et. al. Energy losses of Q-balls. *Astropart. Phys.*, 15:137, 2001.

[4] IceCube Collaboration: A. Achterberg et al. First Year Performance of the IceCube neutrino telescope. *Astropart. Phys.*, 26:155, 2006.

[5] J. Kusenko et. al. Experimental Signatures of Supersymmetric Dark-Matter Q-Balls. *Phys. Rev. Lett.*, 80:3185, 1998.

[6] J. Lundberg et. al. Light tracking for glaciers and oceans – Scattering and absorption in heterogeneous media with Photonics. *arXiv:astro-ph/0702108, submitted to Nucl. Instr. and Meth. A*, 2007.

[7] K. Antipin et al. Search for Relativistic Magnetic Monopoles with the Baikal Neutrino Telescope. *Proc. of the First Workshop on Exotic Physics with Neutrino Telescopes. C. de los Heros (editor) Uppsala University, January 2007. ISBN 978-91-506-1913-3 astro-ph/0701333*, page 80.

[8] M. Ambrosio et al. Final results of magnetic monopole searches with the MACRO experiment. *Eur. Phys. J. C*, 25:511, 2002.

[9] Y. Takenaga et al. Search for Neutral Q-balls in Super-Kamiokande II. *arXiv:hep-ex/0608057*, 2006.

[10] A. Polyakov. Spektr tschastiz w kwantowoi teorii polya. *Pisma Zhournal ETP*, 20:430, 1974.

[11] P.B. Price and M.H. Salamon. Search for Supermassive Magnetic Monopoles using Mica Crystals. *Phys. Rev. Lett.*, 56:1226, 1986.

[12] A. De Rujula and S.L. Glashow. Nuclearites - a novel form of cosmic radiation. *Nature*, 312:734, 1984.

[13] G. t'Hooft. Magnetic Monopoles in Unified Gauge Theories. *Nucl. Phys. B*, 79:276, 1974.

[14] D. Tompkins. Total Energy Loss and Cherenkov Emission from Monopoles. *Phys. Rev. B*, 138:248, 1965.

Effect of the improved data acquisition system of IceCube on its neutrino-detection capabilities

DMITRY CHIRKIN[1] FOR THE ICECUBE COLLABORATION[2]
[1]*Lawrence Berkeley National Laboratory, Berkeley, CA, U.S.A.*
[2]*see special section of these proceedings*
dchirkin@lbl.gov

Abstract: The IceCube data acquisition system is capable of recording information about all photons registered by its photomultiplier tubes for up to 13 microseconds for each sensor with high precision. A time resolution of 3 ns and charge resolution of 30% of all one photoelectron pulses within each sensor's event record is achieved. The improvement in quality of the data reconstruction due to the improved design of the experiment is estimated and its effect on the IceCube capabilities as a neutrino detector is discussed.

Introduction

The ability of IceCube optical sensors to record information about all photon registered by their PMTs has not yet been fully utilized in the data analysis (see, e.g., [1]). While the much improved timing and energy resolution are being used to improve upon the energy resolution of the detected muon events [2], this contribution attempts to demonstrate the improvement in muon neutrino analysis due to the ability to separately detect individual photoelectrons with their respective times and charges (shown in Figure 1).

The goal of selecting muon neutrinos in the presence of a 10^6 times higher background of atmospheric muons is to maximize the signal yield at a low background level, while achieving the best possible resolution with least mis-reconstruction of signal events.

In this preliminary study we present the analysis of one month of data collected by a 9-string IceCube detector configuration in year 2006. Data reconstruction algorithms using only the first photon per sensor were compared with those incorporating the full multi-photon information. The angular resolution achieved in both cases is very similar; however, the number of badly mis-reconstructed signal events is lower for multi-photon reconstruction. Using the additional information available from all

recorded photons leads to the correspondingly improved separation of signal and background and allows one to to achieve the required background reduction while retaining a higher signal yield.
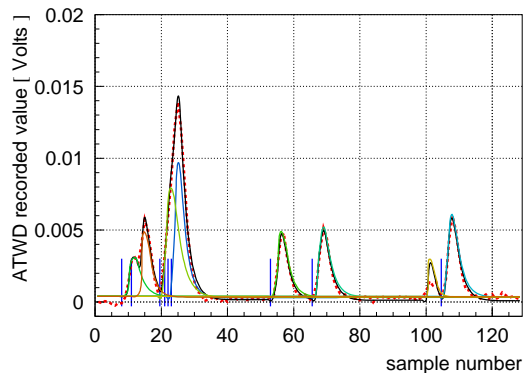
Figure 1: A typical PMT signal trace recorded by the faster digitizer of an IceCube optical sensor. The trace contains 128 samples, 3.3 ns. per sample. Results of 2 different photon deconvolution methods shown agree well. Blue vertical lines denote the hit times of the first method. The black fit line with colored lines denote deconvolved pulses of the second method. The data is shown with a red dashed line.

A new method of combining cuts to optimize background reduction is presented. First, a robust

Figure 2: Distribution of the deviation of the reconstructed from the true direction for the studied simulated data sample shown after some cuts.
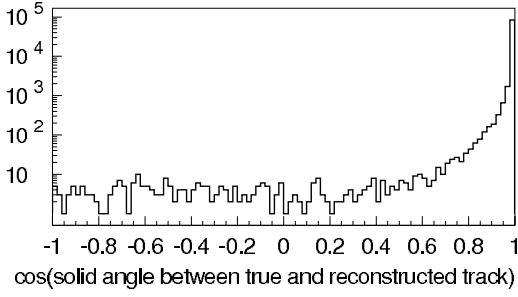
definition of angular resolution of reconstructed muon direction in simulated data is introduced. The cuts are optimized to maximize the angular resolution of the remaining events, and then are tightened to remove the background of misreconstructed events.

Angular resolution and cut optimization

The precision of the track reconstruction methods is determined from the deviation of the reconstructed result from the true track direction from the simulation (typical distribution shown in Figure 2). It was not possible to describe all such distributions at different reconstruction quality levels with a single shape depending only on the distribution width. Therefore the following very general definition was introduced instead: the *angular resolution* α of a given simulated data sample is chosen so that 2/3 of the data have reconstructed result deviate from the true track direction by less than the resolution, and 1/3 by more. This simple definition allows one to calculate the angular resolution α easily for all data quality levels, providing a good measure of the effectiveness of the quality cuts.

The cut parameters were chosen to have the following property: as the value of the cut on the parameter is lowered (i.e., the cut becomes stronger), the angular resolution α, as defined above, improves.

Several reconstructions were performed in succession. These differed by the ice description used in the calculation of the photon scattering probabilities, by whether the muon energy was allowed

to vary during the reconstruction, and whether all recorded photons or only first recorded photons were used.

For each reconstruction several quantities have the "cut property" defined above: minus reduced log likelihood of the reconstructed result, closest approach distance from the reconstructed track to the center of gravity of hits, relative uncertainty and variation of the energy measure, and uncertainty in the zenith and azimuth angles (defined as the range in the parameter in which the log likelihood stays above its maximum minus 0.5). Additionally the differences in the direction of different reconstruction results were formed. One more parameter appeared necessary: 1 over the total length of the track defined as the distance between two farthest from each other projections of hits on the reconstructed track. Parameters with similar distributions were grouped together, resulting in 7 groups. In each group the maximum value of the parameters in the group was chosen as the parameter of the group.

Cuts c_i, $i = 1, ..., 7$ were applied to the parameter groups defined above in such a way as to maximize the angular resolution α for each given fraction of events r left after the cuts. The fastest decent approach was chosen to optimize the cuts: starting with a full dataset, at each step reducing the fraction of the events left by the amount δr the cuts were adjusted by the amount proportional to $\partial \alpha / \partial c_i$.

Since the relative and overall cut strength depends on the number of degrees of freedom available during the reconstruction, cuts were optimized individually for event groups with different number of sensors with signal (here called channels) N_{ch} from the simulated dataset. This resulted in a set of cuts, one representation of which, describing achievable efficiencies (fractions of events left, r_n) for given α and N_{ch}, here called *efficiency matrix*, is shown in Figure 3. In order to determine the cut sets needed to achieve a certain angular resolution α the efficiency matrix is consulted to determine the fractions of events r_n with given $n = N_{ch}$. The set of cuts strong enough to leave only a fraction r_n of events that were used in the efficiency matrix evaluation are then the cuts that reduce the data to a set with the desired angular resolution α.
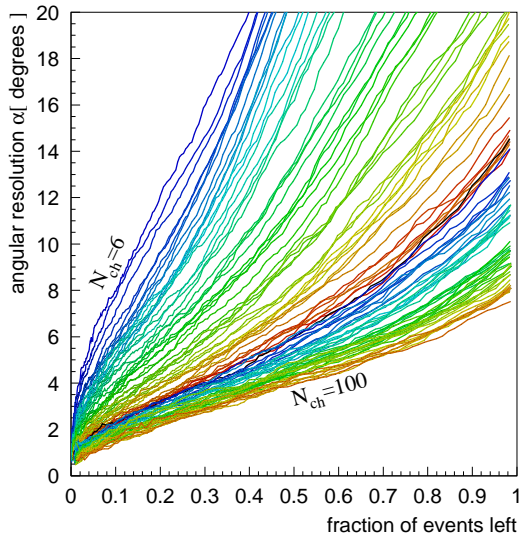
Figure 3: Efficiency matrix shows for each N_{ch} the best achievable angular resolution α at each given fraction of events left after applying cuts (this definition is equivalent to that given in the text).

To study the improvement in data analysis due to the availability of information about multiple pulses from each sensor the parameters corresponding to the multi-photon reconstructions were removed from the cut groups defined above. The resulting efficiency matrix looks nearly identical to the one shown in Figure 3 except that points on the lines correspond to somewhat more constrained cut values as compared to the multi-photon-enabled efficiency matrix. Therefore the first-photon-only cuts are just as effective as the complete cut set in improving the angular resolution α for a given data reduction fraction. This, however, is to be expected for a self-sufficient cut set, meaning that more cuts do not improve the angular resolution for a given fraction with the used angular resolution definition.

Nevertheless, as shown in the following section, at the final neutrino selection cut levels there is a substantial improvement in both the angular resolution α of the final sample and the fraction of events retained, indicating that the outliers of the angular distribution are reduced in the analysis employing the full cut set, showing the clear advantage of the method utilizing all recorded pulses.
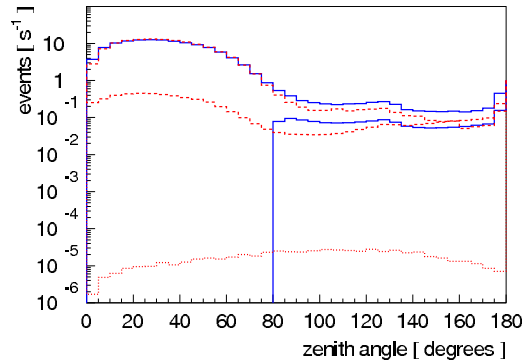

Figure 4: Initial zenith angle distribution (no cuts): red dashed lines: upper: downgoing muon background, lower: coincident downgoing shower background; red dotted line: muons from atmospheric muon neutrinos; upper blue line: reconstructed data; lower blue line: reconstructed data with cut of zenith angle above 80 degrees applied to all reconstructions.

Atmospheric neutrino search

Figure 4 shows the zenith angle distribution of reconstructed tracks in real and simulated data. The data remaining after the cuts on the zenith angle for all reconstructions are applied contains mostly poorly reconstructed downgoing background events that fall into the tail of events reconstructed with wrong direction shown in Figure 2. The data shown in Figure 2 is at the cut level corresponding to an angular resolution α of 4 degrees; misreconstructed events are suppressed by more than 4 orders of magnitude at this cut level. Without any cuts the level of misreconstructed events is higher, about 2 orders of magnitude below the peak, matching the level of misreconstructed events in Figure 4. By applying successively stronger cuts corresponding to lower values of angular resolution α the background of misreconstructed events can be reduced until most of the events reconstructed as upgoing are, indeed, upgoing.

To determine the angular resolution α required to suppress the background of misreconstructed events below the signal of upgoing events successively stronger cuts are applied. At each cut level the data left after the cuts is compared to simulation of both background and signal, as shown in
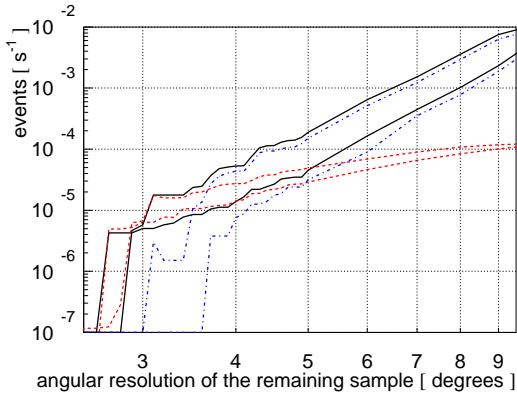
153

Figure 5: Events remaining at different cut levels corresponding to requested values of angular resolution α. Black solid: data; red dashed: muon neutrino simulation; blue dashed-dotted: background simulation. Upper curves are for full cut set; lower curves are for first-photon-only cut set.
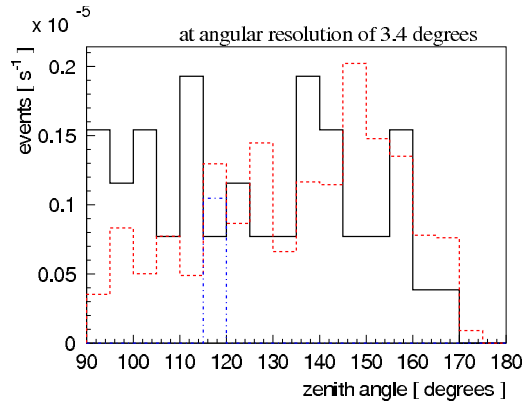

Figure 6: Zenith angle distribution at final cut level. Black solid line: data; red dashed: muon neutrino simulation; blue dashed-dotted: one event remaining from the background simulation.

Figure 5. The cut level required to achieve the desired signal purity can thus be selected. The 50% purity is achieved at the intersection points of simulated background and neutrino lines in Figure 5: at angular resolution α=3.7 with 96 events left for the full cut set, and at angular resolution α=4.9 degrees with 90 events left for the first-photon-only data set. At the same signal purity level the angular resolution α of neutrino events in the remaining sample is 30% better for the full set.

It is more difficult to estimate the purity and number of events left as the cuts are tightened more, due to the limited amount of simulated data at the time this paper was written. However, following the lines of Figure 5, one could estimate the angular resolution α and number of events left at $\sim 90\%$ purity level of 3.4 degrees and 46 events (shown in Figure 6) for the full cut set, and 3.6 degrees and 22 events for the first-photon-only cut set. This indicates that at the highest signal purity levels the number of neutrino events is more than doubled when incorporating the full information about all pulses into the analysis.

Conclusions

A new approach to background rejection in IceCube is taken: instead of optimizing cuts to max-

imize signal over background, cuts are first optimized to maximize the angular resolution α of single muon tracks while retaining as many of the events as possible. Then the cuts corresponding to successively better values of angular resolution α are applied until the desired signal purity is achieved.

This approach allowed us to study the effect of including the complete information on all pulses recorded by the optical sensors of the detector. The number of signal events retained at the highest purity levels doubled (important for diffuse analysis), while the angular resolution α at somewhat relaxed cuts improved by 30 %.

References

[1] Pretz, J. for the IceCube Collaboration, these proceedings
[2] Zornoza, J. for the IceCube Collaboration, these proceedings
[3] Karle, A., these proceedings

Improved Cherenkov light propagation methods for the IceCube neutrino telescope

J. LUNDBERG[1], FOR THE ICECUBE COLLABORATION[2]
[1]*Division of High Energy Physics, Uppsala University, Uppsala, SE*
[1]*johan.lundberg@tsl.uu.se,* [2]*see special section of these proceedings*

Abstract: In the field of neutrino astronomy, optically transparent media like glacial ice or deep ocean water are commonly used as detector medium. Elementary particle interactions are studied using in situ light detectors recording time distributions and fluxes of faint photon fields of Cherenkov radiation, typically generated by ultra-relativistic muons. For simulations of such photon fields, the IceCube collaboration uses a versatile software package, PHOTONICS, which was developed to determine photon flux and time distributions throughout a large volume with spatially varying optical properties. Photons are propagated and time distributions are pre-calculated as binary photon tables for fast and transparent access from event simulation and reconstruction. This is the main tool by which IceCube event simulations take into account how depth and wavelength dependent variations of the optical properties of the South Pole glacier distort the footprints of elementary particle interactions.

Introduction

In optical high energy neutrino astronomy, light from charged particle interactions is observed using a large number of sensors (photomultipliers) placed in transparent natural media like glacial ice, lake water, or deep ocean water. Successful simulation and reconstruction of such events relies on accurate knowledge of light propagation within the detector medium. The typical scattering lengths in these detector media are of the order of tens to hundreds of metres. Since this scale is comparable to the typical sensor spacing for neutrino telescopes, scattering effects can not be ignored, and analytical calculations do not suffice. The problem is further complicated by the anisotropy of the light emitted in particle interactions and the heterogeneity of natural detector media.

The software package PHOTONICS[1] contains routines for detailed photon simulations in heterogenous media like the South Pole glacier. Photon simulation results are pre-calculated and used in event simulation and reconstruction through interpolation of lookup tables for fast and accurate access to photon signal timing and amplitude probabilities.

Photon flux simulation technique

At any location throughout the medium, the local optical properties for a given wavelength are described by the absorption length λ_a, the geometrical scattering length λ_s, and the scattering phase function which is the probability density function for angular deviations at each scatter. For ice, the Henyey-Greenstein (HG) phase function[2] is used to describe the strongly forward peaked scattering. It is completely characterized by a single parameter, the mean of the cosine of the scattering angle, $\tau = \langle \cos\theta \rangle$. For most physical media, a strong correlation between λ_s and τ is observed. One therefore considers the effective scattering length, $\lambda_e \equiv \lambda_s/(1 - \tau)$.

Photons are generated according to emission spectra specific for the given light source (particle physics events or calibration light sources) and propagated throughout the medium in accordance with the heterogeneous propagation medium description. Each photon's spatial and temporal path is calculated and its contribution to the overall light field is recorded in a cellular grid throughout a user defined portion of the simulation volume. The locations of sensors are not fixed, but can be dynam-

ically specified when accessing the simulation results.

The detector efficiency as function of angle and wavelength, as well as the effects of absorption, is accounted for by applying appropriate weights during the photon recording.

The local photon flux is calculated in each recording cell with one of two independent methods. In the volume-density method, photons are propagated in small (typically equidistant) steps between scattering points, so that the contribution to each recording cell is related to the number of photon steps taken in that particular cell. In the surface-crossing method, photons are instead interrupted only at scattering points and recording cell boundaries. The flux contribution is then related to the number of cell boundary crossings, taking into account the projected cell surface area of each cell boundary crossing. The two methods typically give compatible results at a comparable simulation speed, depending slightly on the layout of the simulation grid and the optical parameters.

To improve the speed of the Monte Carlo simulation, importance-weighted scattering is supported; Photons can be propagated using scattering parameters $(\lambda_{e'}, \tau')$, different from those of the physical scattering situation at hand. For example, straighter paths can be oversampled by choosing scattering angles θ from a HG phase function $f_{\tau'}$ with τ' closer to 0, while applying a weight of $f_\tau(\theta)/f_{\tau'}(\theta)$.

The result of the photon simulation is multidimensional binary photon tables, containing the expectation number of photo-electrons produced at photomultiplier tubes and the corresponding differential or cumulative time distributions.

Modeling of glacial ice and applications to neutrino astronomy

A detailed study of the properties of the glacial ice at the South Pole has been performed by the AMANDA collaboration[3]. The ice is very clear in the optical and near UV region with absorption lengths of 20–120 m, depending on wavelength. The effective scattering lengths are around 25 m, less for shorter wavelengths. Both scattering and absorption are strongly depth dependent. The vari-
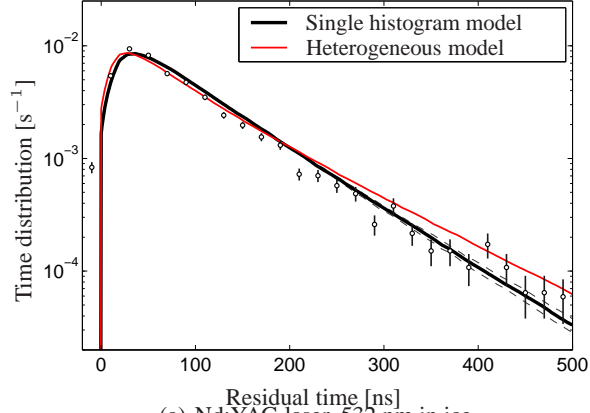
(a) Nd:YAG laser, 532 nm in ice
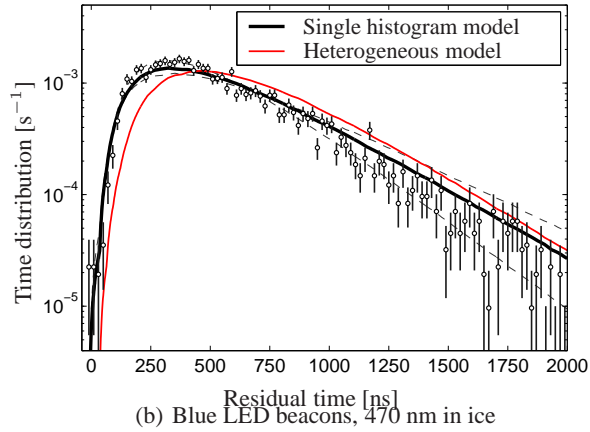
(b) Blue LED beacons, 470 nm in ice

Figure 1: Residual time distributions of simulated light pulses in deep glacial ice. In (a), for a 532 nm Nd:YAG isotropic laser pulse, emitted at a depth of 1825 meter, as seen from a horizontal distance of 75 m. In (b), for an upward pointing 470 nm LED emitter located at a depth of 1580 m as seen from a horizontal distance of 140 m. The black dots show two time distributions of glacial ice surveys[3], with vertical Poissonian error bars. The thick black lines show our results using the scattering and absorption parameters of these particular source–receiver combinations, and thin dashed lines represents the model uncertainty. The thin (red) lines show the simulation results with the heterogeneous ice model[3] which was constrained by other data.
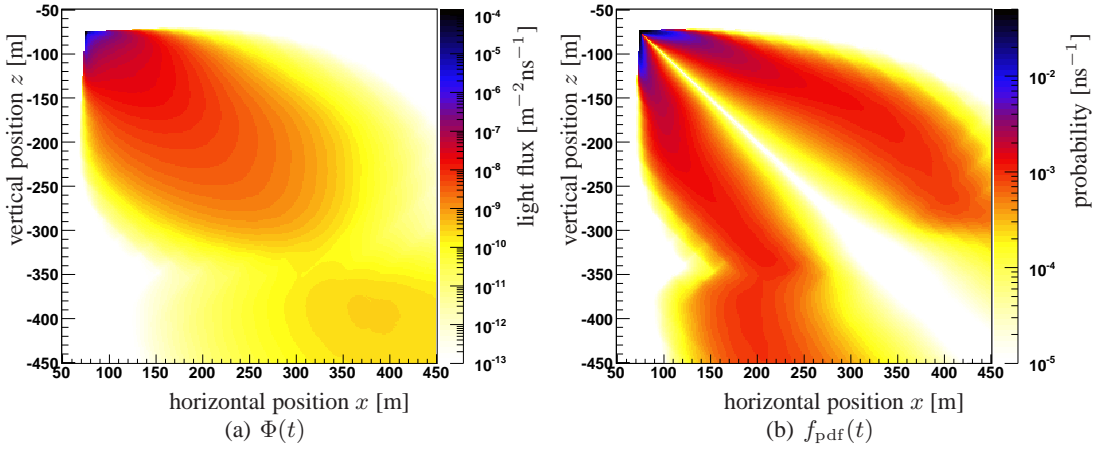
156

Figure 2: A snapshot of the light distribution produced by a simulated ultra-relativistic muon which entered from below, at an angle $\Theta_s = 135°$ diagonally towards the glacier surface ($\Theta_s = 180°$ would be straight upwards) passing through the origin at a depth of 1730 m below the glacier surface. Stronger fluxes $\Phi(t)$ are observed both above and below the particularly dusty region around $z = -350$ m which has stronger scattering and absorption. Scattering causes a bending of the Cherenkov light cone, most easily seen in the differential probability distribution $f_{pdf}(t)$, whose time integral is by definition normalized to unity at each spatial location. Inhomogeneities in the optical properties of the medium cause the additional structure seen in the figure, especially around -350 m.

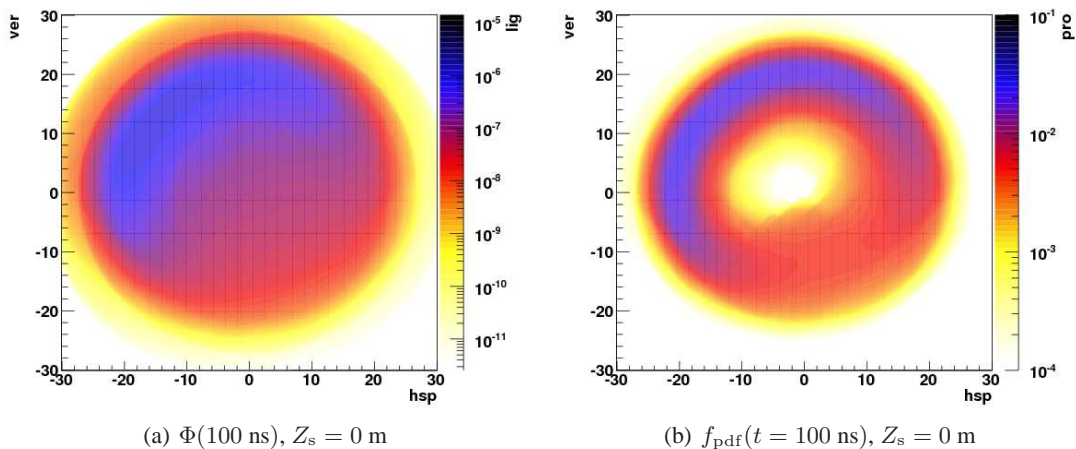Figure 3: The figures show the simulated light flux, $\Phi(t)$ and the probability distribution $f_{pdf}(t)$ of the light emitted from an idealized shower placed 1730 m below the glacier surface. The snapshot is taken $t = 100$ ns after light emission at the origin. The shower direction is $\Theta_s = 135°$, as for the muon in figure 2.

ations at depths greater than 1450 m, where air bubbles no longer exist, are explained by changes in climatic conditions which correlate with concentrations of insoluble dust deposits. At each 10 m depth interval, the effective scattering and absorptions lengths, λ_e and λ_a as function of wavelength were determined. As an example, the time distributions corresponding to two different wavelengths and light source–receiver positions were calculated and compared with experimental distributions, see figure 1.

The photon propagation and recording methods were applied to various idealized event types, such as the light emission from minimum ionizing muons, and from electromagnetic showers generated when ultra-relativistic electrons interact with the detector medium. Using a charged particle propagator such as MMC[4], the photon tables of idealized events types are dynamically combined to describe realistic composite events. The PHOTONICS photon simulation results are accessed directly through ROOT compliant C++ interfaces. The IceCube simulation programs query these interfaces and apply detector specific details such as simulation of electronics, data acquisition and triggers. For event reconstruction, PHOTONICS provides individual photon probability density functions (pdfs), and the expected number of detected photons. These are used by track-fitting algorithms, for example maximum-likelihood routines. The interface also delivers photon arrival times randomly drawn from the cumulative arrival time distributions.

Figure 2 shows the light distribution of a simulated minimum ionizing muon traveling diagonally upwards, on its way through the point $x = 0, z = 0$. At the front of the track, we observe a cross section of the unscattered Cherenkov wavefront, followed by a diffuse light cloud as the photons are scattered away from the geometrical Cherenkov cone. We also observe a weak deflection of the photons with higher flux $\Phi(t)$ both above and below the dusty ice region near $z = -350$ m.

Figure 3 shows a cross section of the light distribution of a simulated shower at a depth of 1730 m, 100 ns after light emission. Ultra-relativistic electrons deposit their energy much quicker than muons, confining most of the light emission to the vicinity of the interaction point, depending on

energy. At the same time, light may propagate hundreds of meters into glacial layers with very different optical properties. Shower-like event are more dependent on a complete implementation of variations in ice properties with depth since the localized light emission makes it harder to reconstruct the lepton direction. The use of PHOTONICS with heterogeneous ice models makes it possible for IceCube to adequately handle such events.

Conclusion

New photon propagation methods were implemented, and are in use in the simulation and reconstruction of particle physics events for IceCube. The PHOTONICS program is used for calculating and tabulating light distributions of calibration sources and ultra-relativistic charged particles, as a function of time and space in the heterogeneous South Pole glacier. The full depth and wavelength dependent ice description of [3] was implemented. Shower-like events (induced by ultra-relativistic electrons) are more sensitive to depthwise ice property variations than are muons. This is increasingly important for higher energies, as light propagates further into different glacial layers. The IceCube simulation can fully take into account how depth and wavelength dependent variations of the optical properties of the South Pole glacier distort the footprints of elementary particle interactions.

References

[1] J. Lundberg, P. Miocinovic, K. Woschnagg, T. Burgess, J. Adams, S. Hundertmark, P. Desiati, and P. Niessen, Light tracking through ice and water - Scattering and absorption in heterogeneous media with PHOTONICS Nucl. Instr. and Meth. A (2007), doi:10.1016/j.nima.2007.07.143

[2] L. Henyey and J. Greenstein, Diffuse radiation in the galaxy , Astrophys. Journal, vol. 93 (1941) 70

[3] AMANDA Collaboration: M. Ackermann et al, J. Geophys. Res. 111 (2006) D13203

[4] D. Chirkin and W. Rhode. Proceedings of the XVII International Cosmic Ray Conference (ICRC), Hamburg, Germany, 2001, p. 1017.

Reconstruction of high energy muon events in IceCube using waveforms

S. GRULLON[1], D.J. BOERSMA[1], G. HILL[1], K. HOSHINA[1], K. MASE[2] FOR THE ICECUBE COLLABORATION[A]

[1] *The IceCube Project, UW Madison, 222 West Washington Avenue, Madison WI, USA*
[2] *Chiba University, Yayoi-tyo 1-33, Inage-ku, Chiba-shi 263-8522, Japan*
[A] *See special section of these proceedings*
grullon@icecube.wisc.edu

Abstract:

We present a method to reconstruct the geometry and energy of high energy muon tracks in IceCube. Through a log-likelihood optimization procedure, an event hypothesis is obtained by maximizing the agreement of the expected amount of light (as function of time) in the optical modules with the shapes of the pulses recorded in the optical modules. This reconstruction method aims to use all information contained in the waveforms recorded in the IceCube digital optical modules (DOMs), by comparing those waveforms directly with the expected arrival time distribution of Cherenkov photons at the DOM after emission from a hypothetical track, taking into account the optical properties of the South Pole ice. We expect that this method will be effective in particular for highly energetic events in which a significant fraction of the DOMs records many photo-electrons. Currently, for simulated events within an energy range of $100\,TeV$ to $32\,\mathrm{PeV}$ which were reconstructed as throughgoing, we obtain an energy resolution of 0.34 in $\mathrm{Log}(E/\mathrm{GeV})$ and an angular resolution of $0.62°$.

Introduction

The IceCube telescope is being deployed in the Antarctic ice with its main goal to detect high energy neutrinos arriving from astrophysical sources. Nearly one third of the detector is installed and currently operational [1]. When fully deployed, the instrumented volume will be approximately $1\,\mathrm{km}^3$.

When a neutrino interacts in the ice in or near the detector, it produces a track or cascade signature. Some of the Cherenkov light emitted by the charged lepton and secondary charged particles triggers the DOMs. A DOM digitizes the signal from a $10\,\mathrm{inch}$ photo-multiplier in two ways: with an analog transient waveform digitizer (ATWD) and with a fast analog to digital converter (fADC) [2].

The main purpose of the ATWD is to record precise timing information of photons arriving in DOMs relatively close to the track or cascade. Therefore, it reads the same signal in 3 channels operating on different gains. Each channel has up to 128 bins with a bin witdh of $3.6\,\mathrm{ns}$. The main purpose of the fADC is to measure pulses with a wider time distribution from a further away track or cascade. It has 256 bins with a bin width of $25\,\mathrm{ns}$, giving a total time window of $6.4\,\mu\mathrm{s}$.

Given that the IceCube neutrino observatory records the full waveform information, a new likelihood reconstruction technique to exploit the full waveform information is the goal of the research described in this paper. Conventional reconstruction techniques [3] ported to IceCube from its predecessor, AMANDA, do not use the complete waveform. This is a reflection of the original AMANDA data acquisition system which recorded only the leading edge time of the pulse, the total charge of the pulse, and the total time over threshold of the pulse. These conventional reconstruction techniques in IceCube utilize this information by extracting pulse shapes from the ATWD or fADC waveforms and reconstruct a cascade or a muon hypothesis based on this information.

In this paper, we focus on the likelihood reconstruction of high energy muon tracks arising from extremely high energy (EHE) neutrinos with energies up to $10^{11} GeV$. EHE neutrinos should be produced when EHE cosmic rays interact with the cosmic microwave background [4]. The significant background due to atmospheric muons presents a major challenge, however. Since the zenith and energy distributions are different for signal and background, good geometry and energy reconstruction are vital for signal detection.

We hope that with the waveform-based event reconstruction method a significant improvement in sensitivity can be achieved for events at a wide energy range from $\sim 10\,TeV$ up to highest energies, $\sim$ EeV. At energies above $1\,\mathrm{PeV}$ we expect to increase the sensitivity by effectively reconstruction the energy of non-contained events.

Method

We define a function which gives the likelihood that the observed waveforms in the DOMs are the result of a given muon track. Using a standard minimizer algorithm, the track's position, direction and energy are found for which the likelihood has a maximum.

Expected photon arrival time distribution at a single DOM

A crucial element in the likelihood function is the description $\mu(t)$ of the expected number of photo-electrons as a function of time in a given DOM for a given muon track. This description consists of the expected total number of photo-electrons μ_{tot} together with a probability density function (PDF) $p(t)$ of the arrival time distribution of a single photon: $\mu(t) = \mu_{tot} \cdot p(t)$.

The μ_{tot} and PDF depend on the energy, direction, and the distance of the track to the DOM, the relative orientation of the DOM with respect to the track, and the optical properties of the ice between the track and the DOM.

At energies of a few hundred TeV and higher, most of the Cherenkov light is not emitted by the muon itself, but by its many secondaries and by the stochastic showers. For our reconstruction of
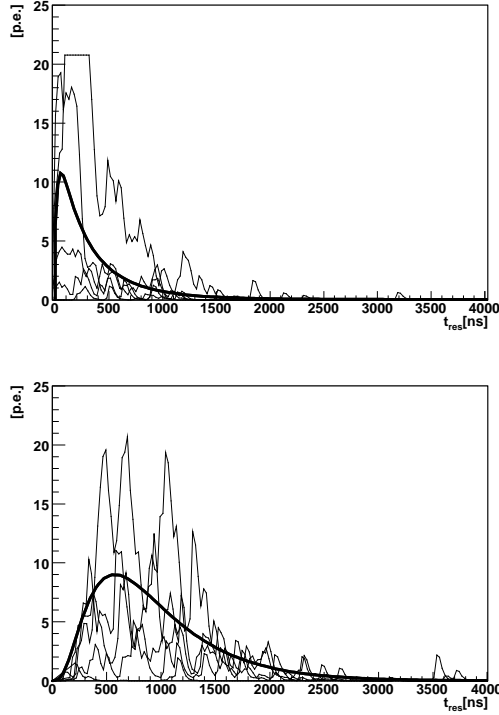

Figure 1: Comparison of the expected photo-electron distribution $\mu(t)$ (thick line) from photonics tables with some actual waveforms from the full MC simulation of high energy muons (thin lines). Upper figure: $1\,\mathrm{PeV}$ at $53\,\mathrm{m}$, lower figure: $100\,\mathrm{PeV}$ at $147\,\mathrm{m}$.

a high energy muon track, we assume that the muon track with stochastic showers can be approximated by an "infinite cascade" which is a string of equidistant average showers each with an energy deposit corresponding to the dE/dX energy loss of the track in the ice.

For the results in this paper, we took μ_{tot} and the PDF from a table generated using the "photonics" light propagation code [5]. An alternative approach uses a parametrization of the average waveforms obtained from the full IceCube simulation.

Fig. 1 shows the comparison between the expected photo-electron distribution $\mu(t)$ as obtained with photonics and individual waveforms as obtained in the full MC simulation.

It should be remarked that the individual waveforms may resemble the expected average waveform only at very high energies and in DOMs close

enough to the track. In most events, the individual waveforms in various DOMs will look different, as shown in Fig. 1. First, individual stochastics near the DOMs may produce fluctuations beyond the statistical (Poissonian) fluctuations from the average as modeled by the infinite cascade approximation. Second, when the $\mu(t)$ times the width a of a single photoelectron pulse is less than 1, then the of course the individual waveforms of the occasional individual photoelectrons will not follow that low PDF.

Poissonian likelihood for waveforms

The conventional reconstruction strategy described in the introduction works well for lower energy muon events in which the total charge corresponds to only a few photo-electrons. High energy muon events on the other hand are characterized by a large amount of deposited light and therefore produce wide, complicated waveforms with many photo-electrons. Reconstructing the geometry of a high energy muon track would benefit from the complete waveform information, as the width of the observed waveforms scales with the distance between the muon track and the DOM. A likelihood reconstruction of the muon energy would also require the complete waveform in order to measure the total amount of light deposited in the IceCube detector since this correlates with the energy of the muon.

The likelihood function using the complete waveform is formulated as follows. What is the probability of observing a waveform $f(t)$ given an expected photo-electron distribution $\mu(t)$? The waveform $f(t)$ is measured from the ATWD or the fADC, and the expected photo-electron arrival distribution is given by the PDF. The expected photo-electron arrival distribution depends on the hypothesis parameters, namely the geometry $\vec{x}$ (position of the muon at $t = t_0$ and its direction) and the energy, E. If you bin the waveform $f(t)$ into K bins, the probability of observing n_i photons in the ith waveform bin given an expectation of μ_i photons in the ith bin is given by Poissonian statistics. The overall probability for a single OM is given by the product over all waveform bins:

$$P(f(t)|\vec{x}, E) = \prod_{i=1}^{K} \frac{e^{-\mu_i}}{n_i!} \mu_i^{n_i} \qquad (23)$$

Taking the log of the Poissonian probability gives us:

$$\log P(f(t)|\vec{x}, E) = \sum_{i=1}^{K} \left(n_i \log \frac{\mu_i}{\mu_{tot}} \right) + N_{pe} \log \mu_{tot} - \mu_{tot} \qquad (24)$$

The first term is a sum over all waveform bins. Each term in the sum $n_i \log \frac{\mu_i}{\mu_{tot}}$ corresponds to the normalized timing probability of observing a photo-electron in the ith waveform bin weighted by the number of observed photo-electrons in the ith bin.

We evaluate Eq. 24 for all DOMs in the ice and sum these values as our log-likelihood function which we then maximize with respect to the free parameters of the track. This amounts to fitting the shape of the PDF to the measured waveform. This allows the reconstruction of not only the geometry of the muon, but also its energy.

One feature that needs to be addressed is the issue regarding the saturation of the waveform which the likelihood formula does not take into account. Currently, saturation is taken into account by simply truncating both the PDF and the measured waveform at some level close to the actual saturation level of the hardware, while sticking to the formalism of Poissonian statistics.

Fitting strategy

When reconstructing the muon track, there are in general six free parameters to fit (the vertex, direction, and the energy). Fitting the geometry and energy separately in three stages turns out to be more efficient than fitting them all at once. We seed the first stage of the reconstruction with a first guess of the geometry and the energy and proceed to fit the geometry only (five free parameters). We then seed the second stage with this result, fitting the energy only (one free parameter). Finally, we use this second stage result to seed a third fit, which refits the geometry again (five free parameters).
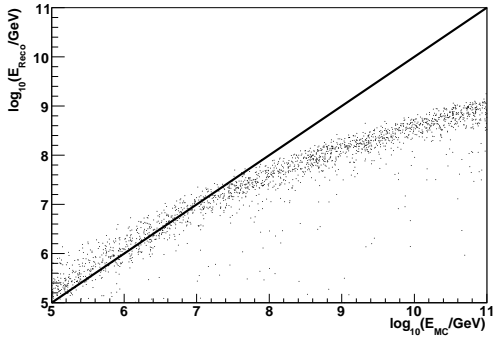
Figure 2: Reconstructed muon energy versus simulated energy for reconstructed tracks that go through the IceCube detector (see text). The diagonal line $E_{reco} = E_{true}$ is added to guide the eye.

Results

The energy reconstruction results are shown in Fig. 2 for a MC event sample simulated with an E^{-1} spectrum and an energy range from $10\,TeV$ to $100\,\mathrm{EeV}$ with 4π coverage in the full 80-string IceCube geometry. Only reconstructed throughgoing muon tracks are selected, which are muon tracks whose point of closest approach to the geometrical center of the IceCube detector is within the IceCube array.

At energies above $\sim 30\,\mathrm{PeV}$, the reconstructed energy is systematically low due to saturation in the DOMs, which is currently not taken into account. The slope of the distribution for energies below 30 PeV may be improved by adjusting the "infinite cascade" model, in particular the relation between the energy of the muon track and the energy in an average shower of the infinite cascade. For energies below 30 PeV, approximately 31% of the events are reconstructed as throughgoing.

For throughgoing muon tracks and $E_{MC} < 30\,\mathrm{PeV}$, the angular resolution (defined as the median of the distribution of angular differences of the reconstructed and simulated muon tracks) is found to be $0.62°$. Our obtained energy resolution is 0.34 in $\mathrm{Log}(E/\mathrm{GeV})$. With the traditional AMANDA style reconstruction about 35% of the events are reconstructed as throughgoing, with an angular resolution of $0.63°$.

Outlook

The waveform based reconstruction as currently implemented performs reasonably well. With a sample of simulated high energy events, we obtain an angular resolution comparable or better than conventional reconstruction methods.

We have identified several aspects of the algorithm and its implementation which can still be improved, including a proper way to use the information of saturated DOMs. This should further improve the energy resolution (currently 0.34 in $\mathrm{Log}(E/\mathrm{GeV})$) and extend the energy range beyond 1EeV. The results of this paper are only for throughgoing muon tracks; we hope to present similar results for high energy non-contained events as well.

The method is in principle not limited to track-like events; it can be applied to events of any signature, such as showers and possibly also muon bundles.

Acknowledgements

References

[1] A. Karle et al. , (IceCube collaboration), these proceedings (abstract 1180)

[2] A. Achterberg et al. , Astroparticle Physics **26** (2006), 155-173

[3] J. Ahrens et al. , *Nucl. Instr. and Meth.* **A** 524 (2004), p. 169-194, arxiv:astro-ph/0407044

[4] K. Greisen, *Phys. Rev. Lett.* **16**, 748 (1966). G.T. Zatsepin and V.A. Kuzmin, *JETP. Lett.* **4**, 78 (1966).

[5] J. Lundberg et al. , arXiv:astro-ph/0702108, submitted to *Nucl. Instr. and Meth.* **A**.

Radio Detection of GZK Neutrinos - AURA status and plans

H. LANDSMAN[1] FOR THE ICECUBE COLLABORATION[2], L. RUCKMAN[3], G. S. VARNER[3]

[1]*Department of Physics, University of Wisconsin, Madison, WI 53706, U.S.A*

[2] *See special section of these proceddings.*

[3] *Dept. of Physics and Astronomy, University of Hawaii, Manoa, HI 96822, U.S.A*

hagar@icecube.wisc.edu

Abstract: The excellent radiofrequency transparency of cold polar ice, combined with the coherent Cherenkov emission produced by neutrino-induced showers when viewed at wavelengths longer than a few centimeters, has spurred considerable interest in an ultimate, large-scale radiowave neutrino detector array. A statistically compelling GZK signal will require at least an order of magnitude improvement in the product of (livetime)x(Effective volume) over existing (RICE, ANITA, e.g.) neutrino detection experiments. Correspondingly, the AURA (Askaryan Underice Radio Array) experimental effort seeks to take advantage of the opportunity presented by IceCube drilling through 2010 to establish the radiofrequency technology needed to achieve $100 - 1000 km^3$ effective volumes. We discuss three test strings co-deployed with IceCube in 2006-07 which combine fast in-ice digitization with an efficient, multi-tiered trigger scheme. Ultimately, augmentation of IceCube with large-scale $(1000 km^3 sr)$ radio and acoustic arrays would extend the physics reach of IceCube into the EeV-ZeV regime and offer substantial technological redundancy.

Introduction and Detection Principle

The Astrophysical high energy neutrinos hold valuable information about their sources, either a point source like GRBs, AGNs, and SGRs, or high energy cosmic rays (through the GZK process). Consequently they can also teach us EHE particle physics in energies unreachable by earthbound accelerators.

As the energy of the neutrino increases the atmospheric neutrino background flux decreases and the interaction cross section of the neutrino increases, which favors the detection of HE neutrinos over low energy ones. On the other hand, the estimated fluxes of those high energy neutrinos exhibit an overall decrease with energy. The combination of a small flux, low neutrino interaction cross section, and limited life span of humans require the construction of large scale detectors to improve the detection probability.

The km^3 scale detectors like IceCube, AMANDA, NEMO and Antares are (will be) made of thousands of photo-multiplier tubes, sensitive to opti-

cal photons. They are sensitive to neutrinos with energies between $10^2 GeV - 10^{10} GeV$. In order to survey the extreme high energy regime of more than $10^{10} GeV$, larger detectors are needed.

In 1968, G.A.Askaryan [1] suggested that cascades generated by high energy charged leptons moving through matter, produce an excess of negative charge moving at relativistic speed, thus emitting Cherenkov radiation. For radiation with shorter wavelength, like optical photons, the phase is random and the electric field is proportional to the square root of the net negative charge developed in the cascade. But for photons with wavelengths longer than the transverse dimensions of the cascade, like RF photons, the radiation is coherent and the electric field is proportional to the negative charge in the cascade. It is expected that neutrinos with energy of$\sim 10^{18} eV$ or more will produce cascades with transverse dimensions of order ~ 0.1 meters, thus emitting coherent RF radiation. Radio-frequency neutrino detectors are therefore more sensitive to such high energy events than optical detectors .

This effect was demonstrated in an accelerator measurement where coherent linearly polarized RF radiation was measured from the interaction of a beam dumped into RF transparent matter (sand, salt and ice)[2]. The simpler installation of radio detectors, the long attenuation length of RF in ice and the sensitivity to EHE events makes the RF region a useful probe for EHE neutrino detection.

Several experiments are already using the Askaryan effect for neutrino detection in Antarctica: The RICE array was deployed with the AMANDA neutrino telescope near the South Pole at depths of 100-300 m. The array consists of 20 dipole antennas covering a volume of $200 \times 200 \times 200 m^3$, and is sensitive between 200 to 500 MHz. RICE established limits on high energy neutrino fluxes as well as investigated the radio-glacial properties of the deep ice [3]. The ANITA experiment, air borne at 40km, observed the Antarctic ice searching for RF emission. The high altitude makes the volume that ANITA covers large (1.5 million km^3), but the short flight time and the refraction of RF photons in the transition from ice to air limits the exposure time and the angular coverage of this experiment [4].

Detector design and 2006/2007 Deployment

In the austral summer of 2006-2007, three Radio Clusters were co-deployed with the IceCube optical array as part of the AURA (Askaryan Under-ice Radio Array) experimental effort. Each cluster consists of up to four broadband dipole antennas, centered at 400MHz, and four metal tubes holding the front-end electronics including filters and amplifiers supporting these antennas: specifically, a 450 MHz notch filter to reject constant noise from the South Pole communication channel, a 200 MHz high pass filter and a $\sim 45dB$ amplifier. An additional $\sim 20dB$ amplification is done at later stage, for a total of $\sim 65dB$ amplification. An additional antenna is used as a transmitter for calibration.

The DRM (Digital Radio Module) within a 13 inch diameter glass sphere contains the triggering, digitization and communication electronics as well as a power converter. It holds the TRACR board(Trigger Reduction And Communication for RICE) that controls the calibration signal and the high triggering level, the SHORT board (SURF High Occupancy RF Trigger) that provides frequency banding of the trigger source, the ROBUST card (Read Out Board UHF Sampling and Trigger) that provides band trigger development, high speed digitization and second level trigger discrimination, the LABRADOR (Large Analog Bandwidth Recorder And Digitizer with Ordered Readout)[5] digitization chip, and a Motherboard that controls the power, communication and timing.

A 260-capacitor Switched Capacitor Array (SCA) continuously observes the input RF channels (two channels per antenna) and an additional timing channel. To reduce power consumption and dead times, the information is held and digitized only when a trigger is received. The sampling speed is two Giga-Samples Per Second, with a 256 ns buffer depth. A 300 MHz on-board Advanced Transient Waveform Digitizer is used for precise trigger timing. A Wilkinson type ADC converts the measured voltage into a count value with a 12-bit dynamic range.

Six cables are connected to the DRM. One for power and communication with the surface and five for the transmitter and receiver antennas. The spacing between the antennas is 13.3 meters, and the total length of the cluster is 40 meters. The AURA cluster is shown in figure 1.

The fast and broadband nature of the Askaryan RF signal is exploited for background reduction. Once the voltage measured on an antenna crosses an adjustable threshold, the digitization is triggered and the signal is split into four frequency bands (200-400 MHz, 400-650 MHz, 650-880 MHz and 880-1200 MHz). If enough frequency bands are present in the signal, the channel associated with this antenna will trigger. In the current settings, at least two out of four bands are needed for triggering to happen. The cluster will trigger if enough channels trigger (current setting requires at least three out of four antennas).

The digitized data is sent to the surface using the IceCube in-ice and surface cables.

IceCube on-going construction activity made it possible to deploy clusters down to 1400 meters deep, a depth that is usually less favored by RF de-

tectors due to warmer ice and high drilling cost. The clusters were deployed on the top of IceCube strings, at depths of 1400 or 400 meters.

Table 1 summarizes the depth and location of the three units. Out of the 8 receivers deployed, 7 receivers are operational. One channel was tested fine before deployment, and most likely damaged during the freeze-in of the water surrounding the cluster after deployment. The data being taken consists of ambient and transient background studies, calibration runs using the AURA transmitter and the in-ice RICE transmitters.

The proximity of the South Pole station and especially the IceCube and AMANDA detectors may cause significant RF noise in the AURA sensitive band of $200 - 1200$ MHz. This noise pattern is being carefully studied and the amplified background noise frequency has a clear enhancement between $200 - 400$ MHz, with an amplitude of about $50mV$ corresponding to 7 ADC bits depth. The noise spectrum and intensity depends on the location of the antenna relative to the DRM and the type of front-end amplifier used. Background studies were also performed with the IceCube and AMANDA detectors turned off. Figure 2 shows sample waveforms taken for background studies with and without the transmitter antenna on for a single antenna.

2008 Deployment and beyond

The concept of a GZK radio frequency detector, deployed in shallow depths or in a surface array had been suggested more than 20 years ago [6]. A future large scale GZK $100km^2$ scale detector will be a hybrid of different Cherenkov radiation detection techniques, allowing composite trigger and coincidence and can be built around IceCube. The long attenuation length of the ice (hundreds of meters), makes the South Pole ice a natural choice for deploying a RF detector.

In the next season (2007-2008) we plan to continue our efforts to design and build a shallow GZK neutrino detector. We will continue to use the IceCube deep holes and existing deployment and DAQ infrastructure for deploying additional clusters. We will investigate different depths $(1400, 200, < 100$ meter and surface) and study the noise in lower frequencies $(< 200$MHz$)$ since the acceptance is ex-
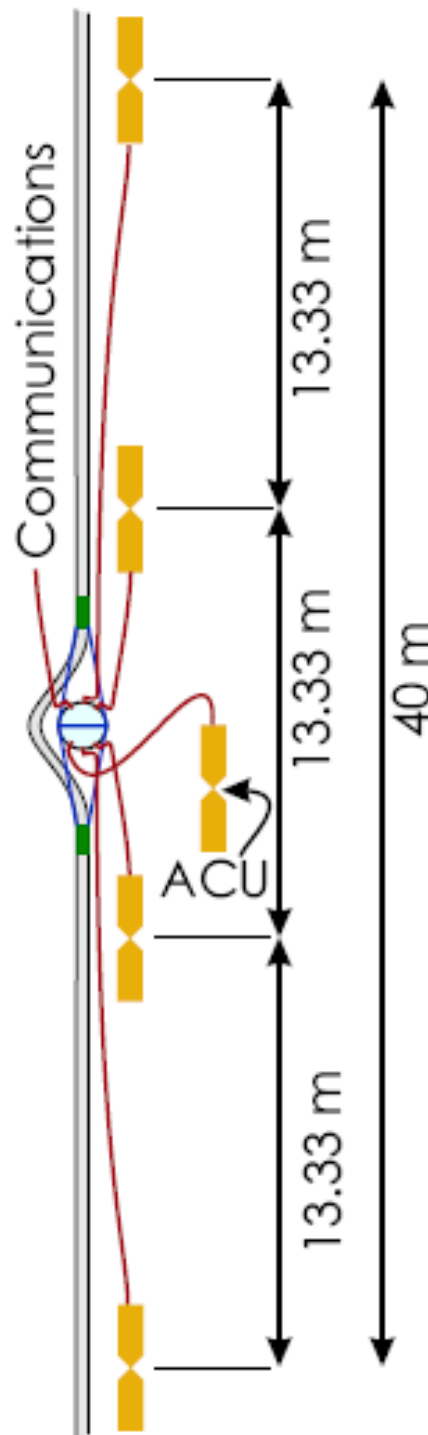
Figure 1: The radio cluster, made of a DRM (Digital Radio Module), and 5 antennas (4 receivers and a transmitter).

Cluster	num. Transmitters	num. Receivers	Location (x,y,z) in m	Front end amplifier brand
1	1	4	$(50, 500, -1400)$	Miteq
2	1	4	$(220, 210, -250)$	LNA-SSA
3	1	0	$(195, 120, -1400)$	None

Table 1: Locations of the deployed clusters. Coordinates are relative to IceCube center array at surface.
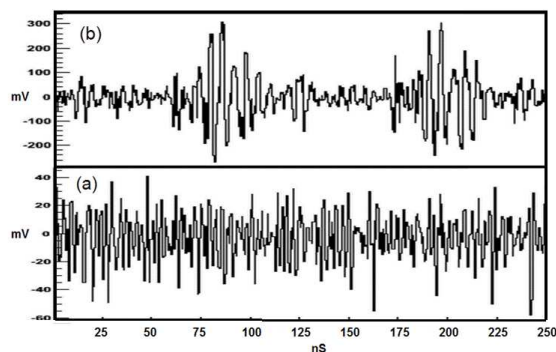

Figure 2: Wave form signals for a single antenna for background and calibration runs. (a) Background only (b) In ice transmitter pulse.

pected to increase with wavelength, albeit at the expense of timing resolution.

A cluster will also be deployed $\sim$ $1km$ away from the IceCube array to study the ice and environment away from the IceCube array, and investigate possible solutions to communication and power distribution challenges that a large scale array presents. A surface array of radio detectors is relatively easy to deploy, but the refractive index difference between the ice, firn (soft ice layers on top of the glacier) and air decreases the angular acceptance of a surface detector due to total reflection of rays propagating between the layers. On the other hand, deeper deployments in depths of tens to hundreds of meters increases the technical difficulties and cost of such an array.

The design of the cluster will be similar to last year's clusters with possible minor changes to the antennas and electronics. By deploying at different depths and locations the RF properties of the ice, the suitability of ice for such of detector and studies of different cluster designs will be checked, while building a sub-GZK detector that will be able to detect HE events, reconstruct vertices, and look for events coincident with IceCube.

Once completed, IceCube is expected to measure about 1 GZK event per year. A sucessful GZK detector deployed on surface or in shallow depth will have to measure at least $\sim 10GZK$ events a year. A hybrid of the RF array and IceCube will give sub-samples of coincidences events with cross-calibration capabilities and unique signal signatures.

Summary

Three radio clusters were deployed at the South Pole as an extension to the IceCube array. In the next year, we plan to deploy additional clusters to have a sufficient 3D array for vertices reconstruction, make radio-glaciological measurement at different depths and distances from the Ice-Cube array, and check the suitability of the Ice-Cube environment for RF detection. These are the first steps toward building a $100km^2$ GZK detector built around IceCube. Such a detector will be a powerful tool in investigating the EHE neutrino world.

Acknowledgements

References

[1] G.A. Askaryan, JETP 14, (1962) 441.; JETP 21, (1965) 658.

[2] P.W. Gorham *et al.* (ANITA collaboration), hep-ex/0611008

[3] I. Kravchecko et al., Phys. Rev. D73, (2006) 082002.

[4] S.W. Barwick *et al.*, Phys. Rev. Lett. 96 (2006) 171101.

[5] G.S. Varner *et al.*, physics/0509023

[6] Gusev and Zheleznykh, JETP 38, (1983) 505.